Canadian
Journal of Physics

EDITORIAL BOARD

Canadian
Journal of Physics

THE QUANTIZATION OF CLASSICAL SPIN THEORY[1]

By S. SHANMUGADHASAN

ABSTRACT

The antisymmetric spin tensor of rank two used to describe the rotational motion of a particle is assumed to satisfy the constraint condition that the velocity 4-vector is orthogonal to it. Since the dipole moment is proportional to the spin tensor, this condition leads always to a purely magnetic dipole in the rest system of the particle. Frenkel has indicated how the action principle for the classical equations of motion can be set up treating the above constraint condition as a supplementary condition. The Hamiltonian dynamics of a system having supplementary conditions and Lagrange undetermined multipliers has been discussed recently by Dirac. Dirac's method and results previously obtained give the required Hamilton–Jacobi equations and Poisson Brackets of the dynamical variables. The cases where the particle behaves like a pure gyroscope and a symmetrical top are treated. When there is an interacting field, it is assumed that the action of the field is given by the effective 4-vector potential without further specification. The orthogonality of the velocity to the tensor dual to the spin tensor can be imposed as an alternative constraint condition. This possibility is discussed briefly. The quantum formulation is completed with the help of the standard analogy rules.

1. INTRODUCTION

The present paper is part of a systematic study of the quantization of the classical theory of spinning particles begun earlier. In the previous papers (14, 15, 16) on this subject, there is no connection between the translational motion and the rotational motion of the particle. That is, there is no relation between the velocity 4-vector of the particle and the antisymmetric tensor of rank two used to describe the spin angular momentum of the particle. Then, since the dipole moment is taken to be proportional to the spin of the particle, it is possible for a particle which has a purely magnetic dipole moment in some rest system to develop in a suitable external field an electric moment perpendicular to its magnetic moment in some other rest system. The elementary particles known in nature do not seem to behave in this fashion. Because of this, the quantum theory corresponding to such a classical theory may not be applicable to the experimentally observed particles.

Some authors hold that the spin angular momentum is described in a relativistic theory by an antisymmetric tensor of the second rank which is orthogonal to the velocity 4-vector. Then the spin tensor has only three independent components, and its space–time components vanish in the rest system of the particle. When the dipole moment is taken to be proportional to such a spin tensor, the particle has always a purely magnetic dipole in the rest system. As a consequence

of the above constraint condition the invariant scalar product of the spin tensor and of the tensor dual to it vanishes. Further, in the case of free particles without an interacting field, the invariant square of the spin tensor is a constant. It is assumed to be a constant even when there is an interacting field. This is automatically satisfied when the dipole moment is proportional to the spin tensor. This constant enables one to introduce a fundamental constant of the dimension of a length into the theory. There is an extensive literature (7, 17, 1, 2, 13, 10, 20, 18, 3) on the classical theory of spinning particles using a spin tensor of the above type. The quantization of such classical theories is carried out in this paper.

It may be noted that, when there is no constraint condition on the spin tensor, the momentum 4-vector of the particle is parallel to the velocity 4-vector. But when there is a constraint condition, the momentum 4-vector consists of two parts, one parallel to the velocity and the other (arising from the spin angular momentum) normal to the velocity. "Longitudinal" and "transverse" momenta have appeared as a feature of the theories of the electron set up by Abraham and by Lorentz using extended models for the particle.

Frenkel (7) has shown how the constraint condition can be taken into the variational principle for the equations of motion as a supplementary condition by using a Lagrange undetermined multiplier 4-vector. But he has not discussed the corresponding canonical formalism. Though there have been subsequent attempts (11, 8, 9, 12) to do this, the results obtained are not completely satisfactory. The undetermined multiplier 4-vector is responsible for the difficulty. However, in his scheme of generalized Hamiltonian dynamics, Dirac (5) has dealt with the canonical formalism of a dynamical system of exactly the type considered here. Immediate application of the work of Dirac leads to the required canonical formalism. But the results obtained previously when there is no constraint condition are necessary for the purpose.

The two cases considered are those in which the particle has a total spin angular momentum analogous to that of a pure gyroscope or of a symmetrical top (for brevity referred to thus below). The particles considered are either free or interacting with a field. When there is a field, it is supposed that the effective field is used in the various equations. This field is not specified precisely, because this question has not been satisfactorily settled at present. The dynamics of the field variables is therefore not discussed.

The spin theory considered here evidently shows more interesting mathematical and physical features than the spin theory quantized previously. This paper is devoted only to the canonical formalism and the straightforward quantization using the analogy rules. Other developments and the discussion of the quantum theoretical equations obtained below are reserved for a later paper.

2. HAMILTONIAN DYNAMICS OF THE PURE GYROSCOPE

The usual relativistic notation in Lorentz space, given in (15), is used in this work except when stated otherwise. Let p_μ be the momentum 4-vector, $\dot{z}_\mu \equiv v_\mu$ the velocity 4-vector, $S_{\mu\nu}$ the spin tensor, and $N_{\mu\nu}$ the total spin angular momentum tensor. In the case of the pure gyroscope, $N_{\mu\nu}$ is just $S_{\mu\nu}$. Then, when there is no

interacting field, the conservation of energy, momentum, and angular momentum gives the equations

[2.1]
$$\dot{p}_\mu = 0,$$

[2.2]
$$\dot{S}_{\mu\nu} = p_\mu v_\nu - p_\nu v_\mu,$$

where the dots denote differentiation with respect to the proper-time s. The above and the constraint condition between v_μ and $S_{\mu\nu}$

[2.3]
$$S_{\mu\nu} v^\nu = 0$$

form the complete scheme of equations.

Introduce now the angular velocity tensor $P_{\mu\nu}$ of the rotating particle. $P_{\mu\nu}$ is the velocity corresponding to the quasi-coordinate rotation tensor $Q_{\mu\nu}$, so that $P_{\mu\nu} = dQ_{\mu\nu}/ds$. Let the particle be at the origin of a fixed system of coordinates. Let y_μ be a vector of constant magnitude attached to the particle. When the particle is subjected to an infinitesimal rotation $dQ_{\mu\nu}$, the vector y_μ rotates with the particle, and the change in y_μ when referred to the fixed coordinate system is given by

[2.4]
$$dy_\mu = dQ_{\mu\nu} y^\nu.$$

Similarly

[2.5]
$$\delta y_\mu = \delta Q_{\mu\nu} y^\nu.$$

The change in the tensor $S_{\mu\nu}$ due to an infinitesimal rotation $dQ_{\mu\nu}$ is

[2.6]
$$dS_{\mu\nu} = [dQ.S]_{\mu\nu},$$

so that

[2.7]
$$\dot{S}_{\mu\nu} = [P.S]_{\mu\nu}.$$

Here $[P.S]_{\mu\nu}$ denotes $P_{\mu\lambda} S^\lambda_{.\nu} - P_{\nu\lambda} S^\lambda_{.\mu}$.

The transitivity equation corresponding to the quasi-coordinates $Q_{\mu\nu}$ is easily obtained as follows. From [2.4] and [2.5] one gets

$$\delta dy_\mu = y^\nu \, \delta dQ_{\mu\nu} + dQ_{\mu\nu} \, \delta y^\nu = y^\nu \, \delta dQ_{\mu\nu} + y^\sigma \, dQ_{\mu\nu} \, \delta Q^\nu_{.\sigma},$$

$$d\delta y_\mu = y^\nu \, d\delta Q_{\mu\nu} + y^\sigma \, \delta Q_{\mu\nu} \, dQ^\nu_{.\sigma}.$$

Since $\delta dy_\mu = d\delta y_\mu$, it follows that $y^\nu(\delta d - d\delta)Q_{\mu\nu} = y^\nu[\delta Q \, . \, dQ]_{\mu\nu}$. Since this is true for all y^ν of the specified type, the transitivity equation for $Q_{\mu\nu}$ is

[2.8]
$$(\delta d - d\delta)Q_{\mu\nu} = [\delta Q \, . \, dQ]_{\mu\nu}.$$

For later use this is written in the equivalent form

$$(\delta d - d\delta)Q_{\mu\nu} = \tfrac{1}{4}\{g_{\beta\gamma}(g_\alpha{}^\mu g_\delta{}^\nu - g_\alpha{}^\nu g_\delta{}^\mu) - g_{\alpha\gamma}(g_\beta{}^\mu g_\delta{}^\nu - g_\beta{}^\nu g_\delta{}^\mu)$$
$$+ g_{\alpha\delta}(g_\beta{}^\mu g_\gamma{}^\nu - g_\beta{}^\nu g_\gamma{}^\mu) - g_{\beta\delta}(g_\alpha{}^\mu g_\gamma{}^\nu - g_\alpha{}^\nu g_\gamma{}^\delta)\}\delta Q^{\alpha\beta} \, dQ^{\gamma\delta}$$

[2.9]
$$= C^{\mu\nu}{}_{\alpha\beta\,\gamma\delta} \, \delta Q^{\alpha\beta} \, dQ^{\gamma\delta},$$

say.

The canonical formulation of the equations of motion is carried out here with the help of an action principle. Consider the action integral

[2.10] $$I_1 = \int_{s_0}^{s} L \, ds = \int_{s_0}^{s} (p_\mu v^\mu - \tfrac{1}{2} S_{\mu\nu} P^{\mu\nu}) ds.$$

The integrand of [2.10] (that is the Lagrangian) is positively homogeneous of degree one in the derivatives with respect to the parameter s. Therefore the action integral [2.10] is independent of the parameter s except that s appears in the limits of integration. One can transform to any other parameter provided the limits of integration are the same. Since from [2.8]

$$\delta S_{\mu\nu} P^{\mu\nu} + S_{\mu\nu} \delta P^{\mu\nu} = S_{\mu\nu} \, d(\delta Q^{\mu\nu})/ds,$$

and since $\delta p_\mu = \delta Q_{\mu\nu} p^\nu$, the variation of I_1 gives

[2.11] $$\delta I_1 = (p_\mu \delta z^\mu - \tfrac{1}{2} S_{\mu\nu} \delta Q^{\mu\nu})_s$$

$$+ \int_{s_0}^{s} \{ - \dot{p}_\mu \delta z^\mu + \tfrac{1}{2}(\dot{S}_{\mu\nu} - p_\mu v_\nu + p_\nu v_\mu) \delta Q^{\mu\nu} \} ds,$$

where the suffix s shows that the quantity is taken at the final value s. In forming δI_1 the variations of the dynamical variables are taken to vanish at s_0. As pointed out by Dirac (4), there is no need to vary the limits, since s is arbitrary.

The coefficients of δz^μ and $\delta Q^{\mu\nu}$ in the expression under the integral sign in [2.11] give the correct translational and rotational equations of motion [2.1], [2.2] respectively. Therefore [2.10] is the correct action integral for a free spinning particle without the constraint condition [2.3]. When the equations of motion are taken into account, the remaining terms of δI_1 give the canonically conjugate coordinates and momenta of the dynamical system in the usual way. Thus the Poisson Brackets (henceforth called P.B.'s) satisfied by the momenta p_μ and the coordinates z_μ are

[2.12] $$[z_\mu, z_\nu] = 0, \quad [p_\mu, p_\nu] = 0, \quad [p_\mu, z_\nu] = g_{\mu\nu}.$$

The quasi-momenta conjugate to the quasi-coordinates $Q^{\mu\nu}$ are $- S_{\mu\nu}$. The P.B.'s for the $S_{\alpha\beta}$ variables can be deduced from this by the following analysis.

Let the quasi-coordinates $Q^{\alpha\beta}$ and the true coordinates $q^{\mu\nu}$ be connected by

[2.13] $$dQ^{\alpha\beta} = \tfrac{1}{2} A^{\alpha\beta}{}_{\mu\nu} \, dq^{\mu\nu}, \quad dq^{\mu\nu} = \tfrac{1}{2} B^{\mu\nu}{}_{\alpha\beta} \, dQ^{\alpha\beta},$$

so that

[2.14] $$\tfrac{1}{2} A^{\alpha\beta}{}_{\mu\nu} B^{\mu\nu}{}_{\rho\sigma} = \delta^{\alpha\beta}_{\rho\sigma},$$

where $\delta^{\alpha\beta}_{\rho\sigma}$ is the generalized Kronecker symbol. Then, from [2.13] and [2.9], one gets

$$(\delta d - d\delta) Q^{\alpha\beta} = \tfrac{1}{4} \{ (\partial A^{\alpha\beta}{}_{\mu\nu}/\partial q^{\rho\sigma})(\delta q^{\rho\sigma} \, dq^{\mu\nu} - dq^{\rho\sigma} \, \delta q^{\mu\nu}) \}$$

$$= \tfrac{1}{16} \{ (\partial A^{\alpha\beta}{}_{\mu\nu}/\partial q^{\rho\sigma}) - (\partial A^{\alpha\beta}{}_{\rho\sigma}/\partial q^{\mu\nu}) \} B^{\rho\sigma}{}_{\gamma\delta} B^{\mu\nu}{}_{\lambda\tau} \, \delta Q^{\gamma\delta} \, dQ^{\lambda\tau}$$

[2.15] $$= C^{\alpha\beta}{}_{\gamma\delta \, \lambda\tau} \, \delta Q^{\gamma\delta} \, dQ^{\lambda\tau}.$$

The quasi-momenta $R_{\alpha\beta}$ and the corresponding true momenta p_μ, obtained from the Lagrangian L are connected by

$$R_{\alpha\beta} = \frac{\partial L}{\partial \dot{Q}^{\alpha\beta}} = \frac{1}{2}\frac{\partial L}{\partial \dot{q}^{\mu\nu}}\frac{\partial \dot{q}^{\mu\nu}}{\partial \dot{Q}^{\alpha\beta}} = \tfrac{1}{2}p_\mu,\ B^{\mu\nu}{}_{\alpha\beta},$$

so that $p_\mu = \tfrac{1}{2}A^{\alpha\beta}{}_\mu,\ R_{\alpha\beta}$. Then, since the p_μ, are true momenta and the $B^{\mu\nu}{}_{\alpha\beta}$ are functions of the true coordinates $q^{\mu\nu}$, the P.B.'s satisfied by $R_{\alpha\beta}$ are given by

$$[R_{\alpha\beta},\ R_{\gamma\delta}] = \tfrac{1}{4}[p_{\lambda\mu}\ B^{\lambda\mu}{}_{\alpha\beta},\ p_{\nu\sigma}\ B^{\nu\sigma}{}_{\gamma\delta}]$$

$$= \tfrac{1}{4}\{B^{\lambda\mu}{}_{\alpha\beta}\ p_{\nu\sigma}[p_{\lambda\mu},\ B^{\nu\sigma}{}_{\gamma\delta}] + B^{\nu\sigma}{}_{\gamma\delta}\ p_{\lambda\mu}[B^{\lambda\mu}{}_{\alpha\beta},\ p_{\nu\sigma}]\}$$

$$= \tfrac{1}{8}\{B^{\lambda\mu}{}_{\alpha\beta}\ A^{\rho\tau}{}_{\nu\sigma}\ R_{\rho\tau}(\partial B^{\nu\sigma}{}_{\gamma\delta}/\partial q^{\lambda\mu}) - B^{\nu\sigma}{}_{\gamma\delta}\ A^{\rho\tau}{}_{\lambda\mu}\ R_{\rho\tau}(\partial B^{\lambda\mu}{}_{\alpha\beta}/\partial q^{\nu\sigma})\}$$

$$= -\tfrac{1}{8}\{(\partial A^{\rho\tau}{}_{\nu\sigma}/\partial q^{\lambda\mu}) - (\partial A^{\rho\tau}{}_{\lambda\mu}/\partial q^{\nu\sigma})\}B^{\lambda\mu}{}_{\alpha\beta}\ B^{\nu\sigma}{}_{\gamma\delta}\ R_{\rho\tau}$$

[2.16]
$$= -2C^{\rho\tau}{}_{\alpha\beta\ \gamma\delta}\ R_{\rho\tau}.$$

The relation [2.15] and relations of the form

$$A^{\rho\tau}{}_{\nu\sigma}(\partial B^{\nu\sigma}{}_{\gamma\delta}/\partial q^{\lambda\mu}) + B^{\nu\sigma}{}_{\gamma\delta}(\partial A^{\rho\tau}{}_{\nu\sigma}/\partial q^{\lambda\mu}) = 0$$

obtained by differentiating [2.14] have been used in the above reduction. Since $R_{\alpha\beta} = -S_{\alpha\beta}$ from [2.11], it follows from [2.9] and [2.16] that

[2.17]
$$[S_{\alpha\beta},\ S_{\gamma\delta}] = -g_{\alpha\gamma}\ S_{\beta\delta} + g_{\beta\gamma}\ S_{\alpha\delta} + g_{\alpha\delta}\ S_{\beta\gamma} - g_{\beta\delta}\ S_{\alpha\gamma}.$$

This has been obtained before in (14, 15, 16) by different methods.

In order to set up the action principle for the complete scheme of equations of motion, the constraint condition [2.3] is treated as a supplementary condition. Then, as in the work of Frenkel (7), the required action integral is

[2.18]
$$I_2 = I_1 + \int_{s_0}^{s} a^\mu\ S_{\mu\nu}\ v^\nu\ ds,$$

where I_1 is given by [2.10] and a^μ is the Lagrange undetermined multiplier 4-vector. I_2 is independent of the parametric representation used. Now

$$\delta I_2 = \delta I_1 + (a^\nu\ S_{\nu\mu}\ \delta z^\mu)_s +$$

[2.19]
$$\int_{s_0}^{s}\{\delta z^\mu \frac{d}{ds}(S_{\mu\nu}\ a^\nu) + \tfrac{1}{2}[S.D]_{\mu\nu}\ \delta Q^{\mu\nu} + S_{\mu\nu}\ v^\nu\ \delta a^\mu\}ds,$$

where $D_{\mu\nu}$ denotes $a_\mu\ v_\nu - a_\nu\ v_\mu$.

The coefficients of δz^μ and $\delta Q^{\mu\nu}$ in the expression under the integral sign in [2.19] give the translational and rotational equations of motion. Note that the new momentum 4-vector is the sum of the unconstrained 4-momentum from [2.10] and of $a^\nu\ S_{\nu\mu}$. The coefficient of δa^μ gives the supplementary condition [2.3]. From [2.19] it is seen that the momenta canonically conjugate to the coordinates a^μ vanish. The canonical formulation of these equations therefore follows the method given by Dirac (5, §8) for systems of this type. Eden (6) calls such a system a constrained holonomic system.

When a dynamical system has coordinates whose canonically conjugate momenta vanish, Dirac does not count these variables as coordinates from the beginning, and does not introduce momenta conjugate to them at all. The Lagrange equations corresponding to such coordinates are treated as supplementary conditions. These supplementary conditions can be expressed in terms of the canonically conjugate coordinates and momenta, and involve the variables, such as a^μ in the present case, which have no conjugate momenta. By treating the supplementary conditions expressed thus as strong equations in the sense of Dirac (4, 5), the variables such as a^μ are defined in terms of the canonically conjugate coordinates and momenta. Then the variables of the type a^μ play no further role in the theory.

Since the momentum 4-vector corresponding to the action integral [2.10] can be written in the form Mv_μ, where M is a constant, the total momentum corresponding to the action integral [2.18] has the form

[2.20] $$p_\mu = Mv_\mu - S_{\mu\nu}\, a^\nu.$$

z_μ and this p_μ satisfy the usual P.B.'s [2.12]. To define a_μ in terms of p_μ and $S_{\mu\nu}$ using Dirac's method, the supplementary condition [2.3] is written, with the help of [2.20], in the form

$$S_{\mu\nu}(p^\nu + S^{\nu\sigma}\, a_\sigma) \equiv 0,$$

where $\equiv$ is used to denote a strong equation. Multiplication of this equation by $S_\rho^{\cdot\mu}$ gives

[2.21] $$S_\rho^{\cdot\mu}\, S_{\mu\nu}\, p^\nu + S_\rho^{\cdot\mu}\, S_{\mu\nu}\, S^\nu_{\cdot\sigma}\, a^\sigma \equiv 0.$$

When $S_{\mu\nu}$ satisfies [2.3], Bhabha (1, equation (22)) has obtained the relation

[2.22] $$S_\rho^{\cdot\mu}\, S_{\mu\nu}\, S^\nu_{\cdot\sigma} \equiv -\tfrac{1}{2} S_{\rho\sigma}\, S_{\alpha\beta}\, S^{\alpha\beta}.$$

Therefore [2.21] becomes $2S_\rho^{\cdot\mu}\, S_{\mu\nu}\, p^\nu - S_{\alpha\beta}\, S^{\alpha\beta}\, S_{\rho\sigma}\, a^\sigma \equiv 0$. Hence

[2.23] $$S_{\mu\nu}\, a^\nu \equiv 2S_\mu^{\cdot\nu}\, S_{\nu\sigma}\, p^\sigma / S_{\alpha\beta}\, S^{\alpha\beta},$$

[2.24] $$a_\mu \equiv 2S_{\mu\nu}\, p^\nu / S_{\alpha\beta}\, S^{\alpha\beta}.$$

Note that $a_\mu\, p^\mu \equiv 0$, $a_\mu\, v^\mu \equiv 0$.

With the help of [2.23], [2.20] becomes $p_\mu = Mv_\mu - 2S_\mu^{\cdot\nu}\, S_{\nu\sigma}\, p^\sigma / S_{\alpha\beta}\, S^{\alpha\beta}$. Squaring both sides of this relation, and taking into account $v_\mu v^\mu = 1$, $S_{\mu\nu} v^\nu = 0$, and [2.22], one gets the Hamilton–Jacobi equation for a constrained pure gyroscope with no interacting field to be

[2.25] $$p_\mu\, p^\mu + (2S_{\mu\lambda}\, S^\lambda_{\cdot\nu}\, p^\mu\, p^\nu / S_{\alpha\beta}\, S^{\alpha\beta}) - M^2 = 0.$$

In view of [2.24], this can be written in the form

[2.26] $$p_\mu\, p^\mu - \tfrac{1}{2} S_{\alpha\beta}\, S^{\alpha\beta}\, a_\mu\, a^\mu - M^2 = 0.$$

The correct classical equations of motion are obtained by choosing a^μ equal to v^μ. If this value of a^μ is inserted in the action integral, then the canonical formalism of Weyssenhoff (19) for a Lagrangian containing the second derivative

of the coordinate can be applied to this action integral. But, because of [2.3], the momenta conjugate to the canonical coordinates equal to the velocity of the particle vanish in the weak sense. Therefore one is led back to Dirac's method for the discussion of the canonical formalism.

Instead of [2.3] it is possible to impose the constraint condition $S_{\mu\nu}^* v^\nu = 0$, where $S_{\mu\nu}^*$ is the tensor dual to $S_{\mu\nu}$. If the dipole moment is taken proportional to the spin tensor, this condition gives a particle with a purely electric moment in the rest system of the particle. This new condition can be treated exactly as before using b^μ as the Lagrange undetermined multiplier 4-vector (in place of a^μ). Then since

$$S_{\rho\mu}^*\, S^{*\mu\nu}\, S_{\nu\sigma}^* \equiv \tfrac{1}{2} S_{\rho\sigma}^*\, S_{\alpha\beta}\, S^{\alpha\beta}, \quad S_{\alpha\beta}\, S^{\alpha\beta} \equiv -\, S_{\alpha\beta}^*\, S^{*\alpha\beta},$$

one gets the strong equations

$$S_{\mu\nu}\, b^\nu \equiv 2 S_{\mu\nu}^*\, S^{*\nu}_{.\sigma}\, p^\sigma / S_{\alpha\beta}^*\, S^{*\alpha\beta}, \quad b_\mu \equiv 2 S_{\mu\nu}^*\, p^\nu / S_{\alpha\beta}^*\, S^{*\alpha\beta},$$

defining b_μ in terms of p_μ and $S_{\mu\nu}^*$. The Hamilton-Jacobi equation in this case (with no interacting field) is

[2.27] $$p_\mu\, p^\mu + (2 S_{\mu\lambda}^*\, S^{*\lambda}_{.\nu}\, p^\mu\, p^\nu / S_{\alpha\beta}^*\, S^{*\alpha\beta}) - M^2 = 0,$$

or

[2.28] $$p_\mu\, p^\mu - \tfrac{1}{2} S_{\alpha\beta}^*\, S^{*\alpha\beta} b_\mu\, b^\mu - M^2 = 0.$$

Consider now the case of a particle interacting with a field. It is assumed without further comment that the interaction of particle and field is completely specified by the effective potential 4-vector A_μ and the field $f_{\mu\nu}$ derived from it in the usual manner. The interaction contributes suitable terms to the action integral. The correct equations of motion for a particle interacting with a field follow from the action integral (independent of the parameter)

[2.29] $$I_3 = \int_{s_0}^{s} \{ (M - \tfrac{1}{2} C S_{\rho\sigma}\, f^{\rho\sigma})(v_\lambda\, v^\lambda)^{\frac{1}{2}} + e A_\mu\, v^\mu - \tfrac{1}{2} S_{\mu\nu}\, P^{\mu\nu} + a^\mu\, S_{\mu\nu}\, v^\nu \} ds,$$

where M and C are arbitrary constants. For

$$\delta I_3 = [\{ (M - \tfrac{1}{2} C S_{\rho\sigma}\, f^{\rho\sigma}) v_\mu + e A_\mu - S_{\mu\nu}\, a^\nu \} \delta z^\mu - \tfrac{1}{2} S_{\mu\nu}\, \delta Q^{\mu\nu}]_s$$

$$+ \int_{s_0}^{s} [\{ e v^\nu (\partial_\mu\, A_\nu - \partial_\nu\, A_\mu)_{x=z} - \tfrac{1}{2} C S_{\rho\sigma}\, \partial_\mu\, f^{\rho\sigma}$$

$$- \frac{d}{ds} ((M - \tfrac{1}{2} C S_{\rho\sigma}\, f^{\rho\sigma}) v_\mu - S_{\mu\nu}\, a^\nu) \} \delta z^\mu$$

[2.30] $$+ \tfrac{1}{2} \{ \dot{S}_{\mu\nu} + [S.D]_{\mu\nu} - C [S.f]_{\mu\nu} \} \delta Q^{\mu\nu} + S_{\mu\nu}\, v^\nu\, \delta a^\mu] ds,$$

where ∂_μ denotes $\partial / \partial x^\mu$ and where $v_\lambda\, v^\lambda$ has been replaced by unity after the variation.

The new momenta p_μ conjugate to z^μ are

$$p_\mu = (M - \tfrac{1}{2} C S_{\rho\sigma}\, f^{\rho\sigma}) v_\mu + e A_\mu - S_{\mu\nu}\, a^\nu.$$

p_μ and z_μ satisfy the usual P.B.'s [2.12]. The quasi-momenta canonically conjugate to the quasi-coordinates $Q^{\mu\nu}$ are again $-\, S_{\mu\nu}$, so that the variables $S_{\alpha\beta}$ again.

satisfy the P.B.'s [2.17]. If π_μ denotes $p_\mu - eA_\mu$, then the definition of a_μ in terms of the other variables is obtained exactly as before except that p_μ must be replaced by π_μ in the calculations. Thus, when there is a field,

[2.31] $$a_\mu \equiv 2 S_{\mu\nu} \pi^\nu / S_{\alpha\beta} S^{\alpha\beta},$$

[2.32] $$\pi_\mu = (M - \tfrac{1}{2} C S^{\rho\sigma} f_{\rho\sigma}) v_\mu - 2 S_{\mu\nu} S'_{.\sigma} \pi^\sigma / S_{\alpha\beta} S^{\alpha\beta},$$

The Hamilton–Jacobi equation is then

[2.33] $$\pi_\mu \pi^\mu + 2(S_{\mu\lambda} S'_{.\nu} \pi^\mu \pi^\nu / S_{\alpha\beta} S^{\alpha\beta}) - (M - \tfrac{1}{2} C S_{\rho\sigma} f^{\rho\sigma})^2 = 0,$$

or

[2.34] $$\pi_\mu \pi^\mu - \tfrac{1}{2} S_{\alpha\beta} S^{\alpha\beta} a_\mu a^\mu - (M - \tfrac{1}{2} C S_{\rho\sigma} f^{\rho\sigma})^2 = 0,$$

where a_μ is now defined by [2.31].

The canonical formalism of a dynamical system is complete once the Hamilton–Jacobi equations and the P.B.'s satisfied by the various dynamical variables are known.

3. HAMILTONIAN DYNAMICS OF THE SYMMETRICAL TOP

The total spin angular momentum of the symmetrical top is given by

[3.1] $$N_{\mu\nu} = S_{\mu\nu} + K[S.\dot{S}]_{\mu\nu},$$

where K is an arbitrary constant. When there is no constraint condition of the form [2.3], the correct action integral for this particle interacting with a field has been found previously in (15). It has been seen above how the action integral for the constrained system can be obtained from the unconstrained system. In the notation of this paper, the correct action integral (independent of the parameter) for the Bhabha–Corben equations of a constrained symmetrical top interacting with a field is therefore

[3.2] $$I_4 = \int_{s_0}^{s} \{ (M - \tfrac{1}{2} C S_{\rho\sigma} f^{\rho\sigma})(v_\lambda v^\lambda)^{\frac{1}{2}} + e A_\mu v^\mu - \tfrac{1}{2} S_{\mu\nu} P^{\mu\nu} - \tfrac{1}{4} K \dot{S}_{\rho\sigma} \dot{S}^{\rho\sigma} (v_\lambda v^\lambda)^{-\frac{1}{2}} + a^\mu S_{\mu\nu} v^\nu \} ds,$$

where a^μ is again the undetermined multiplier 4-vector. For

$$\delta I_4 = [\{ (M + \tfrac{1}{4} K \dot{S}_{\rho\sigma} \dot{S}^{\rho\sigma} - \tfrac{1}{2} C S_{\rho\sigma} f^{\rho\sigma}) v_\mu + e A_\mu - S_{\mu\nu} a^\nu \} \delta z^\mu - \tfrac{1}{2} N_{\mu\nu} \delta Q^{\mu\nu}]_s$$

$$+ \int_{s_0}^{s} [\{ e v^\nu f_{\mu\nu} - \tfrac{1}{2} C S_{\rho\sigma} \partial_\mu f^{\rho\sigma} - \frac{d}{ds}((M + \tfrac{1}{4} K \dot{S}_{\rho\sigma} \dot{S}^{\rho\sigma} - \tfrac{1}{2} C S_{\rho\sigma} f^{\rho\sigma}) v_\mu - S_{\mu\nu} a^\nu) \} \delta z^\mu$$

[3.3] $$+ \tfrac{1}{2} \{ \dot{N}_{\mu\nu} + [S.D]_{\mu\nu} - C[S.f]_{\mu\nu} \} \delta Q^{\mu\nu} + S_{\mu\nu} v^\nu \delta a^\mu] ds,$$

where $v_\lambda v^\lambda$ has been replaced by unity after the variation.

From [3.3], the momenta p_μ conjugate to z^μ are given by

[3.4] $$p_\mu = (M + \tfrac{1}{4} K \dot{S}_{\rho\sigma} \dot{S}^{\rho\sigma} - \tfrac{1}{2} C S_{\rho\sigma} f^{\rho\sigma}) v_\mu + e A_\mu - S_{\mu\nu} a^\nu,$$

and the quasi-momenta conjugate to the quasi-coordinates $Q^{\mu\nu}$ are $- N_{\mu\nu}$, where $N_{\mu\nu}$ is defined by [3.1]. z_μ and p_μ satisfy the usual P.B.'s [2.12]. The analysis used

to deduce [2.17] can be applied here to give the P.B.'s of the total spin angular momentum variables $N_{\alpha\beta}$, which are

[3.5] $[N_{\alpha\beta}, N_{\gamma\delta}] = - g_{\alpha\gamma} N_{\beta\delta} + g_{\beta\gamma} N_{\alpha\delta} + g_{\alpha\delta} N_{\beta\gamma} - g_{\beta\delta} N_{\alpha\gamma}$,

in agreement with the results of (15, 16). However, the method does not give the P.B.'s satisfied by the variables $S_{\alpha\beta}$, $\dot{S}_{\alpha\beta}$, which are essential for the canonical formalism. But the P.B.'s satisfied by these variables have been discussed in detail in (15, 16), and the results obtained there are taken over in the following work. Since $S_{\alpha\beta} S^{*\alpha\beta} = 0$ here, these P.B.'s are

[3.6]
$$
\begin{cases}
[S_{\alpha\beta}, S_{\gamma\delta}] = 0, \\
[S_{\alpha\beta}, \dot{S}_{\gamma\delta}] = (g_{\alpha\gamma} g_{\beta\delta} - g_{\beta\gamma} g_{\alpha\delta} - 4S_{\alpha\beta} S_{\gamma\delta}/S_{\rho\sigma} S^{\rho\sigma})/K, \\
[\dot{S}_{\alpha\beta}, \dot{S}_{\gamma\delta}] = 2(g_{\alpha\gamma} N_{\beta\delta} - g_{\beta\gamma} N_{\alpha\delta} - g_{\alpha\delta} N_{\beta\gamma} + g_{\beta\delta} N_{\alpha\gamma})/K^2 S_{\rho\sigma} S^{\rho\sigma}, \\
[N_{\alpha\beta}, S_{\gamma\delta}] = - g_{\alpha\gamma} S_{\beta\delta} + g_{\beta\gamma} S_{\alpha\delta} + g_{\alpha\delta} S_{\beta\gamma} - g_{\beta\delta} S_{\alpha\gamma}, \\
[N_{\alpha\beta}, \dot{S}_{\gamma\delta}] = - g_{\alpha\gamma} \dot{S}_{\beta\delta} + g_{\beta\gamma} \dot{S}_{\alpha\delta} + g_{\alpha\delta} \dot{S}_{\beta\gamma} - g_{\beta\delta} \dot{S}_{\alpha\gamma}.
\end{cases}
$$

a_μ is defined in terms of p_μ and S_μ, by writing the constraint condition [2.3], with the help of [3.4], in the form

$$S_{\mu\nu}(\pi^\nu + S^{\rho\sigma} a_\sigma) \equiv 0.$$

Hence

[3.7] $$a_\mu \equiv 2S_{\mu\nu} \pi^\nu / S_{\alpha\beta} S^{\alpha\beta},$$

and from [3.4], $\pi_\mu = (M + \tfrac{1}{4}K\dot{S}_{\rho\sigma} \dot{S}^{\rho\sigma} - \tfrac{1}{2}CS_{\rho\sigma} f^{\rho\sigma})v_\mu - 2S_{\mu\lambda} S^\lambda_{.\nu} \pi^\nu / S_{\alpha\beta} S^{\alpha\beta}$. The Hamilton–Jacobi equation for the constrained symmetrical top is therefore

[3.8] $\pi_\mu \pi^\mu + (2S_{\mu\lambda} S^\lambda_{.\nu} \pi^\mu \pi^\nu / S_{\alpha\beta} S^{\alpha\beta}) - (M + \tfrac{1}{4}K\dot{S}_{\rho\sigma} \dot{S}^{\rho\sigma} - \tfrac{1}{2}CS_{\rho\sigma} f^{\rho\sigma})^2 = 0$,

or

[3.9] $\pi_\mu \pi^\mu - \tfrac{1}{2}S_{\alpha\beta} S^{\alpha\beta} a_\mu a^\mu - (M + \tfrac{1}{4}K\dot{S}_{\rho\sigma} \dot{S}^{\rho\sigma} - \tfrac{1}{2}CS_{\rho\sigma} f^{\rho\sigma})^2 = 0$,

with a_μ defined by [3.7]. When there is no field, the Hamilton–Jacobi equation becomes

[3.10] $p_\mu p^\mu - \tfrac{1}{2}S_{\alpha\beta} S^{\alpha\beta} a_\mu a^\mu - (M + \tfrac{1}{4}K\dot{S}_{\rho\sigma} \dot{S}^{\rho\sigma})^2 = 0$,

where a_μ is now $2S_{\mu\nu} p^\nu / S_{\alpha\beta} S^{\alpha\beta}$. This completes the canonical formulation of the symmetrical top.

4. QUANTIZATION

The quantum theory of a given dynamical system is obtained from the canonical form of the classical theory by using well-known rules. The quantum state of a system is described by a vector called a ket vector in the terminology of Dirac. The classical dynamical variables are replaced by the corresponding linear operators which operate on the ket vectors in the ket vector space. The linear operators are in general noncommuting. The required commutation relations are obtained from the P.B.'s satisfied by the dynamical variables according to the

rule $\xi\eta - \eta\xi = i\hbar\ [\xi,\eta]$ where ξ, η are any two variables. The Schrödinger wave equations of the quantum theory are obtained from the Hamilton–Jacobi equations by equating to zero the quantity obtained by making the operator formed from the left-hand side of the Hamilton–Jacobi equation act on the ket vector. That is, the Hamilton–Jacobi equation $F = 0$ leads to the Schrödinger equation $F|\rangle = 0$, where $|\rangle$ denotes the ket vector. Since one is dealing with noncommuting operators, ambiguities may arise in the order of the factors when one has to deal with products of two or more variables. The order of the factors must be chosen in such a way that the quantum theoretical scheme obtained is consistent.

The above rules can be applied to the various Hamilton–Jacobi equations and P.B.'s considered above to obtain the corresponding quantum theoretical schemes. The variables $S_{\alpha\beta}$ are noncommuting in the case of the pure gyroscope. Also the π_μ variables are noncommuting. But if the Hamilton–Jacobi equations are taken in the form [2.26], [2.28], [2.34], [3.9], or [3.10], then the apparent ambiguity is removed. This completes the quantization of the spin theory considered here.

REFERENCES

1. BHABHA, H. J.   Proc. Indian Acad. Sci. A, 11: 247. 1940.
2. BHABHA, H. J. and CORBEN, H. C.   Proc. Roy. Soc. (London), A, 178: 273. 1941.
3. COSTA DE BEAUREGARD, O.   Le théorie de la relativité restreinte. Masson et Cie, Paris. 1949. Ch. IV.
4. DIRAC, P. A. M.   Lecture Series at the Second Summer Seminar of the Canadian Mathematical Congress. 1949.
5. DIRAC, P. A. M.   Can. J. Math. 2: 129. 1950.
6. EDEN, R. J.   Proc. Roy. Soc. (London), A, 205: 564. 1951.
7. FRENKEL, J.   Z. Physik, 37: 243. 1926.
8. GINSBURG, V. L.   J. Phys. (U.S.S.R.), 8: 33. 1944.
9. GINSBURG, V. L.   Trudy Fiz. Inst. Akad. Nauk. S.S.S.R., Fiz. Inst. im. P.N. Lebedeva, 3, No. 2: 193. 1946.
10. HARISH-CHANDRA.   Proc. Roy. Soc. (London), A, 185: 269. 1946.
11. KRAMERS, H. A.   Zeeman Verhandelingen. Martinus Nijhoff, The Hague. 1935. p. 403.
12. LATTES, C. M., SCHÖNBERG, M., and SCHÜTZER, W.   Anais acad. brasil. cienc. 19: 193. 1947.
13. MATHISSON, M.   Proc Cambridge Phil. Soc. 37: 40. 1942.
14. SHANMUGADHASAN, S.   Proc. Cambridge Phil. Soc. 43: 106. 1947.
15. SHANMUGADHASAN, S.   Can. J. Phys. 29: 593. 1951.
16. SHANMUGADHASAN, S.   Can. J. Phys. 30: 226. 1952.
17. THOMAS, L. H.   Phil. Mag. (Ser. 7), 3: 1. 1927.
18. WEYSSENHOFF, J.   Acta Phys. Polon. 9: 26, 46. 1947.
19. WEYSSENHOFF, J.   Acta Phys. Polon. 11: 49. 1951.
20. WEYSSENHOFF, J. and RAABE, A.   Acta Phys. Polon. 9: 7. 1947.

A SIMPLIFIED IONIZATION GAUGE CIRCUIT[1]

By F. J. Fitz Osborne[2]

ABSTRACT

By measuring the ratio of ion current to electron current present in the usual ionization gauge, an extremely stable circuit has been developed, comparing favorably with standard circuits. A simple calibration made during construction makes this gauge direct reading. The circuit may be used for outgassing the gauge, and for leak hunting, being very sensitive in this respect. It incorporates a safety cutoff. It has relatively few controls, and is extremely cheap. For several months we have operated gauges in this laboratory with several types of circuit, and find that the one described in this paper is simpler and more rugged although just as useful and versatile as our modified Rainwater instrument.

The ionization gauge is now one of the more popular devices for measuring high vacuum. Stable operation of such a gauge requires battery supplied potentials or fairly elaborate stabilizing circuits such as that developed by Rainwater (1). In general such circuits are based on grid current stabilization with consequent extra power supplies and high current tubes, and a proportionate high cost of construction.

Two circuits were built and tested in the laboratory in an attempt to simplify the circuit but retain the conventional features. The first made use of a tubeless stabilizer built around a specially wound saturable reactor. This proved practical but was not considered satisfactory because of high power dissipation and particularly because of the necessity of using nonstandard components.

Sibati, Tuzi, and Kumagai (2) have recently pointed out that the measure of vacuum is really the ratio of electron to ion currents in the gauge. They produced a circuit for a particular application in which by measuring this ratio directly they avoided variations and instability caused by effects acting on both currents simultaneously (i.e. varying filament emission). The circuit described below is a refinement of their design and includes modifications which increase the utility of the instrument.

OPERATION

The operation of the circuit (Fig. 1) is as follows. The ionization gauge filament current is adjusted by means of the 2 ohm rheostat until the meter switch S_1 on the A position indicates that the normal grid current (10 ma. for 1949 and VG 2 gauges) is flowing. This value is marked on the meter face. The grid current of the gauge passes through the metering shunt, and then through the resistor R_1, where it produces a grid voltage for the left 6AC7.

The vacuum range switch S_2 and the resistor R_1 are then placed on zero and the circuit balanced by means of the 5K potentiometer as indicated by the meter reading zero when switched to the center or measuring position B. The meter has been altered to be zero centering for simplicity of measurement, but since a null method is used this is not a necessity.
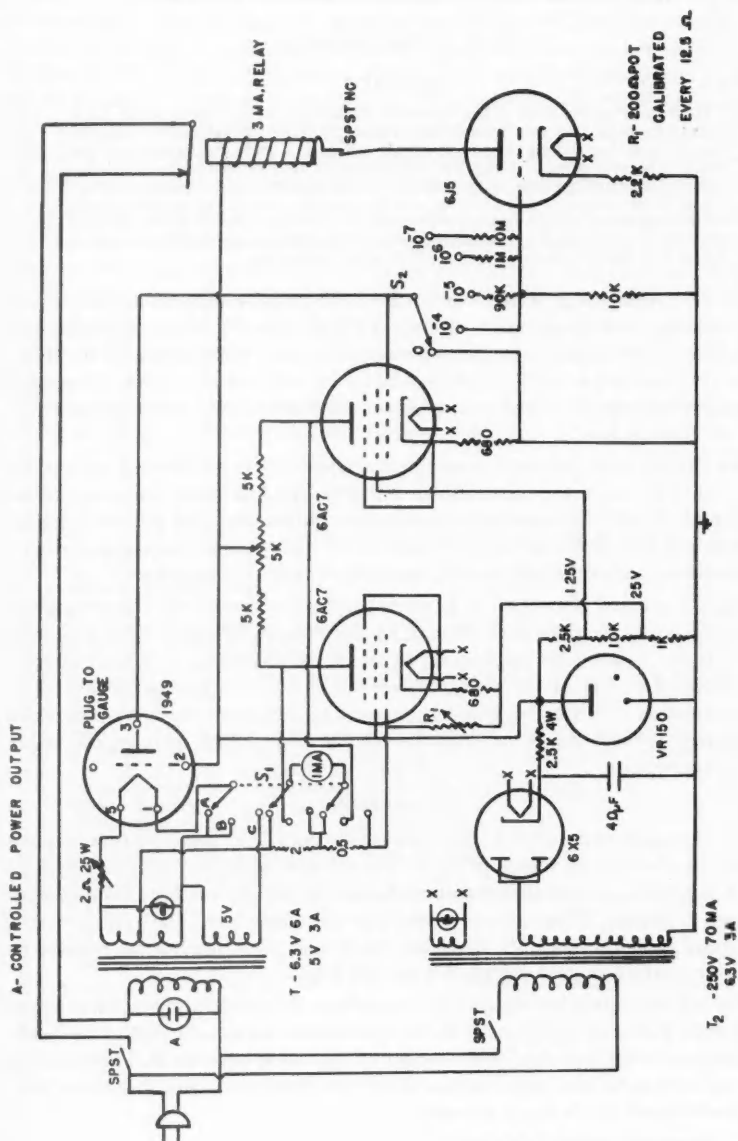
FIG. 1. Ionization gauge circuit.

By selecting R_1 and the plate current resistor, a null reading will be obtained on the meter (B position). The values of the resistor settings necessary for balance enable us to calculate the ratio of plate to grid current, and from the manufacturer's data, the controls may be calibrated directly in pressure units. Thus in Fig. 1, the plate current resistors indicate factors of 10^{-4}, 10^{-5}, 10^{-6}, and 10^{-7} mm. of Hg respectively, while R_1 gives a multiplying factor which is continuously variable from 1–20. The vacuum is read as being equal to multiplying factor times the vacuum factor.

Degassing is done by means of the metering switch, which when shifted to the C position connects an extra 5 volt winding in series with the gauge filament and shunts the meter so that the current may be read. This current may be adjusted by the 2 ohm rheostat.

Leaks in the system to which the gauge is attached may be detected by using the effect of ether on the emission of the gauge filament. At balance, an increase in the filament emission caused by the ether vapor has no effect on the meter reading, and it is therefore necessary to turn off one side of the balance circuit. This may conveniently be done by setting the vacuum range switch to zero. If the balance potentiometer is then used to bring the meter on scale and the fine vacuum potentiometer R_1 set to some convenient value, any abrupt change in the emission will affect the meter. This method is more sensitive than simple metering of the grid current inasmuch as the fluctuations are amplified. The setting of R_1 controls the amount of amplification and thus the sensitivity of the circuit as a leak detector.

The safety relay is also operated by the ionization gauge plate current, which in passing through a 10K resistor changes the voltage on the grid of the 6J5. Should the current become too large, the relay in the plate of the 6J5 closes and cuts off the gauge filament, as well as any auxiliary apparatus plugged in at A.

MODIFICATIONS

The circuit published by Sibati *et al.* required batteries for the proper plate voltage. The design presented here eliminates the batteries by the use of pentodes. Examination of Fig. 1 shows that the cathode, control grid, and screen grid of one side of the balance circuit are maintained an extra 25 volts above ground by a voltage dividing network. This 25 volts is the plate voltage for the gauge tube. The balance between the grid current tube and the ion current tube is not disturbed because the plate current of a pentode is virtually independent of the plate voltage over a reasonable range.

The divider method of supplying the voltage for the plate of the gauge makes the voltage somewhat dependent upon the grid current, but the effect is small enough to be neglected because of two factors (a) a high divider current minimizes variations in the plate voltage with variations in grid current over the normal drift range; (b) small changes in plate voltage of the usual ionization gauge produce very small changes in the sensitivity.

The gauge circuit utilizes a null method of measurement, which is for some applications a disadvantage. By suitable choice of the circuit constants, the gauge

has been made direct reading when at null. For gauge tubes other than the RCA 1949, the resistor R_1 must be recalibrated according to the sensitivity of the gauge tube. For use when a null reading is not desirable, the meter face might be calibrated in units above or below balance. It must be emphasized however, that such readings are only approximate because when the instrument is off balance, variations in the ionization gauge conditions change the calibration.

CONCLUSION

The entire instrument may be built for about fifty dollars as contrasted with two hundred dollars for the conventional circuit. The circuit is quite portable and very convenient to use. As well as performing the usual measurements, it should be useful where variations in vacuum are to be studied or vacuums reproduced as in the source of a mass spectrometer. The scale is linear and well spread, the accuracy being determined by the gauge data and the resistor calibration.

REFERENCES

1. RAINWATER, J.   Rev. Sci. Instruments, 13: 118. 1942.
2. SIBATI, H., TUZI, Y., and KUMAGAI, H.   Rev. Sci. Instruments, 23: 54. 1952.

A PRISMATIC SUBSTRUCTURE FORMED DURING SOLIDIFICATION OF METALS[1]

By J. W. Rutter[2] and B. Chalmers[3]

ABSTRACT

Single crystals of tin grown from the melt under a wide range of conditions are shown to exhibit a fibrous structure which manifests itself as parallel ridges ("corrugations") on the free surface of the specimen and as a hexagonal network ("hexagonal cells") on the growing solid–liquid interface. The center of each cell projects into the liquid. Segregation of impurities is shown to occur during solidification in a manner intimately related to the structure. The structure is suppressed by growth at low speeds or under a steep temperature gradient. The size and regularity of the elements of the structure depend upon speed of growth, temperature gradient, and impurity content. A theory is advanced which accounts for the origin and observed properties of the structure. This theory shows that the structure consists essentially of a particular distribution of impurities resulting from nonequilibrium solidification.

INTRODUCTION

This research was undertaken as part of a study of solidification of metals at the Department of Metallurgy, University of Toronto. Its purpose was to investigate a particular substructure known to occur in metal crystals grown from the melt. The results of two other pieces of research, forming part of the solidification study, have been reported previously. One concerns another substructure known as "striations" (9), which occurs in crystals grown from the melt; the other concerns dendritic growth (11).

The structure to be described here consists of parallel elements of rodlike form, having the appearance shown in Fig. 1 when viewed from a direction perpendicular to their axis. They form in a direction approximately parallel to the direction of growth. The cross section of each element is approximately hexagonal, as shown in Fig. 2. This structure was observed as early as 1934 by Buerger (1), who referred to it as a "lineage structure". His experimental information was not sufficient to allow a satisfactory explanation of its existence to be given. The most recent work concerning this phenomenon is that of Pond and Kessler (7) reported in 1951. These workers recognized only thermal effects and, as a result, their experiments were incomplete. They failed to give a satisfactory explanation of the existence and observed properties of the structure. A criticism of their paper will be published elsewhere (4).

In contrast to the work of Pond and Kessler, the present work consists of an investigation of the phenomenon in terms of thermal, constitutional, and crystallographic conditions. This broader approach to the problem has made it possible to develop a theory which accounts for the observed facts.

MATERIALS AND METHODS

The principal material used in this research was "Chempur" tin, supplied by Messrs. Johnson, Matthey and Company, of London, England. The purity of this material is stated to be 99.986%, with the major detectable impurities lead, bismuth, iron, antimony, and copper.

Specimens were produced by growth from the melt, using the technique described by Chalmers (2). This technique allows growth of specimens consisting of a controlled number of crystals, each with a predetermined crystallographic orientation. This is accomplished by growing specimens from "seed" crystals of known orientation. Growth is carried out in a horizontal graphite container or "boat". This has the important advantage of yielding a specimen with one surface which solidifies out of contact with the container. The heat required to melt the tin is supplied by a small nichrome-wound furnace mounted on a trolley and placed around the boat. Removal of the furnace at a controlled rate allows solidification to proceed at the desired speed. The rate of movement of the interface separating solid and liquid, that is, the speed of solidification, depends upon the rate at which the latent heat of fusion can be conducted away from the interface into the solid. The speed of solidification is not, in general, equal to the speed of movement of the furnace. With this method of growth, heat flow in the specimen is approximately linear. The technique has been used for many metals, with modifications according to the temperature, atmosphere, and boat material required in each case. A complete description of this technique has recently been given by Chalmers (3).

In order to record the speed of growth of a specimen, the surface of the liquid was disturbed at regular intervals during growth, causing a ripple to be frozen in at the position occupied by the top of the solid–liquid interface at that time (9).

The solid–liquid interface was exposed for subsequent observation by rapidly pouring the liquid out of the boat at the desired stage of growth (11). This was accomplished either by tilting the boat or by removing a graphite stop to allow the liquid to run out.

Determinations of crystallographic orientation were made by means of back reflection Laue X-ray diffraction photographs. These were analyzed by the method due to Greninger (6).

Modifications of the general techniques noted above, and also other special techniques, were used in this research. They will be described in connection with the observations which they yielded.

EXPERIMENTAL OBSERVATIONS

Introduction

For the sake of convenience, a definition of speeds of growth from the melt follows:

Designation	Speed Range
Slow	Less than 1 mm. per min.
Intermediate	1 mm. per min. to 13 mm. per min., approximately
Fast	Greater than 13 mm. per min., approximately

PLATE I
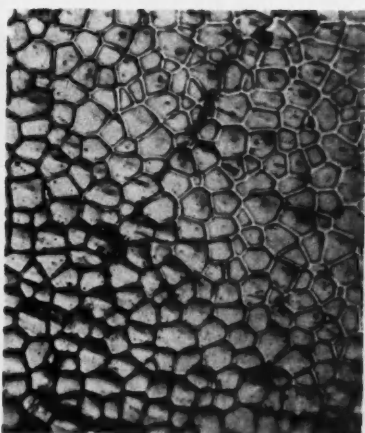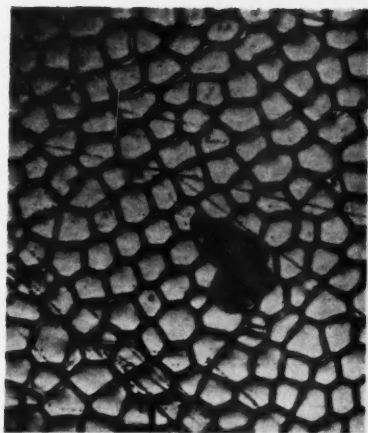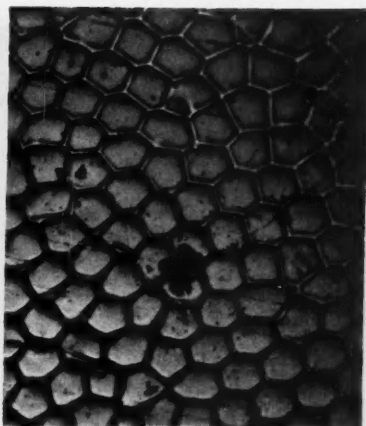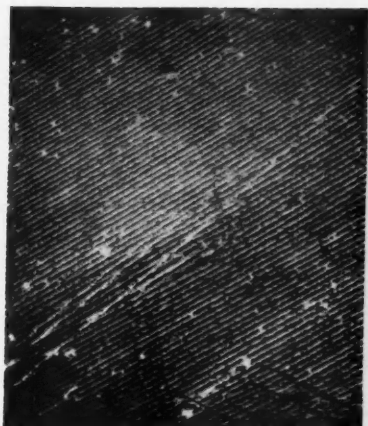
Fig. 1. (Upper left) Unetched free surface of tin crystal, showing corrugations. Magnification 20×. Oblique illumination.

Fig. 2. (Upper right) Decanted interface of tin crystal. Speed of growth 4 mm. per min. Magnification 100×. Bright field illumination.

Fig. 3. (Lower left) Decanted interface of tin crystal. Speed of growth 7.5 mm. per min. Magnification 100×. Bright field illumination.

Fig. 4. (Lower right) Decanted interface of tin crystal. Speed of growth 13 mm. per min. Magnification 100×. Bright field illumination.

PLATE II
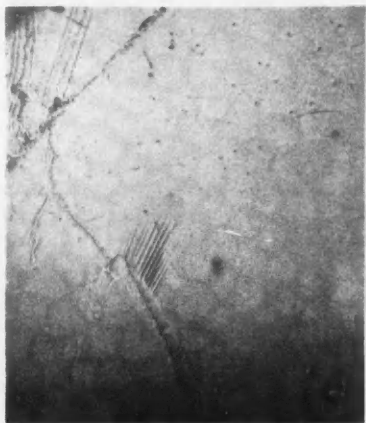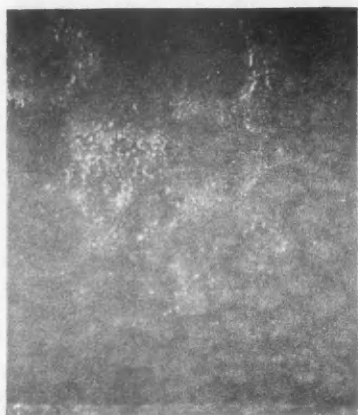
FIG. 5. (Upper left) Section of tin crystal, cut by means of etching solution. Magnification 200×. Dark field illumination.

FIG. 6. (Upper right) Section of silver crystal, cut electrolytically. Magnification 75×. Dark field illumination.

FIG. 7. (Lower left) Decanted interface of tin crystal showing breakdown of hexagonal cells at slow speeds of growth. Speed of growth 0.5 mm. per min. Magnification 75×. Bright field illumination.

FIG. 8. (Lower right) Decanted interface of tin crystal showing disappearance of cellular structure at slow speeds of growth. Speed of growth 0.4 mm. per min. Magnification 75×. Bright field illumination.

PLATE III
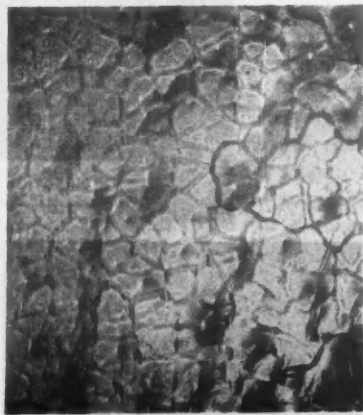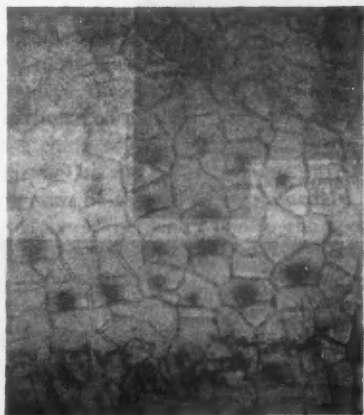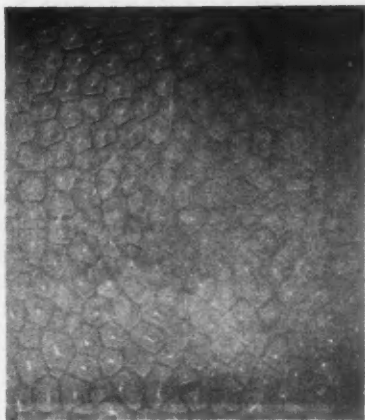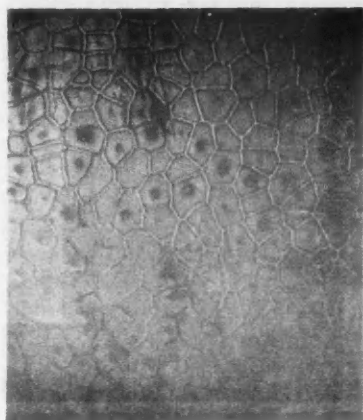
FIG. 9. (Upper left) Decanted interface. Chempur tin plus 0.1% lead. Speed of growth 3.6 mm. per min. Magnification 75×. Bright field illumination.

FIG. 10. (Upper right) Decanted interface. Control sample, Chempur tin. Speed of growth 3.8 mm. per min. Magnification 75×. Bright field illumination.

FIG. 11. (Lower left) Decanted interface. Chempur tin plus 0.3% antimony. Speed of growth 3.9 mm. per min. Magnification 75×. Bright field illumination.

FIG. 12. (Lower right) Decanted interface. Chempur tin plus 0.3% lead. Speed of growth 3.8 mm. per min. Magnification 75×. Bright field illumination.

PLATE IV

DIRECTION OF GROWTH

DIRECTION OF GROWTH
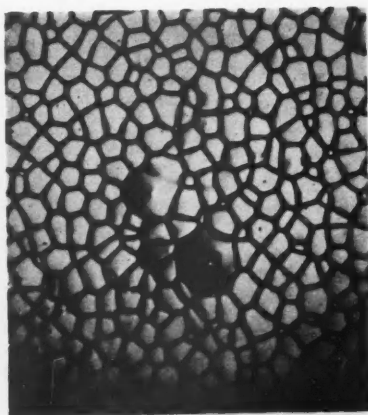
These limiting speeds mark changes in the structure found in specimens grown by the method described previously. However, these structural changes depend upon factors other than speed. Therefore, the definition is restricted to specimens grown under conditions closely similar to those usually used in this research. Modification of the limiting speeds given above will be dealt with subsequently.

The top, free surface of unetched crystals of tin grown in the intermediate speed range shows a "corrugated" appearance at low magnification (Fig. 1). The corrugations (as they will be called hereafter) are actually ridges running along the surface of the specimen. They are not visible on the sides of the specimen which solidified in contact with the graphite boat. Examination of the interface exposed by decanting the liquid metal during growth in the intermediate speed range reveals a network of cells, roughly hexagonal in shape, as shown in Figs. 2, 3, and 4. Using oblique lighting, it was found that the center of each cell projects into the liquid metal with respect to the boundary of the cell. This observation was confirmed by making a light scratch on the decanted interface of a specimen with a glass rod which had been drawn to a fine point. Examination with a microscope showed that, where the scratch was not too deep, it existed only in the center of each cell crossed, and it was therefore concluded that the boundaries are depressed with respect to the centers of the cells.

The question arises whether the structures described above are surface or volume phenomena. In order to answer this question, a tin crystal was cut chemically with ferric chloride etching solution. The etching reagent was applied locally to the specimen by means of a fine nylon thread which was driven around two pulleys, through a tray of etching solution, and over the specimen. Pressure of the thread on the specimen was very light, so that it only served to convey the fresh etching solution to the cut being made and to get rid of the reaction products. This method of cutting leaves a strain-free surface. Fig. 5 is a photomicrograph of the surface obtained by cutting a tin crystal in this manner, approximately perpendicular to the specimen axis. It shows that the cellular structure persists in the interior of the crystal. Fig. 6 was obtained from the surface exposed by cutting electrolytically a silver crystal which showed the corrugation structure. These photomicrographs show that the cellular structure persists in the interior of the crystal and is, therefore, a volume phenomenon. It is concluded that the corrugations and cells are two views of one structure consisting of parallel elements of prismatic form, each having a cross section which is approximately hexagonal.

FIG. 13. (Upper left) Decanted interface of tin crystal showing enlarged cells which appear at fast speeds of growth. Speed of growth 12 mm. per min. Magnification 75×. Bright field illumination.

FIG. 14. (Upper right) Branching of corrugations on free surface of tin bicrystal. Magnification 75×. Bright field illumination.

FIG. 15. (Center) Autoradiograph of lead crystal containing antimony. Magnification 4×. Copied from original by transmitted light.

FIG. 16. (Lower left) Decanted interface of tin crystal, showing suppression of the cellular structure by a steep temperature gradient. Temperature gradient in liquid during growth was 75 C.° per cm. Speed of growth 2.8 mm. per min. Magnification 75×. Bright field illumination.

FIG. 17. (Lower right) Area adjacent to Fig. 16. Disappearance of the cells was caused by the steep temperature gradient present.

Corrugation and Cell Size

Several specimens were produced in which the [110] direction was parallel to the specimen axis and the (001) plane parallel to the top, free surface. Conditions of growth were the same for each except for the modifications imposed by withdrawing the furnace at a different rate in order to obtain a different speed of growth for each specimen. Measurements of the spacing between corrugations were made on these samples by using a microscope with a travelling stage. It was found that the spacing is a function of the speed of growth, becoming smaller as the speed is increased. This relation is shown in Fig. 18. Each point plotted represents the average of approximately 15 measurements made on one specimen.
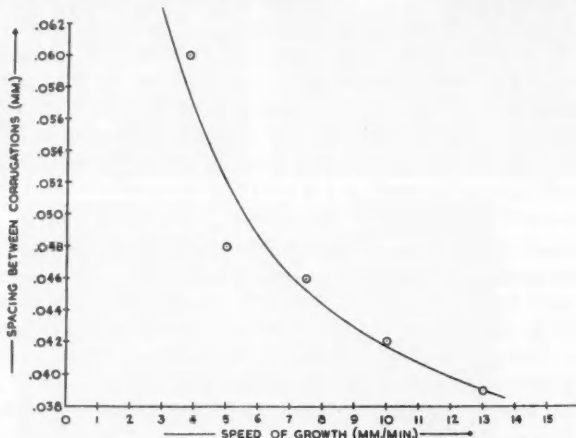
FIG. 18. Corrugation spacing vs. speed of growth.

A decanted interface was obtained on each crystal of this series. From photomicrographs of these interfaces, the average cell diameter was measured. It was found to correspond, within experimental error, to the measurements of corrugation spacing as a function of speed of growth given in Fig. 18.

As shown by Figs. 2, 3, and 4, the cells in any one specimen may vary considerably in size. The corresponding corrugation spacing behaves in the same way. It must, therefore, be noted that the measurements above give only the average dimensions. The regularity of size and shape of the cells which is evident at speeds of about 5 mm. per min. is lost, to some extent, at higher and lower speeds.

No measurements were made of the extent to which the centers of the cells project into the liquid with respect to the cell boundaries. However, for the intermediate speed range, it is estimated that this extent, on the decanted interface. is of the order of one-tenth of the cell diameter. It was observed that the average height of the cell centers increases as the speed of growth increases in this speed range. It should be noted that if the cell boundaries take the form of very narrow

grooves during growth, then part of the liquid which they contain will be retained by surface tension when decantation is carried out. Therefore, the depth of the cell boundaries observed on a decanted interface may not be the same as that which was in existence during growth of the crystal.

Direction of Formation of Corrugations

· Several crystals were grown in which the (001) plane was parallel to the free surface of the specimen and the [110] direction made an angle ϕ with the specimen axis. In each case, the speed of growth was varied along the length of the specimen. Measurements of corrugation direction were made on these specimens with a microscope fitted with a rotating stage which was calibrated in tenths of a
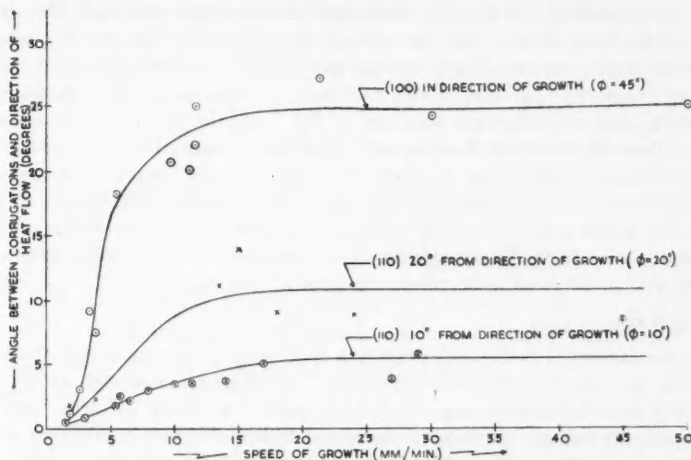
FIG. 19. Direction of formation of corrugations.

degree. These measurements showed that at the lower end of the intermediate speed range (1 or 2 mm. per min.) the corrugations tend to form in a direction parallel to the direction of heat flow, independent of the angle ϕ. For a given value of ϕ the direction of the corrugations tends more and more towards the [110] direction as the speed is increased. For a given speed, the angle between the corrugations and the direction of heat flow increases as ϕ is increased. The form of this relationship is shown in Fig. 19 and is in qualitative agreement with the same relation for striations studied by Teghtsoonian and Chalmers (9). The lack of quantitative agreement must be due to a difference in experimental conditions other than speed of growth since it has been observed that corrugations and striations never cross, but always run in the same direction in the same regions of the specimen.

Bounding Planes of the Structural Elements

From the photomicrographs (Figs. 2, 3, and 4) of decanted interfaces, which are cross-sectional views of the corrugation structure, it is clear that the boundary

planes of the elements do not run in any preferred crystallographic directions. The hexagonal boundary lines appear to be randomly oriented.

Growth at Slow Speeds

As the speed of growth approaches the lower limit of the intermediate range, the corrugation spacing and cell size become relatively large and do so quite rapidly, as indicated in Fig. 18. The corrugations then cease to be visible and the surface of the specimen appears smooth, on their scale of size. Observations on the decanted interface are difficult under these limiting conditions because of the narrow range in which the structure changes and the fact that precise knowledge of the speed of growth when decanting took place is not readily obtainable. Conditions of growth do, in general, vary over the interface obtained. However, observations have shown that the cellular structure first degenerates into a system of bands, approximately vertical and parallel, as shown in Fig. 7. This occurred at a speed of growth of about 0.5 mm. per min. under the experimental conditions used to produce the specimen of Fig. 7. As the speed is decreased still further, these bands vanish, leaving only a few widely-spaced boundaries having the appearance shown in Fig. 8. These boundaries can be identified as striation boundaries (9), and are visible in Fig. 7 also. It is concluded that the conditions of growth which occur when the furnace is withdrawn at a rate which gives growth at slow speeds will not support the existence of the corrugation structure. The striations still exist under these conditions.

Growth at High Speeds

The attainment of fast speeds of growth is marked by the appearance of visible dendritic growth, and dendritic formations can often be observed on the free surface of unetched specimens grown at high speeds (11). These dendrite "heads", as they are called, are portions of the metal which solidified in advance of the general solid–liquid interface. No corrugations are visible in the dendrite "head" itself, but they are present over the rest of the surface, which was produced by advancement of the general interface.

At the lower limit of the high speed range, a small percentage of the cells present on the interface become enlarged. They increase greatly in diameter and the center of each enlarged cell projects much farther into the liquid metal than the neighboring cells, as shown in Fig. 13. Enlarged cells in all stages of development, from slight enlargement visible only under the microscope to projections visible to the unaided eye, have been observed in specimens of Chempur tin. It is concluded that the cellular structure which occurs in the intermediate speed range becomes unstable under the conditions of growth brought about by removing the furnace at a rapid rate, without forced cooling of the specimen, to secure a high speed of growth. Observations indicate that these enlarged cells may be the beginnings of dendrite stalks (11). Again, it should be borne in mind that the speed at which enlarged cells first appear depends upon the details of the experiment. Working with lead of 99.999% purity, Weinberg and Chalmers (11) found that dendrites can only grow into a supercooled liquid. Their specimens were grown by the method used in this research.

Incubation of Corrugations

Striations and corrugations are both present in the seed crystals which are normally used, and these continue into the crystal grown from the seed. However, it is possible to produce specimens grown at any desired speed which contain an area that is free from striations (9). By using a seed which is narrower than the crystal being grown, an area ("*A*" in Fig. 20) is produced where the crystal widens and in which new striations must nucleate, since those present in the seed do not continue into this area although the orientation of the seed crystal is maintained. A considerable incubation period is found for the striations so that they may not be present for a distance of a centimeter or more from the graphite insert. However, the corrugations were found to be in existence as close to the insert as observations could be made. Owing to the curvature of the surface caused by surface tension, close examination was not possible at less than 1 or 2 mm. from the insert.
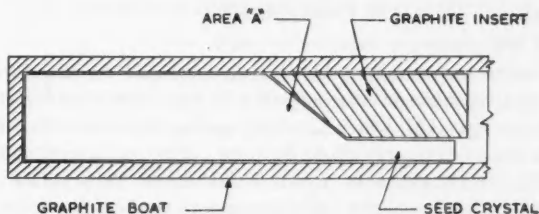
FIG. 20. Position of striation-free area.

It is possible to grow a bicrystal (two-grain specimen) in which the boundary between the crystals runs in a direction different from that of the striations and corrugations. Thus, in one grain of a bicrystal, an area can be produced which is free from striations owing to their long incubation period, by causing the boundary to run in a direction similar to that of the edge of the graphite insert mentioned above. The corrugations and striations form independently in the two parts of the bicrystal and do not cross the crystal boundary. Fig. 14 is a photomicrograph taken on the boundary of such a bicrystal. It is seen that the corrugations do not require an incubation period and, in fact, fill in the region where new corrugations are required by branching. One corrugation appears to run continuously beside the boundary, and branching from it occurs when its distance from the existing corrugations becomes somewhat larger than normal for the speed of growth. The appearance at the boundary on the decanted interface of cells which are larger than normal is in accord with this observation.

It is of interest to note that the crystal boundary does, in general, follow the cell boundaries from the top to the bottom of the specimen. There are exceptions to this, and cases are often found where a crystal boundary cuts across a cell on the interface of a specimen. It is possible that this may be due to movement of the crystal boundary subsequent to solidification.

Orientation Differences

To determine whether orientation differences exist in the corrugation structure, X-ray back reflection Laue photographs were made from the top surface and the decanted interface of a number of specimens, including both striated and non-striated areas. Good angular resolution was obtained by using a fine pinhole made from a length of glass thermometer tubing. The piece used was 45 mm. in length, with a bore of elliptical cross section measuring 0.22×0.11 mm. A specimen-to-film distance of 8 cm. was used, and this gave an X-ray spot which covered about 60 cells on the interface of a specimen, or 5 to 10 corrugations on the free surface. Individual orientation differences, between neighboring elements of a structure of the size of the corrugations, could not be measured with this arrangement.

The Laue photographs obtained showed spots which had a fine structure different from that obtained for striations (9). In photographs obtained from striated areas, the normal structure given by striations was present also. Detailed analysis of the spots indicated that orientation differences of up to 15 min. of arc, and random in direction, exist in the corrugation structure.

Segregation of Impurities

A radioactive tracer technique was used to determine the disposition of small amounts of impurity in single crystals grown by the method used in this research. Radioactive antimony 124, which is a beta–gamma emitter with a 60-day half-life, was selected as the impurity to be used owing to its availability; lead of purity 99.999% was chosen as the parent metal because the addition of antimony to lead causes the most usual effect of depression of the liquidus temperature. The corrugation and cell structure described for tin occurs also in the case of lead of 99.999% purity. A specimen was grown using this lead with $\frac{1}{10}$th% by weight of the radioactive antimony added to it. It was desired to make an autoradiograph of the free surface of the specimen. For this purpose, the surface must be very clean. To produce the required surface on lead, which oxidizes rapidly at its melting point compared to tin, a special technique of growth was used (10).
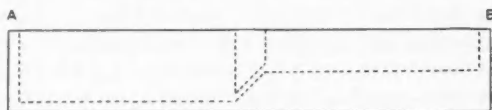
Fig. 21. Graphite boat of special design, used to obtain specimens which had a clean, oxide-free surface.

To obtain a clean, oxide-free surface, the specimen was grown under a nitrogen atmosphere in a special graphite boat. This boat was made in two levels, connected by a narrow hole, as shown in Fig. 21. It was placed in a Pyrex tube through which a small flow of nitrogen gas was maintained and the moving furnace was placed around the tube. The unalloyed metals were located initially in the upper half of the boat and melted from end B (Fig. 21) towards the hole. Melting of the metal adjacent to the hole allowed the liquid filling the upper half of the boat to run into the lower level, leaving the oxide in the upper half and

giving a melt which had a very clean surface. A Geiger counter showed later that some of the radioactive antimony remained in the upper half of the boat. As a result, it is probable that the antimony content in the specimen was only about 0.05%. The specimen was solidified, without seeding, from the hole towards end *A* of the boat at a speed which ranged from 0 to 10 mm. per min., approximately. It was found to consist of one large crystal with a few smaller ones at the end which solidified last.

The specimen was placed on a Kodak nuclear track plate (N.T.B. type) with the top, free surface in contact with the emulsion, for an exposure of 28 hr. A portion of the autoradiograph thus obtained is reproduced in Fig. 15; it shows clearly segregation of the radioactive antimony into lines running at a small angle to the specimen axis. The spacing and direction of these lines were found to be the same as the spacing and direction of the corrugations visible on the specimen.

After the specimen was annealed for 23 hr. at 300°C. in a nitrogen atmosphere, another autoradiograph was made from the free surface; this showed that the lines of radioactive antimony had disappeared during the annealing.

It was concluded from these observations that segregation of small amounts of impurity occurs during freezing and that this segregation is intimately related to the corrugation structure, since it occurs with the same spacing and direction.

The autoradiograph also revealed a variation of average antimony content along the axis of the specimen. Average blackening of the plate was greater at the end of the specimen which solidified last, becoming progressively less as the end which solidified first was approached. This showed that the average antimony content of the solid increased progressively along the specimen as solidification proceeded. This distribution was relatively unaffected by annealing for 23 hr. at 300°C.

"Banding", which is a segregation of impurities into layers transverse to the direction of solidification, is also visible in Fig. 15. This effect has been reported previously for polonium in bismuth and for gold in silver (8).

Visible Effects of Impurity Addition

Using Chempur tin as the starting material, two series of specimens were prepared with increasing impurity content in each. Lead was added as impurity in one series, and antimony in the other. Added lead lowers the liquidus temperature of tin, while antimony raises it. Thermal conditions, specimen and apparatus geometry, and crystallographic orientation were the same during growth for each specimen. The speed of growth was 3.7 ± 0.5 mm. per min. when decantation was carried out in each case.

The structure is very sensitive to impurities. Figs. 9, 10, and 11 show that, in both cases, the addition of impurity caused an increase in average cell size and a decrease in cell regularity. An increase in impurity content caused a marked increase in the length of the projections formed on the growing interface.

When Chempur tin was used, the solid–liquid interface appeared clearly defined to the unaided eye during growth of the specimen. Addition of lead or antimony to the extent of 0.1% or more caused the interface to become much less

well-defined on the surface of the growing specimen. Agitation of the melt showed that a thin layer of liquid existed on the surface to a distance of about 1 mm. behind the average position of the interface below the surface. Since the top surface is a particular case of cell boundaries, this observation indicates a marked difference in solidification temperature between the cell boundaries and cell centers. This is in accord with the observation of segregation of impurities shown by autoradiography, because the temperature at which solidification can begin in a metal depends upon its composition.

Effect of Temperature Gradient

To determine the effect which the temperature gradient present along the specimen axis during growth has upon the cellular structure, several specimens of Chempur tin were grown from a seed crystal which was water-cooled at one end. The seed crystal was fused to a tin block cast around a copper coil which carried the cooling water. The temperature gradient present at the time of de-
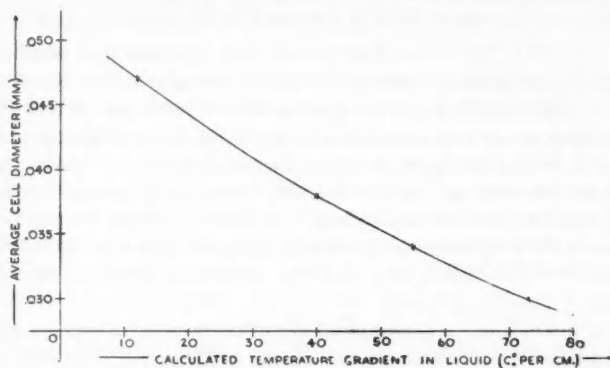
Fig. 22. Cell diameter vs. temperature gradient in liquid, for speed of growth of 5 mm. per min.

canting was varied by altering the position, along the boat, at which decantation was carried out. The average temperature gradient in the solid was known from the temperature of the cooling water and that of the solid–liquid interface. From this, the temperature gradient in the liquid was calculated, approximately.

It was found that the cell size decreases as the temperature gradient is increased, as shown in Fig. 22. For a given speed of growth, a critical temperature gradient is reached at which the cellular structure breaks down, as shown by Figs. 16 and 17, in the manner described for slow speeds of growth. It is concluded that the structure can be suppressed by a sufficiently steep temperature gradient. For example, a temperature gradient in the liquid adjacent to the interface of about 75 C.° per cm. is just sufficient to suppress the structure in a specimen of Chempur tin when the speed of growth is 2.8 mm. per min.

Observations on the corrugations showed that the temperature gradient does not affect their direction of growth.

The speed of growth of a specimen from the melt is determined by the rate at which the latent heat can be conducted away from the solid–liquid interface into the solid. This rate of removal of heat is controlled by the difference between the temperature gradients in the liquid and in the solid adjacent to the interface. The usual method of obtaining a high growth rate is to increase the speed of movement of the furnace, with no provision for cooling the solid end of the specimen. This method was used in the experiments relating cell size and corrugation spacing to speed of growth, described previously. Since the interface temperature, which is the highest temperature in the solid, must remain nearly constant and no forced cooling is used, the temperature gradient in the solid must be relatively unaffected by speed of movement of the furnace. The lowest temperature in the liquid is fixed, since it is the interface temperature, and, as a result, the temperature gradient in the liquid is affected relatively to a much greater extent. A high speed of furnace movement produces a small temperature gradient in the liquid by moving the hottest point away from the interface. It will be seen, therefore, that an increase in speed brought about by this method is accompanied by a decrease in the temperature gradient in the liquid.

The question arises whether cell and corrugation size are controlled by speed of growth, by temperature gradient, or by both. Suppose that temperature gradient in the liquid were the only factor controlling cell size. Since an increase in speed of growth causes a decrease in the temperature gradient in the liquid, it would be concluded from Fig. 18 that a decrease in the temperature gradient in the liquid produces a decrease in cell size. However, the results described in this section show clearly that an increase in temperature gradient in the liquid causes a decrease in cell size. Since these two statements are contradictory, the original hypothesis that the temperature gradient in the liquid is the only factor controlling cell size must be incorrect. It is therefore concluded that an increase in speed of growth causes a decrease in cell size.

Summary of Observations

(1) Under the conditions established during growth from the melt in the intermediate and fast speed ranges, the solid–liquid interface and the free surface of a specimen are not plane or uniformly curved over distances greater than about 0.05 mm. It is concluded that a smooth interface is unstable under these conditions.

(2) This instability leads to the production of a fibrous structure in the crystal. The structure manifests itself as parallel ridges (corrugations) on the top, free surface of the specimen and as cells, roughly hexagonal in shape, on the growing solid–liquid interface. The center of each cell projects into the liquid with respect to the cell boundary.

(3) Added to lead as an impurity, radioactive antimony segregates during solidification of the lead in the intermediate speed range. The antimony appears as lines which have the same spacing and direction as the corrugations present in the specimen. In addition to this effect, there is also a progressive increase in average impurity content from the part of the specimen which solidified first to

the part which solidified last, as well as segregation into bands transverse to the direction of growth.

(4) In the case of Chempur tin, the cell diameter and corrugation spacing are of the order of 0.05 mm. This size is decreased by an increase in growth rate and by an increase in temperature gradient in the liquid metal; it is increased by an increase in impurity content.

(5) The regularity of the corrugation and cell structure is influenced by speed of growth, temperature gradient, and impurity content. The cells are most regular in size and shape when growth is carried out at speeds near the middle of the intermediate range; this regularity is lost to some extent with increase or decrease in speed. An increase in impurity content causes a decrease in cell regularity. An increase in temperature gradient along the specimen axis causes an increase in cell regularity, except as noted in (9) below.

(6) The bounding planes of the structure are randomly oriented with respect to the crystallographic axes of the specimen.

(7) Under conditions of growth at the lower limit of the fast speed range, established by moving the furnace at a suitable rate without forced cooling of the specimen, a small percentage of the cells present on the interface become greatly enlarged in comparison to their neighbors. A further increase in speed produces visible dendritic growth.

(8) Under the conditions in existence during growth at the lower limit of the intermediate speed range, the corrugations cease to be visible and the hexagonal cell structure degenerates into a system of bands, approximately vertical and parallel. These bands vanish with further reduction in speed of growth and the solid–liquid interface then appears smooth. The striations are still present after the corrugations and cells have disappeared completely.

(9) The structure of corrugations and cells can be suppressed by the use of a sufficiently steep temperature gradient along the specimen axis.

(10) No observable incubation period is required for initiation of the structure in an area into which it is not propagated.

(11) Orientation differences, random in nature and up to approximately 15 min. of arc, exist in the structure.

(12) The direction of formation of the structure depends upon the crystallographic orientation of the specimen and the speed of growth. The preferred direction of growth in tin is [110]. It is approached more closely as the speed of growth is increased. The direction of formation is not influenced by the temperature gradient present.

(13) The structure has been observed in specimens of tin, lead, zinc, aluminum, nickel, silver, and copper.

THEORY OF CORRUGATION AND CELL FORMATION

It must be emphasized that the metal used in this research was not completely pure; it is, of course, impossible to remove all the impurity from a sample of metal. However, the impurities were usually present to such an extent as to be

soluble in the solid parent metal. It is therefore necessary to consider what can occur during solidification of metal of such composition that it forms a single phase, at least just after solidification.

Equilibrium Solidification

Solidification under equilibrium conditions is represented by the equilibrium diagram. It will be assumed that the solid is a single phase, continuous with the pure metal. Under this assumption, the equilibrium diagram can take either one of two alternative forms, as shown in Figs. 23 and 24. The binary equilibrium diagram will be used here for simplicity because the principles which it represents apply also to systems having more than two constituents.
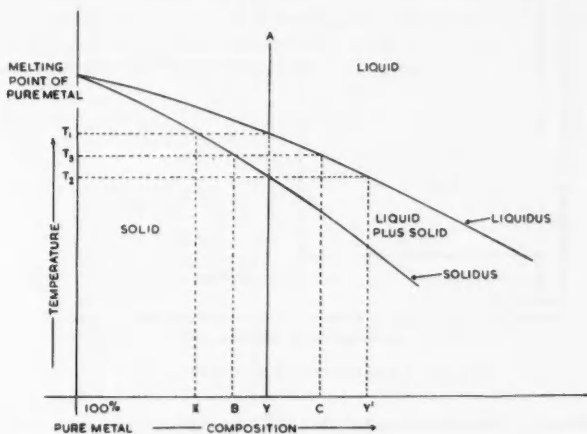
Fig. 23.
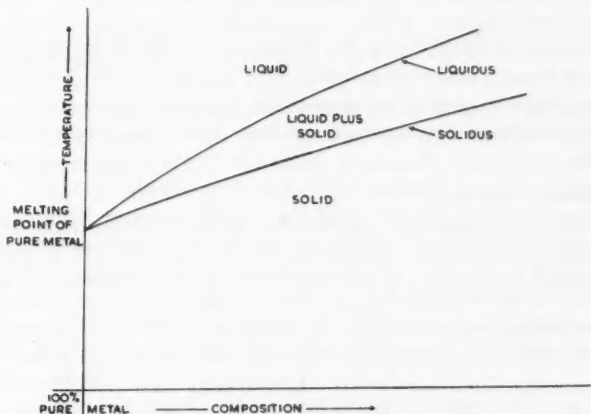
Fig. 24.

As shown by the equilibrium diagram, at any stage in the process of equilibrium solidification, the solid present is all of one uniform composition and is in equilibrium with liquid which is all of another uniform composition. This situation is illustrated by Fig. 25, which indicates the distribution of the minor constituent along the axis of a specimen that is being solidified from one end under equilibrium conditions. The uniformity of composition must be maintained by the process of diffusion. Since diffusion is a relatively slow process, particularly in the solid state, specimens produced by the method used in this research do not solidify under equilibrium conditions, especially at intermediate and fast speeds of growth.
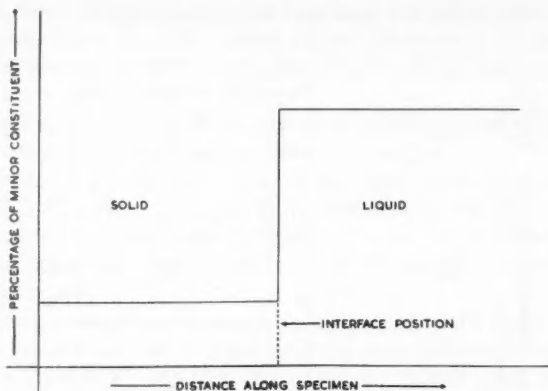
FIG. 25. Equilibrium impurity distribution.

The equilibrium diagram does not give information concerning nonequilibrium freezing, but it does tell what will happen if an indefinite period of time is available for the process to occur. Accordingly, the liquidus may be regarded as a plot of the temperature at which it is possible for freezing to begin, against composition, and the solidus as a plot of the temperature at which it is possible for melting to begin, against composition. For example, liquid of composition Y (Fig. 23) can begin to solidify at temperature T_1, if nucleation occurs in it, and not above T_1; solid of composition Y can begin to melt at temperature T_2, and not below T_2.

Nonequilibrium Freezing

Suppose that a specimen has been partly solidified, as illustrated in Fig. 26, and allowed to reach equilibrium at an interface temperature T_3, composition of the solid B, and composition of the liquid C (Fig. 23). Assume that the solid–

FIG. 26.

liquid interface is a plane surface, perpendicular to the axis of the specimen. If now the temperature gradients are modified to allow extraction of latent heat from the interface into the solid, solidification will start from an equilibrium condition.

The first solid which forms must be of composition B; if the composition were to the right of B in the diagram, the solid would melt. As solidification proceeds, the composition of liquid and solid must move to the right in the equilibrium diagram to reach the final over-all composition of Y. However, time is not allowed during nonequilibrium freezing for the diffusion of impurity, which is necessary to maintain uniform composition throughout the solid and throughout the liquid, to occur. The impurity concentration change must originate at the interface where freezing is taking place and, as a result, the concentration of impurity in the liquid must increase in the neighborhood of the solid–liquid interface. The impurity distribution in the liquid will then take the form shown in Fig. 27.
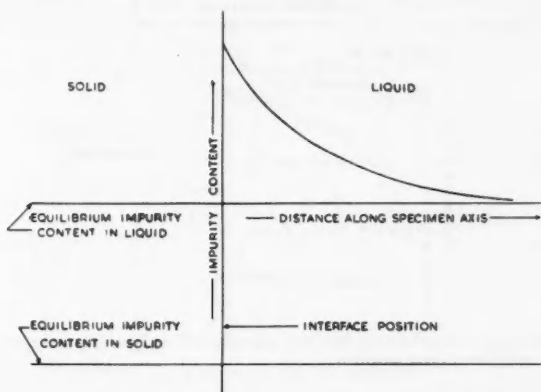
Fig. 27. Impurity distribution in liquid along a line perpendicular to the interface under nonequilibrium conditions.

Since the impurity concentration in the liquid adjacent to the interface is increased, the temperature at the interface must fall, or the impurity content must decrease again, before solidification can proceed. This is because the temperature at which it is possible to obtain solidification decreases as impurity content increases. Under nonequilibrium conditions, diffusion is slow, but temperature changes are relatively rapid. Therefore, starting from equilibrium, an increase in impurity content in the neighborhood of the interface will be accompanied by a decrease in interface temperature as solidification under nonequilibrium conditions proceeds. The curve of Fig. 27 can then be interpreted as in Fig. 28, where the temperature at which freezing can begin in the liquid is plotted as a function of distance from the interface.

If the temperature distribution in the liquid is as shown by the straight line in Fig. 28, then it is seen that each element of the liquid between the interface

and a parallel surface at distance X from it is at a temperature below that at which it is possible for solidification to begin. That is, each element of this volume is below its equilibrium liquidus temperature, and is therefore in an unstable condition since it would begin to solidify if nucleation were to occur in it. Part of this layer can solidify without extraction of heat from it.

Since this layer of liquid is below its equilibrium liquidus temperature, it is supercooled. However, the supercooling is, in this case, caused primarily by the composition changes which have occurred in the liquid, rather than by thermal changes such as might be brought about by rapid cooling of the melt (11). Super-cooling caused by composition changes will be referred to here as "constitutional supercooling".
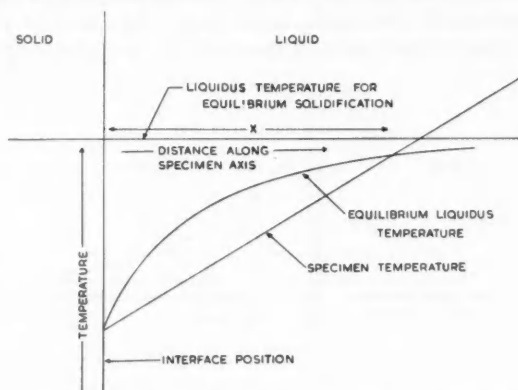
FIG. 28. Variation of equilibrium liquidus temperature and of specimen temperature with distance from interface during growth.

Consider a small element of volume, fixed at some distance in the liquid ahead of the original interface position. As the advancing solid–liquid interface approaches it, the impurity concentration in this volume element must increase and, therefore, more impurity must enter it than leaves it while the interface is approaching. As a result, the impurity content vs. distance curve must be as shown in Fig. 27 to cause this necessary increase. Since the equilibrium liquidus temperature is approximately a linear function of composition, in general, over the range under consideration, the equilibrium liquidus temperature vs. distance curve must have the form shown in Fig. 28.

Suppose that the possible spontaneous solidification without heat extraction which can occur in the unstable layer of liquid is initiated by the solid crystal present. Part of the liquid will then solidify, forming a small projection on the plane interface as shown in Fig. 29. Assume that the projection is stable, and grows at the same rate as the adjacent interface. The temperature at the surface of the projection is open to question; suppose that the entire interface, including the projection, is an isothermal. If this is the case, lateral heat flow will occur into

the projection from the adjacent liquid, reducing the amount of latent heat which can be conducted through the projection and suppressing its growth. Therefore, if the projection is stable, the interface cannot be an isothermal.

If the tip of the projection, B, and the point A on the plane interface (Fig. 29) are growing at the same rate and temperature, then the distribution of impurity in the liquid adjacent to each will be the same, as shown in Fig. 29. As a result, a concentration gradient will exist between point B and a neighboring point, C, in the liquid, and diffusion of impurities will take place from B towards C, reducing the concentration at B and increasing it at C. The liquid adjacent to the tip of the projection will be depleted by this diffusion of impurities and, therefore, solidification will be able to take place at a higher temperature there. The liquid

SOLID   IMPURITY CONTENT   LIQUID

THROUGH POINT A

IMPURITY CONTENT IN LIQUID FOR EQUILIBRIUM SOLIDIFICATION

A   C — DISTANCE ALONG SPECIMEN AXIS

THROUGH POINT B

B — DISTANCE ALONG SPECIMEN AXIS

IMPURITY CONTENT
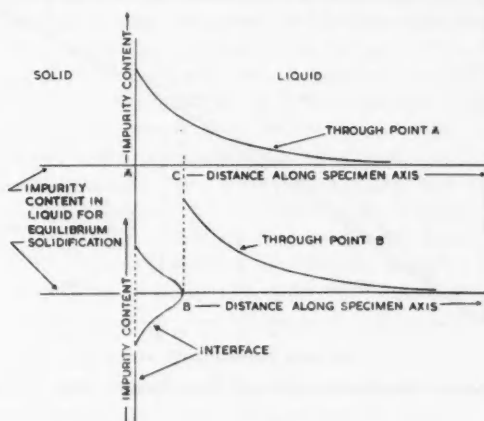
INTERFACE

FIG. 29. Growing interface with projection.

adjacent to A will be enriched in impurities and thus solidification must take place at a lower temperature in that region. As a result of this diffusion, point B can continue to grow at the same rate as point A, although the temperature at B is higher than at A. It is clear that as a projection forms on a plane interface, diffusion of impurities will enable its tip to grow at a higher temperature and will force the adjacent plane interface to grow at a lower temperature. The resulting interface, therefore, cannot be an isothermal unless the conductivity of the solid or liquid is infinite.

The effect of a higher temperature at the tip of the projection on the thermal conditions is illustrated in Fig. 30, where temperature is plotted as a function of distance along the specimen axis. In Fig. 30, the temperature vs. distance curves are drawn as straight lines. This would be the case for linear heat flow were it not for the specific heat which is evolved owing to the fall in temperature of all parts of the material during growth. This causes the slope of the temperature vs. distance curves to increase continuously from the hot (liquid) end to the cold

(solid) end of the specimen if the heat flow is linear. However, the temperature must be uniform across the specimen at large distances from the interface both in the solid (T_c) and in the liquid (T_H) and, therefore, the relative positions of the curves shown in Fig. 30 will not be affected. It is seen that the temperature along a line parallel to the direction of heat flow through the tip of the projection, B, is higher at all points near the interface than at corresponding points on a similar line through A. Therefore, lateral heat flow must occur from the projection to the neighboring solid and liquid. Because of this lateral heat flow, more latent heat can be removed at the projection than at the neighboring interface. This promotes growth of the projection while suppressing growth of the interface adjacent to it.
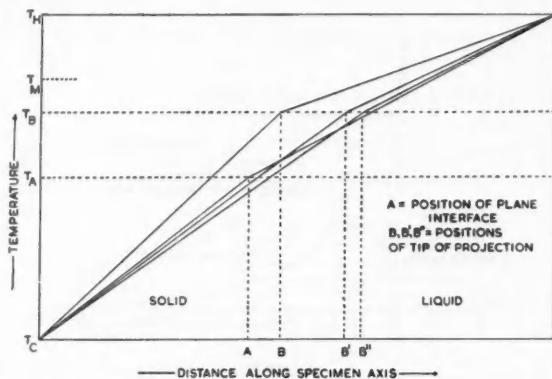
FIG. 30. Temperature distribution along specimen through plane interface and through projection.

The above considerations show that if a projection is formed on a plane, growing interface, both diffusion and thermal conditions are established which favor growth of the projection relative to the interface adjacent to it. It is therefore concluded that such a projection will be stable and will persist as long as the conditions of growth necessary for its initial formation are maintained.

There is a limit to the extent to which a projection can advance into the liquid and still maintain favorable heat flow conditions. The temperature, T_B, at B cannot rise above the solidification temperature, T_M, of the pure metal and the lowering of the temperature, T_A, of the interface adjacent to the projection will be limited by the amount of impurity which can build up there in view of the process of diffusion into the main body of liquid. If conditions such as those shown in Fig. 30 for the point B' are reached, lateral heat flow into the base of the projection will begin and this will have attained large proportions if the point B'' is reached by the tip of the projection. This unfavorable heat flow would suppress growth of the projection and, as a result, a projection can advance only to a limited extent into the liquid with respect to the interface adjacent to it.

Growth of a projection in a direction parallel to the interface is hindered by the accumulation of impurity accompanying it. There is no possibility of diffusion of impurity comparable to that which can take place at the tip of the projection.

It will be seen that the alternative possible form of the equilibrium diagram, shown in Fig. 24, does not basically alter the arguments presented above. In this case, diffusion of impurity would occur towards a projection, resulting in the same thermal conditions and a similar, though reversed, diffusion pattern.

The diffusion of impurities parallel to the interface from a projection and the lateral heat flow produced both cause a local reduction in the extent of the zone of liquid which is below its equilibrium liquidus temperature and also in the number of degrees by which it is below that temperature. These effects reduce the probability of spontaneous initiation of solidification in the zone of liquid around the projection, or suppress growth of another projection if it does start in that region. However, at some distance from the projection, conditions at the interface will be practically unaffected by its presence. The influence of the projection will extend to the circumference of a circle, the size of which is governed by the rate of diffusion of impurities in the liquid and the thermal diffusivity of the liquid and solid. Outside this circle, the conditions which gave rise to the first projection still exist. Therefore, a number of projections, each with its own "circle of influence", will form on an initially plane interface if the unstable constitutionally supercooled zone of liquid is established during nonequilibrium freezing. It is, therefore, concluded that the solid–liquid interface should consist of an array of projections when growth under such nonequilibrium conditions takes place.

Summary of Theory

(1) Accumulation of impurities in the liquid adjacent to a growing solid–liquid interface occurs during nonequilibrium freezing.

(2) This accumulation of impurities results in the formation, adjacent to the growing interface, of a layer of liquid which is below its equilibrium liquidus temperature and is, therefore, in an unstable state. It is necessary that the equilibrium liquidus temperature vs. distance curve and the temperature vs. distance curve in the liquid should intersect as shown in Fig. 28 to produce this effect of constitutional supercooling.

(3) A spontaneous solidification, without heat extraction, is initiated in this unstable zone at the solid–liquid interface by the large crystal present, resulting in formation of a small projection on an initially plane or uniformly curved interface.

(4) Diffusion of impurity from the liquid at the tip of the projection to the surrounding liquid occurs. This allows solidification at the tip of the projection to proceed at a higher temperature than at the plane interface and forces solidification to occur in the region around the base of the projection at a lower temperature than at the plane interface.

(5) This rise in temperature at the tip of the projection produces the favorable thermal condition of lateral heat flow from the projection to the surrounding

liquid and solid, promoting growth of the projection. This favorable thermal condition is maintained only if the projection does not extend into the liquid beyond a certain amount, provided that the temperature increases away from the interface into the liquid.

(6) The factors noted above should result in formation of an array of projections on an initially smooth solid–liquid interface during nonequilibrium solidification.

DISCUSSION

The theory which has been presented shows that, if certain conditions are met during solidification, a smooth solid–liquid interface is unstable and that this instability should result in the production of an array of projections on the growing interface. This accounts qualitatively for the presence of the cellular structure observed on the decanted interface. The diffusion of impurities away from the tips of the projections must result, according to the theory, in a difference of impurity content between the center and the boundary of each element of the structure. Such segregation was found by using the radioactive tracer technique, as described previously. If the equilibrium diagram is as shown in Fig. 23, the cell boundaries should be enriched in impurities, while in the case of Fig. 24 the cell boundaries should be depleted in impurities. The fact that the impurities are dispersed by annealing shows that they must have taken up their position during freezing, in agreement with the theory. It is clear, both theoretically and experimentally, that the structure consists essentially of a particular distribution of the impurities contained in the specimen. The features of this structure, as observed experimentally, will now be discussed in relation to the theory.

The decrease in volume of the metal on solidification causes a lowering of the liquid level in the boat as solidification proceeds. As a result, some of the liquid contained in those vertical cell boundaries which terminate at the top, free surface of the specimen will run out before it can solidify, producing the ridges which are here called corrugations.

The formation of the first few cells on an interface which is initially plane will occur at random, resulting from chance initiation of spontaneous solidification in the zone of unstable liquid. This randomness must decrease as the number of projections increases and the possible sites become occupied, but the initial complete formation will be comparatively random. The projections which survive this initial period will continue to grow as long as growth conditions are not changed, and it is to be expected that some lateral growth of each projection will occur if growth conditions are not the same on all sides of it. If the "circles of influence" of two projections overlap, then growth will be slower on the neighboring faces than on the outside faces, resulting in translation of the axes of the projections parallel to the interface and away from each other. The projections will therefore tend to adjust themselves in such a way that their circles of influence fit together in the most advantageous way; they can best do this by forming a close-packed array. This will result in hexagonal boundary lines between elements of the structure, and accounts for the shape of the cells observed on a decanted interface.

The size of the cells will be controlled by the following factors which are properties of the material of the specimen:

(*a*) The probability of spontaneous solidification occurring at the interface when the liquid adjacent to it is below its equilibrium liquidus temperature by a given amount.

(*b*) The coefficient of volume diffusion of the impurities in the liquid metal.

(*c*) The thermal diffusivities of the liquid and solid metal.

It appears very difficult to estimate the cell size which will result from simultaneous operation of these factors. No attempt to do so will be made here.

The effect of various conditions of growth on cell size may be deduced qualitatively:

(*a*) If the temperature gradients in the liquid and solid are steep, a high proportion of the latent heat liberated at each projection will be conducted into the solid in a direction parallel to the specimen axis, and a relatively small proportion will be conducted parallel to the interface. This will cause a reduction in the "circle of influence" of each projection and, therefore, a reduction in cell size should occur as the temperature gradient along the specimen axis is increased. This has been shown experimentally to be the case.

(*b*) When the speed of growth is high, little time is allowed for diffusion of impurities parallel to the interface. The "circle of influence" of a projection is, therefore, reduced as the speed of growth is increased and the cell size must reduce accordingly, as is observed experimentally.

(*c*) If the total impurity content in a specimen is increased, the length of the projection will be increased because the width of the unstable zone of liquid has been increased. These longer projections may be expected to exert an influence over a large area on the interface. The cell size should, therefore, increase as the impurity content is increased, as was observed.

Some irregularity of the structure is to be expected on the basis of chance initiation of spontaneous solidification in the unstable zone of liquid. However, by means of lateral growth, the projections should tend to form a very regular structure. For this to occur, there must be the possibility of establishing very uniform thermal and diffusion conditions at the growing interface. At speeds of growth well within the intermediate speed range, the cellular structure shows no asymmetry. That is, the cells do not tend to be elongated in any particular direction. But at speeds of about 0.5 mm. per min., asymmetry does occur in a very pronounced manner, as shown by Fig. 7. The appearance of the vertical lines shown there can be accounted for by convection set up in the liquid. It is therefore probable that the lack of regularity observed in the cell structure as these slow speeds are approached is due to the effects of convection. The process of convection is a relatively slow one and, therefore, it only has a noticeable effect at speeds near the lower end of the intermediate range, where it has time to operate and where the extent of the projections is not large enough to break up possible convection paths. At speeds approaching the fast range, little time is

available for diffusion parallel to the interface. It seems likely that this is the cause of cell irregularity at these speeds.

The bounding planes of the elements of the structure will be determined initially by the positions on the interface in which the projections first form. Since this is governed by random initiation of spontaneous solidification in the unstable zone of liquid, the bounding planes should show no preferred orientation except that imposed by subsequent adjustment of the projections into a close-packed arrangement. This is in agreement with the observations.

As noted previously, the achievement of a high growth rate by rapid removal of the furnace, without forced cooling of the solid, is brought about largely by a reduction in the temperature gradient in the liquid. Since it is the rise in temperature from the interface to the hot end of the boat which controls the extent to which the projection can grow ahead of the average position of the interface, a condition will be reached on lowering of the temperature gradient in the liquid such that they may grow practically to an unlimited extent. Under these conditions, one projection may grow ahead of its neighbors. If this occurs, greater diffusion of impurity will be possible, and it will continue to grow ahead into the liquid, since the restraining influence of the temperature gradient is not present. As the projection moves into regions free from the influence of neighboring projections, conditions will be established along it similar to those existing at a plane, growing solid–liquid interface, and growth perpendicular to the axis of the extended projection will become possible. It will then increase in width. This accounts for the appearance on the interface of enlarged cells at high speeds of growth. Finally, secondary projections may form on the extended one when it has advanced to a region uninfluenced by conditions at the interface from which it grew. This may account for the production of dendrites at high speeds of growth. It should be noted, however, that the formation of enlarged cells, and perhaps dendrites, is a result of heat flow and diffusion conditions established in the liquid, and not directly of the speed of growth (11).

It will be seen from Fig. 28 that when the temperature vs. distance curve is tangent at the interface to the curve relating equilibrium liquidus temperature to distance, then there exists in the liquid no region which is below its equilibrium liquidus temperature. When this condition is attained, no projections can form and a smooth interface will be stable. If the speed of growth is slow, more time is available for diffusion of impurities into the main body of the liquid and, therefore, the slope of the equilibrium liquidus temperature vs. distance curve will be relatively small. This results in reduction of the unstable zone of liquid as the speed of growth is reduced and finally in its disappearance, for a fixed temperature gradient in the liquid. This accounts for the disappearance of the corrugation structure at low speeds of growth. It is clear that an increase in the temperature gradient in the liquid will reduce the extent of the unstable zone, and therefore a sufficiently steep temperature gradient will suppress the structure for a given speed of growth. This is in accord with the observations.

The experimentally observed absence of any appreciable incubation period for formation of the corrugation structure is predicted by the theory. As soon as any

area comparable with the size of a cell is formed into which the existing structure is not propagated, then is established the condition of a plane interface, with, adjacent to it, a zone of liquid which is below its equilibrium liquidus temperature. A new element of the structure may then form, or branching of the existing corrugations may occur as is usually observed.

If solidification occurs at a given fixed rate, the impurity concentration near the interface of the specimen should reach a certain value, determined by equality of the rate of accumulation of impurity caused by movement of the interface and the rate of diffusion of the impurity into the main body of liquid. However, when the impurity content at the extreme hot end of the boat is affected by diffusion of impurities from the interface, the concentration will rise there. This will affect the concentration gradient along the specimen, resulting in an increase in the average impurity content at the interface and an accompanying decrease in average interface temperature. The solid formed will then be less pure than before. Therefore, there should be a gradual increase in impurity content along the specimen after the impurity concentration at the hot end of the liquid is affected. This accounts for the observed increase in average impurity content along the specimen towards the end which solidified last. The effect which has been called "banding" is not accounted for by the theory presented here.

The existence of orientation differences in the corrugation structure seems to bear no direct relationship to the mechanism of their formation. It is possible that the projections formed on the interface may be very thin near the tip and, therefore, mechanically very weak near the solidification temperature. Such a thin tip would not be detected by the decantation technique. Mechanical disturbances would bend such thin sections, producing small, random orientation differences of the type noted in X-ray photographs made from specimens having a corrugation structure. The existence of such orientation differences is, therefore, not inconsistent with the theory.

Existing information is insufficient to explain the direction of formation of the corrugations. The effect appears to be one of preferential deposition from liquid to solid on certain crystallographic planes, in a manner similar to that which causes development of crystallographically defined faces on crystals grown from solution or from the vapor phase. This effect is not inconsistent with the theory presented here; it modifies the direction of the axis of a projection forming on the interface.

The theory developed is in no way restricted in application to one metal. It demands only that a small quantity of impurity be present in the metal used. The occurrence of the structure in many metals, therefore, is in agreement with the theory.

It has been shown that the observed properties of the substructure are in qualitative agreement with those predicted by the theory. It appears impossible, at present, to derive quantitative values. However, it is possible to obtain an estimate of the coefficient of volume diffusion of impurities in the liquid metal.

According to Frenkel (5), the diffusion coefficients of widely different dissolved substances in the liquid state differ from each other by a factor of 10 at most;

they are much less temperature-sensitive than diffusion coefficients for the solid state; and there is only a relatively slight variation from one solvent to another. Therefore, the exact nature of the impurities present in a specimen should have little effect as far as diffusion is concerned, and for the purpose of estimating the diffusion coefficient it is reasonable to assume that the only impurity present is lead.

When the specimen temperature vs. distance curve becomes tangent at the solid–liquid interface to the equilibrium liquidus temperature vs. distance curve (Fig. 28), the cellular structure is suppressed. This critical temperature gradient can be transformed into a concentration gradient with the aid of the equilibrium diagram. It was observed that a temperature gradient of approximately 75 C.° per centimeter was just sufficient to cause suppression of the structure at a speed of growth of 2.8 mm. per minute in a specimen of Chempur tin. The lead–tin equilibrium diagram shows a drop in the liquidus temperature of about 1.8 C.° per 1% increase in lead content near the tin end. The majority of the impurities present in Chempur tin give approximately this change in liquidus temperature with composition. Taking the specimen density as 7.3 gm. per cm.^{3}, the concentration gradient at the interface is:

$$\frac{dc}{dx} = \frac{75}{1.8} \times 0.073 \text{ gm. per cm.}^3 \text{ per cm.}$$

The rate of movement of impurity down this concentration gradient per unit area of interface is then:

[1] $$\frac{dQ}{dt} = D\frac{dc}{dx} = \frac{D \times 75 \times 0.073}{1.8} \text{ gm. per cm.}^2 \text{ per sec.}$$

where Q = quantity of material,

t = time,

D = coefficient of diffusion,

c = concentration,

x = distance from interface.

This rate of movement of impurity down the concentration gradient can be estimated in another way. Fig. 12 shows a portion of the decanted interface of a specimen of Chempur tin which contained 0.3 weight per cent of lead. This specimen was grown in the usual manner at a speed comparable to that used for the specimen which was grown under a steep temperature gradient as noted above. The appearance of a second phase at the cell boundaries, as shown by Fig. 12, gives an indication of the impurity content in the liquid near the interface. An average impurity content at the interface of one-half the solubility limit of lead in solid tin at the melting point seems a reasonable estimate. This value is about five times the average impurity content of the specimen as a whole. For tin containing 0.014% lead (the purity of Chempur tin), this increase of five times gives a concentration at the interface of:

$$5 \times 7.3 \times 0.00014 \text{ gm. per cm.}^3$$

Judging from the equilibrium diagram, about 70% of the impurity present in an element of liquid is rejected into the remaining liquid when the element freezes. Hence, the quantity of material which is diffused into the liquid may be estimated for the specimen grown at a speed of 2.8 mm. per min. as follows:

Volume swept out per second by moving interface

$$= \frac{2.8}{60} \times \frac{1}{10} \text{ cm.}^3 \text{ per sec. per cm.}^2 \text{ of interface.}$$

Amount of impurity diffused into liquid per second

$$[2] \qquad = 0.7 \times \frac{2.8}{600} \times 7.3 \times 0.00014 \times 5 \text{ gm. per cm.}^2 \text{ per sec.}$$

Equations [1] and [2] give the diffusion coefficient as 5.5×10^{-6} cm.^{2} per sec., or about 0.5 cm.^{2} per day. According to Frenkel, the diffusion coefficients of gold in molten lead and tin at 500°C. are equal respectively to 3.19 and 4.65 cm.^{2} per day. Agreement between these values and that calculated above is considered satisfactory in view of the approximations made in the calculation.

Although the calculation is only an estimate, it does verify that the rate of diffusion of impurities in the liquid metal is that required by the theory. It is clear that the structure formed is essentially a particular distribution of the impurities present in the metal used.

ACKNOWLEDGMENTS

REFERENCES

1. BUERGER, M. J.   Z. Krist. 89: 242. 1934.
2. CHALMERS, B.   Proc. Roy. Soc. (London) A, 175: 100. 1940.
3. CHALMERS, B.   In course of publication.
4. CHALMERS, B. and RUTTER, J. W.   Discussion of the work of Pond and Kessler (Reference 7) for Trans. Am. Inst. Mining Met. Engrs.
5. FRENKEL, J.   Kinetic theory of liquids. Oxford University Press, London. 1946. p. 201.
6. GRENINGER, A. B.   Trans. Am. Inst. Mining Met. Engrs. 117: 61. 1935.
7. POND, R. B. and KESSLER, S. W.   J. Metals, 3: 1156. 1951.
8. STEWART, M. T., THOMAS, R., WAUCHOPE, K., WINEGARD, W. C., and CHALMERS, B. Phys. Rev. 83: 657. 1951.
9. TEGHTSOONIAN, E. and CHALMERS, B.   Can. J. Phys. 29: 370. 1951.
10. THOMAS, W. R.   Unpublished work.   Department of Metallurgy, University of Toronto. 1951.
11. WEINBERG, F. and CHALMERS, B.   Can. J. Phys. 29: 382. 1951.

INTERFERENCE EFFECTS IN THE SMALL ANGLE SCATTERING OF X RAYS BY SMALL PARTICLES[1]

By G. E. Noakes[2] and Elizabeth J. Allin

ABSTRACT

Interparticle interference effects have been observed in the small angle X-ray scattering from 30 samples prepared by the evaporation of gold colloids containing spherical particles of uniform size. The position of the interference maximum was found not to be the same for all samples containing particles of the same size. Calculation verifies that the position of this maximum is dependent on the radial distribution of the particles. It cannot be used for size determinations unless this distribution is known. The predicted variation of the slope at small angles of the ln I vs. h^2 curve with particle distribution was confirmed experimentally. This method of size determination is unsatisfactory whenever interference effects are present. It is suggested that size determinations based on the positions of the form function-maxima are almost independent of particle distribution even in concentrated samples. A unique determination of the particle distribution from the position and shape of the interference maximum would appear to be impossible even if the size were known.

INTRODUCTION

The intense scattering produced close to the direct beam when X rays pass through a sample containing very small particles has been known for more than 20 years and its distribution has been used by a number of investigators to determine the size of the particles or density fluctuations present in the sample. It seems to have been first observed by Gray and Zinn (10) and by Krishnamurti (15) in 1930 in experiments with amorphous carbon. Theoretical expressions for the intensity in terms of the angle of scattering, the wave length of the radiation, and the size of the inhomogeneity producing the scattering were derived independently by Guinier (11) and Hosemann (12) in 1939. The assumptions made were that the particles were all of the same size and shape and randomly oriented; that refraction, absorption, and multiple scattering were negligible; that there was no particle to particle interference; and that the X rays were monochromatic and perfectly collimated. Early experimental work (3, 5, 13, 14) was carried out with dilute samples in which the average separation between particles was much greater than the diameter of the particles themselves. The particle size deduced was of the right order of magnitude and, even though no exact checks were available from independent determinations by a different method, this gave some confirmation of the validity of the assumptions made in the derivation of the formulae used. Later the theory was generalized to apply to samples in which particles of a given shape were assumed to have a given size distribution (18). Some consideration was given to cases in which the particles were arranged in groups such as the atoms in chain molecules or fibers (3, 5, 14). In 1948 Bergmann (2) drew attention to the fact that with concentrated samples of any type the assumption that there is no interparticle interference is invalid and that, if the particles are all of the same size and shape, the intensity of the scattering is given by the product of the form function of the particles and the

Fourier transform of the particle distribution. In 1949 Yudowitch (19) carried out experiments using concentrated samples of colloidal gold deposited on aluminum foil and observed for the first time with spherical particles a maximum in the distribution of the intensity of the scattered radiation attributable to particle to particle interference. The work to be described here was undertaken to extend the observations on concentrated samples. Colloidal gold was used to give spherical particles, the intention being to go on to other shapes. However, the results were such that the work with colloidal gold was extended.

EXPERIMENTAL METHODS AND RESULTS

The samples studied were composed of gold particles deposited on aluminum foil by the evaporation of a drop of concentrated gold colloid. Seven sols were prepared by the method described by Zigmondy and from these 30 samples were deposited and used to produce scattering patterns. The concentration of the sol, the amount used, and the rate of drying were varied in attempts to obtain different distributions in samples containing particles of the same size. The particle size and size distribution in each sol was determined from photographs of each preparation taken with an RCA electron microscope at a magnification of $21,000 \pm 3\%$. The particles appeared closely spherical and the radii found in this way were: $135 \pm 20, 195 \pm 25, 235 \pm 35, 265 \pm 40, 340 \pm 35, 430 \pm 30, 490 \pm 50 \text{Å}$.

The X-ray tube was of the Ott-Selmayr type with an aluminum target and was operated from a full-wave, condenser filtered supply at 4000 v. (estimated ripple ± 40 v.) and 25 ma. The camera was an evacuated cylinder attached to the X-ray tube by a flexible bellows in such a way that the same aluminum foil served as window for both. The collimator consisted of two slits each 0.8 mm. by 0.25 mm. mounted parallel to each other 10 mm. apart. The aluminum foil bearing the sample was mounted directly behind the second slit and the scattering patterns were recorded on Eastman no-screen X-ray film placed 300 mm. behind the sample. The film was calibrated by means of a step filter of eight steps of aluminum foil increasing by 0.0075 mm. per step. Assuming the coefficient of absorption to be that for the K_a radiation the curves of density versus intensity were linear and independent of voltage for voltages up to 4000 v. This was taken to indicate that at voltages up to 4000 v. the window together with the foil on which the sample was mounted gave satisfactory filtration of the white radiation. Photographs made at voltages as high as 7000 v. showed no observable difference in the intensity distribution at angles greater than 0.004 radians from those made at 4000 v. The region of angles smaller than this would not have been used in any case because of the magnitude of the collimation error at such small angles.

Exposure times ranged from 8 to 30 hr. and all the photographs showed evidence of particle to particle interference although the maximum due to this was not in most cases very sharp. The logarithm of the intensity was plotted against $k = 2\pi\epsilon/\lambda$ where ϵ is the angle of scattering and $\lambda = 8.32 \text{Å}$, the wave length of the radiation. Theoretically the position of the interference maximum
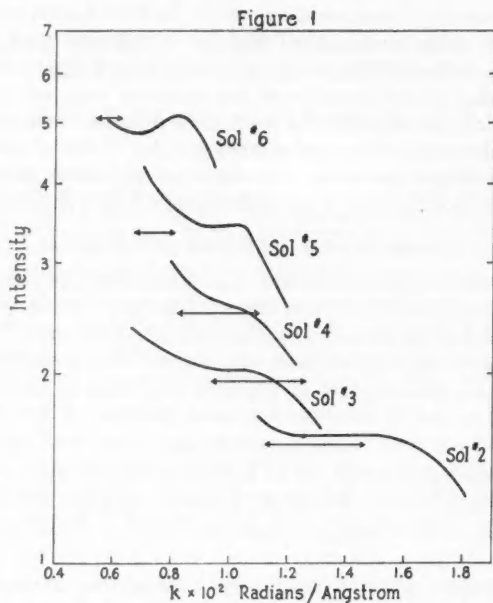
Figure 1

In order to separate the various curves the intensity values have been multiplied by a different arbitrary constant in each case.   Absolute intensities were not measured.

Figure 2
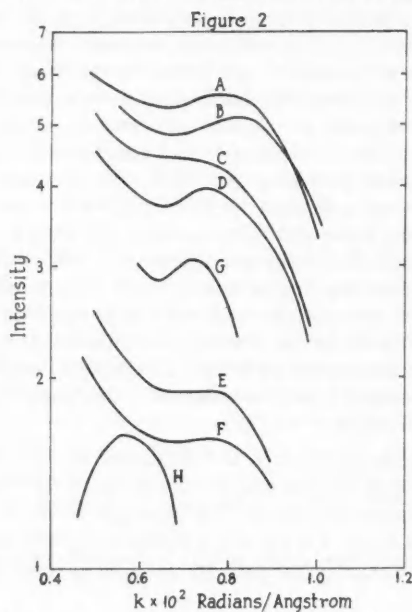
In order to separate the various curves the intensity values have been multiplied by a different arbitrary constant in each case.   Absolute intensities were not measured.

is a function of kR only and for the same radial distribution of spherical particles should occur at the same value of kR for particles of all radii. For the one sample for which Yudowitch determined it he found it to be at $kR = 2.5$. Fig. 1 shows typical curves for five different samples, the double-pointed arrow accompanying each curve indicating the range within which k should lie if $kR = 2.5$ and R varies between the limits given by the electron microscope photographs. In three of the cases shown the maximum lies well outside this range; in only one near the center of it. Fig. 2, curves A, B, C, D, E are for five different samples prepared from sol No. 6 $(R = 430 \pm 30\,\text{Å})$. Curve F is for the same sample as curve E but the pattern was photographed with collimator slits of a different size. The sharpness of the maximum varies with the preparation of the sample and small changes in its position are observed. Over 60 patterns were photographed in all and the results shown in Figs. 1 and 2 are typical.

Earlier determinations of particle size with dilute samples were made in general by plotting $\ln I$ against k^2 and measuring the slope of the curve at small angles. For spherical particles the scattering is given (11) by $I = MN^2\phi^2(kR)I_e$, where M is the total number of particles, N the number of electrons per particle, and I_e the intensity scattered by a single electron.

$$\phi(kR) = 3\left(\frac{\sin kR - kR \cos kR}{k^3 R^3}\right)$$

and k, ϵ, λ have the same meaning as before. At small enough values of kR this approximates closely to $I = MN^2 e^{-k^2 R^2/5}$ and the slope of the $\ln I$ vs. k^2 curve gives $R^2/5$. For concentrated samples the above expression for the intensity is multiplied by a factor which depends on the distribution of the particles and it might be expected that the shape of the curve would be changed even at small angles. This was pointed out by Lund and Vineyard (17). For colloid No. 6 curves $\ln I$ vs. k^2 were plotted for different sample preparations and the slope was found to vary significantly from one to another although the particle size must have remained the same and only the arrangement could have varied. This method of size determination is therefore not capable of high accuracy if concentrated samples are used.

DISCUSSION

A graph of $\phi^2(kR)$ vs. kR for $0 < kR < 6$ is shown in Fig. 3a. $\phi^2(kR)$ decreases rapidly with increasing kR and shows intensity maxima and minima, the positions of the maxima for $0 < kR < 48$ and their relative intensities being listed in Table I, columns 1 and 2. Interparticle interference was taken into account by Yudowitch by assuming a distribution similar to that for a monatomic liquid and using an equation derived by Gingrich and Warren (9) based on the assumption that the particle density is zero at distances from the center of the origin particle less than the particle diameter, is a maximum at $r = D$, and has a lower constant value for r greater than D. This equation is:

$$I = MN^2\phi^2(kR)[1 + P\{5 \sin(2kR)/2kR - 6\phi(2kR)\}]I_e$$
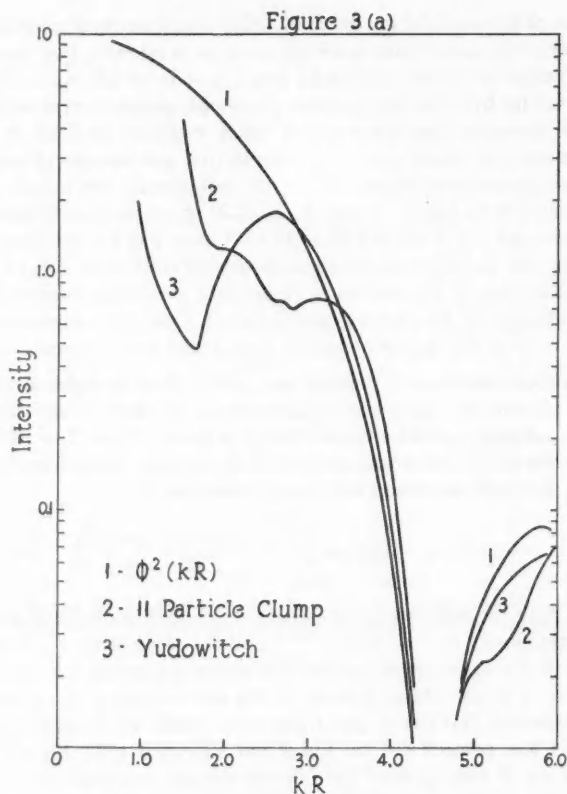
FIG. 3a.   Intensities as calculated multiplied by 100 for curves 1 and 3 and by 10 for curve 2.

TABLE I

VALUES OF kR AT WHICH INTENSITY MAXIMA OCCUR FOR VARIOUS ASSUMED PARTICLE
DISTRIBUTIONS AND THE RELATIVE INTENSITIES OF THOSE MAXIMA

$\phi^2(kR)$		Yudowitch formula		5-particle clump		11-particle clump		27-particle clump	
		2.535	2700	2.85	1700	3.08	1000	2.845	3250
								5.633	100
5.78	100	5.89	100	6.11	100	6.208	100	6.504	76
9.10	17	9.24	19	9.30	19	9.53	17	9.335	25
12.32	5.1	12.50	5.8	12.45	6.0	12.43	5.1	11.874	5.6
								12.818	5.7
15.515	2.0	15.608	2.3	15.647	2.5	15.685	2.3	15.784	3.1
18.689	0.98	18.764	1.1	18.744	1.2	18.89	1.0	18.616	1.4
21.854	0.52	21.917	0.60	21.933	0.62	22.00	0.54	22.141	0.67
25.013	0.31	25.062	0.35	25.033	0.36	25.12	0.33	25.174	0.40
28.167	0.19	28.215	0.22	28.256	0.23	28.30	0.20	28.348	0.25
31.320	0.12	31.362	0.14	31.379	0.15	31.40	0.13	31.381	0.18
34.470	0.086	34.508	0.10	34.526	0.11	34.55	0.092	34.545	0.11
37.619	0.060	37.655	0.070	37.690	0.073	37.75	0.064	37.825	0.080
40.767	0.043	40.799	0.050	40.796	0.053	40.843	0.046	40.869	0.059
43.914	0.032	43.943	0.037	43.941	0.040	44.007	0.034	43.976	0.044
47.060	0.024	47.088	0.028	47.095	0.030	47.143	0.026	47.113	0.033

where P indicates the closeness of packing and $0 < P < 1$. Values of kR corresponding to the maxima of this expression for $P = 0.5$ with their relative intensities are given in columns 3 and 4 of Table I. Except for the additional one at $kR = 2.5$ these maxima lie in nearly the same positions and have nearly the same relative intensities as those for $\phi^2(kR)$, the general effect of the second factor being to shift the maxima to slightly higher values of kR, the discrepancy decreasing as kR increases. A graph of this function for $0 < kR < 6$ is also shown in Fig. 3a.
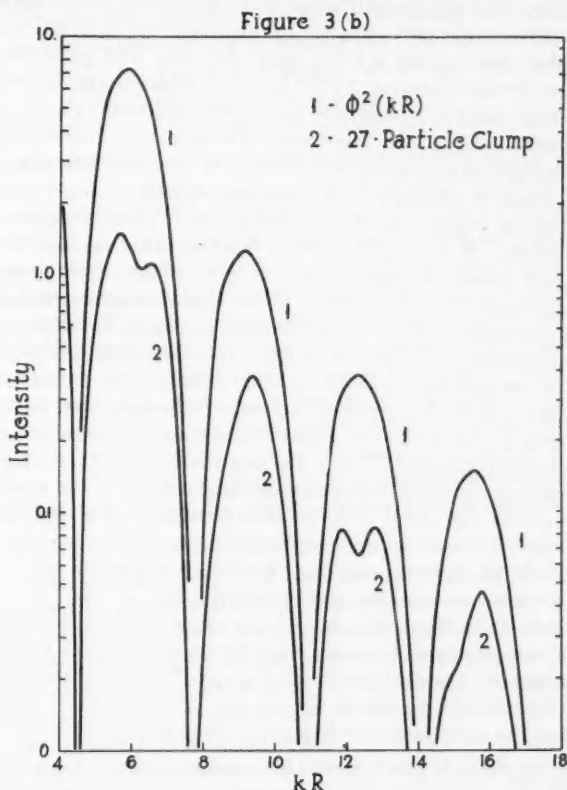
FIG. 3b. Intensities as calculated multiplied by 1000 for curve 1 and by 10 for curve 2.

Other possible distributions lead to substantially the same result. As examples of this the position and relative intensities of the maxima of the expressions derived by Lund and Vineyard (17) for 5 and 11 particle clumps are listed in Table I, columns 5, 6, 7, 8. Except for the maxima at 2.85 and 3.08 respectively the positions and relative intensities are again close to those for ϕ^2. Fig. 3a includes a graph for a sample consisting of randomly-oriented 11-particle

clumps of the type assumed by Lund and Vineyard. Only for very large clumps would one expect to observe a complete set of maxima corresponding to the Debye-Sherrer rings of the usual powder pattern. To further emphasize this the pattern for a cubic 27-particle clump in which the particles are assumed to be arranged on a simple cubic lattice of spacing D is given in the last two columns of Table I and graph 2 of Fig. 3b.

In 1951 Yudowitch (20) determined the particle size of Dow latex 580G, lot 3584, assuming the particle distribution in his samples to be the same as he had assumed earlier for the gold samples. He identified the observed maxima with those secondary shape maxima which occur at values of kR greater than 15, and found a value for the diameter of 2780 Å $\pm$ 6%. Observations were not made at sufficiently small angles to make detection of the interference maximum possible. Had he assumed simply that there was no interparticle interference and used the positions of the ϕ^2 maxima in his calculations he would have obtained 2774 Å with about the same probable error. Five-particle clumps would have given the same value as the original assumption and 11- or 27-particle clumps of the type referred to above 2790 Å. In 1952 a similar determination was made by Danielson (4) using a focusing monochromator to give more nearly monochromatic radiation and so increase the accuracy of the experimental determination of the positions of the maxima. Working in the same region of kR values and assuming the same distribution as Yudowitch he found the diameter to be 2698 Å averaging values for all the maxima observed, or 2689 Å using only the outermost three. Another determination by Leonard, Anderegg, Kaesberg, and Beeman (16) in which the first 17 shape maxima were measured and weighted in proportion to the angle of scattering gave 2713 Å, the statistical accuracy of the mean being $\pm$ 3 Å. These last results included measurements on one of the samples used by Yudowitch and it was found to give values consistent with those for the other samples studied. It would appear therefore that provided one ignores the "interference" maximum and uses only the "secondary shape function" maxima the error due to ignorance of the particle distribution is, even in concentrated samples, likely to be less than that of the experimental measurements. Conversely the fact that use of a given distribution gives values within this error is no proof that the assumed distribution is actually that present in the sample. Use of the interference maximum for particle size determination without some knowledge of the distribution could give errors as high as 30%.

Knowing the particle size it should be possible to obtain from the position of the interference maximum and its intensity relative to the shape function maxima some information concerning the particle distribution. Two possibilities have been discussed: 1. an arrangement similar to that in a monatomic liquid and 2. an arrangement similar to that in a polyatomic gas. The first of these leads to an interference maximum at $kR = 2.5$ and the second to a maximum at a value of kR somewhat greater than this, and larger for clumps containing a greater number of particles. The experimental intensity distributions which we observed are in general in disagreement with the former but can be accounted for by the latter. When the mean value given by the electron micrographs is

assumed to be the true radius of the particles, the observed interference maximum occurs at values of kR considerably greater than 2.5. Curve H, Fig. 2 shows the intensity maximum assuming arrangement 1 and curve G that for an 11-particle clump. If clumping does occur it is unlikely that all clumps contain the same number of particles arranged in exactly the same way. The maximum would be expected to be broad and its position could not be exactly predicted. It was found that different samples gave distributions with maxima in slightly different positions. The change was in general less between two samples containing particles of the same size than between two samples containing particles of different size. It does not seem unreasonable to suppose that the distribution of clumps would be more similar in the first case than in the second. The electron micrographs showed a tendency of the particles to form clumps, and Danielson refers to the same feature of the photographs of Gerould (8) of latex particles.

The above discussion is based on the assumption of a given particle distribution and a comparison of the experimentally obtained dependence of scattering intensity on scattering angle with that predicted. If $\phi^2(kR)$ is known, and it might be found from, say, a study of a dilute system containing similar particles, a Fourier transformation should enable one to obtain the distribution function. Methods of doing this have been suggested (1). However, it is almost certain that a large number of particle distributions would give a good approximation to the experimental curve and it seems unlikely that the work involved would be justified. Fournet and Guinier (6, 7) have recently approached the problem from a different point of view and have derived an expression for the scattered intensity involving only the size, shape, and mutual potential of the particles. The expression includes the effect of particle distribution without any assumption as to the nature of the distribution function but requires a value of the interparticle potential and the relative concentrations of the samples studied.

CONCLUSIONS

Samples containing different kinds of particles and prepared in different ways will have different particle distributions, and only one type has been studied experimentally. However, the following general conclusions based on our observations would seem to be justified. In concentrated samples interparticle interference effects are present and lead to (*a*) a maximum or at least a plateau in the scattering at angles smaller than those at which the form function maxima occur, (*b*) a change in the slope of the ln I vs. k^2 curve at small angles, and (*c*) a shift in the form function maxima. This third effect is small particularly for maxima at large kR values and in general interference effects can be neglected in size determinations from the form function maxima. The error thus introduced is less than that of the experimental measurements. The second effect is quite large and invalidates particle size determinations in concentrated samples from the value of this slope. The position of the maximum referred to in (*a*) is determined by the radial distribution of particles in the sample and without a knowledge of the latter cannot be used to give better than an order of magnitude estimate of the particle size. No unique determination of the particle distribution

from the position and shape of this maximum appears possible even if the
particle size and shape are known.

REFERENCES

1. BAUER, S. H.   J. Chem. Phys. 13: 450.   1945.
2. BERGMANN, G.   Phys. Rev. 74: 1209.   1948.
3. BISCOE, J. and WARREN, B. E.   J. Applied Phys. 13: 364.   1942.
4. DANIELSON, W. E.   Special Tech. Rept. No. 15, Calif. Inst. Technol., Pasadena, Calif. 1951.
5. FANKUCHEN, I. and MARK, H.   J. Applied Phys. 15: 364.   1944.
6. FOURNET, G.   Compt. rend. 228: 1801.   1949.
7. FOURNET, G. and GUINIER, A.   J. phys. radium, 11: 516.   1950.
8. GEROULD, C. H.   J. Applied Phys. 21: 185.   1950.
9. GINGRICH, N. S. and WARREN, B. E.   Phys. Rev. 46: 248.   1934.
10. GRAY, J. A. and ZINN, W. H.   Can. J. Research, A, 11: 291.   1930.
11. GUINIER, A.   Ann. phys. 12: 161.   1939.
12. HOSEMANN, R.   Z. Physik, 113: 781.   1939; 114: 133.   1939.
13. JELLINECK, M. H. and FANKUCHEN, I.   Ind. Eng. Chem. 37: 198.   1945.
14. KRATKY, O. and SEKORA, A.   Naturwissenschaften, 31: 46.   1943.
15. KRISHNAMURTI, P.   Indian J. Phys. 5: 473.   1930.
16. LEONARD, B. R., ANDEREGG, J. W., KAESBERG, P., and BEEMAN, W. W.   J. Applied
    Phys. 23: 152.   1952.
17. LUND, L. H. and VINEYARD, G. H.   J. Applied Phys. 20: 593.   1949.
18. SHULL, C. G. and ROESS, L. C.   J. Applied Phys. 18: 295.   1947.
19. YUDOWITCH, K. L.   J. Applied Phys. 20: 174.   1949.
20. YUDOWITCH, K. L.   J. Applied Phys. 22: 214.   1951.

FURTHER MEASUREMENTS ON THE γ RAYS PRODUCED BY NEUTRON CAPTURE IN BERYLLIUM AND CARBON[1]

By G. A. Bartholomew and B. B. Kinsey

ABSTRACT

New measurements have been made of the neutron capture radiation from beryllium and carbon using a more sensitive pair spectrometer. From beryllium, γ rays with energies of 6.81 and 3.41 ± 0.06 Mev. were detected. The former is the ground state γ ray previously reported. The 3.41 Mev. γ ray, which has an intensity of about 0.25 photon per capture, seems to be due to the excitation of the first excited state in Be^{10}. From carbon, in addition to the 4.95 Mev. ground state γ ray previously reported, a γ ray was found with an energy of 3.68 ± 0.05 Mev. and with an intensity of about 0.3 photon per capture. No γ rays were observed which could be associated with the excitation of the level at 3.9 Mev. in C^{13}.

INTRODUCTION

In a previous paper (10) we have described the results of preliminary measurements of the neutron capture γ rays from beryllium and carbon. In the present paper we report the results of new measurements made with an improved model of the pair spectrometer. This instrument provides coincidence counting rates 10 times greater than were available in the old instrument. The experimental arrangement has been described briefly in another paper (11). The details of the instrument and the method of intensity and energy measurement will be fully described in a forthcoming paper (9).

The sample materials used were similar to those employed in the previous investigation (10). The carbon was in the form of a graphite cylinder, 8 in. long, 4 in. in diameter, and of exceptionally high purity. Two beryllium samples were used; one consisting of blocks of sintered beryllia, again of unusual purity, the other of beryllium metal. Both samples were enclosed in Dural containers with Bakelite ends. The use of Bakelite ends removed the aluminum capture radiation which interfered seriously with the spectrum obtained in the previous investigation.

BERYLLIUM

The pair spectrum obtained with the beryllium oxide sample is shown in Fig. 1. The peak A is the ground state γ ray in Be^{10} previously reported. The peaks near 7.5 Mev. are due to a small amount of aluminum and lead capture radiation not completely removed by the collimating system. The γ rays, B at 5.9 and C at 4.9 Mev., do not correspond to any of the known excited states in Be^{10}. The γ ray C has the energy of the ground state γ ray in C^{13} and may therefore arise from neutron capture in the Bakelite ends of the sample container or it may be due to a small impurity of silicon which was found, by spectrographic analysis, to be present in the beryllium oxide to the extent of about 0.05%. The peak at B is difficult to account for; it may be only a statistical fluctuation or it may correspond to a γ ray produced by an impurity in the beryllium oxide or to a
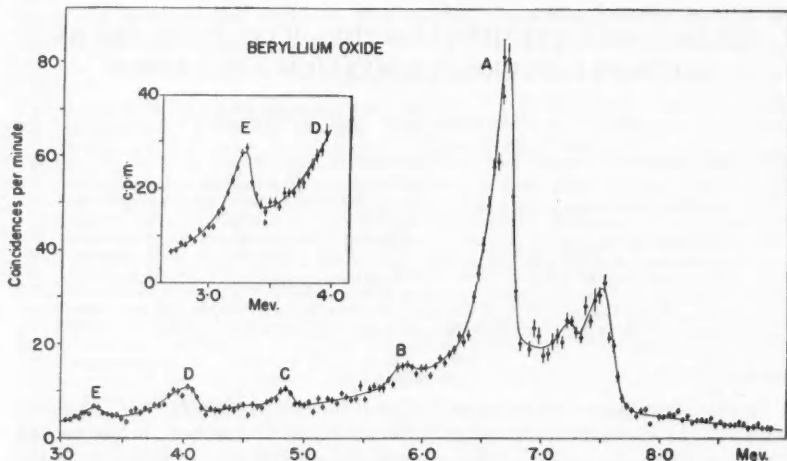
FIG. 1. Capture γ-ray spectrum produced by beryllium oxide. The insert shows part of the spectrum obtained with a sample of beryllium metal. Line width: 200 kev.

γ ray emitted by the material used as a filler in the Bakelite. Although it has the energy of one of the principal γ rays of the iron spectrum, it cannot be ascribed to this element, for the other strong iron capture γ rays are absent. Of the remaining impurities, lead (concentration 0.05%) could contribute only to the peak near 7.5 Mev. and calcium, copper, magnesium, and titanium, of which the concentrations were found to be less than 0.005%, do not produce prominent γ rays at 5.9 Mev. The γ ray D is produced by neutron capture in the bismuth block situated in the experimental hole between the sample and the reactor (11).

The γ ray E is not very distinct in the spectrum obtained with the beryllium oxide sample. The results of additional measurements made with metallic beryllium are shown in the insert, Fig. 1. Capture radiation produced by impurities in the metal obscured the high energy beryllium spectrum obtained with this sample. It was used therefore, to obtain only the relative peak counting rates of the γ rays E and A.

The energy of the γ ray E is 3.41 ± 0.06 Mev. which is in good agreement with the value of 3.375 ± 0.010 Mev. found by Buechner and Strait (3) for the energy of an excited state in Be^{10}. Since the neutron binding energy of Be^{10} is 6.816 ± 0.006 Mev. (9) it follows that the energy of the γ ray producing the excited state is about 3.44 Mev. This energy differs from the observed γ ray energy by only 30 kev., an amount which is less than the resolution of the instrument and the accuracy of the measurements. If we identify the γ ray E with that producing this excited state, it is clear that the γ ray emitted by this state is superposed on E and the counting rate at the peak must correspond to the sum of their intensities. Using the calculated counting efficiency curve for the spectrometer, and assuming that this state and the ground state are the only ones produced by neutron capture, we find that the intensity of each cascade

γ ray is about 0.25 photon per capture and that that of the ground state γ ray is 0.75 photon per capture.

CARBON

The pair spectrum obtained with the graphite sample is shown in Fig. 2. In order to obtain the maximum counting rate, even at the sacrifice of resolving power, the results of Fig. 2 were obtained with a thick lead radiator and with
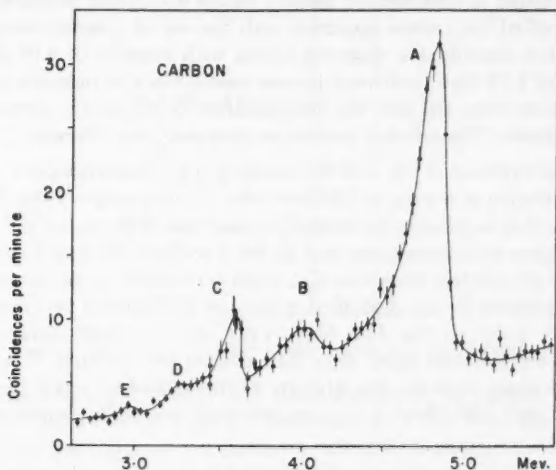
Fig. 2.   Capture γ-ray spectrum produced by carbon.   Line width: 200 kev.

the slits covering the counters at their maximum width. In this figure the ground state γ ray at 4.95 Mev. is very distinct, and there is a clear indication of two other γ rays, B near 4.2 Mev. and C at 3.68 ± 0.05 Mev. The γ ray B is clearly due to capture in the bismuth block. The presence of two further γ rays, D at 3.38 ± 0.05 Mev. and E at 3.04 ± 0.05 Mev., is suggested, but their existence cannot be confirmed because of the inadequate statistical accuracy of the experimental points.

The γ ray C is quite distinct and the coincidence peak is readily reproducible. It is curious that this peak did not appear in the previous investigation, in which the same graphite sample was used. There is, however, some indication in the previous results of an increase in the counting rate in this energy range. As will be shown below, the γ ray C is emitted in the transition from the second excited state to the ground state in C^{13}.

Both the γ rays D and E may be emitted by the impurities which undoubtedly produce the high background observed above 5 Mev. The γ ray E, however, has an energy which corresponds to that of the first excited state in C^{13} and might be produced in a transition between that state and the ground state. The γ ray D cannot be associated with any of the known excited states of C^{13}. We have not attempted to examine this part of the spectrum in any greater

detail, for the use of better experimental conditions would involve a severe loss in counting rate and measurement would be exceedingly slow and difficult. Even if the presence of these γ rays were confirmed, their interpretation must remain obscure, for in a material such as graphite, which has a very low capture cross section, the presence of some relatively strongly absorbing impurities is inevitable.

It is interesting to compare the present results with those obtained by Wilson (19) who studied the carbon spectrum with the use of a deuterium-filled ionization chamber counter. He observed γ rays with energies of 4.95 ± 0.05, 4.1, 3.65, 3.4, and 3.05 Mev., and since he also used a block of bismuth to attenuate the direct beam from the pile, the interpretation of his results corresponds with that given above. The relative intensities, however, are different.

There is no evidence in Fig. 2 of the presence of a coincidence peak corresponding to the emission of a γ ray of 3.9 Mev. which is the energy of the third excited state of C^{13}. If it is present, its intensity is less than 0.06 photon per capture. If then we assume that transitions only to the 3.68 Mev. state and to the ground state occur, the relative peak counting rates correspond to an intensity of 0.30 photon per capture for the 3.68 Mev. γ ray and 0.70 photon per capture for the ground state γ ray. If the 3.08 Mev. γ ray, E, is actually present, then its intensity is certainly no more than 0.10 photon per capture. If we take into account this upper limit for the intensity of the 3.08 Mev. γ ray, the intensities of the 4.95 and 3.68 Mev. γ rays become 0.63 and 0.26 photon per capture respectively.

DISCUSSION

In Be^{10}, two excited states at 3.37 and 6.3 Mev. (7) are known to exist between the ground state and the neutron binding energy (Fig. 3). There is no evidence in the present results for the excitation of the latter level. From shell theory considerations we should expect the ground state of Be^9 to be of odd parity. It has recently been shown (6) by angular distribution measurements of the protons from the Be^9 (d,p) Be^{10} reaction that both the ground state and the 3.37 Mev. state of Be^{10} have a parity different from that of the ground state of Be^9. Thus the emission of both of the γ rays leading to these states must produce a change in parity. Since the spin of Be^9 is 3/2 and that of the even–even nucleus Be^{10} is presumably zero, the angular momentum radiated by the ground state γ ray can be 1 or 2 units and that γ ray therefore is either of the electric dipole or of the magnetic quadrupole type. However, the excited state at 3.37 Mev., being the first of an even–even nucleus, very probably has a spin of 2 units, and since the intensities of the two γ rays are at least comparable, it is very likely that both are of the electric dipole type.

The ground state of C^{13} has a spin of 1/2 and it has been shown (5) that its parity is different from that of C^{12}, i.e., it is presumably odd. Three excited states with energies of 3.08, 3.68, and 3.88 Mev. are definitely known to exist between the ground state and the neutron binding energy (12, 15) while the existence of an excited state near 1 Mev. originally observed in the B^{10} (α,p) C^{13} reaction now seems to be doubtful (1, 4, 12). There is no evidence for the presence of
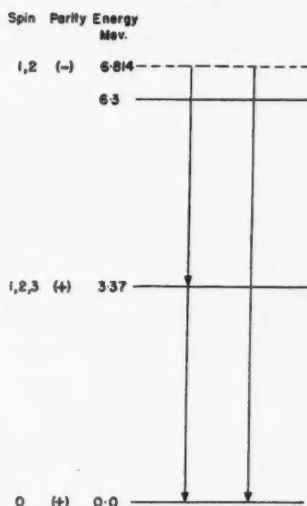
Fig. 3.   Energy level diagram of Be^{10} showing observed neutron capture γ rays.

levels between 3.88 and 4.95 Mev. (7). From a study of the angular distribution of the protons from the C^{12} (d,p) C^{13} reaction (14) it has been shown that the 3.08 Mev. state has a spin of $1/2$ and even parity. This assignment is consistent with the observation that electric dipole radiation is emitted in the transition from this state to the ground state (16). Recent measurements by Rotblat (15) indicate that the 3.68 Mev. state has a spin of $1/2$ or $3/2$ and odd parity and that the 3.88 Mev. state has a spin of $3/2$ or $5/2$ and even parity. It is reasonable to assume therefore that the excited states of C^{13} follow the same order as those of the mirror nucleus N^{13} which, from a study of the proton resonances in carbon (8), have been shown to be $S_{1/2}$, $P_{3/2}$, $D_{5/2}$.

The levels of C^{13} are shown diagrammatically in Fig. 4 where the observed properties of the levels are given on the left and the level order, inferred from the comparison with the levels of N^{13}, is given on the right. The broken line at 4.95 Mev. represents the neutron binding energy of C^{13} and the γ rays observed to follow neutron capture are shown by vertical arrows. The γ rays in cascade with those shown have energies too low to be detected by the pair spectrometer.

On the basis of the level assignments assumed in Fig. 4 it follows that both the ground state γ ray and the γ ray producing the 3.68 Mev. excited state are of the electric dipole type. It also follows that the γ ray producing the excited state at 3.88 Mev. is electric quadrupole and that the γ ray emitted in the transition from that state to the ground state is magnetic quadrupole. This state of affairs would account for the fact that no 3.88 Mev. γ ray was observed.

Thomas (17, 18) has pointed out that a good fit with the low energy s-wave neutron scattering data in C^{12} can be obtained if it is assumed that the level associated with the scattering is that at 3.08 Mev. This state may also be the
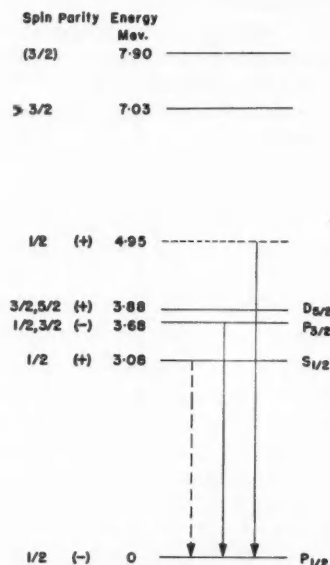
FIG. 4. Energy level diagram of C^{13} showing observed neutron capture γ rays.

one responsible for thermal neutron capture, for no other S states have been found below an excitation of 7.9 Mev., and it is probable that none exist below 8.6 Mev. (2, 13). Although no direct transition to this state is expected theoretically, transitions to this state from the two higher levels are possible. The observed intensity of the 3.08 Mev. γ ray, less than 0.1 photon per capture, fixes an upper limit to the combined probabilities of transitions from the two higher states.

REFERENCES

1. BLUNDELL, M. and ROTBLAT, J. Phys. Rev. 81: 144. 1951.
2. BOCKELMAN, C. K., MILLER, D. W., ADAIR, R. K., and BARSCHALL, H. H. Phys. Rev. 84: 69. 1951.
3. BUECHNER, W. W. and STRAIT, E. N. Phys. Rev. 76: 1547. 1949.
4. BUECHNER, W. W., STRAIT, E. N., SPERDUTO, A., and MALM, R. Phys. Rev. 76: 1543. 1949.
5. BUTLER, S. T. Phys. Rev. 80: 1095. 1950.
6. EL-BEDEWI, F. A. Proc. Phys. Soc. (London), A, 65: 64. 1952.
7. HORNYAK, W. F., LAURITSEN, T., MORRISON, P., and FOWLER, W. A. Revs. Modern Phys. 22: 291. 1950.
8. JACKSON, H. L. and GALONSKY, A. I. Phys. Rev. 84: 401. 1951.
9. KINSEY, B. B. and BARTHOLOMEW, G. A. Can. J. Phys. To be published.
10. KINSEY, B. B., BARTHOLOMEW, G. A., and WALKER, W. H. Can. J. Phys. 29: 1. 1951.
11. KINSEY, B. B., BARTHOLOMEW, G. A., and WALKER, W. H. Phys. Rev. 83: 519. 1951.
12. MALM, R. and BUECHNER, W. W. Phys. Rev. 81: 519. 1951.
13. MILLER, D. W. Phys. Rev. 78: 806. 1950.
14. ROTBLAT, J. Nature, 167: 1027. 1951.
15. ROTBLAT, J. Phys. Rev. 83: 1271. 1951.
16. THOMAS, R. G. Phys. Rev. 80: 138. 1950.
17. THOMAS, R. G. Phys. Rev. 81: 148. 1951.
18. THOMAS, R. G. Phys. Rev. 81: 661. 1951.
19. WILSON, R. Phys. Rev. 80: 90. 1950.

SECOND-ORDER BEAMS OF SLOTTED WAVE GUIDE ARRAYS[1]

By H. Gruenberg

ABSTRACT

It is shown that the radiation pattern of slotted wave guide arrays may contain small second-order beams even for slot spacings less than a free-space wave length. These beams are usually split with a minimum or even a null in the plane containing the array and main beam. Since patterns are normally taken in this plane, the second-order beams have until now escaped attention, as far as the writer is aware. Methods of suppressing these beams are discussed.

I. INTRODUCTION

In the design of slotted wave guide arrays for high-gain antennas it is customary to use the theory of linear arrays to obtain radiation patterns. For certain wave guide arrays this is not quite justified.

Consider, for instance, the array consisting of longitudinal slots in the broad face of a rectangular wave guide (Fig. 1). The slots will radiate only if they are displaced from the center line of the guide face. The amount of radiation depends on the offset. A broadside array can be obtained by spacing the slots about a guide wave length apart on one side of the center line because they will then be excited approximately in phase. Such an array would have large second-order diffraction beams which would make it unsuitable for most purposes. The second-order beams come about because the slot spacing is larger than the free-space wave length (2). It is generally argued that this defect can be eliminated and, at the same time, the broadside feature of the array retained, by spacing the slots approximately half a guide wave length apart and reversing the phase of alternate slots by staggering about the center line.

The above reasoning is based on the theory of linear arrays and tacitly assumes that the small displacement of the slot radiators from a straight line has negligible effect on the radiation pattern. It will be shown in the following that such an assumption is, in general, not justified. The array of Fig. 1 actually has
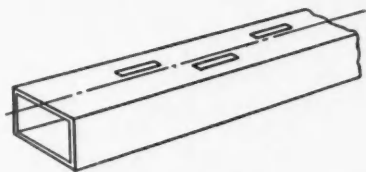

Fig. 1. Slotted wave guide array.

second-order beams even for slot spacings of half a wave length. These beams are, however, to be found closer to the plane of the slots and not in the plane

containing the guide axis and the main beam. Since radiation patterns are usually only taken in the latter plane these second-order beams have so far escaped detection, as far as the writer is aware.

In a properly constructed array the size of the second-order beams depends on the magnitude of the slot offsets relative to the wave length. For practical arrays they may be 10% or more of the main beam in terms of field strength. They will be larger in arrays of comparatively short electrical length because of the necessity of using larger slot conductances and hence larger offsets. In some applications such as merchant marine radar in narrow waters, where all spurious radiation more than about five degrees from the main beam should be kept down to 30 or 40 decibels below the main beam, a knowledge of these side lobes will be of prime importance.

II. SECOND-ORDER BEAMS DUE TO SLOT OFFSET

To simplify the analysis of the slotted wave guide array, it will be assumed that all slots have the same offset from the center line. This is true for a resonant array with uniform excitation for all slots. Nevertheless the assumption is reasonable for most practical arrays, as can be seen from the following arguments. Usually a tapered amplitude distribution is employed along the array to reduce the side lobe level. For this reason most of the power is radiated by relatively few slots at the center of the array. Furthermore, the slot offset usually varies little from slot to slot near the center of the array since the offsets are approximately proportional to the square root of the required slot excitation (6, 7). Thus the error introduced in calculating the radiation pattern will be small if the actual array is replaced by two parallel linear arrays separated by twice the "weighted" mean offset (Fig. 2). This weighted mean will be close to
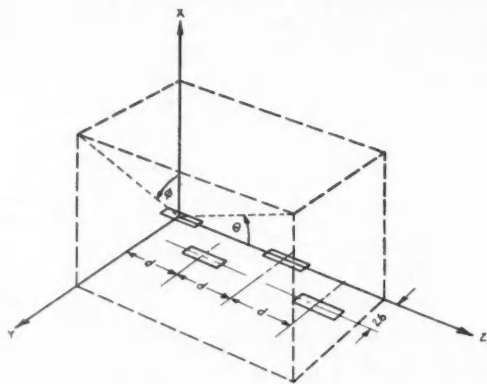
FIG. 2.   Reference system for idealized array.

the offset of the slot which is most strongly excited, usually a slot near the center of the array.

By Babinet's principle (1) the radiation pattern of a slot in an infinite conducting plane is identical with that of a linear antenna in free space. For a slot
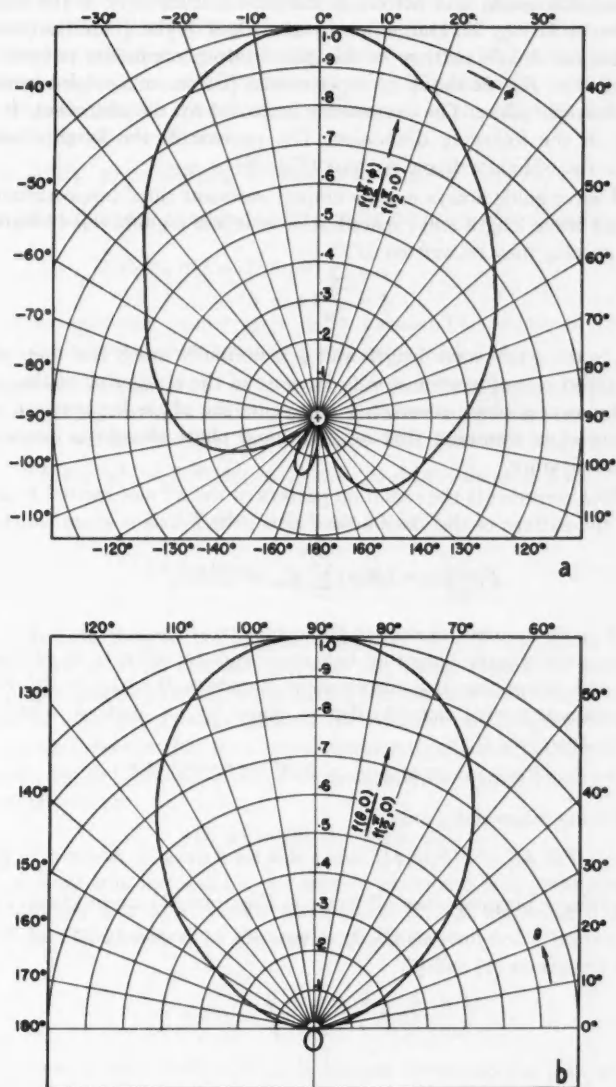
FIG. 3. Radiation pattern of a single slot in X-band rectangular wave guide. Slot offset 0.1 in. Wave length 3.2 cm.

(a) Transverse plane ($\theta = 90°$).
(b) Longitudinal plane ($\phi = 0°$).

in a rectangular guide this pattern is modified considerably in the transverse plane ($\theta = \frac{1}{2}\pi$ in Fig. 2). Diffraction by the edges of the guide transforms the omnidirectional dipole pattern in this plane into a cardioidal pattern with a small back lobe. Fig. 3a shows an experimental pattern of a single resonant slot in the transverse plane. The asymmetry is caused by the slot offset. It will be neglected in the following discussion. The pattern in the longitudinal plane ($\phi = 0$) is the ordinary dipole pattern (Fig. 3b).

Slotted wave guide arrays usually employ resonant slots (approximately half a free-space wave length long) spaced at or near half a guide wave length apart. The slot spacing may be written as

[1]
$$d = \frac{\lambda_g}{2\pi}(\pi + \psi)$$

where λ_g is the guide wave length and ψ is normally much less than one. The array is called resonant when $\psi = 0$. Because of the staggering of the slots and the accompanying phase reversal, ψ represents the phase lag between any two consecutive slots assuming that no additional phase change is introduced by the slot admittance.

If $C_n f(\theta,\phi)$ represents the radiation pattern of the nth slot excited to an amplitude C_n, the pattern of the "half-array" along the Z-axis is given by (Ref. 3)

[2]
$$F_1(\theta,\phi) = f(\theta,\phi) \sum_{n=0}^{N-1} C_{2n} \, e^{j2n(\beta d \cos\theta - \psi)}$$

where $2N$ is the number of slots in the complete array, $\beta = 2\pi/\lambda$, and λ is the free-space wave length. The other half-array may be taken to be identical with the first one except that it is displaced by distances 2δ and d in the Y- and Z-directions respectively, and retarded in phase by an angle ψ. The resultant pattern is, therefore,

[3]
$$F(\theta,\phi) = F_1(\theta,\phi)[1 + e^{j(2\beta\delta \sin\theta \sin\phi + \beta d \cos\theta - \psi)}]$$

or considering magnitudes only,

[4]
$$|F(\theta,\phi)| = 2|F_1(\theta,\phi)| \; |\cos \tfrac{1}{2}(2\beta\delta \sin\theta \sin\phi + \beta d \cos\theta - \psi)|.$$

$|F_1|$ will have maxima when all terms in Equation [2] are in phase, i.e., when

[5]
$$\beta d \cos\theta_p - \psi = p\pi \qquad p = 0, \pm 1, \pm 2, \ldots.$$

From Equations [1] and [5]

[6]
$$\cos\theta_p = \frac{p\pi + \psi}{\pi + \psi} \cdot \frac{\lambda}{\lambda_g}.$$

Normally λ/λ_g is close to 0.7 and $|\psi| < 1$. Only the values $p = 0$ or $p = \pm 1$ will lead to real values of θ. These will be denoted by θ_0 and $\theta_{\pm 1}$. The first value gives the position of the main beam, the last two the positions of the second-order beams for the half-array. For small values of ψ the main beam will deviate only slightly from the array normal and the second-order beams will make angles of about 45° with the latter.

To analyze the pattern of the complete array we must examine the coefficient of $|F_1(\theta,\phi)|$ in Equation [4]. For any array of reasonable gain this coefficient is a very slowly varying function of θ compared to $|F_1|$. Hence the positions of main and secondary beams will still be given by Equation [6]. It is interesting to note what happens to these beams as a function of the offset 2δ. Substituting Equation [5] in [4] one obtains

[7] $$|F(\theta_p, \ \phi)| = 2|F_1(\theta_p, \ \phi)| \cos(\beta\delta \sin \theta_p \sin \ \phi + \tfrac{1}{2}p\pi).$$

For zero offset the peak amplitude of the main beam ($p = 0$) becomes

[8] $$2|F_1(\theta_0, 0)| = 2f(\theta_0, 0)\sum_{n=0}^{N-1} C_{2n}$$

while the second-order beams ($p = \pm 1$) vanish. This must, of course, be expected (2) since zero offset means a linear array with $d < \lambda$.

For small values of δ (i.e. $\beta\delta \ll 1$) it is easily seen from Equation [7] that the main beam will remain substantially unaltered since $\cos(\beta\delta \sin \theta_0 \sin \phi) \approx 1$ for $\beta\delta \ll 1$. There will however be "split" second-order beams of magnitude

[9] $$|F(\theta_{\pm1}, \ \phi)| = 2|F_1(\theta_{\pm1}, \ \phi)| \ |\cos \ (\beta\delta \sin \theta_{\pm1}\sin \ \phi \pm \tfrac{1}{2}\pi)|$$

$$\approx 2|F_1(\theta_{\pm1}, \ \phi)| \ \beta\delta \sin \theta_{\pm1} \sin \ |\phi|$$

$$= 2\beta\delta \sin \theta_{\pm1} \sin \ |\phi| \ f(\theta_{\pm1}, \ \phi)\sum_{n=0}^{N-1} C_{2n}.$$

These beams have nulls in the longitudinal plane ($\phi = 0$) containing the main beam, the plane in which normally patterns are taken. They have two maxima each in planes placed symmetrically about the plane $\phi = 0$. Hence the term "split beams". To get a rough idea of the position and magnitude of these maxima we shall assume that the three-dimensional radiation pattern of a single slot is given by the product of the radiation patterns in the longitudinal and transverse planes, i.e.

[10] $$f(\theta, \ \phi) = f(\theta, 0) \cdot f(\tfrac{1}{2}\pi, \ \phi).$$

This is certainly true for a slot in an infinite plane and is approximately true for a rectangular slot in a circular wave guide (5) for the range $0 < \theta < \pi$, $0 < |\phi| < \tfrac{1}{2}\pi$. The position of the peaks of the second-order beams is then given by

[11] $$\theta = \theta_{\pm1} = \cos^{-1}\left(\frac{\pm \ \pi + \psi}{\pi + \psi} \cdot \frac{\lambda}{\lambda_g}\right)$$

and

[12] $$f(\tfrac{1}{2}\pi, \ \phi) \sin \ |\phi| = \text{maximum}.$$

A plot of this function using the experimental radiation pattern of Fig. 3a shows broad maxima in the neighborhood of $\phi = \phi_1 = \pm \ 50°$ (Fig. 4). The maximum value of the function is about $0.5 \ f(\tfrac{1}{2}\pi, 0)$.
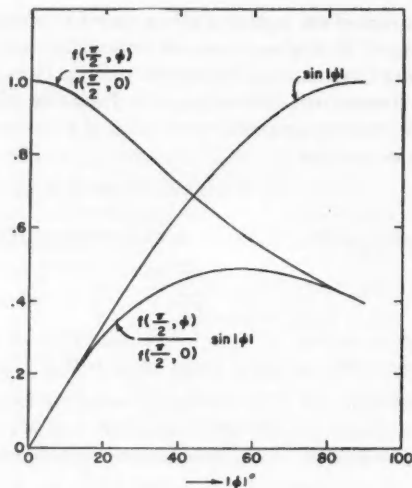
FIG. 4. Plot of $\dfrac{f(\frac{1}{2}\pi,\phi)}{f(\frac{1}{2}\pi,0)}\sin|\phi|$.

From Equations [8], [9], and [10] we get for the ϕ-dependence of the second-order beams expressed as fractions of the peak of the main beam:

[13] $$S(\phi) = \beta\delta \sin\theta_{\pm 1}\sin|\phi|\frac{f(\frac{1}{2}\pi,\ \phi)}{f(\frac{1}{2}\pi,\ 0)}\frac{f(\theta_{\pm 1},\ 0)}{f(\theta_0,\ 0)}.$$

Since θ_0 does not differ appreciably from $\frac{1}{2}\pi$ and the radiation pattern of a single slot is very broad, little error is introduced when replacing $f(\theta_0, 0)$ by $f(\frac{1}{2}\pi, 0)$.

Substituting

$$\frac{f(\frac{1}{2}\pi,\ \phi_1)}{f(\frac{1}{2}\pi,\ 0)}\sin|\phi_1| \approx 0.5,$$

$$\sin\theta_{\pm 1} \approx 0.7,$$

and

$$\frac{f(\theta_{\pm 1},\ 0)}{f(\frac{1}{2}\pi,\ 0)} \approx 0.7,$$

yields

[14] $$S_{\max} \approx \frac{1}{4}\beta\delta \approx 1.5\frac{\delta}{\lambda}.$$

For a typical wave guide array, 50 wave lengths long or so, δ may be $\lambda/20$ so that 7.5% second-order beams can be expected. Shorter arrays will have larger slot offsets and correspondingly larger second-order beams.

III. SECOND-ORDER BEAMS DUE TO UNSYMMETRICAL EXCITATION

In the foregoing it was assumed that the two "half-arrays" are equally excited. This would imply that pairs of slots are driven with the same amplitude which is not a customary design procedure. Usually, the amplitude distribution

along the array is chosen to obtain a desired radiation pattern. Since this fixes the fraction of total power radiated by each slot, the excitation of two consecutive slots will, in general, not be equal. This effect can be taken into account by assuming an equivalent fractional difference Δ' in the excitation of the two half-arrays.

Certain mechanical imperfections may also produce asymmetry in excitation. Consider, for instance, that the slots are cut in a guide with nonuniform wall thickness. The slot offsets are measured from a center line which is laid out on the outside of one of the broad faces of the guide. If the thicknesses of the two side walls are not equal, all slots are effectively shifted to one side. The true offsets for the slots of one half-array are then too large by an amount ϵ, those for the other half-array too small by the same amount. The fractional difference in the two mean offsets is $2\epsilon/\delta$. Since the power radiated by each slot is proportional to its conductance, which in turn is roughly proportional to the square of the offset, the amplitude of excitation of each slot varies as the offset. The mean fractional difference in the excitation of the two half-arrays may therefore be taken as

$$[15] \qquad \Delta'' = \frac{2\epsilon}{\delta}.$$

The radiation pattern for such an unsymmetrically excited array would then be given by

$$[16] \qquad |F(\theta, \phi)| = |F_1(\theta, \phi)| \, |(1 + \Delta) + e^{j(2\beta\delta \sin\theta \sin\phi + \beta d \cos\theta - \psi)}|$$

where $\Delta = \Delta' + \Delta''$. Again maxima will occur when θ is given approximately by Equation [5]. Then,

$$[17] \quad |F(\theta_p, \phi)| = |F_1(\theta_p, \phi)| \sqrt{4(1 + \Delta) \cos^2 (\beta\delta \sin \theta_p \sin \phi + \tfrac{1}{2}p\pi) + \Delta^2}.$$

Since $\Delta \ll 1$ and $\beta\delta \ll 1$, the main beam is still given by Equation [8], but the expression for the ϕ-dependence of the second-order beams becomes

$$[18] \qquad |F(\theta_{\pm 1}, \phi)| = |F_1(\theta_{\pm 1}, \phi)| \sqrt{4 \sin^2 (\beta\delta \sin \theta_{\pm 1} \sin \phi) + \Delta^2}$$

$$\approx |F_1(\theta_{\pm 1}, \phi)| \sqrt{(2\beta\delta \sin \theta_{\pm 1} \sin \phi)^2 + \Delta^2}$$

or, in terms of the peak of the main beam,

$$[19] \qquad S(\phi) = \frac{1}{2} \frac{f(\theta_{\pm 1}, \phi)}{f(\tfrac{1}{2}\pi, 0)} \sqrt{(2\beta\delta \sin \theta_{\pm 1} \sin \phi)^2 + \Delta^2}$$

$$\approx \frac{1}{2} \frac{f(\theta_{\pm 1}, 0)}{f(\tfrac{1}{2}\pi, 0)} \frac{f(\tfrac{1}{2}\pi, \phi)}{f(\tfrac{1}{2}\pi, 0)} \sqrt{(2\beta\delta \sin \theta_{\pm 1} \sin \phi)^2 + \Delta^2}.$$

This expression reduces to Equation [13] for an ideal array ($\Delta = 0$). The second-order beams will be split with a null in the $\phi = 0$ plane and maxima at $\phi \approx \pm 50°$. For an array with all slots in line ($\delta = 0$) but with unsymmetrical excitation of the type considered, the second-order beams will have the same ϕ-dependence as the main beam. They will have a maximum in the plane $\phi = 0$, given by
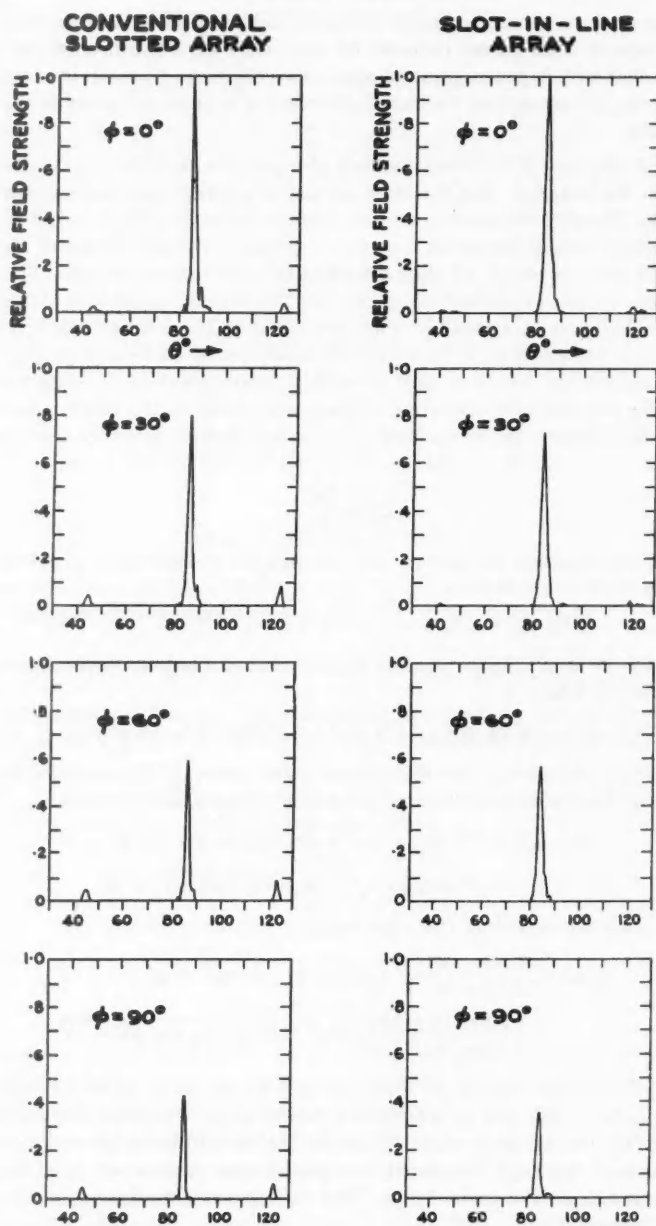
FIG. 5. Experimental radiation patterns of conventional and slot-in-line wave guide arrays.

[20] $$S_{max} = \frac{1}{2} \frac{f(\theta_{\pm 1}, 0)}{f(\frac{1}{2}\pi, 0)} \Delta \approx 0.35 \; \Delta.$$

Comparison with Equation [15] shows that this may place very close tolerances on the positions of the slots if a high-gain antenna with a low level of spurious radiation is required.

In an actual array both δ and Δ will, in general, be different from zero. Since Δ is almost always much smaller than $\beta\delta$, unsymmetrical excitation will have negligible effect on $S(\phi)$ except in the neighborhood of $\phi = 0$. The amplitude of the second-order beam in the $\phi = 0$ plane will no longer be zero but will be given by $S(0) \approx 0.35 \; \Delta$. It may amount to a few per cent of the main beam unless the guide is carefully selected and very close mechanical tolerances are held.

IV. EXPERIMENTAL VERIFICATION

The results derived in the last two sections were verified for a number of arrays of the type shown in Fig. 1. Fig. 5 shows patterns taken for an array of 60 slots at 1-in. spacing cut in standard X-band wave guide (0.900 in. by 0.400 in. inside dimensions). The array was designed for approximately cosine-amplitude distribution and about five per cent loss in the load. The offset of the center slots was 0.065 in. At an operating wave length of 3.20 cm. the slot spacing corresponded to about 204°. Hence $\psi = 24°$. From Equation [6] the main beam should make an angle of 4.8° with the array normal and the second-order beams should lie along the conical surfaces given by the polar angles $\theta_{+1} = 44.5°$ and $\theta_{-1} = 123.0°$. The second-order beams should therefore be spaced 40.7° and 37.8°, respectively, from the main beam in radiation patterns taken in any axial plane ($\phi = $ constant). This is borne out by experiment (see Fig. 5).

The ϕ-dependence of the two second-order beams was calculated from Equation [13] and Fig. 3. The experimental data (Fig. 6) are seen to agree quite well with theory if a mean slot offset of 0.060 in. is used. This offset differs by less than 10% from that of the center slot. The discrepancy near $\phi = 0$ can be accounted for easily by assuming slight asymmetry in the excitation of the two half-arrays ($\Delta \approx 0.07$). This small amount of asymmetry could be fully explained by an "equivalent" offset error of 0.002 in. (Equation 15). Part of the asymmetry may however be due to the fact that the array was not designed to have pairs of slots of equal excitation. Just how much is due to each cause is difficult to assess since over-all mechanical tolerances on the array were certainly not better than 0.001 to 0.002 in.

The appearance of the second-order beams can be visualized in three dimensions from Fig. 7.

V. SUPPRESSION OF SECOND-ORDER BEAMS

Two methods have been proposed to suppress second-order beams in wave guide arrays, both of which were tried successfully.

In one scheme an array is used with all slots in line. The slots are excited at the desired amplitude and phase by displacing the side walls of the wave guide
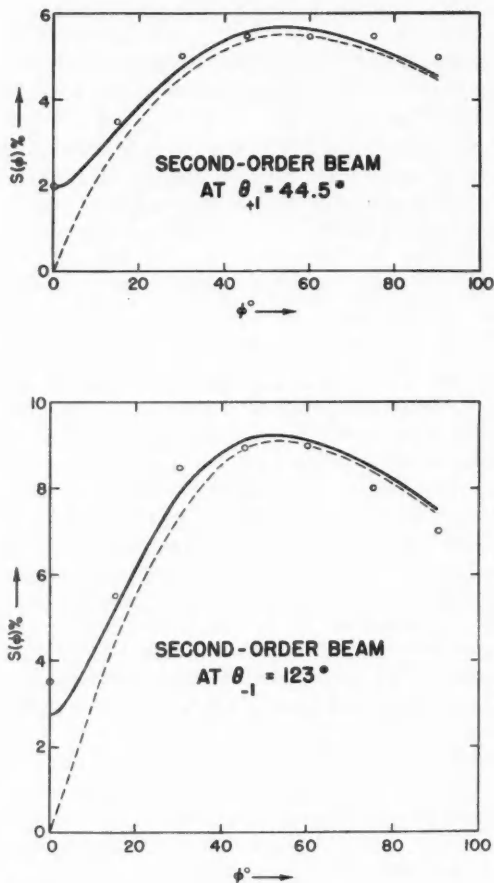
FIG. 6. ϕ–dependence of second-order beams.
Dashed line: calculated for $\delta = 0.060$ in., $\Delta = 0$.
Solid line: calculated for $\delta = 0.060$ in., $\Delta = 0.07$.
Circles: experimental points.

instead of the slots (Fig. 8). For a comparatively long array the corrugations in the walls will not be too deep and will not seriously affect the operation of an array with nonresonant slot spacing. Second-order beams of the type discussed in the last section for $\delta = 0$ may still occur, but they can be minimized by very close mechanical tolerances. The mechanical construction of such an array is more expensive than the usual design since the wave guide has to be made of four separate parts: corrugated walls, top and bottom plates. The parts must be
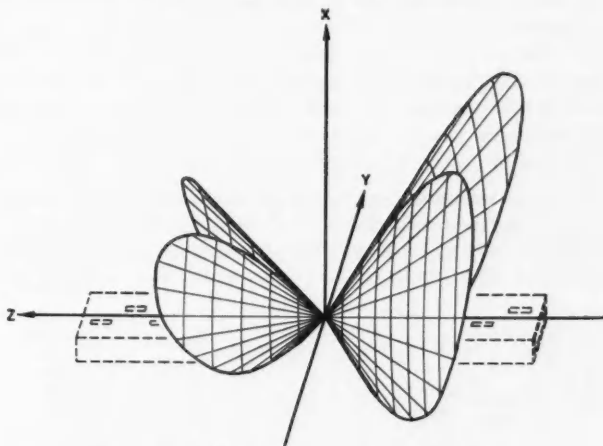
FIG. 7.   Three-dimensional sketch of second-order beams.
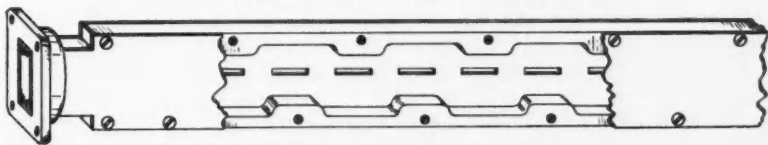
FIG. 8.   Slot-in-line corrugated-wall wave guide array.

properly bonded to ensure a good contact. Fig. 5 shows the extent to which second-order beams can be suppressed with reasonable mechanical tolerances.

The second method employs a conventional wave guide array fitted with a horn incorporating a narrow parallel-plate section (Fig. 9). If the width of the
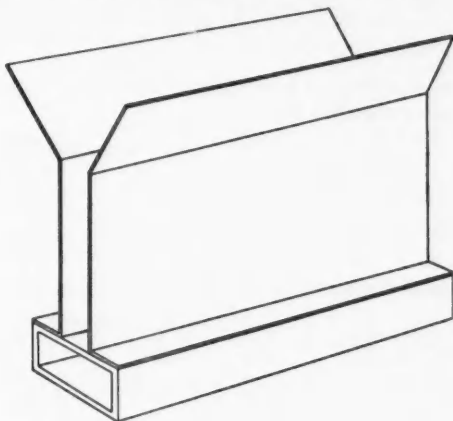
FIG. 9.   Wave guide array with parallel-plate section and horn.

parallel-plate region is less than half a wave length, only the two lowest modes will be propagated. In this manner asymmetries in the field, caused by the staggering of slots about the center line, will not appear at the mouth of the horn and second-order beams resulting from slot offset will be effectively suppressed provided that the length of the parallel-plate section is of the order of a wave length or longer. Some residual second-order beams caused by unsymmetrical excitation may still be present as in the case of the slot-in-line array.

The mechanism of second-order beam suppression can best be understood by a consideration of the field excited in a parallel-plate region by an array of slots. For simplicity, consider an infinite array with constant slot offset (Fig. 10).
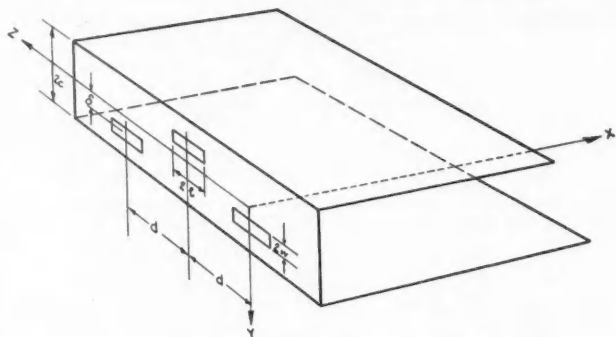
FIG. 10. Parallel-plate region excited by an array of slots.

Assume that the slots in the half-array on one side of the center line of the guide are excited by a voltage V_0 at their center, while the slots of the other half-array are excited by a slightly different voltage $V_0(1 - \Delta)$. The voltage distribution along each slot may be taken as sinusoidal with a maximum at the center and nulls at the ends of the slot.

Considering first only one half-array, the tangential electric field in the $x = 0$ plane may be represented by

[21]
$$\begin{cases} E_y(0) = \dfrac{V_0}{2w} \cos \dfrac{\pi}{2l}(z - 2\,qd) & \text{for} \begin{cases} 2qd - l < z < 2qd + l \\ \delta - w < y < \delta + w \\ q = 0, \pm 1, \pm 2, \ldots \end{cases} \\ E_y(0) = 0 & \text{everywhere else.} \end{cases}$$

We can write this field in terms of a double Fourier expansion

[22]
$$E_y(0) = \sum_{n=0}^{\infty} A_n \cos \frac{n\pi}{2c}(y + c) \sum_{m=0}^{\infty} B_m \cos \frac{m\pi z}{d}$$

where

[23]
$$
\begin{cases}
A_0 = \dfrac{V_0}{2c}, \\[2mm]
A_n = \dfrac{V_0}{c}\dfrac{\sin\,(n\pi w/2c)}{n\pi w/2c}\cos\dfrac{n\pi(c+\delta)}{2c}, \quad n \neq 0 \\[2mm]
B_0 = \dfrac{2}{\pi}\dfrac{l}{d}, \\[2mm]
B_m = \dfrac{4}{\pi}\dfrac{l}{d}\dfrac{\cos\,(m\pi l/d)}{1-(2ml/d)^2}, \quad m \neq 0.
\end{cases}
$$

By inspection, a solution of the wave equation within the parallel-plate region satisfying boundary conditions at $y = \pm c$ and reducing to Equation [22] at $x = 0$ is

[24]
$$
\begin{cases}
E_y(x) = \displaystyle\sum_{n=0}^{\infty}\sum_{m=0}^{\infty} A_n\, B_m \cos\dfrac{n\pi}{2c}(c+y)\cos\dfrac{m\pi z}{d}\,e^{-\Gamma_{nm}x}, \\[3mm]
E_z(x) = \displaystyle\sum_{n=0}^{\infty}\sum_{m=0}^{\infty} -\dfrac{n\pi}{2c\Gamma_{nm}} A_n\, B_m \sin\dfrac{n\pi}{2c}(c+y)\cos\dfrac{m\pi z}{d}\,e^{-\Gamma_{nm}x}, \\[3mm]
E_x(x) = 0
\end{cases}
$$

if we choose

[25]
$$
\Gamma_{nm}^2 = \left(\frac{n\pi}{2c}\right)^2 + \left(\frac{m\pi}{d}\right)^2 - \beta^2.
$$

The above field components also satisfy Maxwell's divergence equation and hence represent *the* unique field solution. Only waves travelling in the positive x-direction are considered here since it is assumed that the parallel-plate region is matched to free space by a properly flared horn at some distance from the plane of the slots.

Since $d \approx \lambda_g/2 \approx \lambda/1.4$, Equation [25] shows that all but two modes can be suppressed by selecting $2c < \lambda/2$. The two propagated modes are: the TEM-mode $(n = 0,\ m = 0)$ and the TE$_{01}$-mode $(n = 0,\ m = 1)$. The propagation constants for these modes are

[26]
$$
j\beta = j\frac{2\pi}{\lambda} \quad \text{and} \quad j\beta_{01} = j\frac{2\pi}{\lambda}\sqrt{1 - \left(\frac{\lambda}{2d}\right)^2}
$$

respectively. At sufficiently large distances from the plane of excitation the electric field will only have a transverse component which, from Equations [24] and [25], is given by

[27]
$$
E_y(x) = \frac{V_0}{2c}\frac{4}{\pi}\frac{l}{d}\,e^{-j\beta x}\left[\frac{1}{2} + \frac{\cos\,(\pi l/d)}{1-(2l/d)^2}\cos\frac{\pi z}{d}\,e^{j(\beta-\beta_{01})x}\right].
$$

This expression is independent of y and the slot offset δ. The field excited by the second half-array will therefore be given by a similar relation, except that V_0 is replaced by $V_0(1 - \Delta)$ and z by $z + d$.

By superposition, the total field at the aperture plane $(x = x_0)$ of the horn will be of the form

[28] $$E_y(x_0) = \frac{V_0}{2c}\frac{4l}{\pi d}e^{-j\beta z_0}\left[1 + \Delta\frac{\cos(\pi l/d)}{1 - (2l/d)^2}\cos\frac{\pi z}{d}e^{j(\beta-\beta_{0.1})z_0}\right]$$

$$= E_0\left[1 + (\Delta_1 + j\Delta_2)\cos\frac{\pi z}{d}\right].$$

The value of x_0 actually should be slightly modified because of the somewhat different propagation constants in the flared portion of the horn, but the effect is small and irrelevant to the following discussion.

It is seen that the effect of slot offset has disappeared in the aperture field. With perfectly symmetrical excitation ($\Delta = 0$) the aperture is uniformly illuminated and no second-order beams will appear in the radiation pattern. Some asymmetry in the excitation will, however, produce small amplitude and phase ripples in the aperture illumination. These ripples have a wave length of $2d > \lambda$ and may be expected to produce second-order beams. The radiation pattern can be calculated in the usual manner (4) as the Fourier transform of the aperture field, viz:

[29] $$R(\theta) = \int_{-D}^{D} E_y(x_0)\,e^{+j\beta z\cos\theta}\,dz.$$

The length of the aperture is $2D$, and θ is measured from the positive Z-axis as before. Substituting from Equation [28] and omitting all irrelevant factors, one obtains

[30]
$$R(\theta) = \frac{\sin(\beta L\cos\theta)}{\beta L\cos\theta}$$
$$+ \frac{1}{2}(\Delta_1 + j\Delta_2)\left[\frac{\sin(\beta\cos\theta - \pi/d)L}{(\beta\cos\theta - \pi/d)L} + \frac{\sin(\beta\cos\theta + \pi/d)L}{(\beta\cos\theta + \pi/d)L}\right].$$

The first term respresents the pattern due to a uniform amplitude distribution, the other two terms represent the effect of the ripples. It is apparent that the latter terms are exact replicas of the first term, but reduced in size and shifted so that their main peaks occur at

$$\theta = \cos^{-1}\left(\pm\frac{\pi}{\beta d}\right) = \cos^{-1}\left(\pm\frac{\lambda}{\lambda_g}\right).$$

Comparison with Equation [11] shows that these are exactly the positions of the second-order beams for a resonant array. At these positions the first term in Equation [30] will be entirely negligible in the case of a high-gain array. Hence the magnitude of the second-order beams, again expressed as a fraction of the main beam, will be

[31] $$S_{max} = \frac{1}{2}|\Delta_1 + j\Delta_2| = \frac{\Delta}{2}\frac{\cos(\pi l/d)}{1 - (2l/d)^2}.$$

For conventional arrays

$$\frac{l}{d} \approx \frac{\lambda/4}{\lambda_g/2} \approx \frac{1}{2}\frac{\lambda}{\lambda_g} \approx 0.35.$$

Hence,

[32] $$S_{max} \approx 0.45\Delta.$$

This maximum occurs in the plane $\phi = 0$ and the ϕ-dependence of these residual second-order beams is the same as for the main beam. The size of these second-order beams is only slightly larger than that of the corresponding beams for the slot-in-line array (Equation 20). Again these residual beams may be reduced to a minimum by proper symmetrical design and close mechanical tolerances. It is well to point out that symmetrical design includes symmetrical placing of the parallel-plate region and proper bonding to the wave guide.

The above remarks are substantially unaltered for an array with tapered amplitude distribution.

REFERENCES

1. BOOKER, H. G.   J. Inst. Elec. Engrs. (London), 93: 620.   1946.
2. FRY, D. W. and GOWARD, F. K.   Aerials for centimetre wave-lengths.   Cambridge University Press, London, 1950.   pp. 101–107.
3. RAMO, S. and WHINNERY, J. R.   Fields and waves in modern radio.   John Wiley & Sons, Inc., New York.   1944.   pp. 460–462.
4. SILVER, S.   Microwave antenna theory and design.   McGraw-Hill Book Company, New York and London.   1949.   p. 174.
5. SILVER, S. and SAUNDERS, W. K.   J. Applied Phys. 21: 745.   1950.
6. STEVENSON, A. F.   J. Applied Phys. 19: 24.   1948.
7. WATSON, W. H.   Physical principles of wave guide transmission and antenna systems. The Clarendon Press, Oxford.   1947.   p. 80.

PHOTONEUTRON CROSS SECTIONS IN SILICON AND CALCIUM[1]

By R. G. Summers-Gill,[2] R. N. H. Haslam, and L. Katz

ABSTRACT

Using the dropping apparatus and dose monitoring method previously reported, the cross sections for the reactions $Si^{28}(\gamma, n)Si^{27}$ and $Ca^{40}(\gamma, n)Ca^{39}$ have been measured by detecting positron activities in the residual nuclei. The $Si^{28}(\gamma, n)Si^{27}$ cross section has a peak value of 21 mbarns at 20.9 Mev. and an integrated cross section to 24 Mev. of 0.070 Mev-barns. The threshold energy is 16.9 ± 0.1 Mev. The $Ca^{40}(\gamma, n)Ca^{39}$ cross section has a peak value of 15 mbarns at 19.3 Mev. and an integrated cross section to 24 Mev. of 0.065 Mev-barns. The threshold is 15.8 ± 0.1 Mev.

A comparison of our results with the neutron yield measurement of Price and Kerst at 18 and 22 Mev. gives good agreement. A further comparison with the neutron yield work of Baldwin and Elder is made.

The sharp discontinuity in (γ, n) yields using lithium γ rays observed by Wäffler and Hirzel is explained as a threshold effect. Integrated cross sections increase more or less smoothly with Z.

In addition, improved values for the half-lives of the residual nuclei Si^{27} and Ca^{39} have been measured. These are 4.45 ± 0.05 and 1.00 ± 0.03 sec. respectively.

SILICON

Pure silicon metal powder molded into cylindrical samples with paraffin was irradiated in the X-ray beam of the 25 Mev. betatron at the University of Saskatchewan. Irradiations were generally 20 sec. in duration. Using the dropping apparatus (6) the samples were positioned within one second after irradiation around a Victoreen 1B85 thyrode where the short-lived positron activity was measured.

Sixteen decay curves obtained for irradiations with maximum bremsstrahlung energies below 24.5 Mev. were analyzed to yield a mean half-life of 4.45 ± 0.05 sec. This value is in good agreement with that previously reported by Wäffler and Hirzel (25). Any 6.3 sec. Al^{26} activity formed by the reaction $Si^{28}(\gamma, {}^n_d p)Al^{26}$ is negligible* at these energies.

The (γ, p) reactions in the two less abundant silicon isotopes are observed but the half-lives (2.30 min. and 6.6 min.) are so long compared to that of Si^{27} that little of these activities is formed in the short irradiations used.

The maximum bremsstrahlung energy of the betatron is controlled to within 0.1 Mev., using the integrator-expander circuit previously described (15). The complete activation curve, repeated on several occasions, is shown in Fig. 1. The threshold of the reaction was found to be 16.9 ± 0.2 Mev., which agrees favorably with earlier determinations (18, 3) and with the reaction energy 16.60

* *The calculated threshold for this reaction is 23.5 Mev. using recent mass defect values (21) and the reaction energy for the reaction $Al^{27}(\gamma, n)Al^{26}$ (3). Assuming a cross section of the same shape and magnitude as has been observed (17) for the reaction $S^{32}(\gamma, {}^n_d p)P^{30}$, the saturated specific activity per atom Si^{26} per 100 r. becomes 2.4×10^{-21} at 24.5 Mev. Since the saturated specific activity per atom Si^{28} per 100 r. for the reaction $Si^{28}(\gamma, n)Si^{27}$ is 3.38×10^{-17} at this energy, the $(\gamma, {}^n_d p)$ induced activity is much less than 1% at any energy we have used.*
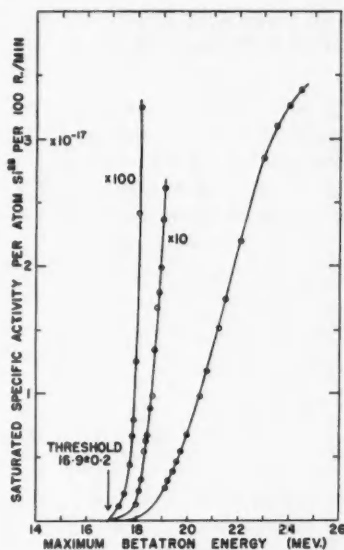
FIG. 1. The activation curve for the reaction $Si^{28}(\gamma, n)Si^{27}$. The initial portion is shown multiplied by 10 and by 100.

$\pm$ 0.21 Mev. calculated from recent mass defects published by Motz (21) and taking the end point energy of the positrons from Si^{27} as 3.48 $\pm$ 0.10 Mev. (4).

The absolute ordinates of this curve were obtained by a direct comparison of the 10.1 min. activity produced in copper foils and the 4.45 sec. activity produced in flat silicon powder samples at 22 Mev. The absolute specific activity for the reaction $Cu^{63}(\gamma, n)Cu^{62}$ has previously been measured in this laboratory (10, 14). A more complete description of the method of comparison is included in the previous paper (6).

CALCIUM

Pressed calcium hydroxide samples were irradiated for five seconds to obtain the short-lived Ca^{39} activity which was counted using the dropping apparatus. Decay curves followed for approximately three minutes showed that only the desired short-lived activity and 118 sec. O^{15} were present to any appreciable extent. After this background was subtracted, the mean half-life was found to be 1.00 $\pm$ 0.03 sec. This value is in good agreement with earlier work (8).

The relative activation curve was obtained using calcium hydroxide cylinders irradiated at maximum betatron energies ranging from 15 to 24 Mev. The threshold of the reaction is well-defined at 15.8 $\pm$ 0.1 Mev. McElhinney *et al.* (18) previously reported the threshold to be 15.9 $\pm$ 0.4 Mev. The relative curve was subsequently normalized at 22 Mev. by a direct calcium–copper comparison. Calcium metal disks were used for this purpose. Oxidation was

minimized by keeping the disks under kerosene except during actual use. The normalized activation curve is shown in Fig. 2.
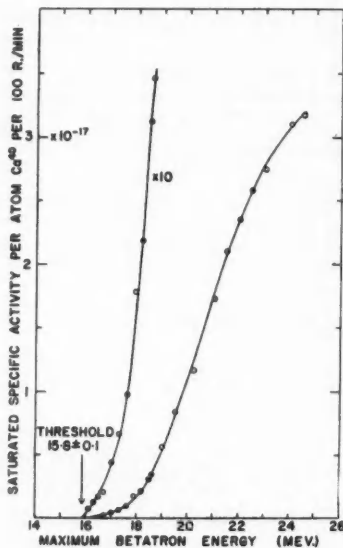
Fig. 2.   The activation curve for the reaction $Ca^{40}(\gamma, n)Ca^{39}$.   The initial portion is shown multiplied by 10.

DISCUSSION OF RESULTS

While the shapes of the activation curves are determined within 5%, the authors feel that the absolute magnitudes of the activities and hence of the cross sections may be in error by as much as 20%. This error is due to un-
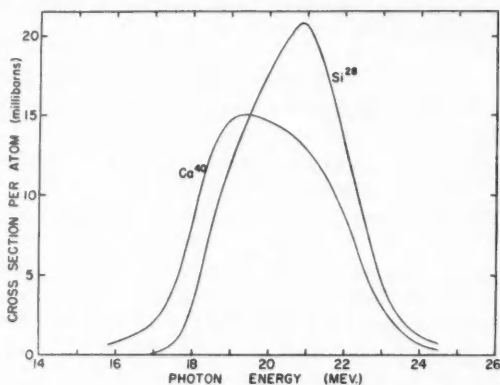
FIG. 3.   Cross section curves for the reactions $Si^{28}(\gamma, n)Si^{27}$ and $Ca^{40}(\gamma, n)Ca^{39}$.

certainties in the self-absorption corrections necessary and, further, to the error in the absolute value of the cross section for the normalizing reaction $Cu^{63}(\gamma, n)Cu^{62}$.

Using the photon difference method of analysis (12), the cross section curves of Fig. 3 were obtained. Both exhibit the usual resonance shape. Table I lists complete characteristics of each curve. Data for the reaction $S^{32}(\gamma, n)S^{31}$ are included for comparison (6). The ordinates of the cross section curve in this reference were in error and have been corrected by multiplying by 0.6.

TABLE I

CHARACTERISTICS OF CROSS SECTION CURVES

	$Si^{28}(\gamma, n)Si^{27}$	$S^{32}(\gamma, n)S^{31}$	$Ca^{40}(\gamma, n)Ca^{39}$
Threshold (Mev.)	16.9 ± 0.2	15.0 ± 0.1	15.8 ± 0.1
Peak cross section (mbarns)	21	15	15
Energy of peak (Mev.)	20.9	20.1	19.3
Half width (Mev.)	3.5	4.5	4.2
Integrated cross section to 24 Mev. (Mev-barns)	0.070	0.069	0.065

The present work is in very good agreement with the neutron yield data reported by Price and Kerst (23). Their results are, of course, for the natural elements while the present data are for single principal isotopes only. Since the abundance of each of the principal isotopes in these elements is over 90%, the results should be comparable. Table II contains a comparison of the neutron

TABLE II

NEUTRON YIELDS PER MOLE PER ROENTGEN

Element	Present work		Price and Kerst	
	18 Mev.	22 Mev.	18 Mev.	22 Mev.
Si	7.58×10^2	1.27×10^5	$< 10^3$	1.45×10^5
S	2.23×10^4	1.47×10^5	$< 10^3$	1.4×10^5
Ca	1.04×10^4	1.41×10^5	7.8×10^3	1.33×10^5

yields per mole per r. at 18 Mev. and 22 Mev. for silicon, sulphur, and calcium as determined by Price and Kerst and by our method.

Agreement is well within experimental error in every case except for sulphur at 18 Mev. Since the $S^{32}(\gamma, n)S^{31}$ threshold is 15 Mev., it is difficult to understand the low neutron yield reported by Price and Kerst at 18 Mev.

Baldwin and Elder (2) have determined the neutron yields from silicon, sulphur, and calcium using the X-ray beam from a 50 Mev. betatron. Yields were measured using a rhodium foil neutron detector. A Victoreen enclosed in a $\frac{1}{8}$-in. lead intensifier recorded the dose.

We have used the presently determined cross sections (up to 24 Mev.) to calculate the neutron yield due to the (γ, n) reaction in the principal isotope of silicon, sulphur, and calcium at a maximum betatron energy of 50 Mev. The method of computation is similar to that reported by Johns *et al.* (10). The

theoretical Schiff spectrum (1, 24) for an electron energy of 50 Mev. was corrected using total absorption coefficients for transmission through the donut walls and monitor. To a close approximation, this gives the spectral distribution reaching the sample. This spectrum was then further modified using real absorption coefficients for the absorption in 5.75 cm. of Lucite. The Victoreen response curve of Johns *et al.* (10) was then used to obtain the number of photons per cm.^{2} per "Lucite roentgen" per Mev. region reaching the sample. McElhinney and Siewers (19) have found experimentally that for a betatron operated at 50 Mev., a Victoreen enclosed in $\frac{1}{8}$-in. lead reads 2.68 times higher than the same Victoreen at the center of a Lucite cube 11.5 cm. on an edge. The ordinates of the absolute photon spectrum obtained above were therefore divided by 2.68 to obtain $P(E)$, the number of photons per cm.^{2} per "lead roentgen" per Mev. region.

The neutron yield per mole per "lead roentgen" at 50 Mev. due to the (γ, n) reaction is then

$$6.02 \times 10^{23} \int_{E_{th}}^{50} \sigma_{\gamma,n} P(E) \, dE$$

which we have approximated by

$$6.02 \times 10^{23} \int_{E_{th}}^{24} \sigma_{\gamma,n} P(E) \, dE.$$

The values so calculated are compared with the total neutron yields from the natural elements as measured experimentally by Baldwin and Elder in Table III.

TABLE III

Neutron yields per mole per "lead roentgen" at 50 Mev.

	Si	S	Ca
(γ, n) contribution for principal isotope only	$0.72 \pm 0.2 \times 10^5$	$0.73 \pm 0.2 \times 10^5$	$0.67 \pm 0.2 \times 10^5$
Total neutron yield for natural element from Baldwin and Elder	$1.2 \pm 0.5 \times 10^5$	$1.9 \pm 0.7 \times 10^5$	$2.3 \pm 0.9 \times 10^5$

The relatively large errors involved prevent the drawing of definite conclusions but it appears probable that the (γ, n) reaction is the most important source of neutrons for silicon and sulphur up to 50 Mev.

In contrast, the measured neutron yield for calcium at 50 Mev. appears to be considerably larger than the yield for the (γ, n) reaction in Ca^{40}. Since Ca^{40} constitutes 96.9% of the natural element, the extra neutrons could scarcely be due to larger (γ, n) cross sections in the heavier isotopes. Furthermore, it appears unlikely that the $Ca^{40}(\gamma, n)Ca^{39}$ cross section has a long tail of sufficient magnitude to account for the high neutron yield observed at 50 Mev.

It should be remembered that $_{20}Ca^{40}$ is magic in both neutrons and protons. Thus, while having a normal gamma absorption cross section, the Ca^{40} nucleus

might possibly have a suppressed single neutron emission probability. De-excitation would then occur preferentially by the emission of two or more neutrons, or by the emission of a proton and a neutron. If single neutron emission is suppressed it seems probable that single proton emission would also be. It would be of interest, therefore, to measure the proton yield for calcium.

In an investigation of the relative (γ, n) yields in various elements irradiated with lithium γ rays, Wäffler and Hirzel noted a pronounced increase in yield between $Z = 20$ and $Z = 21$. We have investigated this effect by calculating from cross section curves determined in this laboratory (5, 9, 7, 13, 17, 14, 10,

TABLE IV

Atomic number	Parent isotope	Relative (γ, n) yield using Li γ rays		(γ, n) threshold (Mev.)	Integrated cross section (Mev-barns)
		Calculated	Wäffler & Hirzel		
6	C^{12}	0	0	18.7	0.046
7	N^{14}	0.57	0.3	10.8	0.030
8	O^{16}	0.46	0.3	15.6	0.062
9	F^{19}	3.3	2.5	10.7	0.076
12	Mg^{24}	1.1	1.3	16.2	0.057
13	Al^{27}	1.9	2.7	14.0	0.045
14	Si^{28}	0.78	0.7	16.9	0.070
15	P^{31}	11.4	—	12.4	0.13
16	S^{32}	4.6	4.1	15.0	0.069
17	Cl^{35}	—	3.7	—	—
19	K^{39}	(12)	4.5	13.2[a]	—
20	Ca^{40}	3.4	2.0	15.8	0.065
21	Sc^{45}	(14)	25	12.0[b]	—
22	Ti^{46}	(12)	29	13.3[c]	—
24	Cr^{50}	—	22	—	—
26	Fe^{54}	44	38	13.8	0.48
28	Ni^{58}	47	—	12.0	0.34
29	Cu^{63}	100	100	10.9	0.66
	Cu^{65}	147	150	10.2	1.11
30	Zn^{64}	140	62	11.6	0.99
32	Ge^{76}	—	114	—	—
34	Se^{82}	—	155	—	—
35	Br^{79}	—	73	—	—
	Br^{81}	132	83	10.2	1.06
37	Rb^{87}	203	200	9.0	1.68
42	Mo^{92}	134	115	13.3	0.85

[a] *Reference 18.*
[b] *Calculated using semiempirical formula.*
[c] *Reference 22.*

16, 11, 12) the yield to be expected using lithium γ rays. The energy and intensity of the lithium γ rays measured by Walker and McDaniel (26) have been used. The values so obtained (normalized to a yield of 100 for the $Cu^{63}(\gamma, n)Cu^{62}$ reaction) are listed in the third column of Table IV. In the fourth column the values of Wäffler and Hirzel are tabulated. In all cases where comparison is possible it is seen that agreement is satisfactory within the fairly wide limits of error. In Fig. 4, the relative yields are plotted as a function of Z. A trend towards higher yield values with increasing Z is observed together with sharp fluctuations from element to element.
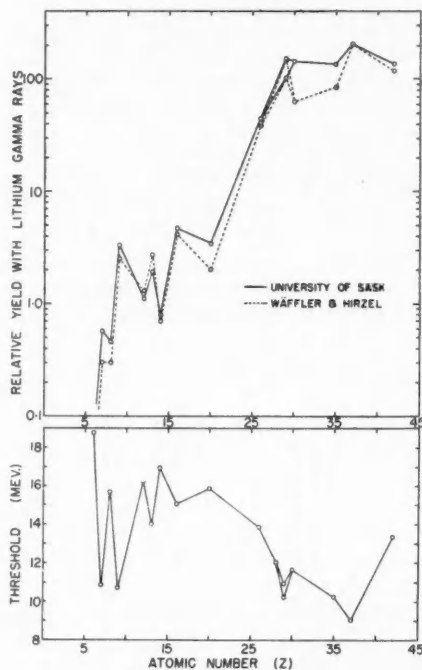
FIG. 4.   The correlation between the relative (γ, n) yield, using lithium γ rays, and the reaction threshold.

These fluctuations (particularly the sharp break between $Z = 20$ and $Z = 21$) may be completely explained in terms of varying reaction thresholds. Where known, the (γ, n) thresholds are listed in column 5 of Table IV. These values are plotted versus Z on the lower part of Fig. 4. For all cases where the data are known, the relative yields are high where the thresholds are low and vice versa. This is to be expected since the activities are produced by γ rays of energy little more than the threshold energies of the reactions. Direct comparison in the immediate neighborhood of calcium cannot be made since the cross sections of K^{39}, Sc^{45}, and Ti^{46} have not been measured. However, the reaction thresholds in K^{39} and Ti^{46} have been determined and the threshold for the reaction Sc^{45} $(\gamma, n)Sc^{44}$ can be obtained approximately using an empirical mass formula (20). Assuming cross sections in these nuclei similar to the observed cross section in Ca^{40} and shifting the energy scale appropriately, the three additional relative yields have been calculated. The threshold effect nicely accounts for the large yields observed in scandium and titanium. The observed K^{39} yield, however, is much less than that so calculated. The cross sections for the reactions $K^{39}(\gamma, n)$ K^{38} and $Sc^{45}(\gamma, n)Sc^{44}$ are soon to be measured in this laboratory. A further comparison will be made at that time.

In column 6 of Table IV, the integrated cross sections measured in this laboratory are tabulated. The values for the reactions $N^{14}(\gamma, n)N^{13}$, $O^{16}(\gamma, n)O^{15}$, and $Br^{81}(\gamma, n)Br^{80*}$ have been obtained assuming the cross sections to be symmetrical. While fluctuations from element to element exist, within experimental error it appears evident that the integrated (γ, n) cross sections increase for the most part smoothly with Z.

ACKNOWLEDGMENTS

REFERENCES

1. ADAMS, G. D.   Phys. Rev. 74: 1707.   1948.
2. BALDWIN, G. C. and ELDER, F. R.   Phys. Rev. 78: 76.   1950.
3. BECKER, R. A., HANSON, A. O., and DIVEN, B. C.   Phys. Rev. 71: 466.   1947.
4. BOLEY, F. I. and ZAFFARANO, D. J.   Phys. Rev. 84: 1059.   1951.
5. HASLAM, R. N. H., JOHNS, H. E., and HORSLEY, R. J.   Phys. Rev. 82: 270.   1951.
6. HASLAM, R. N. H., SUMMERS-GILL, R. G., and CROSBY, E. H.   Can. J. Phys. 30: 257.   1952.
7. HORSLEY, R. J., HASLAM, R. N. H., and JOHNS, H. E.   Phys. Rev. 87: 756.   1952.
8. HUBER, O., LIENHARD, O., SCHERRER, P., and WÄFFLER, H.   Helv. Phys. Acta, 16: 33.   1943.
9. JOHNS, H. E., HORSLEY, R. J., HASLAM, R. N. H., and QUINTON, A.   Phys. Rev. 84: 856.   1951.
10. JOHNS, H. E., KATZ, L., DOUGLAS, R. A., and HASLAM, R. N. H.   Phys. Rev. 80: 1062.   1950.
11. KATZ, L., BAKER, R. G., and MONTALBETTI, R.   Can. J. Phys.   To be published.
12. KATZ, L. and CAMERON, A. G. W.   Can. J. Phys. 29: 518.   1951.
13. KATZ, L. and CAMERON, A. G. W.   Phys. Rev. 84: 1115.   1951.
14. KATZ, L., JOHNS, H. E., BAKER, R. G., HASLAM, R. N. H., and DOUGLAS, R. A.   Phys. Rev. 82: 271.   1951.
15. KATZ, L., McNAMARA, A. G., FORSYTH, P. A., HASLAM, R. N. H., and JOHNS, H. E.   Can. J. Research, A, 28: 113.   1950.
16. KATZ, L., PEASE, L., and MOODY, H.   Can. J. Phys. 30: 476.   1952.
17. KATZ, L. and PENFOLD, A. S.   Phys. Rev. 81: 815.   1951.
18. McELHINNEY, J., HANSON, A. O., BECKER, R. A., DUFFIELD, R. B., and DIVEN, B. C.   Phys. Rev. 75: 542.   1949.
19. McELHINNEY, J. and SIEWERS, D. C.   Natl. Bur. Standards (U.S.), Rept. 1000.   1951.
20. METROPOLIS, N. and REITWIESNER, G.   Table of atomic masses.   Technical Information Service, Oak Ridge, Tenn.   1950.
21. MOTZ, H. T.   Phys. Rev. 81: 1061.   1951.
22. OGLE, W. E. and ENGLAND, R. E.   Phys. Rev. 78: 63.   1950.
23. PRICE, G. A. and KERST, D. W.   Phys. Rev. 77: 806.   1950.
24. SCHIFF, L. I.   Phys. Rev. 70: 87.   1946.
25. WÄFFLER, H. and HIRZEL, O.   Helv. Phys. Acta, 21: 200.   1948.
26. WALKER, R. L. and McDANIEL, B. D.   Phys. Rev. 74: 315.   1948.

ENERGY LOSS OF HIGHLY CHARGED PARTICLES PRODUCED BY FISSION AND BY COSMIC RAYS

SECTION I. OBSERVATIONS OF FISSION FRAGMENTS[1]

By Pierre Demers

ABSTRACT

Measurements on the range of the tracks of fission fragments recorded in special laboratory-made emulsions are reported. The origin was marked so that observations on length not possible otherwise were made. Stopping power and straggling for such tracks in different media are discussed. It is shown that the range of one fragment is little dependent on the range of the other paired fragment. The blackening of the two tracks near the origin is on the average unequal, that of the light fragment L being darker. It is inferred that ionization is greater near the origin for the L fragment. Knock-on protons allow a range velocity curve to be drawn, and evidence is advanced to prove that the light associated particles are indeed knock-on protons.

1. INTRODUCTION

Several years ago, a study was made and published briefly (8) of the tracks of fission fragments with laboratory-made, very fine grained emulsions. Such emulsions possess a remarkable discriminating power for the high ionizing powers encountered, which range between 1 and 13 Mev. per micron of emulsion. The width and the opacity vary markedly along these tracks which appear like narrow continuous lines, and the small grain allows one to recognize very small details. While visual observations of opacity often are satisfactory when done by an experienced observer, and may provide in some cases as much information as can be deduced by other means, they are subjective. Photometric measurements of light intensity, in addition to removing the subjective feature of visual appraisal of the track's opacity and width, would yield absolute values of these quantities, and would open a new field to investigations on tracks recorded in nuclear emulsions. This led us to the building of a special photometer, which was briefly described in its initial form by Demers and Mathieu (12), and which will be described further in Section II.

The discriminating power displayed by such emulsions would seem to make them an ideal tool for studying strongly ionizing recoil particles visible in cosmic ray stars and heavy cosmic ray primaries. While this study is still underway, it has been deemed convenient to present some first results concerning mostly identification of heavy particles, in subsequent sections.

2. EMULSIONS USED

Three kinds of special emulsions have been used. One is *very small grained*. It is obtained by the following method: 4.5 gm. of Minute Rapid gelatine of General Foods are swollen and dissolved in 50 cc. of water, then 25 cc. of ethyl alcohol are added, a 400 cc. beaker being used; this is solution C which is brought to 50–60°C. before use. No thermostat is used, avoiding undue delays; the solution stays warm enough from the heat of precipitation evolved. To solution C are

added 0.3 cc. of solution B containing 420 gm. potassium bromide per 1000 cc. of solution. Then at equal rates, from burettes conveniently controlled, 30 cc. of solution B and 30 cc. of solution A containing 600 gm. silver nitrate per 1000 cc. of solution are poured simultaneously into beaker C. The precipitation of silver bromide being completed, the emulsion is cooled and kept in the refrigerator overnight, the jelly is then broken into small shreds, which are washed in running cold water for one hour, collected, kept at about 5°C., and melted and coated at will. This is formula II of Ref. (9) in which the particular gelatine gives an especially fine grain and a good discriminating power.

The second kind of emulsion is *small grained*, similar to that of formula II, but perhaps a little coarser and more sensitive, so that it shows delta rays. It was obtained by the double jet method described in Refs. (10, 11).

The third kind has a *medium-sized grain*. It is more sensitive and shows electron tracks of 100 to 200 μ. Its discriminating power is poorer, although a track ionizing 1000 times minimum is not yet saturated and still shows some gaps. It was obtained by the triple jet method of Ref. (11).

Finally some measurements were made also in Ilford and in Eastman emulsions.

3. OBTAINING PAIRS OF TRACKS OF FISSION FRAGMENTS

A three layer method was designed and used. The very fine grained emulsion described above is melted at about 45°C., a thin layer of it, E_1, is laid on a glass slide 3 in. $\times$ 1 in. and dried. Thickness then should be about 20 μ.

In the meanwhile, a suspension of ammonium uranate is prepared. A 1% solution of uranyl acetate $UO_2(CH_3CO_2)_2$ is mixed with a 1% solution of ammonium hydroxide NH_4OH. Concentrations are approximate. The turbid solution is centrifuged gently, and decanted. The product of the reaction is a sparingly soluble compound called ammonium uranate, of ill-defined composition, v. g. $UO_3(NH_4)_2 H_2O$. The decanted residue is mixed with cold water, centrifuged again, and this washing operation is repeated. Too many washings may damage the precipitate, and a trace of ammonia in the wash water seems useful. When the appropriate conditions of precipitation and washing have been achieved, a yellowish jellylike mass results, the exact consistency of which is important for what follows. If it is too coarse instead of gelatinous, the gap between the pairs of tracks marking their common origin will be too large. This gelatinous mass is put in suspension with some water and spread on the slides already covered with layer E_1. The layer of uranium compound U should be very thin. If it is too thin no track shows up; if there is a large amount of it, numerous fission tracks record, but the central gap is excessive. The practice followed has been to rapidly cover the slide with the nearly colloidal suspension and then to shake it briskly to remove the excess. The coating then may be uneven but it will be satisfactory at least in some areas. As a help in this and subsequent phases of the manipulation, it is advisable to add methyl violet to the suspension of ammonium uranate. This has no photographic effect whatever, it disappears at the time of fixing, but until then it stains strongly the particles of the uranium compound, and thereby shows where this has spread on the slide.

The slides are left once more to dry, a third, thin layer of the same emulsion, E_2, is added, and the slides are dried a third time. The plates are sensitized by bathing for one-half minute in a 1% solution of triethanolamine $(C_2H_4OH)_3N$, and dried. They are irradiated and developed as rapidly as possible to avoid accumulating too many alpha ray tracks from the uranium, which disintegrates steadily.

Some other method might be tried to produce a very thin layer of a uranium compound. Evaporation of the element *in vacuo* onto layer E_1 might be tried for instance, or perhaps the U layer might be formed on another support and transferred to the sensitive slide if direct deposition would induce fogging. On the other hand, other chemical compounds might suitably replace the one used here.

Irradiation was performed in the Zero Energy Experimental Pile Zeep, to accumulate a flux of about 10^9 slow neutrons per cm.[2] The level of irradiation is limited by the single grain background formed, which may be tolerated. Reduction of the background to fission track ratio was not accomplished by enclosing the slide in a castle of lead or of bismuth, which seemed to make the matter worse, perhaps because of the capture gamma rays produced in them. The best procedure found was to house a single plate wrapped in black paper in a hole in the graphite reflector. It seemed that most of the background arose from the emulsion itself, thicker emulsions being much more fogged. This would be explained if it is assumed that the fog is caused by the $n\gamma$ reaction in the silver and bromine, and by the subsequent β decay of the radioactive products so formed. The fog would then be a second order effect of the thickness of the emulsion layers in contact.

Time between the second drying and development was usually less than a day. Development was for 5 to 10 min. in D19 formula of Eastman Kodak at 20 – 22°C. A stop bath was not necessary, but the acid fixing formula F5 was used. Often the layers peeled away from one another and from the glass support at some time during the processing, especially at the time of entering the fixer. Vaseline around the edges would prevent the emulsion from leaving the glass, but the two layers may not come back exactly in coincidence after the final drying. It was found necessary to draw, with a pen laden with molten vaseline, lines crossing each other to form completely enclosed rectangles of less than 10 mm. side. The narrow strips covered with vaseline are not very much wetted, are not processed, and do not come off; after the final drying, coincidence is good and the vaseline is then removed. The processing does not remove the U layer, at least not completely. After being fixed, the plates are washed in the usual way, and then treated with 50% alcohol before drying. This contracts the layers if they have become separated, and helps them to dry back in good coincidence.

A somewhat similar technique has been described by Vigneron and Bogaardt (22). Layer E_1 is that already existing on an Ilford C_2 or E_1 plate 25 μ thick. Layer U is prepared out of a uranium oxide powder fractionated by partial sedimentation so as to select grains of diameter nearly one micron. A suspension of this in a dilute gelatine solution is laid on top of E_1, dried, covered with layer

E_2, and left again to dry before irradiation. Layer E_2 is the sensitive layer of another similar Ilford plate, like C_2 or E_1, which is swollen in cold water, removed by scraping with a spatula, and laid face down on layer U. This method dispenses with the preparing of the emulsion, and apparently brings less inconvenience from the layers peeling away. His grains appear as somewhat transparent crystals of $0.5–1$ μ between the tracks of the two fragments, so that the central gap marking the origin may be smaller in our procedure. Also the emulsion we used seems to show a better discrimination. Vigneron (21) has published measurements done with this method.

4. OBSERVATIONS ON PAIRED FISSION TRACKS

Upon examination of the developed plate, fission fragments may be seen originating at random angles from the nearly transparent and insensitive U layer. This layer is revealed, where it is thin, by a gap between the pair of fission tracks. Where it is thick enough to show its yellowish appearance, the fission tracks springing out of it are more numerous, with a large gap between them. The origin is somewhere along the gap, between those parts of the tracks which show up, so the longer the gap the greater the uncertainty on the point of origin. We have assessed as a rule an upper limit of 1.5 μ to the gap for precise length measurements, although the gap was in cases as small as $0.1 - 0.2$ μ. If the origin is arbitrarily taken in the center of the gap in each case, then it is seen that an upper limit of the corresponding error induced is 0.75 μ on the length of either track, and 1.5 μ on their difference. It may be recalled that 1 μ of emulsion is the equivalent of 0.039 mgm. per cm.^{2}, which is the equivalent of about 0.028 mgm. per cm.^{2} of Al for a velocity of 1 to 2.10^9 cm. per sec. for α rays. However the gap is not made of emulsion but of a uranium compound. Although its stopping power has not been investigated, it should not be very much greater than twice that of the emulsion; no corresponding correction has been attempted, so on this account the ranges for either fragment in the emulsion as given may be too short by some 0.75 μ in the case of the larger gaps.

The marking of the origin, or the fact that the two tracks forming a pair are visible at a time, may be put to use in the following ways. The paired tracks are unequal in 98% of cases as found in the present investigation, so as a rule a long track L and a short track S may be defined, making up two well-defined groups the properties of which may be investigated. These two groups stand out in a statistical analysis of the ranges of single tracks obtained otherwise, but here the qualification of each track is unambiguous, except in two cases out of a hundred. It is known from semitheoretical arguments, confirmed for instance by Boggild, Arroe, and Sigurgeirsson (2), that the longer track belongs to the lighter fragment and carries more energy.

Pertinent data regarding fission taken mostly from (6) are summarized in the following list. The energies are in the inverse ratio of the masses from momentum conservation, as long as the neutrons emitted are neglected, and the masses should have a sum equal to 236 minus that of the neutrons emitted at the instant of fission, that is 233.

Number of neutrons emitted: 3
Most probable energy of light, long range, high energy group L':   92.7   Mev.
Most probable energy of heavy, short range, low energy group S':   59.0   Mev.
Their ratio: 1.57
Their sum: 151.7   Mev.
Most probable mass of L':   94
Most probable mass of S':   139
Their ratio: 1.48
Width at half maximum of the mass distribution curve (L' or S'):   16
Width at half maximum of the energy distribution for L':   12   Mev.
Same for S':   20   Mev.

Besides confirming the existence of two length groups, one may ascertain the difference in length $D = L - S$ in individual cases, and this may be studied as a function of total length $T = L + S$, or of some feature of either track. For a given L value, the distribution in S, D, and T may be studied, etc.

Finally, other distinguishing features may be investigated in the two associated tracks, in conditions of recording and of observing which are very similar for both tracks in a pair. In particular any difference between the blackening near the origin may be estimated with confidence.

According to cloud chamber observations (3), the S tracks leave considerably more frequent visible recoils, but no obvious difference of the kind appeared in the emulsion. Features now generally known are displayed in Figs. 1 – 4, and in Figs. 19 to 24 of Ref. (9). The tracks thin down near the end, because electron capture increases with reduced velocity, and diminishes their ionizing power; however at the very end, there is an increase of ionization and of visible blackening attributed to nuclear encounters. These nuclear collisions cause multiple scattering all along the track, and the knock-on nuclei show up more numerously at the very end. In Fig. 2, the nearly right angle forking shows that the fission fragment has collided with a particle of nearly the same mass, silver or bromine, rather than carbon, nitrogen, or oxygen. Fig. 3 shows what is probably a close collision with a carbon, nitrogen, or oxygen nucleus, while in Fig. 1B small bumps are attributed to distant collisions with hydrogen nuclei. Fig. 25 of Ref. (9) shows what is either a collision with silver or bromine, or a triple fission. Figs. 4 and 5, same phenomena as in Fig. 1 of Ref. (8), show phenomena with the origin marked. Fig. 26 of Ref. (9) shows fission tracks recorded in Eastman 548. Lark-Horowitz and Miller (15) were the first to observe fission tracks in this last emulsion.

Fifteen hundred complete pairs of fission tracks have been observed, and 129 were found suitable for measurements: gap short enough, slope 10% or less, and no distortion. It is believed that any distortion modifying the length by more than about 2% was detected, since a 5% distortion was very obvious from the aspect of the track: the grains were either crowded together, or pulled apart with the appearance of gaps. On these 129 tracks, measurements of length and some concerned with opacity were made.

5. LENGTH MEASUREMENTS

The frequency distributions obtained for L, S, D, and T are shown in Fig. 6. The combined curve C is also shown. This is obtained by adding up the frequency of all lengths of single tracks ignoring whether they are S or L tracks; it could

PLATE I
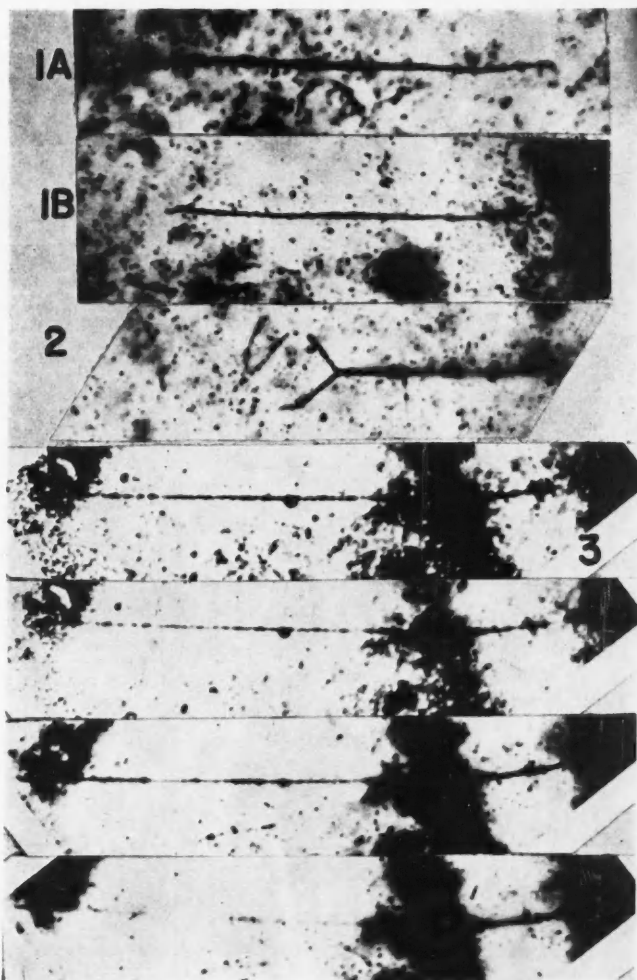
Fig. 1*A* and *B*. Complete fission tracks, center not marked. Note the gradual thinning down, and the more numerous recoils near the ends.

In 1*B*, a few very short knock-on protons were visible under the microscope. Very fine grain emulsion.

Fig. 2. Collision with a heavy nucleus, silver or bromine, recognized by the nearly right angle. A fine grain emulsion.

Fig. 3. Three particles, their range complete in the field. One event, three negatives, four prints. The long range one may be emitted at the instant of fission, or be a carbon, nitrogen, or oxygen knock-on nucleus. From its density it is much more ionizing than α rays such as the one visible in one of the prints. Scale is smaller than in the other photographs.

Very small grain emulsion, center not marked.

PLATE II
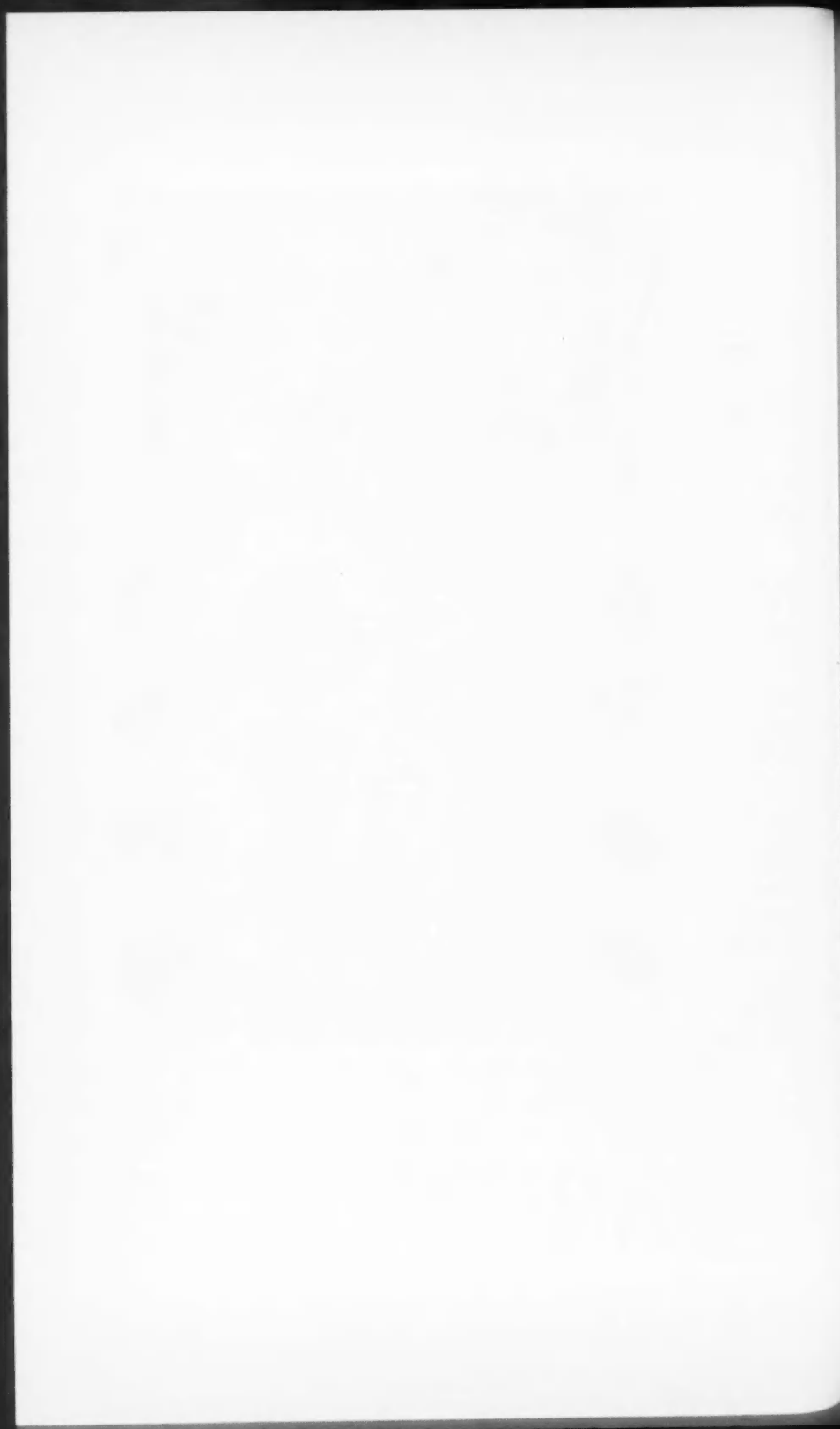
FIG. 4. Long and short tracks with origin marked. One event, three negatives. Note the difference of blackening near the center, L being blacker than S.

FIG. 5. Long track L on the left looks blacker than S. One event, two negatives. An α ray is emitted coming accurately from the marked origin.

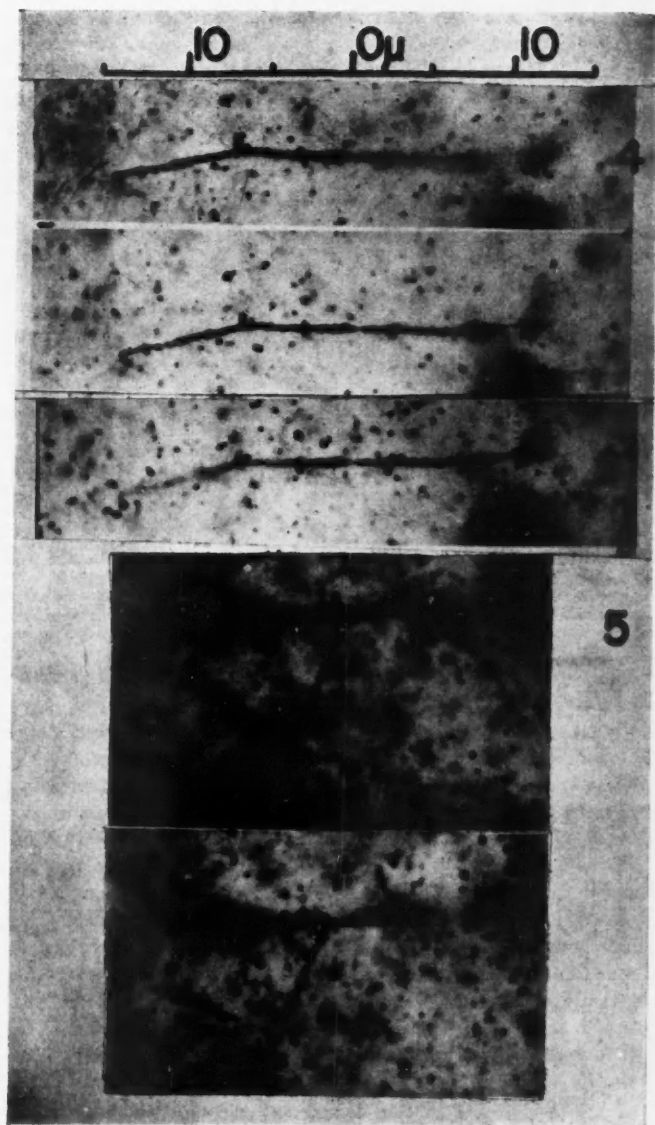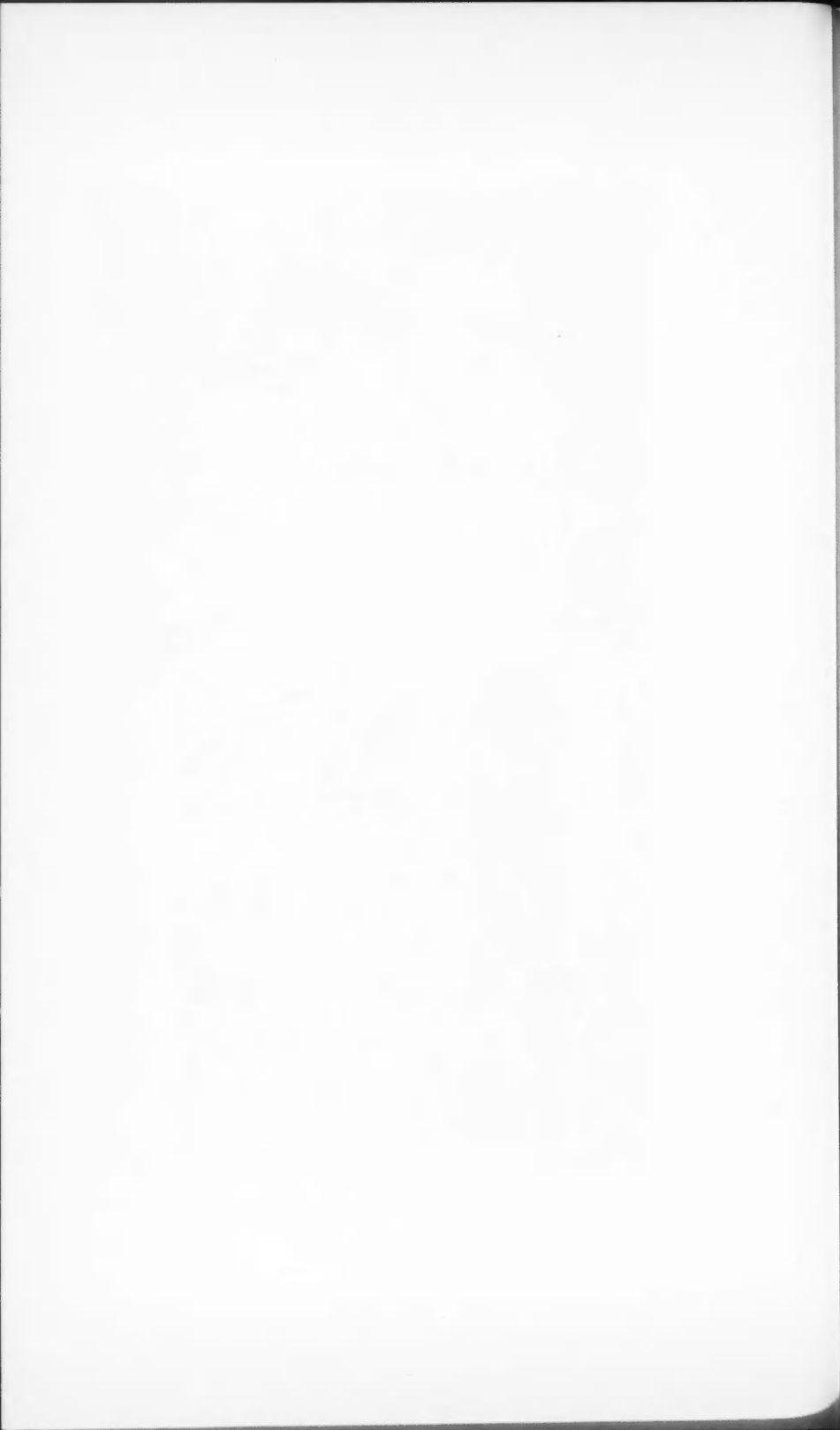also be drawn from an experiment with two layers, U and E, providing layer U were thin enough. Two humps may then be recognized but not so distinctly as on the separate curves. Curves S and L overlap to some extent which would naturally be impossible if only single tracks were available as in a two layer experiment. However there is no contradiction here, since definition is by the difference observed in each case: some S tracks are indeed longer than some L tracks belonging to another pair. There are two cases of equal lengths $S = L$, at $T = 42$ and 52 divisions.
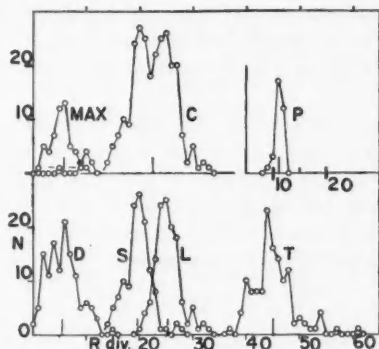

FIG. 6. Frequency distribution on 129 pairs. Total length T, long track L, short track S. difference $L - S = D$, combined L and S distribution C. Distance MAX from the origin of maximum of blackening sometimes observed; for the two humps marked minus $-$, abscissae should be negative, $+$ is direction of L particle. Length of N_{14} (n, p) C_{14} protons P. Average values of R are shown by a vertical bar. One division $= 0.565 \mu$.

We may wonder how many times the difference D is taken with the wrong sign. To make the question more precise, we know that there exist well-distinct S' and L' groups, S' being heavier and less energetic. Cases of symmetrical fission where masses and energies are equal are known, from chemical and ionization chamber evidence, to be extremely scarce. Then if a given mass and energy always gave the same total range, and if we were able to recognize in our measurement the S' and the L' tracks, we should always find the S' track to be shorter than L'. The fact that 2% of measurements give equal S and L, or S' and L' tracks suggests that sometimes the S' track is longer than L', on account of some range straggling. Then the difference $D' = L' - S'$ would be negative. Therefore, on the basis of length measurements alone, cases may happen where a small positive difference D corresponds to a small negative value of D', and this cannot be told in individual cases on the basis of length measurements alone. However the frequency of $D' = 0$ is the same as that for $D = 0$, that is 2%, and as it seems safe to assume that the distribution decreases rapidly at negative values of D', from the appearance of the distribution in D, the total frequency of negative values of D' ought to be less than say 1 or 2%.

In other words, the difference between the ranges may lead to a proper attribution of masses in 97 – 96% of cases, while in 2% of cases, decision cannot be made, and in another 1 – 2%, decision should be reversed.

6. STOPPING POWER

The stopping power was determined for the alpha particles of U_{II} in the same emulsion but not in the same plates. Those alpha ray tracks which are seen in the three-layer plates originate in the U layer, and have traveled in this a distance impossible to appraise, which reduces their visible path by an unknown amount. Although the U layer is preferably nowhere thicker than 2 or 3 μ it is transparent and very difficult to tell, except when it is thick, from the adjacent E_1 and E_2 layers by simple inspection; since for range measurements only nearly horizontal tracks are taken, the uncertainty is of the order of the thickness $\div \sin \theta$, θ being between 0 and 5°. This uncertainty on the origin does not exist for the fission fragments, because the limits of the U layer are marked by tracks showing up on both sides of it.

The stopping power was measured in layers of similar emulsions containing about 0.05% $UO_2(CH_3CO_2)_2$. It was also determined in the three layer plates by observing the $N_{14}(n,p)C_{14}$ protons P which showed weaker but distinct tracks. Their range was very exactly the same as in the layers containing added uranyl acetate. Recoil protons reaching an energy of 6 Mev. were also visible, which indicates the sensitivity of the emulsion. Table I shows these results.

TABLE I

RANGES AND STOPPING POWERS

Number of tracks in these measurements	129				33	22
	L	S	D	T	P	αU_{II}
Nature of tracks						
Number of divisions equal to 0.565 μ	25.34	19.71	5.63	45.04	11.21	33.25
Length in μ	14.32	11.14	3.17	25.45	6.33	18.79
Length in cm. of air after B., B., and L. (3)*	2.54	1.95	0.59	4.49	(1.03)	(3.19)
From (17)	–	–	–	–	1.06	3.21
Stopping powers derived	1774	1750	1861	1764	1674	1708
Length in cm. of air if stopping power for U_{II} is adopted $= 1708$	2.45	1.90	0.54	4.35	1.08	3.21

Names of authors are abbreviated in this way in the tables.

Standard deviation on L and S is about 0.2 divisions, and on T and D about 0.3. It is seen that the stopping power is higher for the fission fragments than for α rays and for slow protons, although its value may not be as large as mentioned by Boggild, Minnhagen, and Nielsen (1835). Our ranges are apparently longer than those found by most other authors, probably because we used a more sensitive emulsion, showing the end of the track which may be lost otherwise since it ionizes less.

Table II gathers data from other authors. Those of Vigneron (21) may serve as a comparison for the separated groups in the emulsion, and also those of Green and Livesey (13) but in their case, the center was marked only when it was the origin of a long-range alpha particle. We should then expect less energy to appear in the two main fragments. Those of Green and Livesey, and those of Tsien, Hoh, Chastel, and Vigneron (20) may serve also for the values of T. Cloud chamber values are also added from Boggild, Arroe, and Sigurgeirsson (2), and Boggild, Brostrom, and Lauritsen (3).

TABLE II

COLLECTED DATA ON RANGES (MICRONS OF EMULSION OR CENTIMETERS OF AIR REDUCED BY ASSUMING THE SAME STOPPING POWER AS FOR P_O, OR FOR U_{II} ALPHAS)

	L	S	D	T	D/T
Our results: microns of emulsion	14.32	11.14	3.17	25.45	0.129
centimeters of air	2.45	1.90	0.54	4.35	0.129
V. (21), emulsion Ilford E_1: microns of emulsion	13.4	10.4	3.00	23.8	0.126
T., H., C., and V. (20), Ilford C_2	—	—	—	24.5	—
G. and L. (13) emulsion Ilford B_1 desensitized by uranyl acetate 1%	—	—	—	24	—
Same, 2%	—	—	—	23.5	—
Same, 4%	—	—	—	23.0	—
Same, Ilford C_2	—	—	—	24.0	—
Same, Ilford C_2 when a particle of range greater than 50 μ is emitted	12.5	9.8	2.7	22.3 (23.2)	0.121
Same, range greater than 5μ	—	—	—	22.9	—
T., H., C., and V. Ilford C_2 when a third particle is emitted	13.0	10.5	2.5	23.5	0.106
M. (18), wet NTB	—	—	—	27	—
Same, when an α ray is emitted	—	—	—	25.3	0.123
B., A., and S. (2) in Xe, cm. of air	2.3	1.8	0.5	5.1	0.098
A, same	2.39	1.94	0.41	4.33	0.094
A; B., B., and L. (3)	2.5	1.9	0.6	4.4	0.136
He, same	3.0	2.3	0.7	5.3	0.132
He; B., A., and S.	2.8	2.3	0.5	5.1	0.098
D_2, same	2.25	1.89	0.36	4.14	0.087
H_2, same	2.11	1.77	0.34	3.88	0.088
B., M., and N. (4) in air, absolute determinations	2.54	1.95	0.59	4.49	0.132
K., M., and S. (14) Pu fragments in air	from 2.9 to 1.95		0.95 (max.)	(4.49)	0.212 (max.)

In this table, it is curious that the D/T ratios are small for all elementary gases, of all masses, ignoring the older values, on the one hand, and large for air and emulsion, on the other hand, the observed variation being of the order of 50%.

7. STATISTICAL ANALYSIS

The ability to see the two tracks of each pair allows us to plot a three dimensional representation as in Fig. 7. Here length L is in abscissae, S in ordinates; since $L > S$, all points lie on the right of the diagonal $D = L - S = 0$. Differences D and total length $T = L + S$ are equal along diagonals at right angles to each other. For each pair of integral values of L and of S, the observed frequency has been written, which is the third coordinate. Analogous diagrams with energies replacing ranges were plotted by Jentschke and Prankl, Flammersfeld, Jensen, and Gentner, Deutsch and Ramsey, and Brunton and Hanna (6) who survey the literature.

Contour lines joining points of equal frequencies have been drawn, the statistics being not very satisfactory for this purpose; however, the peak would then be placed at $L = 25.5$, $S = 19.5$, $T = 45$, $D = 6$, which agrees nearly with the observed averages. The contour lines near the peak seem to be somewhat elongated parallel to the axis of D.
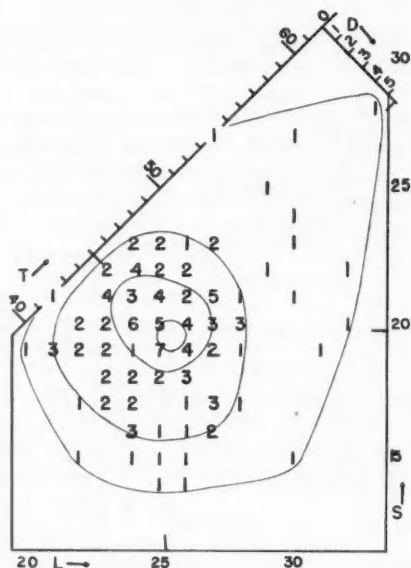
Fig. 7. Statistical analysis of 129 associated pairs. Length of L track in abscissae, of S track in ordinates, number of cases is shown. Total length T, and difference D may be read on oblique axes. Tentative contour lines connect points of equal frequencies.

From data such as that illustrated we may select a value of L, seek what are the values of S, D, and T associated with it, and plot their frequency distribution; then select another value of L and repeat the operation, etc. To preserve statistical significance, we have done this, but by choosing only two groups of L values. Similarly we have chosen two groups of S values, and looked for the frequency distributions of L, D, and T; and also two groups of D values in turn, and looked for the distribution of S, L, and T. We have chosen four groups of T values and looked for the distribution of D values. The results are shown in Table III and in Fig. 8.

The most interesting conclusion derived from this analysis is the following: the length of the long track is little dependent on the length of the short track with

TABLE III

STATISTICAL ANALYSIS OF PAIRS OF FISSION TRACKS
ONE DIVISION = 0.565 MICRONS

A

	$20 - 33$	$20 - 25$	$26 - 33$	Differences of the averages
Groups of L values				
Number of cases	129	74	45	
Average L	25.34	23.77	27.45	3.68
Average S	19.71	19.46	20.05	0.59
Average D	5.63	4.31	7.40	3.09
Average T	45.04	43.23	47.50	4.27

	B		
			Differences of the averages
Groups of S values	14 – 20	21 – 28	
Number of cases	83	46	
Average S	18.35	27.17	3.82
Average L	25.02	25.91	0.89
Average D	6.67	3.73	− 2.94
Average T	43.37	48.09	4.72

	C		
			Differences of the averages
Groups of D values	0 – 5	6 – 15	
Number of cases	62	67	
Average D	3.16	7.91	4.75
Average S	21.06	18.46	− 2.60
Average L	24.22	26.37	2.15
Average T	45.29	44.84	− 0.45

	D			
Groups of T values	36 – 43	44 – 45	46 – 48	49 – 61
Number of cases	39	39	36	15
Mean of extremes	39.5	44.5	47	55
Average $D = \overline{D}$	6.07	5.58	4.94	6.25
$\overline{D}$/mean of extremes	0.154	0.125	0.105	0.114

which it is associated, and conversely, the length of the short track depends little on the length of the associated long track. The variations of D and T may be viewed as necessary consequences of the above.
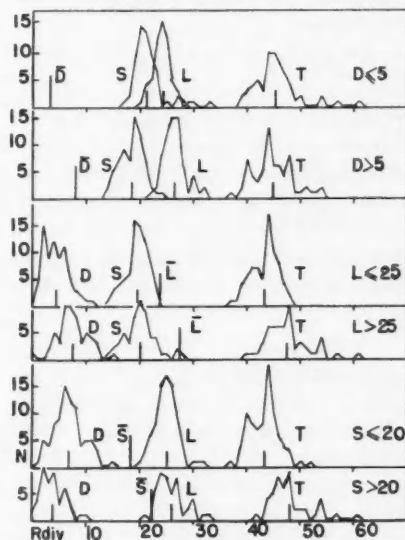

FIG. 8. Distribution curves of three length elements, a fourth one being chosen. The chosen element is mentioned at right, and its mean value is shown in its place. Note how little L (or S, or T), varies with chosen S, (or L, or D).

Another conclusion is that the total length is almost independent of the assumed difference, and conversely, that the difference in length is almost independent of the total length assumed. The variations of L and S observed with the two groups of values of D are then necessary consequences of the above. The relative difference in length D/T, though, decreases with increasing T.

A more precise form may be given to these statements by writing the derivatives. The assumed quantity is taken as the independent variable, and finite differences in the averages are assimilated with differentials. Then the following list of relations and values is obtained.

$$d\bar{S}/d\bar{L} = 0.16, \qquad\qquad d\bar{L}/d\bar{S} = 0.23,$$
$$d\bar{D}/d\bar{L} = 1 - d\bar{S}/d\bar{L} = 0.84, \quad d\bar{D}/d\bar{S} = d\bar{L}/d\bar{S} - 1 = -0.77,$$
$$d\bar{T}/d\bar{L} = 1 + d\bar{S}/d\bar{L} = 1.16, \quad d\bar{T}/d\bar{S} = 1 + d\bar{L}/d\bar{S} = 1.23,$$
$$d\bar{L}/d\bar{D} = 0.453,$$
$$d\bar{S}/d\bar{D} = d\bar{L}/d\bar{D} - 1 = -0.547,$$
$$d\bar{T}/d\bar{D} = d\bar{L}/d\bar{D} + d\bar{S}/d\bar{D} = -0.095,$$
$$d\bar{D}/d\bar{T} \sim 0.25/13 = 0.0192.$$

The last value is only approximate. These quantities are not all statistically independent. It is noteworthy that $d\bar{S}/d\bar{L}$ and $d\bar{L}/d\bar{S}$ as defined are not simply reciprocal one of the other; they are both positive.

These partial derivatives concerning range values have a parallel in the energy determinations of paired fragments. For instance, quantities similarly defined may be read off Fig. 12 of Ref. (6); calling S' the energy of the low energy group, and L' the other paired energy,

$$d\overline{S'}/d\overline{L'} \sim d\overline{L'}/d\overline{S'} \sim 0.2 \text{ to } 0.25.$$

The energy of one fragment is almost independent of the value chosen for the paired fragment, and more precisely one energy increases on the average a little if the other energy is increased. Our observation on ranges agrees with this one even to the approximate numerical value of the derivatives. The data on energy distribution do not lend readily to a similar comparison of $D' = L' - S'$ and $T' = L' + S'$.

No direct comparison may be made with published ranges, although the necessary observations have been made by several authors (4), (13), (18), (20), and (21).

8. STRAGGLING OF THE RANGES

We may take as a measure of the straggling, half of the smallest interval of length comprising 67% of cases, i.e. 87 out of 129 in the present instance. This interval is equal to 2σ if the distribution is gaussian, σ being the standard deviation. The results are shown in Table IV which also comprises data as given by the authors, or else derived by the procedure outlined from the published figures. Units are microns of emulsion or centimeters of air for range, and the figures represent the standard deviations. Straggling on the whole is seen to vary considerably in various media, and the data collected would seem of considerable interest for the theory of energy loss and of straggling of ranges.

TABLE IV

STRAGGLING OF THE RANGE OF FISSION FRAGMENTS

	L	S	D	T	P	αU_{II}
Our results	1.13/14.32 7.9%	1.27/11.14 11.4%	1.64/3.17 51.6%	1.70/25.45 6.65%	0.40/6.33 6.35%	0.62/18.69 3.3%
Emulsion Ilford E₁, V. (21)	1.0/13.4 7.5%	1.1/10.4 10.6%	—	1.4/23.8 5.87%		
Ilford C₂, G. and L. (13)	—	—	—	1.65/24 7.2%		
Same, T., H., C., and V. (20)	—	—	—	2.95/24.5 8.28%		
Same, G. and L., when a long-range particle is emitted, Fig. 7 of Ref. (13)	1.1/12.5 8.8%	1.15/9.8 11.7%	—	—		
Same Fig. 8 of Ref. (13)	—	—	—	1.5/22.0 6.54%		
G. and L., Ilford B₁, 2% UO₂(CH₃CO₂)₂	—	—	—	1.44/23.5 6.13%		
Same, 4%	—	—	—	1.15/23.0 5%		
In air, B., M., and N. (4)	0.175/2.54 6.9%	0.13/1.95 6.7%	—	0.2/4.49 4.44%	0.041/1.03 4.0%	0.1/3.19 3.19%
In D₂ gas, B., A., and S. (2)	0.113/2.25 5.0%	0.08/1.89 4.23%	—	0.198/4.14 4.76%	—	—
In H₂ gas, same	0.135/2.11 6.4%	0.1/1.77 5.65%	—	0.14/3.88 3.6%	—	—
In He gas, same	0.125/2.8 4.45%	0.175/2.3 7.6%	—	0.1/5.1 1.96%	—	—
In A, same	0.175/2.39 7.3%	0.15/1.94 7.75%	—	0.23/4.33 5.3%	—	—
In Xe, same	0.15/2.3 6.5%	0.175/1.8 9.7%	—	0.15/4.1 3.65%	—	—
Pu fission fragments of given masses in air, K., M., and S. (14)	4.97%					
Energy distribution, half-width at half height (6)	6/92.7 6.47%	10/59 16.9%				
Standard deviation 1/1.18 times the former quantity	5.5%	14.3%				

The data of Vigneron are the only ones directly comparable with ours, and they are seen to agree quite well. The slightly smaller deviations he found may indicate better measuring technique, however the difference may also be real and not instrumental: the alternative explanation is based upon the series of determinations of Green and Livesey. The more insensitive the emulsion in their case the smaller the total range and the smaller the straggling, the order of decreasing sensitivity being as follows: C_2, B_1 soaked in 2%, and in 4% uranyl acetate. Our emulsion would fall near C_2, or more sensitive, and Ilford E_1 of Vigneron would fall not far from $B_1 2\%$. In other words, a significant part of the range straggling would occur in the last micron or so of the range of each fragment, which is suppressed from the record in the least sensitive emulsions. So on the whole, the measurements of straggling in the emulsion by various authors are well consistent, the absolute and the relative straggling being always higher for the S group, the same as for the width of the energy distribution, while in gases, straggling is often larger for L.

Data on the straggling in xenon and argon give values near those for the emulsion, which is satisfactory since we expect much of the straggling to arise from nuclear collisions; nuclei of a weight comparable with that of the fragment should then behave similarly. Straggling for the other, lighter gases is somewhat smaller.

A formula given by Livingston and Bethe connects the electronic straggling observable for two different particles in the same medium:

$$\sigma(M, z'_{eff}, R) = M^{-\frac{1}{2}} \sigma(1, 1, R\, z'^2_{eff}/M).$$

The straggling on the right refers to a proton of reduced range $R z'^2_{eff}/M$, and is in the present instance about 2% in air and 3% in the emulsion; then σ for the fission fragments should be of the order of 0.2% and 0.3% respectively. We may deduce that their straggling in air as well as in emulsion is predominantly due to nuclear encounters, with presumably some contribution from the variations in z'_{eff} along the range.

Bohr (5) has discussed the range straggling of fission fragments and his theoretical value is 3% in air, with larger values being expected in media of higher atomic number. Our findings agree with his predictions on this, and also on the importance of the last part of the range for the over-all straggling.

9. COMPOSITION OF STRAGGLINGS

The observable straggling of ranges σ_R for either group L or S may be analyzed as containing three of four component stragglings. Fragments having well-defined mass and energy would not have all the same range. This is due to the straggling of ranges proper σ_1, such as is well known for α rays and protons. Fragments of a given mass do not have all the same energy and their mean range varies with energy; this is a second cause of straggling σ_2, and it is seen easily that $\sigma_2 = \sigma_E/I$, if σ_E is the straggling in the energy distribution of a given mass as emitted in fission, and $I = dE/dR$ is the rate of energy loss at the beginning of the path of the fragment of given mass and mean range. Finally, all fragments in a given group L or S do not have the same mass, and on this behalf, fragments having all

the same energy would show a straggling of their mean range $\sigma_3 = \sigma_M (\partial R/\partial M)_E$, if σ_M is the straggling of masses, and $(\partial R/\partial M)_E$ is the rate of change of mean range R with mass supposing all masses to be emitted with the same energy.

Supposing further that all distributions are statistically independent of one another (which is certainly not quite true for σ_2 and σ_3), that they are gaussian, and that suitable average values are used in the formula,

$$\sigma_R^2 = \sigma_1^2 + \sigma_2^2 + \sigma_3^2 = \sigma_1^2 + \sigma_E^2/I^2 + \sigma_M^2 (\partial R/\partial M)_E^2.$$

In this expression, σ_E and σ_M depend only on the fission process, while the other quantities are also dependent on the medium.

Straggling σ_R could also be analyzed otherwise, by taking account of the charge of the emitted nuclei as another fourth variable. It would be required to add a term σ_4, and the definition of σ_1, σ_2, and σ_3 would have to be modified.

Data existing in the literature allow some computations to be made according to the above formula. Table V gathers these data. The values of σ_R, σ_E, and σ_M are taken from Table IV; the values of I are taken from Part II of this series of

TABLE V

COMPOSITION OF STRAGGLING FOR FISSION FRAGMENTS OF U_{235}

	Emulsion		Air	
	L	S	L	S
σ_R	1.13 μ	1.27	0.175 cm.	0.13
	7.9%	11.4%	6.9%	6.7%
σ_E	5.1 Mev.	8.5	5.1	8.5
I	11.7 Mev./μ	10.6	66 Mev./cm.	60
σ_2	0.44	0.80	0.078	0.141
σ_M	6.8	6.8	6.8	6.8
$(\partial R/\partial M)_E$ upper limit for Pu_{239}	0.069	0.069	0.012	0.012
σ_3 upper limit	0.47	0.47	0.076	0.076
σ_1 derived	0.73	0.56	0.137	—
	5.1%	5%	5.4%	
σ_1 derived if $\sigma_2 = 0$	1.04	0.98	0.156	
	7.3%	8.8%	6.1%	

articles, for the emulsion. Stopping power is taken as 1764 for calculating the value of I in air. According to the said article the value of $(\partial R/\partial M)_E$ should be zero, inasmuch as we find that there is a single range–energy curve for L and S. An upper limit for this quantity is found by taking the approximate slope of a published R vs. M curve, Fig. 4 of Ref. (14), for Pu fragments in air. However, the fragments in this case had not a constant energy but an energy, dependent on the fission process, which decreased with increasing mass, so that the absolute value of the slope was larger than the quantity we require.

Then deducing σ_2 and σ_3, we may derive values of the straggling of ranges proper σ_1. Values found are reasonable for the emulsion, and for L in air, and not

very different from one another. For S in air, σ_2 is larger than σ_E. According to a recent paper of Leachman,* energy straggling σ_E as derived from ionization chamber measurements is partly instrumental; if σ_2 is reduced accordingly, better agreement would obtain in the case of S in air, and values of σ_1 would increase generally.

At any rate, it would seem that σ_1 in air ought to be smaller for S than for L, while in the emulsion, σ_1 is comparable for S and for L.

The straggling measured in air for given masses (14) is the statistical sum of σ_1 and σ_2. From its value of nearly 5%, and taking $\sigma_R = 6.8\%$ for both L and S, the value of σ_3 may be deduced to be 4.6%, or 0.117 cm. for L and 0.09 cm. for S, in approximate agreement with the upper limit found independently of 0.076.

10. BLACKENING OF THE TRACKS NEAR THE ORIGIN

It was noticed that the long track is usually blacker near the origin than the short one belonging to the same pair. Some systematic observations on this matter were made and are summarized in Table VI.

TABLE VI

BLACKENING OF 129 PAIRS OF TRACKS NEAR THEIR ORIGIN. NUMBER OF CASES

	Total number of cases	L above U layer	L beneath U layer	Not recorded
L blacker than S	98	45	41	12
L and S equally black, including one case of equal lengths	16	—	—	16
L less black than S	5	1	2	2
Undecided	9	—	—	9
Equal lengths, one blacker than the other	1	—	—	1
Total	129	46	43	40

The experimental evidence seems quite clear. Out of 118 usable observations on pairs with unequal S and L tracks, 98 or 83% show L blacker than S if the first few microns of each are compared, 16 or 13% show equal blackness, and 5 or 4% show S blacker than L. Statistics display no correlations with L being recorded above or below the U layer. The obvious inference is that L ionizes more than S near its beginning. To agree with the contrary we would have to make an hypothesis like the following.

Suppose that some effect like "solarization" or "reversal" would occur, meaning that a larger value of the rate of energy loss I would bring about a smaller blackening; this situation has never been observed so far for single tracks or for the collective effect of ionizing radiation.

If we try to explain by such a "reversal" the lesser blackening at the beginning of S, since the variation of I along S is no doubt a continuous function, the blackening should increase as we go away from the origin and show a maximum at a point where the values of I become sufficiently small and leave the domain of alleged "reversal". A maximum of the blackening happens along S but seldom,

*Phys. Rev. 87: 444. 1952.

as discussed below. So we may safely conclude that there is no reversal and that L ionizes more than S near the beginning. The difference may be 10%, from a subjective visual appraisal.

The fluctuations in blackening for a given ionization, when such small lengths are considered, may suffice to explain the 17% of cases where the difference is not of the predominant sign. However the possibility is not excluded that at times S ionizes more than L. And it may also happen that sometimes the L really belong to the S' group of heavy fragments, owing to range fluctuation; for such cases, D should be small, as discussed above, and this may be expected to happen in one or two cases here. In this respect it may be significant that the difference D when the blackening of S is greater has an average value of only $3.2 = (1 + 4 + 5 + 2 + 4)/5$, noticeably smaller than the general average $\bar{D} = 5.6$. For the 16 cases of equal blackening $\bar{D} = 5.2$.

These observations, incidentally, confirm the assignment of the L track to the lighter and more energetic fragment: it ionizes more strongly and is longer and therefore carries more energy.

No exactly like observations may here be compared. The discriminating power of emulsions used by other authors was usually insufficient to allow such differential estimation of blackening. However the writer has had the privilege of looking at some plates of Vigneron while visiting his laboratory, and has observed the same kind of difference; the picture of one pair published by Vigneron and Bogaardt also shows, if examined closely, the same difference. The figure of Green and Livesey of a pair associated with an alpha ray shows no detectable difference.

If this difference exists we should be able to tell the origin of the pair of tracks without having to mark it artificially, in an emulsion containing a dissolved uranium compound, since there should be naturally a discontinuity in the blackening, as at the point of occurrence of the $Li(n\ H_3)\alpha$ reaction. Indeed in a very fine grain emulsion, we have been able to do this by visual inspection for one pair in about 10 or 20 suitably oriented. This is just at the limit of what discriminating power over a very short length of track will permit.

In about half of the pairs of fission tracks, the blackening seemed to increase slightly from the origin and present a maximum before diminishing toward the end of one track. The maximum appeared in one case along both tracks of a pair. The effect of side bumps or recoils was corrected for visually, and we attempted to estimate the blackness of the central portion of the track. The position of the maximum found is analyzed in Fig. 6, distances being counted as positive in the direction of L. The explanation of this may lie in the effect of the neighboring inert U layer during development, and in the fluctuations of blackening along the range for a constant ionizing power. The arithmetic mean of the range of the maximum is 5.8, strangely similar to $\bar{D} = 5.63$, but the agreement is probably fortuitous, and not specially significant, since in about half of the 129 pairs, the blackening seemed to decrease right from the beginning. So the average blackening is seen to decrease from the origin, and there is no reason to believe that ionization does not behave likewise in individual cases.

Some confirmation that L is denser than S near the beginning may be seen in the following data concerning measurements in plates containing dissolved uranyl acetate. The maximum of blackening near the center was taken as the origin for measuring L and S. In Eastman 548, 23 tracks, arbitrary divisions,

$$\bar{L} = 14.2 \text{ div.}, \qquad \bar{S} = 12.4, \qquad \bar{D} = 1.8, \qquad \bar{T} = 26.6,$$
$$\sigma_L = 6.2\%, \qquad \sigma_S = 6\%, \qquad \bar{D}/\bar{T} = 6.8\%, \quad \sigma_T = 4.8\%.$$

In a fine-grained emulsion, 43 tracks, arbitrary divisions,

$$\bar{L} = 33.5 \text{ div.}, \qquad \bar{S} = 30.6, \qquad \bar{D} = 2.9, \qquad \bar{T} = 64.1,$$
$$\sigma_L = 7.5\%, \qquad \sigma_S = 6.5\%, \qquad \bar{D}/\bar{T} = 4.5\%, \quad \sigma_T = 5.5\%.$$

If the beginning of the S track were marked by a region of greater density, this region would be taken as the origin in the present measurements, and this would tend to increase the difference between L and S. In fact it is two or three times smaller.

These visual observations were confirmed by photometric measurements, which are described in Section II, which also contains a discussion of the literature. See also Lassen (16), and Mathieu (19).

11. ASSOCIATED α RAYS

In six cases out of 1500 pairs observed, a lighter track was seen originating at the same point as the two heavy fragments. From its appearance in each case it was judged to be an α ray rather than a proton. None stopped in the emulsion, and one had a visible path of 28 cm. of air equivalent. These α rays have now been studied fairly extensively (18), but our observations confirm that emission is from the very origin of the two main fragments, and therefore that the three particles are emitted simultaneously. An upper limit of the delay between emission of the fragments and emission of the α ray, if this is supposed to come from one of the fragments, was attained in one particular case, where the track of the α ray pointed back very exactly to the center of the very short gap marking the origin, within an accuracy estimated as 0.1 or 0.2 μ (Fig. 5). If 10^9 cm. per sec. is taken for the velocity of the fragments, the upper limit for emission of the α ray from the fragment is one or two times 10^{-14} sec. This is probably the shortest time interval in a physical phenomenon ever measured. Green and Livesey (13) have arrived by a similar reasoning to a value 10 times higher, since the origin in their case was not marked.

12. KNOCK-ON PROTONS

Some 30 cases of weak tracks starting from one of the fission tracks, some distance from its origin, were also observed. They were identified as protons from a comparison with surrounding protons and α rays. In eight cases proton and fission tracks were lying nearly flat, and then range and angle measurements were made. From these, the velocity V of the fragment is derived, knowing that of the proton v, and the angle θ between the direction of both;

$$V = v/2 \cos \theta,$$

which follows from conservation laws neglecting the difference between $M/(M+1)$ and unity. The range–velocity relation so obtained is shown in Fig. 9, as a single

straight line passing through the origin; the accuracy does not justify drawing separate curves for S and for L, and no indication is obtained of the hump expected at low velocities, knock-on protons being visible mostly at high velocities. The agreement with the curves used by Bohr (5) as obtained by Boggild, Brostrom, and Lauritsen is reasonable, although our velocities seem to be systematically 10% too high. The equation of our straight line is $V = 6.10^9\ R$, units being cm. per sec. and cm. of air.
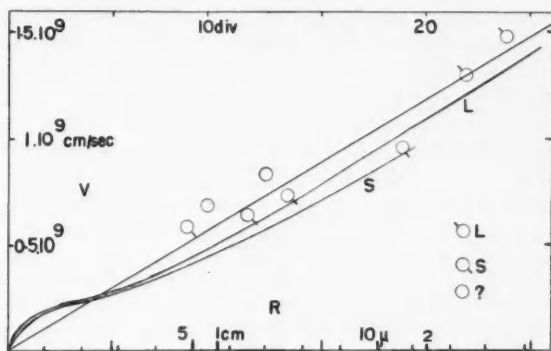

FIG. 9. Range–velocity diagram. Straight line $V = 6.10^9\ R$ if R in centimeters of air fits our points, the two other curves are from Boggild *et al.* (3).

On the other hand, careful examination of fission tracks in good conditions of emulsion and of development showed in cases as many as four or five small bumps, which are believed to be due to numerous very short proton tracks, usually too short to be observed, whose range may be 0.5 or 0.3 μ. Such recoils have been observed by Boggild, Brostrom, and Lauritsen in the cloud chamber, where 20 or 30 may appear distinctly on a single track, they are due to distant collisions on protons, and their frequency was analyzed to yield a range–velocity curve. Those seen in the emulsion might also be put to the same use (See Fig. 1B).

13. LIGHT ASSOCIATED PARTICLES

Cassels, Dainty, and Feather (7), and Allen and Dewan (1) using counter methods, Green and Livesey (13), and Tsien, Hoh, Chastel, and Vigneron (20) using photographic emulsions, have shown that in about 1% of fissions, a light, short range particle is emitted from a region near the center. The angular distribution suggests a more or less right angle of emission θ, although the mean angle is not as near to 90° as the angle of emission of long range associated α particles.

These particles may be emitted at the instant of fission, or else be the result of a collision on a proton occurring along the track of a fragment near its origin. The following evidence favors the second alternative, in agreement with Marshall (18).

In our conditions of observation, it seems unlikely that we should have missed some 15 proton tracks starting from the origin; on the other hand, of the 30 recoil protons seen originating more or less near to the origin, some 15 could well have

been said to originate in the "central region". Such may be the explanation of the observations mentioned in the emulsion. As to the experiments of various authors by counter methods, they were designed to eliminate hydrogeneous material, and if this was really achieved then we might have to revise our own conclusions, and perhaps attribute some of our alleged knock-on protons to proton emission by a flying fragment; but then the agreement of our range–velocity curve obtained on their basis would have to be explained as a coincidence.

On the other hand, the average range for these light particles is, after Tsien *et al.*, about 6 μ, the average angle of emission is about 75°, and if we assume them to be not associated light particles but knock-on protons, then the velocity of the colliding fragment is $1.57.10^9$ cm. per sec., which agrees well with the initial velocity of L, as well as our own measurements on protons that appear some distance from the origin. Again, if we examine and measure Fig. G of Tsien *et al.*, where such a light particle is pictured, we find $\theta = 66°$, proton range is 11.4 μ or 0.86 Mev. or $1.29.10^9$ cm. per sec., hence $V = 1.61.10^9$, at an estimated distance of 0.5 μ from the origin of L. Again the velocity seems a little high, but within the limits of accuracy of angular measurements, the point fits nicely on our range–velocity curve.

ACKNOWLEDGMENTS

REFERENCES

1. Allen, K. W. and Dewan, J. T.   Phys. Rev. 82: 527. 1951.
2. Boggild, J. K., Arroe, O. H., and Sigurgeirsson, T.   Phys. Rev. 71: 281. 1947.
3. Boggild, J. K., Brostrom, K. J., and Lauritsen, T.   Kgl. Danske Videnskab. Selskab. Mat. fys. Medd. 18(4): 1. 1940.
4. Boggild, J. K., Minnhagen, L., and Nielsen, O. B.   Phys. Rev. 76: 988. 1949.
5. Bohr, N.   Kgl. Danske Videnskab. Selskab. Mat. fys. Medd. 18(8): 1. 1948.
6. Brunton, D. C. and Hanna, G. C.   Can. J. Research, A, 28: 190. 1950.
7. Cassels, J. M., Dainty, J., Feather, N., and Green, L. L.   Proc. Roy. Soc. (London), A, 191: 428. 1947.
8. Demers, P.   Phys. Rev. 70: 974. 1946.
9. Demers, P.   Can. J. Research, A, 25: 223. 1947.
10. Demers, P.   Science, 110: 380. 1950.
11. Demers, P.   Science et inds phot. 23: 1. 1952.
12. Demers, P. and Mathieu, R.   Phys. Rev. 75: 1327. 1949.
13. Green, L. L. and Livesey, L. D.   Trans. Roy. Soc. (London), A, 241: 323. 1948.
14. Katcoff, S., Miskel, J. A., and Stanley, C. W.   Phys. Rev. 74: 631. 1948.
15. Lark-Horowitz, K. and Miller, W. A.   Phys. Rev. 59: 941. 1941.
16. Lassen, N. O.   Kgl. Danske Videnskab. Selskab. Mat. fys. Medd. 26(5): 1. 1951.
17. Livingston, M. S. and Bethe, H.   Revs. Modern Phys. 9: 245. 1937.
18. Marshall, L.   Phys. Rev. 75: 1339. 1949.
19. Mathieu, R.   Ann. Acfas, 16: 44. 1950.
20. Tsien, S. T., Hoh, Z. W., Chastel, R., and Vigneron, L.   J. phys. radium, 8: 165. 1947.
21. Vigneron, L.   Compt. rend. 231: 1473. 1951.
22. Vigneron, L. and Bogaardt, A.   J. phys. radium, 11: 283. 1950.

ENERGY LOSS OF HIGHLY CHARGED PARTICLES PRODUCED BY FISSION AND BY COSMIC RAYS

SECTION II. PHOTOMETRIC MEASUREMENTS ON FISSION FRAGMENTS[1]

By Roger Mathieu[2] and Pierre Demers[3]

ABSTRACT

A sensitive and accurate photometer is described, which is designed to measure directly the light intensity transmitted through very small objects placed under the microscope at the highest resolving powers. Tracks of mesons, protons, α rays, and fission fragments were examined with it, characteristic curves relating optical density D and ionizing power I were obtained and show the feature, unusual for light sensitivity, of two sensitive regions separated by a region of very low gamma. The variation of optical density and of width with ionizing power is discussed for three types of emulsion. Measurements on fission tracks are analyzed to derive a single range ionization relation $I = 1.22 + 0.738\ R$, in Mev. and microns, applicable to both heavy and light fragments, in agreement with Section I. The controversial literature on this matter is discussed.

INTRODUCTION

In Section I were described observations on fission fragments, some of which related to the blackening of the tracks in very small grained emulsions. Here a photometer adapted to measurements on such tracks is described and results of its use are discussed.

The transmission coefficient of a substance is ideally measured using a wide uniform sample and a wide beam of parallel light, that is, one having a small numerical aperture. These conditions are more or less approximated in micro-photometers for examining spectral lines on photographic plates. Here however the conditions do not permit a small numerical aperture, unless we sacrifice definition of the tracks, which are 0.2 to 0.4μ in width and induce thereupon strong diffraction figures; the objects themselves are not wide and uniform; and moreover the light intensity liable to fall on short portions of tracks is very small. Such are the difficulties to be envisaged; the two first are theoretical and have a bearing on the interpretation of transmission measurements, and the last is instrumental.

Two methods may be envisaged: either taking a picture of the track and analyzing it, or measuring directly the amounts of light which pass through the microscope and are found in the plane of the image by a photomultiplier tube. For this work we chose the second method, as more liable to give absolute values. Then the use of the photomultiplier is rendered much more easy if the light to be analyzed is interrupted. In a first installation Demers and Mathieu (10) interrupted the light beam between the microscope and the sensitive cell by a needle attached to a tuning fork vibrating at about 500 cycles. This was possible because the needle would cast its shadow on a slit in the image plane before the cell, and, with suitable adjustment, the signal was very steady. The amplified current was sent to an oscilloscope, used as a measuring instrument

much as in the present installation. With it the first absolute measurements of transmission through fission tracks were made and showed values as follows.

In very fine grained emulsion

Beginning of long track L of fission	44%
Beginning of short track S of fission	50%
End of fragment tracks	60%
α-ray track	70%
$N_{14}(n, p)C_{14}$ proton	80%

In emulsion C_2

α ray	54%
Proton	75%

Same, with a stronger development

π meson 20μ from its end	69%
μ meson from the decay of the above, 20μ from its end	67%

Width of the tracks, being the distance between points at half reduction of the transmission: 0.3 to 0.45μ.

These results were obtained with an image magnification of 1000, and a slit 0.1 mm. wide and 1 mm. long for fission fragments and slightly longer in the C_2 emulsion. The width varied remarkably little from the darkest to the weakest tracks. Illumination was Kohler critical in blue-green filtered light.

PRESENT INSTRUMENT

Figs. 1 and 2 show the installation (18, 19). The light beam comes from a mercury vapor lamp fed on 60 cycles providing 120 interruptions per second.
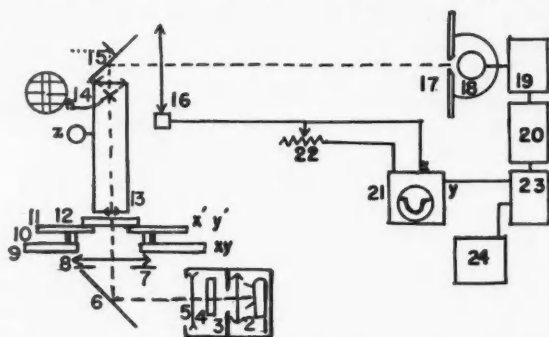
FIG. 1. Over-all diagram of the photometric installation. 1—Mercury vapor lamp; 2—condenser; 3—field diaphragm; 4—Wratten 77A filter; 5—divergent cylindrical lens to widen the light beam, axis parallel to that of 1; 6—microscope plane mirror; 7—aperture diaphragm; 8—condenser; 9—standard x and y movements of the microscope; 10—intermediate rotation θ; 11—z' and y', other movements added; 12—plate being examined; 13—objective $\times 90$; 14—micrometer to locate spot examined in eyepiece $\times 12,5$ compensated B & L coated; 15—mirror system; 16—sweeping mechanism, 1.3 diopter lens movable along x direction in its plane; 17—screen and slit; 18—photomultiplier; 19—HT supply; 20—electronic voltmeter, potentiometer, null circuit; 21—oscilloscope with 22—d–c. potentiometer, controlling x coordinate; 23—linear a–c. amplifier; 24—Esterline Angus recorder.
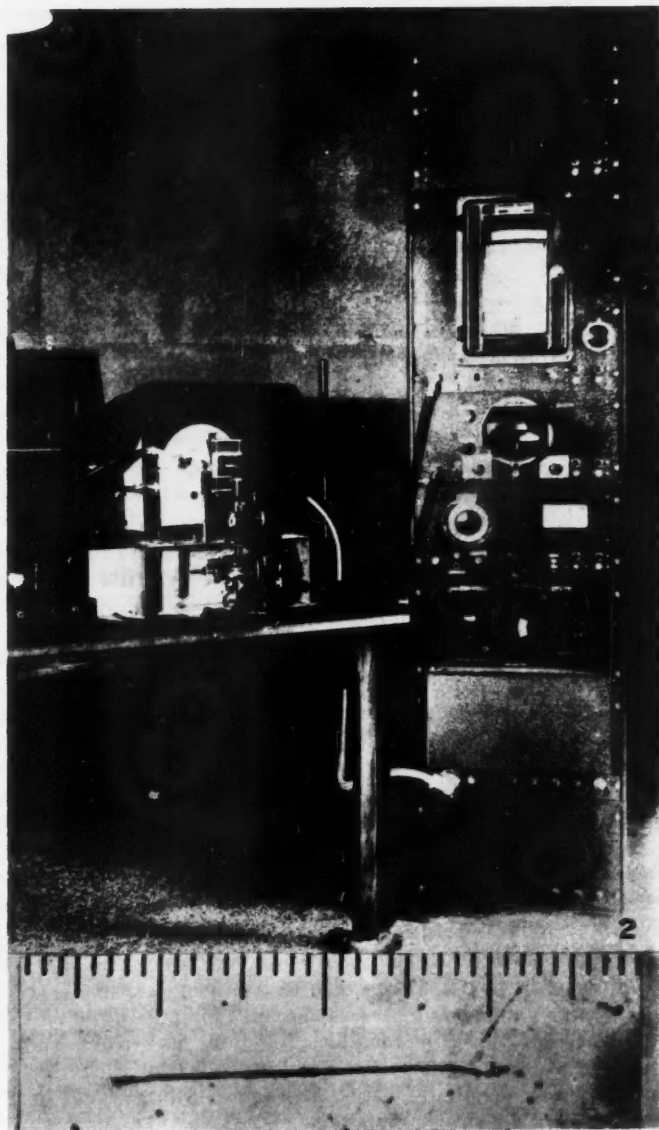
FIG. 2.   Over-all view of the installation; lantern at the left, microscope and photomultiplier housing in the center, the rest of the apparatus at the right.

FIG. 3.   Typical pair of tracks measured.   One division = 1.1μ approximately.

A Wratten 77A filter and the spectral response of the photocell ensure that only the green line 5600 Å is detected. A special rotating stage was used to align tracks properly, see Demers (8, p. 649). A half gilt mirror sent the image on to the screen where it was $1000\times$ the object and permitted direct examination of the field; a second mirror could also be added to avoid the necessity of looking from above. A micrometer made of a glass fiber broken in the center was placed in the eyepiece to help in locating the point being examined. However indirect examination of the image on the screen was perhaps more convenient. The image looked rather pale at first but we found it possible to increase its brightness for only one observer placed in front of it, by using as a screen the mate side of an aluminum foil or a carefully satin-finished plate of aluminum: these surfaces diffuse most of the luminous energy falling upon them perpendicularly in a narrow backward cone. Slits of various sizes were made out of thin aluminum sheets. The image has to be moved across the slit by a movement that we call x. This is provided by optical means, through the lateral displacement of a 1.3 diopter lens placed in the beam between the eyepiece and the screen and mounted on an adjustable support. A large displacement of it moves the image only a little. The x movements are synchronized with those of the recording paper chart by synchronous motors and of the x coordinate of the spot of the oscilloscope by d-c. connections.

The photomultiplier tube 931A receives the light passing through the slit and acts itself as a first amplifying unit of its photoelectric current. It is fed by 1235 v. d-c. regulated to $\pm 0.05\%$. The last collecting stage is fed by another d-c. supply of 210 v. $\pm 1\%$. A cathode follower stage follows whose output may be opposed to that supplied by a Rubicon potentiometer. The null indicator is made of a multivibrator circuit which is triggered as soon as the zero point is passed once in one direction. Acting on the a-c. output it measures a peak value. The output may also be smoothed before measure, by charging a condenser through a rectifying diode.

The output may be amplified further and fed to the y axis of an oscilloscope. Here it may be half rectified by a diode and the resulting wave, combined with the RC circuit of the Y deflecting plates, produces a brilliant spot or base line whose movements are approximately proportional to the signal applied. The x coordinates may be some form of 60 cycles or else through d-c. connections reproduce the movements of the track across the slit.

Finally the output may act on an Esterline Angus recorder after a linear amplifier accurate to $\pm 1\%$. This is used for the final record on a portion of track, the electronic voltmeter is used for absolute calibrations, and the cathodic oscilloscope serves to adjust the conditions before the final record. The over-all accuracy of the Esterline Angus recorder in measuring light intensities is about 1%, as was verified directly by placing a calibrated neutral wedge in front of the entrance slit.

Other photometers have been described for measurements on larger areas under the microscope, by Blau, Rudin, and Lindenbaum (1), by Della-Corte and Ramat (6), and by Friesen and Kristiansson (11). These authors use a slit

larger than the track so that only an integrated effect is measured in their case. Fürth and Oliphant (12) have suggested such measurements with a photometer of their description. Kayas and Morellet (14), and Ceccarelli and Zorn (4) have used long slits to measure the transmission and the width of light and of heavy tracks, respectively.

CONDITIONS OF MEASUREMENTS

Tracks (Fig. 3) should not be inclined by more than 5°, as a rule, with a slit 1μ long, otherwise they will not be accurately in focus over the whole length of the slit. Longer slits would require a lesser slope. Very careful orientation of the track to render its image parallel to the slit, and very careful focusing are necessary to make the best of the possible accuracy. Visual focusing is insufficient; the maximum of blackening should be searched finally by watching the spot of the oscilloscope while moving the fine adjustment screw. A 0.1μ difference in focusing makes a significant difference on the transmission measured.

When the parallelism and the focusing are finally found to be good, the automatic scanning is put in operation, and the transmission curve is drawn on the paper recorder. This may be repeated to somewhat better than 1%. It may be noted here that the instantaneous output from the photomultiplier comprises a heavy noise level, comparable to the signal to be measured. The importance of it is negligible in the outcome because of the large time constants introduced throughout. It would be impossible on that account to draw the absorption curve in 0.01 sec. for instance, not unless far more intense sources were available. Presently the curve is drawn in some 50 sec. and, if desired, this time could perhaps be cut down to 10 sec. We may speak in this respect of two conjugated variables connected by the uncertainty principle, luminous intensity and time; time being set at leisure, light intensity may become very well defined.

The length of the slit to be used depends on the purpose. Slits $0.1 \times 0.1\mu^2$ have been used to measure very small and pale individual grains in a weak proton track transmitting about 60% when measured with a long slit; the single grains transmitted $(60 \pm 2)\%$, and their width of the order of 0.3μ could be determined within $\pm 10\%$.

Measurements done with a slit 1μ long at various points along seemingly uniform tracks may show a rather considerable dispersion of transmission values depending on the statistical character of blackening and on the grain structure. With a 5μ slit, extreme values were 50% and 90% while grain counting yielded extreme values of 7 to 9 grains per 5μ along a proton track of residual range 500 to 700μ in a fine-grained emulsion. With a longer slit, say 100μ, there would be little variation caused by this.

In fission tracks, short slits have to be used since the blackening to be investigated changes rapidly with range, and the averaging will be done over several tracks rather than over longer portions of the ranges of each. However on such highly ionizing tracks, the blackening suffers lesser statistical fluctuations than on proton tracks.

The optical meaning of these absolute measurements may be looked into. Objects looking absolutely black in the field, like a heavy scratch or a thick

clump of silver, transmitted 1 to 4%, the average being 3% if the object was below the emulsion and 2% if it was above. Illumination of too large a field outside that examined brings about a slight increase in the above figure. Thickness of emulsions reached 100μ at the time of observation. The difference in the transmission of an opaque object using a coated, and an uncoated otherwise identical 90 ×, 1.3 N.A. apochromat, both of Bausch and Lomb, was less than 1%, so it may be concluded that the coating does not improve the contrast, although it improved transmission by 25%.

This background seems to come mostly from light scattered in the optical path in the oil, in the objective and above. Weak stray light in the room did not matter much until it caused saturation of the photomultiplier, because it is not modulated like the one to be measured. This background of 2 or 3% should really be subtracted from both I and I_0 to obtain true transmission and true density; however in view of its smallness and of the uncertainty as to the exact value to choose, we did not make any correction for it; the correction would have to be done if transmissions reached 10% or so, but the lowest transmission of a track encountered was 20%.

The diffraction figure of a bright point or of a bright narrow line imaged through an optical system is a well-known problem of physical optics; however, that of a narrow black object has apparently not been investigated. The continuous line left by a fission fragment may be assimilated to a narrow black line as a first approximation, the variations in transmission would then correspond with variations in the width of that line. Electron microscope observations show the developed grains as a mass of entangled silver ribbons, so the black line should be replaced in a more accurate theory of image formation, by a somewhat porous structure extending in three dimensions, with a denser and almost continuous core, the individual elements of this structure being much smaller than a wave length or 0.5μ, and even, than the resolving power, 0.22μ. It must be remembered that the light rays contributing to form the image of this structure cross it at nearly all angles on account of the high numerical aperture. As long as the structural elements are nowhere too numerous per unit volume, we may expect the integral $\int D \, dx$ extended over the whole domain of the track's image, where D is the optical density $\log_{10} I_0/I = -\log_{10} T$, to give a measure of the number of these elements per unit length of the track. Assuming similarly shaped absorption curves when D and x are plotted, for various portions of tracks, this integral is proportional to $D_{max} W'$, D_{max} being the central maximum of density and W', the width at half reduction of density.

RESULTS

A slit on the screen of dimensions equivalent to a 1μ length and a 0.1μ width of the object was used. Transmission curves were drawn at various contiguous points along fission tracks with marked origins, obtained in a very fine grained emulsion as described in Section I (9). Seven pairs of tracks were selected that showed few nuclear collisions near the origin, to render the photometric measurements easier. The absorption curves may be read to give minimum transmission,

maximum density, and width at half reduction of transmission; these will be called simply T, D, and W, respectively.

The single values of T found for the seven pairs of long L and S associated tracks are shown as a function of distance from the origin in Fig. 4. In 43 cases
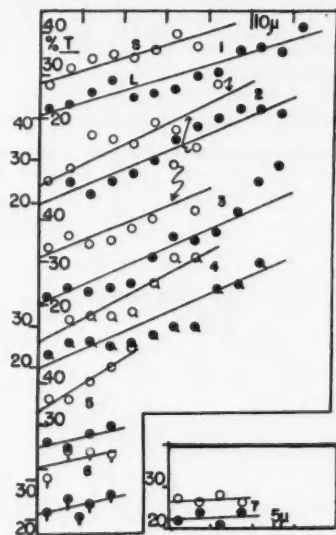

FIG. 4. Transmission T vs. distance from origin, along 7 individual pairs for light L and short S tracks numbered 1 to 7.

out of 44, transmission at equal distances is greater for S. The best straight line is drawn through each series of points, and the S curve is always above the corresponding L curve of the same pair although some S curves are partly below the L curve of another pair. Extrapolated transmissions at the origin make up two groups: S from 42 to 24%, L from 30 to 18%.

The average density at a given distance is shown in Fig. 5 as a function of this distance for the S and the L tracks, giving an initial density of 0.67 and 0.56
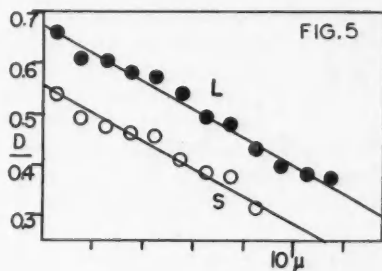
FIG. 5. Average values optical density D vs. distance from the origin for L and S tracks.

for L and S respectively, or transmissions of 22 and 32%. The series of points are well fitted by parallel straight lines. The difference of their intercepts on the distance axis is 4.0μ. If the density were the same function of residual range for both groups of fragments, we would expect the difference to be 3.17μ, equal to that of the ranges as found in Section I. The "extrapolated ranges," defined as the points where $D = 0$ along the straight lines drawn, would be 20.3 for S and 24.3 for L.

Average density is also represented as a function of residual range in Fig. 6. Here residual range is defined as 14.31 or 11.14μ, for L and S respectively, less
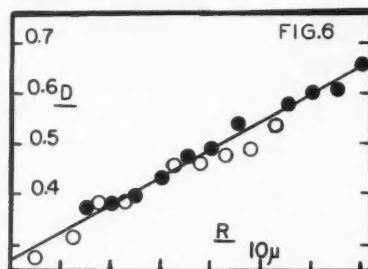
FIG. 6. Average values D vs. range R, R being the difference 14.31 (for L), 11.14 (for S), less distance from the origin.

the distance from the origin. The two series of points agree very well with a single straight line

$$D = 0.27 + 0.028\,R.$$

The agreement would be better if the difference of ranges were arranged to be 4μ instead of 3.17.

Single width measurements are not so accurate, and only the average values found at a given distance in seven pairs of tracks are reported, in Fig. 7. The L track is always wider than the S track at a given distance except in one case. The points are fitted near the origin by two straight lines that are not parallel, and that show widths at the origin of 0.39 for L and 0.34 for S. The small difference appears to be well established.
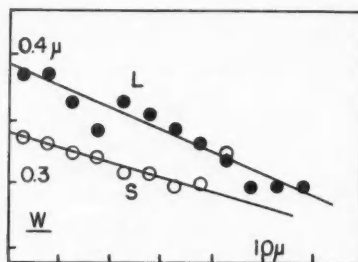

FIG. 7. Average values of width W vs. distance for L and S tracks.

Further analysis of the data is shown in Fig. 8. The number of times each value of W has been found for L, irrespective of range, is shown, and the same for S. Similar measurements are shown for a series of U_I and U_{II} α-ray tracks in the same plate with a very fine grained emulsion, and the same for several short protons from the $N_{14}(n,p)C_{14}$ reaction also in the same plates. Average width is very similar for both, being 0.308 for the protons and 0.310 for the α rays. However, both are clearly narrower than the two kinds of fission tracks.
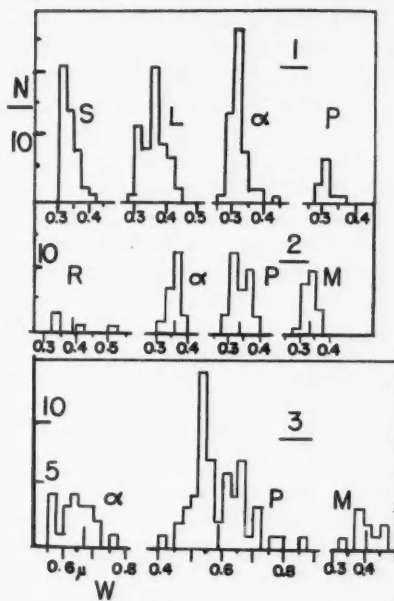
FIG. 8. Frequency distribution of W found for fission tracks, L and S, for recoils R, for α-ray, for proton, and for meson tracks, in very fine grained (1), fine grained (2), and medium-sized grain emulsions (3).

IONIZATION OF FISSION FRAGMENTS

If we assume that a single relation holds between optical density D and rate of energy loss I, for all particles, and if we consider the relation found between D and R, we are led to conclude that a single relation exists between I and R for both fission fragments. We will now attempt to find this relation for the emulsion from an internal analysis of photometric data.

In the range difference (called D in Section I) of 3.17μ, L must then spend the energy difference between the two groups of 33.7 Mev.; so for $I = 10.6$ Mev. per μ, at 1.53μ from the origin, or a range of 12.67μ, $D = 0.62$. This gives us one point of a D vs. I curve.

Another point, less sure since the averaging is extended over a longer range, is given by the average energy expenditure 59 Mev., divided by the range 11.14μ, or $I = 5.3$, while the average density is $D = 0.425$.

CHARACTERISTIC CURVES

Density has also been determined along six α-ray tracks of U_I and U_{II}, where it is found to increase slightly toward the end, as follows:

$R\ (\mu)$:	5	10	15	20	25
I (Mev./μ) :	0.320	0.300	0.200	0.178	0.150
D :	0.167	0.155	0.151	0.135	0.135

Similarly along protons 6μ long, density was 0.07 and rate of energy loss was 0.09 Mev. per μ. At the beginning of a proton 400μ long, of 6 Mev., density was about $0.03-0.05$, and there $I = 0.012$.

We will now represent these data on a doubly logarithmic coordinate system similar to that proposed by Hurter and Driffield for studying the relationship of optical density over a large area—similar to the density of a track D—and of the energy of illumination spent per unit area—similar to energy loss per unit length I. This system, which is well known in ordinary photography, usually yields an S-shaped curve, with a toe at low values of I, starting at the "inertia value" on the I scale; a more or less straight central portion, where the slope is called gamma (γ); and a levelling off at higher intensities; followed sometimes by a reversal or solarization region, where D decreases with increasing I. A second reversal has sometimes been observed, where the curve goes up again.

The curve so obtained (1 in Fig. 9) in the very fine grained emulsion has an inertia value of about 0.01 Mev. per μ, increases slowly, then nearly levels off in
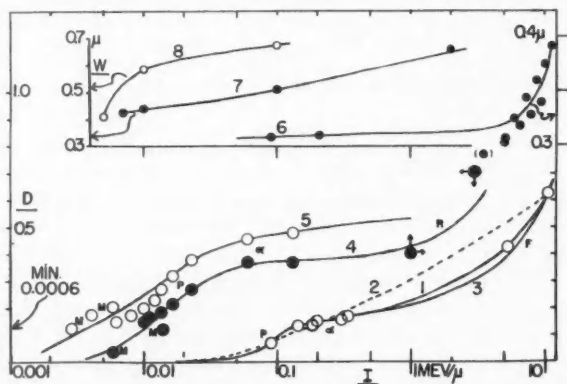

FIG. 9. Characteristic curves optical density D vs. rate of energy loss I: 1—for very fine grained emulsion; 2 and 3—alternative curves rejected from analysis presented in the text; 4—fine grained emulsion; 5—medium-sized grains; 6—width W vs. I for very fine grains, 7—for fine grains, 8—for medium-sized grains.

the region of α rays. The maximum gamma encountered so far is 0.28 at $I = 0.1$. Points are lacking in an intermediate region, but as the curve is drawn the slope gradually increases and in the fission fragment region, gamma must be of the order of 0.8 to 1.2.

This may seem a surprising course for a characteristic curve, since such curves drawn for optical sensitivity sometimes show a downturn after a flat region, but never a marked upturn, in ordinary kinds of emulsions.

However any continuous curve drawn to fit the several α-ray points can hardly have any other general shape. Then further, suppose we take only the average of the α-ray points, and the reliable looking point at the extreme right. Then the nearly straight dotted line 2 drawn in Fig. 9 would fit well enough the three remaining values. From this curve we may derive at each value of D and of R along fission tracks the value of I, then plot the I vs. R diagram shown as a dotted line in Fig. 10. The energy obtained for the heavy fragment $\int I \, dR$ from 0 to 11.14μ is then about 35 Mev., which is very much at variance from 59 Mev. This strongly suggests also that larger values of I should correspond to given D values than are found along the dotted curve.
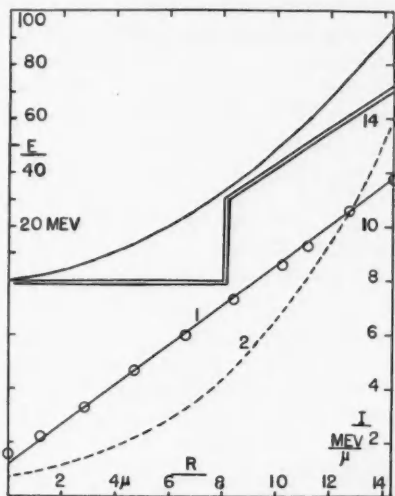
FIG. 10.   Rate of energy loss I vs. range, R, 1 from curve·1 in Fig. 9, curve 2 (rejected) from curve 2 in Fig. 9, and energy E vs. range, for fission fragments, derived from photometric analysis.

On the other hand if we take the full curve 1 as drawn, we find by the same analysis the series of points represented also on Fig. 10. These fit nicely a straight line, and the one drawn has been calculated to agree with the values $D = 0.62$, $I = 10.6$; and $E = 59$ Mev., $R = 11.14$; the linear I vs. R relation implies a second order E vs. R relation:

$$I = 1.22 + 0.738 \, R,$$
$$E = 1.22 \, R + 0.369 \, R^2.$$

For $R = 14.32$, energy is 93.3 according to this formula instead of 92.7, a 0.6% deviation.

If the characteristic curve is drawn to pass beneath the average point for fission fragments, rather than across it, as in 3, Fig. 9, a different linear I vs. R relation obtains, leading to too high energies for the heavy fragment; for instance, 66 Mev. was found in one trial.

So the consistency of the results obtained further suggests that the characteristic curve follows indeed the course shown, which is also suggested by the hypothesis that it should be a continuous line when drawn in the coordinate system chosen.

The I vs. R relation obtained here agrees reasonably well with the average V vs. R relation obtained in Section I, and with other data. In both cases the procedure should be more accurate near the origin than near the end of the range, and should not be expected to give more than the general course of the relationship. However, some sign of the existence of an ionization maximum near the end of the range may be seen in the fact that the extrapolated value of I at $R = 0$ has a finite value. The existence of this maximum is known from the observation of single tracks, which show a maximum of blackening in the last micron of range. However the curve as drawn is intended to bring out the features near the origin and not near the end, and ionization at range zero is an average value.

OTHER CHARACTERISTIC CURVES

In two other emulsions, one with medium and the other with small sized grains, similar photoelectric measurements were carried out along tracks of mesons, of protons, and of α rays. At various points along their range the density was read as follows:

α Rays

$R\ (\mu)$:				40		215	
I (Mev./μ) :				0.132		0.062	
D (small grains) :				0.374		0.37	
D (medium size) :				0.478		0.454	

Protons

R :	100	200	300	400	600	1000	1800
I :	0.023	0.0165	0.0137	0.012	0.01	0.008	0.0062
D (small grains)	0.27	0.215	0.185	0.167	0.15	—	—
D (medium size) :	0.38	0.32	0.27	0.23	0.20	0.175	0.15

μ Mesons

R :		40	200	500	1100
I :		0.014	0.0059	0.0041	0.0029
D (small grains) :		0.12	0.035	—	—
D (medium size) :		—	0.205	0.176	0.124

The corresponding characteristic curves are also shown on Fig. 9. If we compare the curves for the three grain sizes, we notice that larger grains, in the emulsions used, correspond with a lower inertia, and a greater density for a given ionization. The curves at higher ionizations cannot be compared accurately for lack of tracks of known ionization. However, recoil tracks due to cosmic rays have been examined in the fine-grained emulsion. In these recoils, ionization is probably 1 to 3 Mev. per μ, while the densities found range from 0.4 to 0.7.

These data are shown in Fig. 9 with the corresponding uncertainty, and they are enough to show the beginning of an upturn similar to that observed with the very fine grained emulsion.

Nothing of the kind seems to happen with medium-sized grains, recoils are not markedly blacker than α tracks and are often difficult to distinguish from them.

The peculiar shape of the characteristic curve just described calls for some comments. In applying to the same wide range of ionization as considered here his quantitative theory of grain density, Demers (7) concluded that the experimental data could not fit one formula with a single set of the two adjustable parameters. These had to be chosen for each domain of ionizations; higher ionizations I seem to bring in a reaction from less sensitive grains, having a larger inertia parameter "I_0".

A similar reasoning might be applied to the relation between optical density D, and I. Sensitive grains are affected by a small energy expenditure; there exist few grains of medium sensitivity so that medium energy expenditures do not affect many more grains; then numerous grains of small sensitivity are affected by great energy losses. It would be interesting to know whether this behavior has a parallel in the light sensitivity curves of certain specially mixed emulsions, no such behavior being mentioned by Mees (20), nor by Clerc (5).

This first explanation seems formally satisfactory. However it may very well be complemented by a second one. The onset of the second rising portion of the curve is accompanied by the appearance of solid tracks, and it seems most reasonable to connect both phenomena. It seems then that the grains surrounding the ones that have received a strong impression are developed without having themselves an impression from the passing particle. This process is known in ordinary photography and is called development by infection. Development of a grain proceeds by the transformation of a silver bromide crystal into a silver ribbon. This silver ribbon may, under favorable circumstances, pierce the surrounding gelatine envelope of the original grain, and come in contact with a neighboring silver bromide grain, which will then start to develop. It remains to be understood why the conditions favor infection development more when the impression has been strong that when it has been weak, since it is believed that all developed grains are alike.

With the medium-sized grains, development by infection would probably occur only through prolonged development inducing severe fog. Another circumstance may favor infection development with the smaller grains. It is known from certain electron microscope pictures of Hall and Schoen (13) that in Lippmann emulsions, with a grain only a little smaller than those we are dealing with, the developed ribbon of silver extends through the gelatine in a nearly straight line, and its length is many times the diameter of the original silver bromide grain. This tendency of the silver ribbon to penetrate the gelatine may also exist in the two finer grained emulsions, where the silver bromide concentration is 81 to 85% instead of 30 to 40% as in the more dilute Lippmann emulsions.

WIDTH OF THE TRACKS

Width W has been plotted against ionizing power I in Fig. 9 for the very fine grained emulsion. It remains practically constant until the fission region is reached. The increase would be insignificant if widths W' at half reduction of density were measured instead of widths W at half reduction of intensity, that is, all tracks show in this emulsion very nearly the same shape for the absorption curve if D/D_{max} is plotted against coordinate x.

Figs. 8 and 9 also show features of W in two other kinds of emulsions.

CONCLUSIONS ON THE IONIZATION OF FISSION FRAGMENTS

Visual observations of Section I have shown that the average light fragment L leaves a more opaque track than the average S fragment. Our photometric measurements on seven pairs display the same difference for each pair, and allow us to present a single range ionization relation valid for both groups of fragments. The initial ionization deduced is 9.4 and 11.6 Mev. per μ for S and for L respectively, equivalent to 53.3 and 65.8 Mev. per cm. of air, if 1764 is taken for the stopping power.

The ionization curve of fission fragments has been discussed by Bohr (2), who expected a positive difference $I_L - I_S$ near the origin, as we find here. Lamb (16), and Knipp and Teller (15) expected theoretically a negative difference.

The measurements of West (22) and the long series of measurements of Lassen (17) lead to the conclusion that the said difference is negative; these were done with an ionization chamber using pulse analysis. Lassen derived complete range ionization curves, which showed a remarkable course. The two curves are practically parallel at small ranges, if drawn with distance as the abscissa. At about 0.6 cm. from the origin, however, the S curve increases in slope and crosses the L curve to show a higher value of ionization at the origin. These conclusions seem to be adopted by Bohr (3).

On the other hand, Sherr and Peterson (21), by a time analysis of the impulse current collected from an ionization chamber where the fission fragments spend their whole energy, were able to show that there exists a single range ionization curve fitting both groups S and L, in agreement with our results.

It would be interesting to understand the source of the disagreement of the results of West, and of Lassen. It may be said that the operation of an ionization chamber is a complicated one, and that problems like those of ion collection may arise. Our method is very straightforward in comparison. A possible reversal of the D vs. I relation has been ruled out in Section I, and it would be very strange if the D vs. I relation would depend on the nature of the particle. There remains the possibility that gases would behave one way, and condensed matter like the emulsion the other way. We might then expect a marked variation in the D/T ratio of ranges which would be smaller in the gases than in the emulsion. Such ratios are listed in Table II, Section I (9). The best value for a gas is that obtained in air, and this is very nearly the same as in the emulsion. Other ratios in gases are in general smaller, being 0.09 to 0.10 on the average instead of 0.129.

ACKNOWLEDGMENTS

REFERENCES

1. BLAU, M., RUDIN, R., and LINDENBAUM, S.   Rev. Sci. Instruments, 21: 978.   1950.
2. BOHR, N.   Phys. Rev. 59: 270.   1941.
3. BOHR, N.   Kgl. Danske Videnskab. Selskab, Mat.-fys. Medd. 18, No. 8: 1.   1948.
4. CECCARELLI, M. and ZORN, G. I.   Phil. Mag. 43: 356.   1952.
5. CLERC, L. P.   La technique photographique, 4th ed. Publications Paul Montel, Paris.   1947.
6. DELLA-CORTE, M. and RAMAT, M.   Nuovo Cimento, 9: 605.   1952.
7. DEMERS, P.   Can. J. Research, A, 25: 223.   1947.
8. DEMERS, P.   Can. J. Research, A, 28: 628.   1950.
9. DEMERS, P.   Can. J. Phys. 31: 78.   1953.
10. DEMERS, P. and MATHIEU, R.   Phys. Rev. 75: 1327.   1949.
11. FRIESEN, S. and KRISTIANSSON, K.   Nature, 66: 686.   1950.
12. FÜRTH, R. and OLIPHANT, W. D.   J. Sci. Instruments, 25: 289.   1948.
13. HALL, C. E. and SCHOEN, A. L.   J. Optical Soc. Am. 31: 281.   1941.
14. KAYAS, G. and MORELLET, O.   Compt. rend. 234: 1359.   1952.
15. KNIPP, J. and TELLER, E.   Phys. Rev. 59: 659.   1941.
16. LAMB, W. E., Jr.   Phys. Rev. 58: 695.   1940.
17. LASSEN, N. O.   Phys. Rev. 70: 577.   1947.
18. MATHIEU, R.   Ann. ACFAS, 16: 44.   1950.
19. MATHIEU, R.   Thèse de doctorat, Faculté des Sciences, Université de Montréal, Montréal.   1951.
20. MEES, C. E. K.   The theory of the photographic process.   4th printing.   The Mac-Millan Company, New York.   1945.
21. SHERR, R. and PETERSON, R.   Rev. Sci. Instruments, 18: 567.   1947.
22. WEST, D.   Can. J. Research, A, 26: 115.   1948.

ON THE CHARACTERISTIC TEMPERATURES OF SINGLE CRYSTALS AND THE DISPERSION OF THE "DEBYE HEAT WAVES"[1]

By E. J. Post[2]

ABSTRACT

A procedure for the calculation of the number of normal modes of a single crystal is proposed which takes an intermediate position between the methods of Debye and Born–von Karman. The method of Debye is extended to an aniso-tropic continuum, where the cutoff and dispersion phenomena, which are due to the lattice structure, are accounted for in a semiempirical way. It appears possible to define a finite number of characteristic temperatures (one for cubic crystals and at most three for crystals of low symmetry) independent of direction. This ensures a comparatively simple calculation from the phenomenological elastic constants of the crystal, as such retaining one of the pleasing features of Debye's theory, i.e., a straightforward correlation between thermal and elastic data.

The method is applied to eight cubic monatomic crystals for which elastic data are available. The results provide some additional evidence to emphasize the significance of the dispersion of the Debye heat waves.

An application to the hexagonal crystals of cadmium and zinc leads to results similar to those obtained by Grüneisen and Goens who produced with these crystals the first experimental evidence of the dispersion phenomenon using the concept of a characteristic temperature dependent on direction.

In the last section the correlation between the elastic constants of single crystals and the corresponding quasi-isotropic materials is discussed and illustrated with data found in the literature. It is shown that the polycrystalline state is more "elastic" (sometimes very considerably) than the single crystal state. The conse-quences of this "boundary layer elasticity" for the calculation of Θ values are discussed.

INTRODUCTION

While this paper is concerned purely with a seminovel theoretical approach, it should be mentioned that Kelly and MacDonald have concurrently been analyz-ing the equally important problem of the reliable and consistent determination of a significant Θ value from experimental data, both calorimetric and electrical (8). The experimental data used in the present paper have simply been abstracted from published texts.

When introducing his theory of specific heat, Debye himself pointed out that it was quite surprising that his simplified procedure for the calculation of charac-teristic temperatures of crystals, using elastic data of the polycrystalline quasi-isotropic material, checked very reasonably with the experimental data obtained by means of specific heat curve-fitting procedures.

The calculation of the number of normal modes as carried out by Debye was based on a very simple picture of the solid as an essentially isotropic continuum. Born and von Karman at about the same time made an attack on the same problem. For the calculation of the number of normal modes, these authors very rigorously took into account the anisotropic as well as the discrete nature of the crystal. However, the interesting and very suggestive correlation between elastic

and thermal data which was one of the very pleasing features of the Debye theory appeared to be very difficult in their theory because of a lack of detailed knowledge about the lattice forces.

Though Försterling (4) and Grüneisen (5), in a rather cumbersome compromise on the Born–von Karman theory, used the phenomenological elastic data of single crystals, it is perhaps surprising that a more direct approach according to the phenomenological theory of crystal physics has never been made. This approach would take an intermediate position between the Debye and Born–von Karman theories in accounting for the anisotropy of the medium in an *exact* way, whereas the requirements due to the discreteness of the medium will be met in a semiempirical way.

In the next section it will be shown that a "diffuse" system of waves in an anisotropic elastic continuum can be replaced by a system of similar waves in an imaginary isotropic medium having at most three discrete propagation velocities. The three "diffuse" velocities yield three characteristic temperatures, if a common cutoff wave length is introduced.

The dispersion phenomenon, which is a consequence of the lattice structure, will be accounted for by multiplying the characteristic temperatures, which are computed on the basis of a continuum theory, by a coefficient $2/\pi$. This procedure was suggested by E. Schrödinger (13) who showed that a *special* dispersion pattern can be perfectly compatible with the concept of a single characteristic temperature. The dispersion coefficient $\alpha = 2/\pi$ should be regarded as representative for the right order of magnitude. The third section gives some experimental material that provides further systematic support for this point of view.

DEFINITION OF CHARACTERISTIC TEMPERATURE FOR ANISOTROPIC MEDIA

The three simultaneous wave equations for elastic waves in a uniform anisotropic body are (see 12, p. 171, equation 7.17)

$$[1] \qquad c^{lksr}\partial_l\partial_s u_r = \rho\ddot{u}^k \quad \left\{ \begin{aligned} \partial_l &= \frac{\partial}{\partial x^l} \\ l, k, s, r &= 1, 2, 3 \end{aligned} \right.$$

in which the bitensor density of elasticity c^{lksr} has the following symmetry properties (which are independent of the symmetry of the medium)

$$[2]^* \qquad c^{lksr} = c^{klsr} = c^{lkrs} = c^{srlk},$$

ρ is the mass density, and u^k and u_k are components of the displacement vector. A rectangular co-ordinate system will be assumed so that the co- and contravariant or mixed components of quantities are equal (e.g. $u^k = u_k$ or $c^{lksr} = c_l{}^{ksr}$).

Substituting a plane wave solution

$$[3] \qquad u_k = p_k\, e^{i(\omega t + k_l x^l)},$$

writing $k_l = |k|\, n_l$ where n_l is the unit vector of the wave front and $|k|$ the wave

---

*For complete commutability of all indices, the Cauchy relations have to be satisfied. This is, however, usually not the case even for monatomic crystals.

number, and using $\omega/|k| = c =$ phase velocity, equation [1] reduces to a set of homogeneous algebraic equations linear in the amplitude of displacement p_k,

$$[4] \qquad\qquad c^{lksr} n_l n_s p_r = \rho c^2 p^k.$$

Equations [4] define a principal axes problem for the tensor density of valency two,

$$[5] \qquad\qquad \Gamma^{kr} = c^{lksr} n_l n_s.$$

The eigenvectors $\underset{1}{p^k}, \underset{2}{p^k}, \underset{3}{p^k}$ and their corresponding eigenvalues $\underset{1}{c}, \underset{2}{c}, \underset{3}{c}$ give the direction of polarization and corresponding phase velocity of the three elastic waves travelling in the direction n_l. Hence Γ^{kr}, which is itself a quadratic function of wave front direction n_l, contains the propagation behavior for this direction n_l.

If one wants to study a "diffuse" superposition of plane wave solutions of the equations [1], the tensor Γ^{kr} should be submitted to an appropriate averaging procedure. According to [5], Γ^{kr} is obtained by "folding" two tensors, c^{lksr} containing the properties of the material and the tensor $n_l n_s$ representing the wave field. Hence only the latter is affected by the averaging procedure. If all wave front directions are equally probable, $n_l n_s$ reduces to diagonal form,

$$[6] \qquad\qquad n_l n_s \rightarrow \tfrac{1}{3}\,\delta_{ls} = \begin{cases} \tfrac{1}{3}, & l = s \\ 0, & l \neq s \end{cases} \text{ or } \overline{n_l n_s} = \tfrac{1}{3}\,\delta_{ls},$$

and for a diffuse system of waves we may define a Γ^{kr} denoted by $\overline{\Gamma}^{kr}$,

$$[7] \qquad\qquad \overline{\Gamma}^{kr} = c^{lksr} \tfrac{1}{3}\,\delta_{ls} = \tfrac{1}{3}\, c_s^{ksr}.$$

Equations [6] and [7] assume equal a priori probability of propagation directions in the medium. This assumption may be acceptable from a point of view of *classical* (i.e. nonquantized) wave propagation in a *continuous* medium, but as soon as quantum effects, and the discontinuous nature of the lattice, are taken into account one may expect deviations in the high frequency region. However, if one cavils at this point, one might just as well question the hybrid nature of the whole theory of specific heats as an inconsistent mixture of classical and non-classical concepts. The assumption just mentioned is simply an additional feature of this hybrid nature, a feature that remains unnoticed as long as the body is regarded as isotropic.

The suggested procedure for the computation of characteristic temperatures is as follows: Using $\overline{\Gamma}^{kr}$ instead of Γ^{kr} in [4] yields a principal axes problem characteristic of diffuse radiation,

$$[8] \qquad\qquad \overline{\Gamma}^{kr} p_r = \rho c^2 p^k.$$

The three eigenvalues $\underset{1}{c}, \underset{2}{c}, \underset{3}{c}$ of [8] are used to define the characteristic temperatures $\underset{\lambda}{\Theta}$,

$$[9] \qquad\qquad \underset{\lambda}{\Theta} = \frac{2}{\pi}\, \frac{h}{k}\, \underset{\lambda}{c} \left(\frac{3N}{4\pi V}\right)^{\frac{1}{3}}, \quad \lambda = 1,\,2,\,3$$

where h, k, and N are the constants of Planck, Boltzmann, and Avogadro and V

is the specific volume of a gram atom; the coefficient $2/\pi$ is supposed to account for the dispersion (13).

For computational purposes Γ^{kr} may be expressed in the elastic constants according to the notation of W. Voigt (12, p. 160)

$$\Gamma^{11} = \tfrac{1}{3}(c_{11} + c_{66} + c_{55}), \quad \Gamma^{12} = \Gamma^{21} = \tfrac{1}{3}(c_{16} + c_{26} + c_{45}),$$

$$[10] \quad \Gamma^{22} = \tfrac{1}{3}(c_{66} + c_{22} + c_{44}), \quad \Gamma^{13} = \Gamma^{31} = \tfrac{1}{3}(c_{15} + c_{46} + c_{35}),$$

$$\Gamma^{33} = \tfrac{1}{3}(c_{55} + c_{44} + c_{33}), \quad \Gamma^{23} = \Gamma^{32} = \tfrac{1}{3}(c_{56} + c_{24} + c_{34}).$$

For cubic crystals the three roots of the secular equation of [8] are identical, yielding one characteristic temperature only. For trigonal, hexagonal, and tetragonal crystals there are two distinct Θ_λ, and for orthorhombic, monoclinic, and triclinic crystals three distinct Θ_λ.

CORRELATION OF EXPERIMENTAL AND THEORETICAL DATA

A comparison of experimental and theoretical characteristic temperatures computed on the basis of formulae [10], [8], [9] has been made for eight monatomic cubic crystals: diamond, aluminum, gold, copper, silver, tungsten, sodium, and iron. For this type of crystal there is only one characteristic temperature $(\Theta_1 = \Theta_2 = \Theta_3)$. For convenience a table containing elastic and other data for room temperature needed for the calculation is included.

TABLE I

Elastic constants	C (diamond)	Al	Au	Cu		Ag	W	Na	Fe	
$C_{11},10^{10}$ dynes/cm.^{2}	950	108.24	107	186	169	120	512.6	9.5	233	236.9
$C_{12},10^{10}$ dynes/cm.^{2}	390	62.16	157	135	121.5	89.7	205.8	8.0	139.2	140.6
$C_{44},10^{10}$ dynes/cm.^{2}	430	28.41	43.6	82	74	43.6	152.7	5.9	116.2	116.0
References	(1)	(10)*	(11)	(14)	†	(11)	(10)*	(14)	†	(10)*
V	3.4119	9.667	10.445	7.1163		10.282	9.835	23.68	7.115	
ρ	3.52	2.79	18.88	8.933		10.492	18.70	0.9712	7.85	

*Calculated from S_{ik} constants.
†Kindly supplied by Dr. G. Bradfield, National Physical Laboratory, Teddington, England.

The calculated and observed values are collected in Table II. The empirical dispersion coefficient α in Table II is defined by the formula

$$\alpha = \frac{\Theta_{\text{observed}}}{\dfrac{hc}{k}\left(\dfrac{3N}{4\pi V}\right)^{\frac{1}{3}}} = \frac{2}{\pi}\frac{\Theta_{\text{observed}}}{\Theta_{\text{calculated}}}.$$

TABLE II

	C	Al	Au	Cu	Ag	W	Na	Fe
$\Theta_{\text{calculated}}$	1395	334	162	301	189	286	151	370
Θ_{observed}*	1860	390	170	315	215	310	150	420
α, dispersion coefficient	0.849	0.742	0.670	0.666	0.723	0.691	0.632	0.722

*(14). For a discussion of experimental values see (7) and (8).

Sodium is very close to the *special theoretical* value $2/\pi = 0.637$ and diamond shows the greatest deviation.

For hexagonal zinc and cadmium and trigonal mercury one obtains the following table ($\Theta_1 = \Theta_2 \neq \Theta_3$).

TABLE III

	$\Theta_1 = \Theta_2$	Θ_3	Θ_m	Θ Observed*
Zn	268.3	192.8	231.1	250
Cd	177.7	125.8	151.8	172
Hg	73.4	88.5	76.0	96

*(14). For a discussion of experimental values see (7) and (8).

The data needed for the calculation of Θ_λ are found in Table IV.

TABLE IV

	Zn(20°C.)	Cd(20°C.)	Hg(−190°C.)
$C_{11} = C_{22}$, 10^{10} dynes/cm.²	161.0	121.0	36.0
$C_{23} = C_{13}$ "	43.7	44.2	30.3
C_{33} "	54.2	51.3	50.5
C_{12} "	43.2	48.1	28.9
$C_{44} = C_{55}$ "	40	18.5	12.9
C_{66} "	58.9	36.5	3.56
References	(5)	(5)	(6)
ρ	6.920	8.648	14.469
V	9.448	12.998	13.865

Θ_m in Table III is calculated according to the formula

[11]
$$\frac{3}{\Theta_m^3} = \frac{1}{\Theta_1^3} + \frac{1}{\Theta_2^3} + \frac{1}{\Theta_3^3}$$

in order to have a single theoretical value of Θ that may reasonably be compared with those single values of Θ obtained by fitting experimental specific heat data to the T^3 law.

Similar to other theories, introducing more than one theoretical Θ_λ value, the thermodynamic functions are obtained by a superposition of the appropriate Debye expressions. The difference may be hardly noticeable with a single Debye curve, unless for excessive ratios of Θ. Therefore, from an experimental point of view it seems hard to decide in favor of one of the systems involving multiple Θ_λ values. Moreover, the theoretical features may be already beyond comparison.

Apart from Born's theory which has a threefold continuum of Θ_λ values and the present theory which has essentially three Θ_λ values, which may coincide depending on the symmetry properties of the crystal, multiple Θ values have been introduced even for isotropic solids. Brillouin (2) proposed two Θ values corresponding to different cutoff frequencies of transverse and longitudinal waves and Cornish and MacDonald (3) use multiple Θ values that correspond to a frequency wave number relationship made up of discontinuous linear portions. The last theory in essence deals with rather marked dispersion properties; the present theory on the other hand stresses the directional properties of wave propagation, whereas the dispersion is accounted for in a simplified way, such that the number of Θ_λ values is unaffected.

CONCLUSION

For the present any correlation between computed and observed characteristic temperatures is bound to be affected by the unsatisfactory state of the theory. Until now the detailed distribution of the number of vibrational modes as a function of frequency has been computed for a few crystals only and the individual results obtained do not suggest the existence of really constant characteristic temperatures. Whether the concept of characteristic temperature is just a crude but sometimes very useful computational quantity or whether it still has some deeper roots in fundamental theory is beyond the scope of this study.

The material presented shows that there is an alternative way of defining characteristic temperatures for crystals along the lines of a hybrid theory. This definition has important computational advantages and the results obtained by its application appear to support the dispersion hypothesis rather more systematically than the results already obtained by Grüneisen, Goens, and Hoyer (5, 6).

One part of the differences between the procedures of computing characteristic temperatures is due to the method of averaging propagation velocities, whereas another part has a very natural cause, i.e., the elastic moduli of single crystals tend to be higher than the moduli for the corresponding isotropic polycrystalline material. Apparently the boundary layers between the microcrystals are a source of additional elasticity.

The invariants of the elastic bitensors for the single and the polycrystalline states provide the only fair basis of comparison to check this point and Table V gives some data which seem to favor this point of view for the invariant that is most representative for the properties of wave propagation (see appendix).

TABLE V

(In 10^{10} dynes per cm.^{2})

	Al	Au	Cu	Ag	Fe	Cd
$1/3\ I_1$ single crystal	165.1	274.2	350.0	207.2	465.4	146.8
$1/3\ I_1$ polycrystalline	162.1	259.2	285.0	204.3	437.6	105.5

The figures for the isotropic material are derived from data of E and k given in Landolt-Börnstein (9).

Looking at the data for cadmium it is not surprising why this was one of the first materials that added evidence to the dispersion phenomenon. Unfortunately no consistent data for the contraction modulus k of zinc were available.

The use of single crystal data eliminates erratic and unpredictable boundary layer effects when correlating physical properties of the solid state. Table V shows that it is even important to have single crystal data available for scalar properties and the specific heat may be no exception. It is not impossible that accurate specific heat data on single crystals may help to reduce the concept of characteristic temperatures to more tangible proportions.

It should perhaps be emphasized that the so-called "ideal isotropic solid", beloved of many textbook writers, has no place in the present analysis which attempts to deal with real discrete crystals. In particular, it is a specific consequence of the present theory that a cubic crystal, if we ignore violent dispersion, will be characterized thermally by a single characteristic temperature and that there is no place for a decomposition of the heat motion into longitudinal and transverse waves. It has to be understood, unpleasant as it may be for other solid state phenomena like electrical conductivity, that a distinction between longitudinal and transverse waves is fictitious for a system of diffuse waves in a real single crystal.

ACKNOWLEDGMENTS

APPENDIX

The invariants of the elastic bitensor for the general anisotropic case are:

$$I_1 = c^{is}{}_{is} = 3\bar{\Gamma}^s{}_s = (c_{11} + c_{22} + c_{33}) + 2(c_{44} + c_{55} + c_{66}),$$

$$I_2 = c^i{}_i{}^s{}_s = (c_{11} + c_{22} + c_{33}) + 2(c_{12} + c_{13} + c_{23}).$$

For the isotropic case expressed in Young's modulus E and the Poisson contraction ratio k or the Lamé constants λ and μ they are:

$$I_1 = 3E\frac{2 - 3k}{(1 + k)(1 - 2k)} = 3(\lambda + 4\mu), \quad I_2 = \frac{3E}{1 - 2k} = 3(2\mu + 3\lambda).$$

$I_2/9$ is known as the bulk modulus of the material.

I_1, which contains dilatational and shear constants (c_{11}, c_{44}, etc.), is more representative for the properties of wave propagation.

REFERENCES

1. BHAGAVANTAM, S. and BHIRMASENACHAR, J.   Proc. Roy. Soc. (London), A, 187: 381. 1946.
2. BRILLOUIN, L. Wave propagation in periodic structure. McGraw-Hill Book Company, Inc., New York and London. 1946. p. 163.
3. CORNISH, F. H. J. and MACDONALD, D. K. C.   Phil. Mag. 42: 1406. 1951.
4. FÖRSTERLING, K.   Ann. Physik, 61(4): 549. 1920.
5. GRÜNEISEN, E. and GOENS, E.   Z. Physik, 26: 235, 250. 1924.
6. GRÜNEISEN, E. and HOYER, H.   Ann. Physik, 22: 668. 1935.
7. KELLY, F. M. and MACDONALD, D. K. C.   Bull. Am. Phys. Soc. 27(3): 34. 1952.
8. KELLY, F. M. and MACDONALD, D. F C.   Can. J. Phys. 31: 147.   1953.
9. LANDOLT-BÖRNSTEIN. Physikalisch-chemische Tabellen, erster Ergänzungsband. Springer, Berlin. 1927. p. 13.
10. LANDOLT-BÖRNSTEIN. Physikalisch-chemische Tabellen, dritter Ergänzungsband, I. Springer, Berlin. 1935. p. 74.
11. RÖHL, H.   Ann. Physik, 16: 887. 1933.
12. SCHOUTEN, J. A.   Tensor analysis for physicists. Oxford. 1951.
13. SCHRÖDINGER, E.   Handbuch der Physik X. Springer, Berlin. 1926. p. 311.
14. SEITZ, F.   The modern theory of solids. McGraw-Hill Book Company, Inc., New York and London. 1940. p. 377.

A STUDY OF WINDS IN THE IONOSPHERE BY RADIO METHODS[1]

By John H. Chapman[2]

ABSTRACT

Winds in the ionosphere have been studied by a method described by S. N. Mitra using the fading of radio echoes at spaced receivers. A mean daily wind variation of nearly semidiurnal period and about 40 meters per second amplitude has been observed at a nominal height of 110 km. (Region E). The wind variation is consistent with the explanation that it is due to tidal oscillations of the atmosphere. A wind variation consistent with that expected from lunar atmospheric tides has also been detected at this level.

The winds in the F region appear to increase in velocity with an increase of magnetic activity. A similar effect is not observed in the E region except during severe ionospheric disturbances.

I. INTRODUCTION

A radio method of measuring winds in the ionosphere described by S. N. Mitra (8) has been used over a period of a year. Records of the time variations (fading) were made at three receivers, spaced about 100 meters apart at the corners of a right-angled triangle. The fading at any two receivers was observed to be similar, but displaced in time. This displacement was assumed to be the result of the movement of a diffraction pattern across the ground, caused by a corresponding horizontal movement of irregularities in the ionosphere (9, 3, 4). Experimental observations have supported the assumption that an effect due to winds in the ionosphere was measured.

II. EXPERIMENTAL TECHNIQUES

The technique developed by Mitra (8) has been used with little variation. A conventional pulse transmitter on a frequency between 2 and 6 Mc. was situated in the central recording station. Three receiving antennas (tuned loops) were placed at the corners of a right-angled triangle (Fig. 1). Preamplifiers at the base of each loop fed signals to the receivers via coaxial cable. The echo was selected for recording by a gate which brightened the recorder C.R.T. The variation of amplitude of the echo with time was recorded on photographic paper which moved continuously through the camera at a speed of about one foot per minute for four minutes at a time. Fiducial marks were placed on the record by removing the brightening pulse at one second intervals.

The mean time shift between receivers was determined by comparing the times of corresponding maxima and minima on the fading records. The possibility of obtaining erroneous results by neglect of the random fading as opposed to drift fading was minimized by analyzing only those records in which there was a high

degree of similarity in fading between receivers (4). The drift velocity was calculated using the formula given by Mitra (8). The measurements in this paper are referred to the ionosphere in which the drift velocity is one half that on the ground.
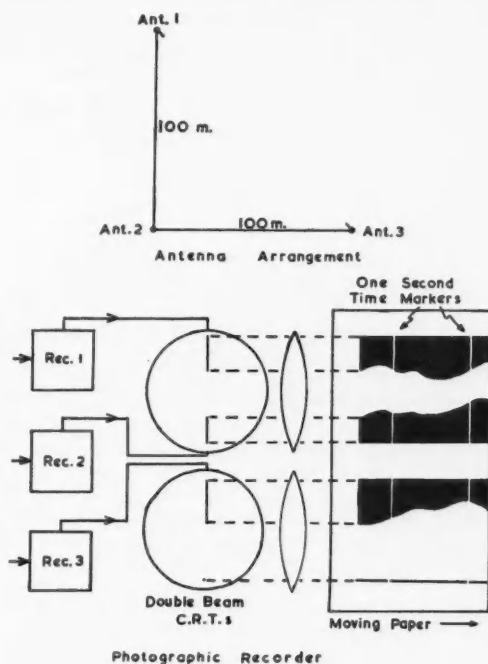

FIG. 1. Receiving antennas and recorder.

Effects due to interference between the two magnetoionic modes were minimized by the use of a transmitting antenna which radiated nearly circularly-polarized waves in the mode least attenuated at the time of observation. During daylight hours, recording was done on a frequency below 3 Mc., when the extraordinary mode was highly attenuated except near the critical frequency.

III. WIND MEASUREMENTS

The program of recording was begun in June, 1950, in Ottawa, and carried on after November, 1950, in Montreal. The program in Montreal was terminated in June 1951. Observations were made continuously for three days each month and occasionally for longer periods. About 500 wind measurements were made, roughly equally divided between E and F region observations.

The histograms showing the wind velocities in the E and F regions are given in Figs. 2 and 3. The mode is about 80 meters per sec. in the case of the E region,
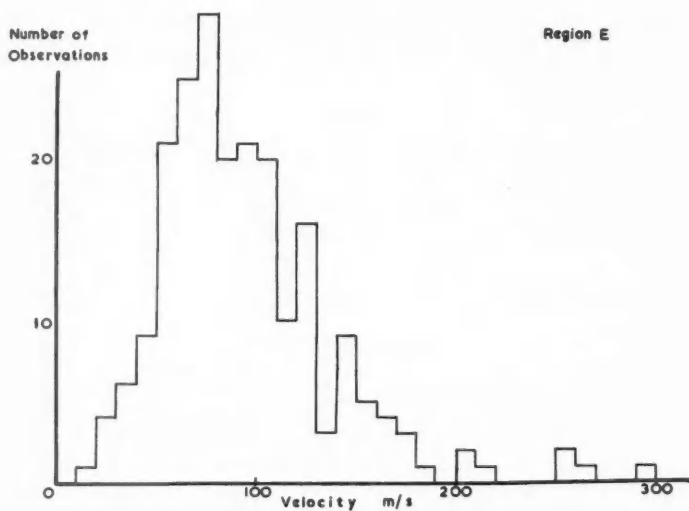
FIG. 2. Histogram of wind velocities in the *E* region.
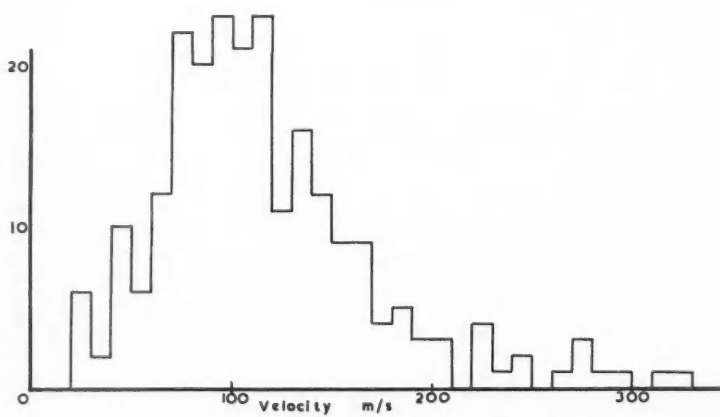
FIG. 3. Histogram of wind velocities in the *F* region.

and 100 meters per sec. in the case of the F. This does not necessarily represent a real difference in the mean wind velocities, since the E region observations are almost entirely restricted to daylight hours.

In Fig. 4 are shown measurements of the wind components from region E for a typical day. The abscissa shows local time of observation, the ordinate the wind
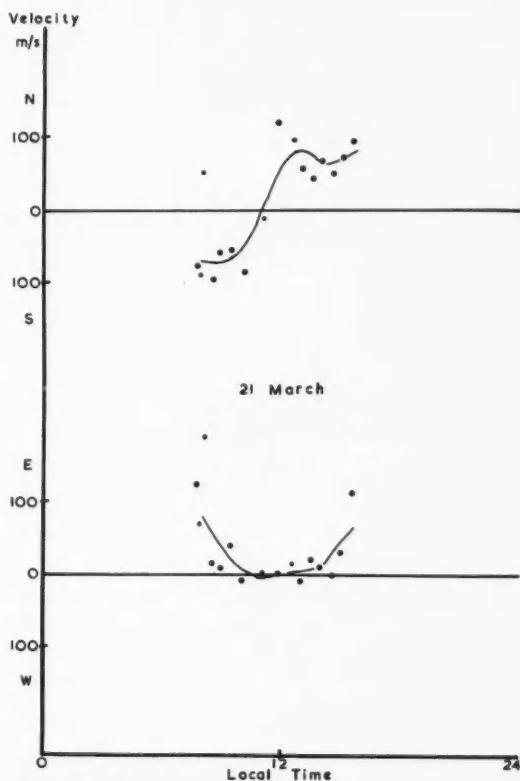
FIG. 4. Wind components, region E, March 21, 1951.

component towards the north or towards the east. A subjective weight is indicated by the size of dot; the large dot representing a more reliable measurement. Such factors as speed and depth of fading, consistency of time shift, and presence of interference affect the relative reliability. The scatter diagram in Fig. 5 shows the wind components for all the observations on region E echoes plotted as a function of time of observation.
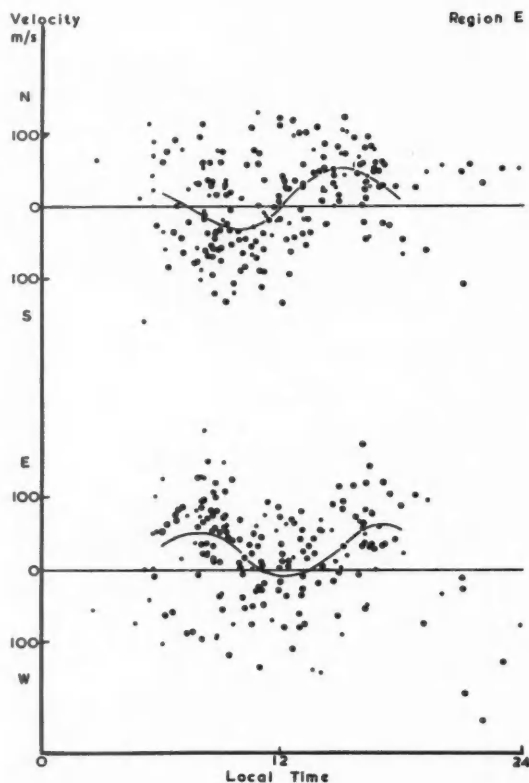
FIG. 5. Scatter diagram of wind components, region E.

The solid line in Fig. 5 was obtained by drawing a smooth curve through the points representing the mean hourly wind components, as shown in Fig. 6. These curves represent a mean daily variation of the wind in region E, and can be recognized in the observations of Fig. 4 for a specific day. The amplitude of the variation is about 40 meters per sec. and is of predominantly 12 hr. period. A periodic variation of 24 hr. period is probably present but cannot be identified because the information is not complete for 24 hr.

No regular diurnal variation has been detected so far in the F region wind measurements. It is uncertain whether this is due to insufficient observations or a real absence of diurnal variations.
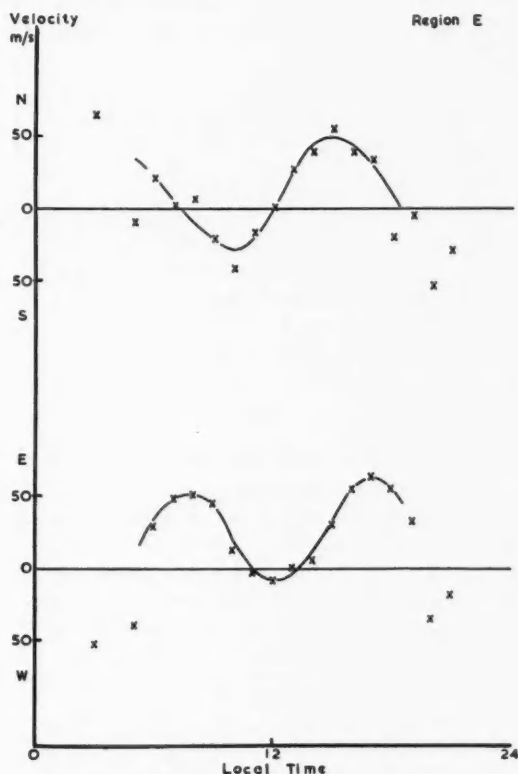
FIG. 6. Hourly averages of wind components, region E.

IV. PERIODIC WIND VARIATIONS

(i) Statistical Tests—Solar

The data of Figs. 5 and 6 have been subjected to statistical tests to determine the significance of the periodic variations. The methods of analysis of variance due to Fisher (6) and of the harmonic dial due to Bartels (2) have been applied to the data. The use of these methods has been described by Appleton and Weekes (1) in connection with the study of the lunar periodic variation of height of the E layer. The variance of the observations about the hourly means was so much less than the variance of the hourly means about the general mean that the probability that the difference could have occurred by chance was less than 10^{-3}. The semidiurnal harmonics of the wind components could have occurred by chance in the data less than once in 10^4 times. The harmonic dial test indicated a

probable error of about half the amplitude of the mean wind harmonic (see Appendix). These tests were applied to the wind components separately, and indicated that significant semidiurnal variations were present. The semidiurnal harmonic components were:

[1]   Northward wind (m./sec.) $34 \sin (2t - 10°)$,
[2]   Eastward wind (m./sec.) $23 \sin (2t - 87°)$

where t is the local solar hour angle.

(ii) Statistical Tests—Lunar

The data were also related to lunar time, and the same procedure applied to determine whether there was a lunar effect present. The solar effect was removed first by subtracting from the wind components for each observation the relevant solar wind components at that time, as determined from Fig. 6.

The mean values of the wind components for each lunar hour were then computed, and the statistical tests applied. An effect dependent upon lunar time was present; the probability of obtaining by chance the difference in variance of the observations about the hourly means compared to that of the hourly means about the general mean lay between 1% and 5%. The probability of obtaining the calculated semidiurnal components by chance from the data was less than 10^{-4}. A further test indicated that other harmonics were below the level of significance. The harmonic dial test showed a probable error again about one half the amplitude of the mean semidiurnal wind harmonic.

The data of Fig. 7 have been referred to 12 lunar hours to increase the reliability of the hourly means. This step was justified since statistical tests show that harmonics other than the 12 hr. harmonic were insignificant. The semidiurnal harmonics of the wind components calculated from this data were:

[3]   Northward wind (m./sec.) $24 \sin (2\tau + 3°)$,
[4]   Eastward wind (m./sec.) $21 \sin (2\tau - 106°)$

where τ is the local lunar hour angle.

(iii) Winds from Semidiurnal Pressure Variations

Two significant features of each pair of wind harmonics solar and lunar are evident. The amplitudes of the wind components towards the north and towards the east are of comparable magnitude, and the northward wind is approximately in phase quadrature leading the eastward wind.

The horizontal air motions to be expected from a periodic pressure variation can be calculated (7, 11). The northward and eastward components of air velocity (at 45°N. latitude) are comparable in amplitude and in phase quadrature with the northward component leading. These conditions are met within the limits of experimental error for both the solar and lunar wind components. The observations are consistent with the postulate that tidal oscillations of the earth's atmosphere, both solar and lunar, are at least partially responsible for the winds in the E region. Conversely, these observations support the view that this aspect of fading of radio echoes has been correctly interpreted. These observations have since been confirmed by Phillips (10).
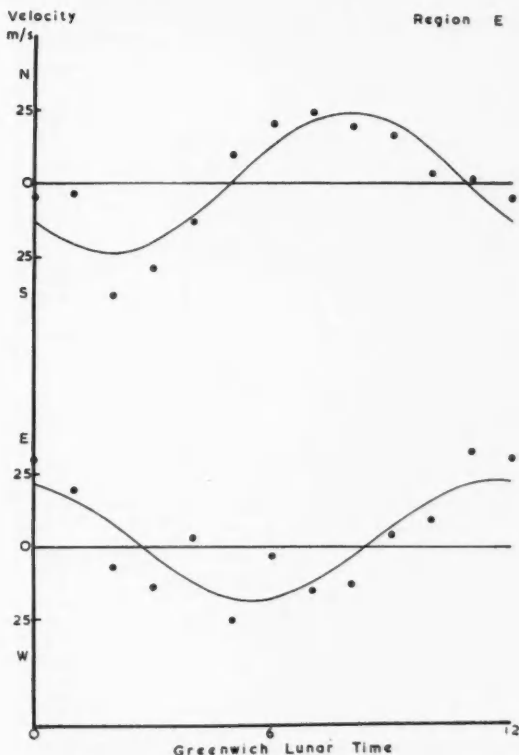
FIG. 7. Hourly means of wind components and lunar semidiurnal harmonics.

V. WINDS AND IONOSPHERIC STORMS

A positive correlation between wind velocity and ionospheric disturbance has been observed, the velocity increasing during storm periods. The K-index of magnetic activity has been used as a continuous measure of ionospheric storminess because of the absence of an alternative index based on ionospheric data. The K-indices from the Dominion Observatory station at Agincourt, Canada, have been employed.

The result of plotting the mean wind velocity against the K-index at the time of observation is shown in Fig. 8 for region E, and in Fig. 9 for region F. The standard deviation of the mean is shown by horizontal bars. Both axes are logarithmic, and the range of variation of the magnetic elements, in gammas, is shown on the ordinate axes along with the K-index.

The graph of Fig. 8 for region E shows that the mean wind velocity is sensibly independent of K-index until K exceeds four. This probably accounts for the success in the search for winds due to tidal pressure oscillations in the E layer.
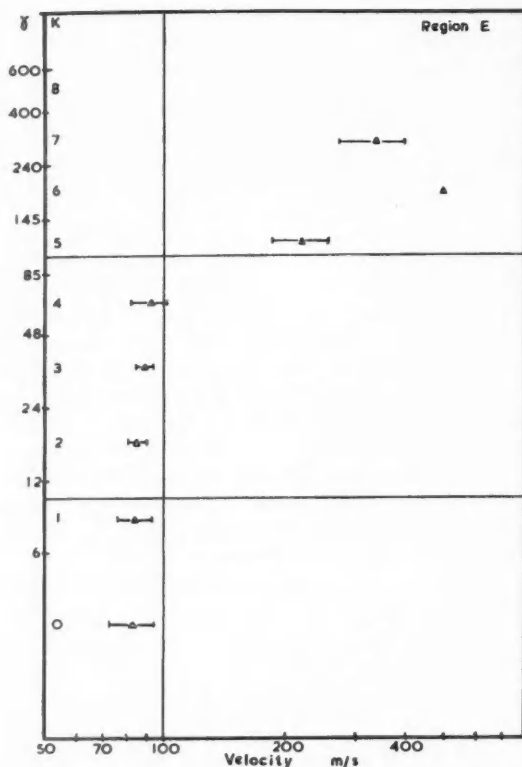
FIG. 8. Mean wind velocity against K-index, region E.

When the K-index was five or greater, higher absorption commonly made echoes too weak for recording. Occasionally echoes from sporadic E were obtained and recorded. Winds from these records almost invariably indicated a very high drift velocity. Only nine observations were obtained during disturbed conditions. Hence the mean wind velocities calculated for the higher K values are relatively unreliable, though the data indicate a rapid increase of velocity during very disturbed times. These nine observations were omitted from the calculations of the periodic variations of the winds.

On the other hand, Fig. 9 for the F region shows that the mean wind velocity increases regularly with an increase of K-index. The coefficient of correlation is 0.4, a significant correlation for the data tested. This is interpreted as showing that cause of winds in the F region is related to the cause of ionospheric disturbances, and that tidal effects, if present, are masked.
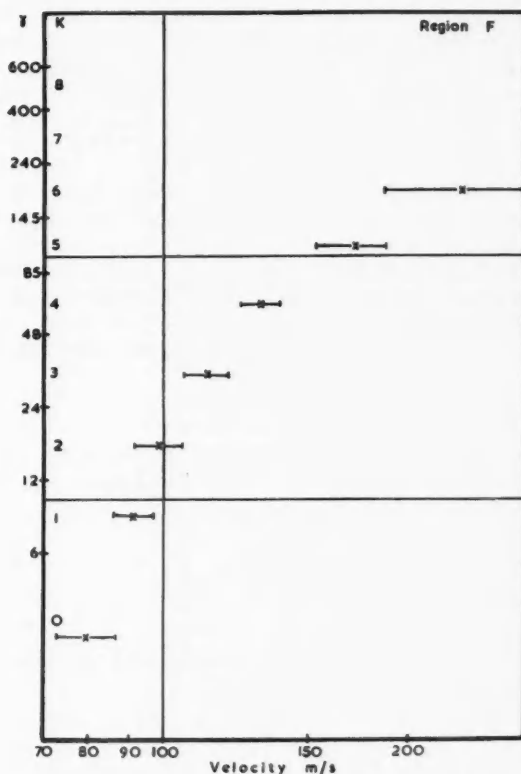
FIG. 9. Mean wind velocity against K-index, region F.

VI. CONCLUSIONS

The result of this study indicates that variations in the drift of the diffraction pattern on the ground from a radio wave in the ionosphere are consistent with the assumption of a drifting ionosphere. This conclusion is based on the detection of semidiurnal wind variations of about 25 meters per sec. amplitude which are expected from solar and lunar pressure oscillations in the E region. The mean wind velocity in the E region is independent of magnetic activity and ionospheric disturbance at least until the K-index exceeds four.

The tidal variations have not yet been detected in the F region, perhaps because of lack of sufficient data. As a consequence, the confirmation of the interpretation of fading as due to drift in the ionosphere has not been obtained for the F region. If the data do refer to winds at this level, it has been shown that the mean wind velocity increases with an increase of magnetic activity.

The measurements described have been referred to one of the main ionospheric layers, E or F. The method of measurement has not indicated the height at which a wind is purported to have been measured, and the method is at present incapable of yielding this information. The level must however be below the level of reflection.

ACKNOWLEDGMENTS

APPENDIX

Methods of Statistical Analysis

The methods which follow have been described by Fisher (6). The final calculations of variance for the solar and lunar variations are shown in Table I where the symbols have the same meaning as Fisher's.

TABLE I

CALCULATIONS OF VARIANCE

	Solar components		Lunar components	
	Northward	Eastward	Northward	Eastward
Variance at each hour	3056	3332	2753	2809
Variance of $\bar{y}_p$ from $\bar{y}$	13,879	12,366	5879	5909
z for difference between variances	.757	.656	.380	.372
0.1% value of z	.541	.541		
5% value of z			.299	.299

The probability of obtaining a value of z by chance 0.1% or 5% of the time is determined from Fisher's Table V for the appropriate value of n (6). Comparison shows that the hourly means are removed from the general mean by such an amount as could have occurred by chance in less than 0.1% of the time in the solar case, and less than 5% in the lunar case. Since Fisher arbitrarily assumes that the 5% figure represents a significant difference in variance, both sets of data show a significant effect dependent upon the time of observation.

The coefficient of correlation r of the data with the Fourier harmonic can be determined from a formula given by Chapman and Bartels (5). The probability of obtaining this coefficient can be determined from the value of the z transformation and its standard deviation σ, as shown in Table II.

The probability of obtaining by chance a value of the ratio of z to its standard deviation of 3.74 is 1 in 10,000, and the ratios shown all exceed this figure. It is concluded that the periodic variations in all the data are significant.

TABLE II

CALCULATIONS OF CORRELATION COEFFICIENT

	Solar components		Lunar components	
	Northward	Eastward	Northward	Eastward
r	.397	.259	.309	.268
z	.420	.268	.318	.275
z/σ	5.90	3.81	4.44	3.84

The harmonic dial test has been described by Bartels (2). The co-ordinates of the mean amplitude vector are X_0 and Y_0. The probable error circle has a radius R such that half the points observed fall inside the probable error circle and half outside. The results are shown in Table III.

TABLE III

CALCULATIONS FOR HARMONIC DIALS

	Solar components, m./sec.		Lunar components, m./sec.	
	Northward	Eastward	Northward	Eastward
X_0	+ 33.5	+ 5.2	− 22.0	− 3.8
Y_0	− 3.8	− 21.2	− 13.5	+ 19.5
R	20.2	8.4	13.7	11.6
$\sqrt{X_0^2 + Y_0^2}$	35.5	21.8	25.8	19.8

The radius R of the probable error circle is about half the mean amplitude vector, indicating that the harmonics are significant and persist over the period of observation.

REFERENCES

1. APPLETON, E. V. and WEEKES, K.   Proc. Roy. Soc. (London), A, 171: 171. 1939.
2. BARTELS, J.   Terr. Magn. Atmos. Elect. 37: 291. 1932.
3. BOOKER, H. G., RATCLIFFE, J. A., and SHINN, D. H.   Trans. Roy. Soc. (London), A, 242: 579. 1950.
4. BRIGGS, B. H., PHILLIPS, G. J., and SHINN, D. H.   Proc. Phys. Soc. (London), B, 63: 106. 1950.
5. CHAPMAN, S. and BARTELS, J.   Geomagnetism. Vol. 2. Oxford University Press, London. 1940. p. 558.
6. FISHER, R. A.   Statistical methods for research workers. Oliver and Boyd, Ltd., London. 1936. para. 35, 39, 40, 41, 44.
7. MITRA, S. K.   The upper atmosphere. Royal Asiatic Society of Bengal, Calcutta. 1948. p. 35.
8. MITRA, S. N.   Proc. Inst. Elec. Engrs. III, 43: 441. 1949.
9. PAWSEY, J. L.   Proc. Cambridge Phil. Soc. 31: 125. 1935.
10. PHILLIPS, G. J.   J. Atmos. Terr. Physics, 2: 141. 1952.
11. WILKES, M. V.   Oscillations of the earth's atmosphere. Cambridge University Press, London. 1949.

132

THE PREPARATION OF SINGLE CRYSTALS AND BICRYSTALS BY THE CONTROLLED SOLIDIFICATION OF MOLTEN METALS[1]

By Bruce Chalmers

ABSTRACT

An account is given of the methods that have been developed for the production of single crystals and bicrystals of a wide variety of metals by controlled freezing of the molten metal in a horizontal "boat". Orientations are controlled by a "seeding" technique. A detailed qualitative analysis is given of the factors associated with the presence of "stray" crystals. Their formation is discussed in terms of nucleation and in terms of their subsequent survival, and attention is drawn to the significance of purity, of speed of growth. and of the temperature gradient in the liquid.

1. INTRODUCTION

Systematic study of the fundamental properties of metals, such as elasticity, plastic deformation, and electrical resistance, has been greatly accelerated by the use of metallic specimens consisting of one crystal or grain only; similarly the study of the properties, behavior, and effects of the boundaries between crystals has been facilitated by the availability of specimens consisting of two crystals with their mutual boundary. Such researches are even more fruitful if the specimens are crystals in which the crystallographic orientations are determined by the experimenter and not by chance. The purpose of this paper is to describe and to discuss a technique that is being applied to a wide variety of metals, namely nickel, copper, gold, silver, aluminum, zinc, lead, tin, indium, and to certain alloys by the author's co-workers, to whom he is indebted for a great deal of detailed information.

2. THE TECHNIQUE

(a) General

The method under discussion, which has been described previously in relation to certain particular examples (2), is to allow the metal to freeze so that it takes up the crystallographic orientation of the "seed", which is a previously prepared crystal of known orientation. The initial "seed" is prepared by melting the metal in a "boat" of the kind illustrated in Fig. 1. The boat is usually made of graphite,
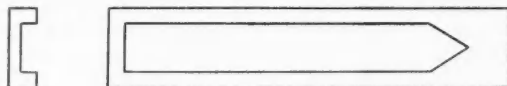

FIG. 1. Boat used for single crystals.

although alundum has been used for nickel (4). The method of heating depends on the metal that is being used, and on whether it is necessary to provide a controlled atmosphere in order to avoid excessive oxidation. Table I shows the boat

material, type of furnace, and atmosphere that have been found to be satisfactory.

TABLE I

Metal	Boat	Furnace			Atmosphere	Speed, mm./min.
Indium	Graphite	Tubular wire wound			Air	10
Tin	{ Graphite { Plaster of Paris	"	"	"	Air	1–25
Lead	Graphite	"	"	"	Air	1–20
Zinc	"	"	"	"	Air, N₂	5
Al	"	"	"	"	N₂, argon	10
Silver	"	"	"	"	Air, N₂	1–10
Gold	"	"	"	"	Air, N₂	1–10
Copper	"	H.F. (indirect)			N₂, vac., argon	5
Nickel	Alundum	Graphite resistor			Argon	2

Provision must be made for the molten metal to cool first at the pointed end, and for cooling to be progressive along the length of the specimen.

For this purpose, a temperature gradient is required; this may be provided by heating at or near one end of the boat and either cooling the other end or allowing it to cool by convection and radiation. The significance of the temperature gradient is discussed below. Movement of the interface between solid and liquid can be produced either by moving the furnace or by reducing the heating current; both methods have been used.

(b) *The Initial Seed*

In order to produce the initial seed for a given metal, it is often desirable to cause freezing to initiate at a single point. For this purpose, a "heat wick" (4) may be used. This consists of a water cooled copper tube to the end of which is attached a small silica or graphite tip. This is placed in contact with the end of the molten metal in the boat and greatly increases the probability of obtaining a single crystal. When a single crystal has been obtained, its orientation is determined, generally by taking a Laue Back Reflection X-ray photograph (using a tungsten target and 3 cm. specimen film distance) and plotting the points as a stereographic projection. This is facilitated by the use of a Greninger net (5) for measuring the positions of the spots on the film.

(c) *Seeding Technique*

The single crystal so obtained can now be used as a "seed" for the production of more single crystals; it is inserted in a suitable boat, the rest of the boat being
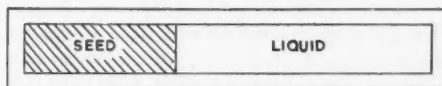

FIG. 2. Seeding technique.

filled with the liquid metal (Fig. 2); temperatures are adjusted so that part of the "seed" is melted, and then the liquid is allowed to freeze progressively from the seed; the new crystalline material will have the same orientation as the seed

unless new crystals have been nucleated. The conditions governing the nucleation of new crystals are discussed below. In some cases, it is necessary to rupture the oxide film which may separate the seed from the molten metal; this is important as failure to do so can either cause the seed to be inoperative (if none of the seed is melted and the film persists) or it can lead to melting of the whole of the seed by the following sequence of events. The molten metal is heated from the hot end of the boat, and the temperature distribution will normally be as shown in Fig. 3a, where X is the distance from the cold end of the boat, and I is the position of the solid–liquid interface. If the oxide film exists, the temperature distribution will instead be of the shape shown in Fig. 3b; if the thermally resistant film now breaks down, which tends to happen at higher temperatures, a considerable length of the seed will be melted very rapidly. If the seed is short, it may be lost completely.
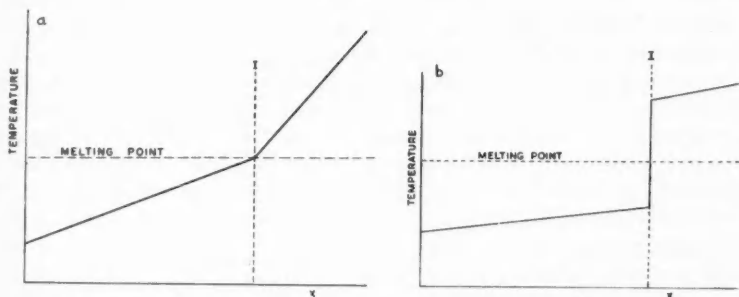
FIG. 3.   Effect of thermal barrier at the interface: (a) no discontinuity, (b) oxide film.

This can be avoided in several ways. The seed may be welded on to the metal in the boat before it is melted; a local source of heat can be used. A second method is to apply extra heat (by means of a small flame) to the region concerned while melting is taking place. The third method is to remove the film by mechanical scraping, for which a glass fiber can often be used. It is usually only necessary to remove the film in one small region for the desired result to be achieved.

(d) Control of Orientation

In general, the orientation of the single crystal first obtained will not be that which is finally required; however, the adjustment of orientation is easily achieved by inserting the seed into the boat at the appropriate angle. The seed may be inclined to the axis of the boat in either a vertical or a horizontal plane (Fig. 4a and b respectively). Movable barriers of graphite, or other boat material, may be used to confine the liquid metal to the required region of the boat. It is found that the maximum change of orientation that can be safely attempted in one stage is about 20°; several successive stages can, however, be used to provide any required change. While any orientation can be obtained by these methods,

it is found that some orientations have a much higher probability of failure by the nucleation of stray crystals than others; this is discussed in Section 3 below.
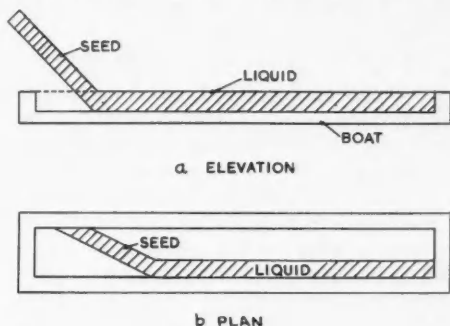

a. ELEVATION

b PLAN

FIG. 4.   Seeding with change of orientation.

(e) *Speed of Growth*

For some purposes, it is desirable to know the speed of advance of the solid–liquid interface — i.e., the speed of freezing. This can be achieved readily by slightly disturbing the liquid metal-at regular intervals of, for example, one minute. Each time this is done, a ripple runs along the surface of the liquid and a slight ridge is formed where the ripple reaches the solid–liquid interface; the distance between neighboring ripples gives the speed of growth. It should be pointed out that, when a moving furnace is used, the speed of advance of the interface does not necessarily equal the speed of movement of the furnace, because the distance from the interface I (Fig. 5) from the end F of the furnace depends on the heat transfer from the furnace to the boat and the liquid metal and on the heat loss by boat and metal to the left of I.
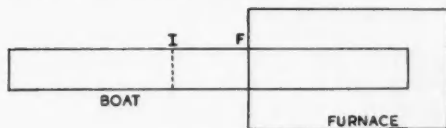
FIG. 5.   Relative positions of boat, interface, and furnace.

These two quantities of heat depend upon the position of the furnace in relation to the ends of the boat. Column 5 of Table I gives an indication of the speeds of growth that have been found to be satisfactory under the conditions used. The cross section of the specimen has usually been: width 1–3 cm., depth 0.3–1.0 cm., length of boat 15–30 cm., thickness of boat (when of graphite) 2–5 mm.

(f) *Condition of the Surface*

For some experimental purposes, the condition of the surface is important; in two major respects the surface may depend on the technique that is used. The

chemistry of the surface may depend on the substance in contact with which the metal is allowed to solidify, and it may also depend on the length of time that the metal has been exposed to that atmosphere. Secondly, the geometry of the surface will depend on the geometry of the boat, on the extent to which the free surface is affected by vibration, and on the effect of surface tension.

It is obviously necessary to use a boat material or lining that does not react with the metal that is being used; it is also necessary to use a vacuum or an atmosphere that does not react too rapidly with the metal. The use of air for the metals of lower melting points is possible from this point of view since the rate of oxidation is fairly low and, if the boat is accessible, the oxide can be skimmed off periodically. For the metals that oxidize too rapidly at temperatures a little above their melting points, it is necessary to enclose the boat in a space in which the desired atmosphere can be maintained; this may be done either by means of a tube which is inside the furnace, or a furnace inside a larger space. Both methods have been used. The main disadvantage in the use of a vacuum is the high rate of evaporation of some metals in a vacuum just above their melting point. This can result in excessive loss of material and in the build-up of the metal on all cool surfaces in the vacuum chamber.

If a smooth surface is required, it is necessary to mount the apparatus so that external vibrations do not cause disturbances of the surface of the liquid metal; a very convenient way of achieving this is for the boat to be supported on a platform that is suspended by strings attached to the ceiling; attachment is made by means of a vertical string at each corner, and oblique strings joining each lower corner to the two neighboring upper corners.

FIG. 6.   Bicrystal technique.

(g) Bicrystals

The techniques discussed above were developed largely to produce specimens consisting of two or three crystals, each of controlled orientation. Such specimens are called bicrystals, tricrystals, etc. The method differs only in obvious details from that described for single crystals; the seed crystals of the required orientations are first produced by the methods described above and then they are placed side by side in the boat. If the combined width of the two seeds is less than the internal width of the boat, it is desirable to separate them with a partition of the kind illustrated in Fig. 6. This is usually of the same material as the boat, but in some cases a thin piece of mica is satisfactory.

The direction of the boundary between the two crystals depends on the orientations of the crystals; this will be discussed in the next section.

3.   DIRECTION OF BOUNDARY GROWTH

It is next necessary to consider the direction in which the boundary is formed when two crystals are caused to grow side by side in the type of apparatus discussed above. This topic is important not only because it frequently determines

the success of a bicrystal experiment, but also because it is closely related to the success of attempts to produce single crystals from the melt.

Experiments on tin have shown that the direction of boundary growth is influenced both by the orientations of the crystals and by the speed of growth. Consider first the case in which one of the crystals is orientated in the way represented in Fig. 7; this method of representation will be adopted henceforth;
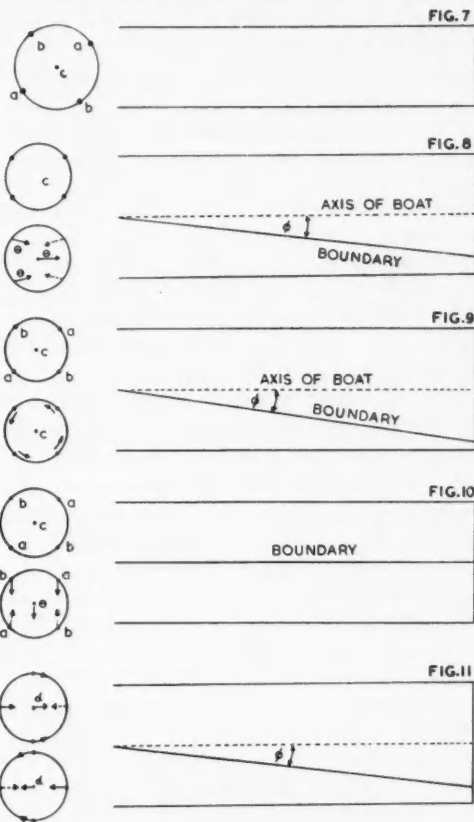

FIG. 7.   Representation of crystal orientation.
FIG. 8.   Bicrystal: rotation about transverse axis.
FIG. 9.   Bicrystal: rotation about normal axis.
FIG. 10. Bicrystal: rotation about longitudinal axis.
FIG. 11. Bicrystal: equal rotations in opposite directions.

it represents the stereographic projection of the a, b, and c axes of the crystal, the plane of the projection being the horizontal plane of the boat. Fig. 8 represents a bicrystal in which one crystal has the orientation of Fig. 7 while the second is rotated through an angle θ. The boundary forms an angle ϕ, which increases with the angle θ but is not sensitive to the speed of solidification.

A second type of rotation is shown in Fig. 9. In this case, the angle ϕ increases with both the speed and the angle θ. The third possible rotation of the second crystal is shown in Fig. 10. In this case, the angle ϕ is zero. This is because both the crystals present the same crystallographic surface to the liquid while growth is taking place. This results in the formation of a boundary parallel to the axis of the boat, when both the crystals have directions of growth that are parallel to this axis. It is, therefore, necessary to consider briefly what is meant by the direction of growth of a crystal. Investigations by Teghtsoonian and Chalmers (7) and by Rutter and Chalmers (6) have shown that two types of substructure are formed during the process of freezing; they are described respectively as "striations" and "corrugations". It has been shown that the walls separating one unit of the substructure from the neighboring one make an angle with the direction of heat flow in the boat that depends on the orientation and the speed of growth. In the case of tin, the striations and the corrugations are parallel to the direction of heat flow when the orientation is that represented in Fig. 7, but when the orientation is changed by either of the rotations shown in Figs. 8 and 9, the direction depends on the angle θ and in the case of Fig. 9 on the speed. It is regarded as reasonable to consider that the real direction of growth of the crystal coincides with the direction of the striations and the corrugations, and is therefore not necessarily identical with the direction of heat flow. The only orientation in which the direction of growth coincides with the direction of heat flow at all speeds is the one shown in Fig. 7; for other orientations, the direction of growth is parallel to the heat flow at low speeds and at higher speeds it approaches progressively towards the [110] direction. This is also the direction in which dendritic growth takes place.

It is observed experimentally that the conditions for growth of single crystals are less critical when they are grown in this orientation than for any other; it is described as the "direction of easy growth". It is found that the direction of easy growth always coincides with the direction of dendrite growth and with the direction towards which crystal growth tends at high speeds in the few cases that have been studied comprehensively. The directions are given below for the cases in which they are known.

Structure	Direction of preferred growth
Face centered cubic	[100]
Hexagonal close packed	[1010]
Tetragonal (tin)	[110]

The direction of the formation of a crystal boundary is completely controlled by the direction of crystal growth in cases in which the orientations of the two crystals are similarly inclined to the direction of heat flow; for example, in the special case illustrated in Fig. 11, the boundary between the two crystals follows the same direction as the striations and the corrugations in the two crystals; at low speeds the boundary will be along the direction of heat flow while at higher speeds it will deviate to an increasing extent as the speed increases. When the directions of easy growth of the two crystals are not identical, the boundary

forms in a direction that depends on these two directions and on the speed in a way that has not yet been investigated.

In addition to the cases discussed above in which the boundary is at least macroscopically smooth, there are some conditions in which the boundary is not smooth. This occurs when the boundary is formed between two dendrites, and it also occurs under other circumstances that have not been definitely established; it is probable that the conditions are that the striations in the two crystals converge towards the boundary so that a very small angle is formed between them.

The conditions outlined above make it possible to produce bicrystal specimens in which the boundary is parallel to the length of the specimen, or to produce tricrystal specimens in which three boundaries meet in a line. Specimens of this kind have been used for studies of the specific energy of crystal boundaries (1).

4. FORMATION OF "STRAY CRYSTALS"

(a) General

The main difficulty in growing single crystals is the fact that "stray crystals" or "strays" sometimes form during the process of freezing. The following analysis of the conditions that govern the formation of strays is consistent with a very large number of observations on a variety of metals, and while it is only qualitative, it is believed to form a useful guide in determining the conditions that will yield a reasonable proportion of successful single crystals or bicrystals.

A "stray" is a crystal of different orientation from that of the seed from which the crystal is being grown. It follows that the stray grows from a nucleus that is crystallographically independent of the growing crystal. In order that a stray may be observed in the final crystal, it must first nucleate and it must then grow. These two aspects will be considered in turn. It is evident from the moderate amounts of supercooling that are observed in experiments such as those of Weinberg and Chalmers (8) that the nucleation that is responsible for the formation of strays must be heterogeneous nucleation; it follows that a stray can only be developed when a nucleus is present and there is sufficient supercooling for that nucleus to be effective. It is observed that most, if not all, strays nucleate at a surface of the specimen, and it is concluded that the nucleus is either a suitable region of the surface of the boat or else it is a particle of oxide or other solid matter that is floating on the surface of the liquid metal. The material and the geometry of the boat no doubt have some effect on the probability of nucleation taking place there, and it is possible that this should be considered more closely when a boat material is being selected. The second condition for nucleation of strays, namely the existence of supercooling, may arise in several ways, as follows: (1) supercooling due to finite rate of freezing, (2) supercooling due to impurities, (3) supercooling due to conduction of heat through the boat instead of through the solid metal, (4) supercooling due to local heat loss from the surface of the liquid metal.

(1) The freezing point of a metal is the temperature at which the solid and the liquid are in equilibrium. If freezing is taking place, it follows that the con-

ditions are not those of equilibrium, and the liquid adjacent to the interface between the solid and the liquid must be below the equilibrium freezing point. The extent to which the interface is below the true freezing point is a function of the rate of advance of the interface—that is, of the rate of freezing. The probability of nucleation taking place in the supercooled layer of liquid can be considered as follows: Fig. 12 represents the variation of temperature along a
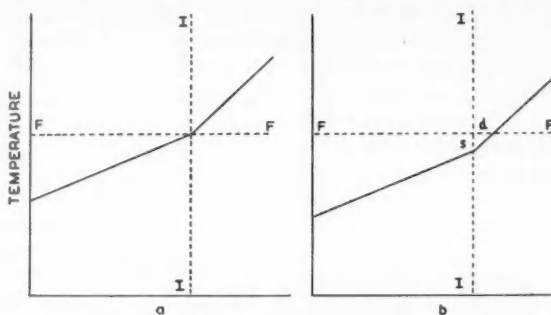

FIG. 12.   Supercooling at the interface.

boat; the line FF is at the true freezing point of the metal. It represents the position of the interface between the solid and the liquid. Fig. 12a represents the conditions when the interface is stationary—i.e., equilibrium conditions. Fig. 12b corresponds to the case when the liquid is freezing. The interface is at a temperature S below the freezing point, and the liquid is supercooled for a distance d from the interface. It is probably roughly correct to suppose that the probability P of nucleation in a given element of volume of liquid is proportional to the amount of supercooling and to the time during which it is supercooled. This would be represented by $\int s\,dt$, where s is the instantaneous amount of supercooling and dt is the time during which that amount of supercooling is maintained. The limits of the integration will be the maximum amount of supercooling S and 0. If it is assumed that S is proportional to the speed of freezing, so that $S = AV$, where V is the speed of freezing, and that the temperature gradient in the liquid is B, then

$$P = \int_0^S s\,dt = \frac{1}{2}\,St = \frac{1}{2}\,\frac{S^2}{BV}$$

from which

$$P = \frac{A^2 V}{2B}.$$

It follows that the probability of nucleation of this type is increased by increasing the speed of freezing, and reduced by increasing the temperature gradient in the liquid. It is not known how important this effect really is since the effect of impurities would be superimposed and in real cases probably exerts a controlling influence.

(2) The effects of impurities must be considered in relation to their effects on the liquidus and solidus temperatures; we will consider an example in which an impurity is present to a small enough extent to be completely soluble in the solid when it is formed, and for which the phase diagram is of the type shown in Fig. 13. Let us suppose that the composition of the impure metal is A. Let us now suppose that freezing takes place infinitely slowly, so that, at any instant, the whole of the solid has the same composition, as a result of diffusion, and that the liquid is also homogeneous. When one half of the material has frozen under such conditions, the whole of the liquid will have the composition L, while the whole of the solid will be of composition S. The remaining liquid, therefore, contains a greater proportion of solute than was in the original liquid.
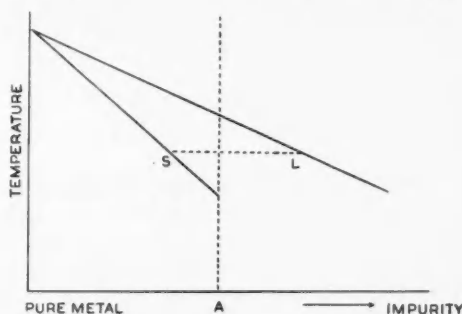
Fig. 13. Effect of an impurity on the melting point.

At any finite rate of freezing, there would not be sufficient time for the homogeneity of the liquid to be maintained; the distribution of solute in the liquid would, therefore, be modified, as shown in Fig. 14, which represents the distribution of solute along the length of the boat. In Fig. 14a, the conditions represented are those of equilibrium, while Fig. 14b represents a case in which the interface is advancing at a finite rate into the liquid; in such a case, the liquid changes its concentration only for a short distance in front of the advancing interface. Since the liquidus temperature depends on the concentration, the two curves of Fig. 14 can be replotted as liquidus against position, Fig. 15.

The real case is shown in Fig. 15, in which the continuous line represents the liquidus of the liquid and the broken line aa represents the temperature distribution in the liquid, on the assumption that freezing takes place at the equilibrium liquidus temperature; if this assumption is not made, and the effect of a finite rate of freezing is taken into account, then the actual temperature distribution is given by the line bb. It will be seen that a larger volume of liquid is supercooled than was the case for the pure liquid. This will increase the value of P, and the extent of this increase will be roughly proportional to the amount of the impurity present. The effect of speed will be even more important than with the pure metal, as lower speed will now have the effect of flattening out the "hump" on the concentration curve, and this will reduce the amount of super-
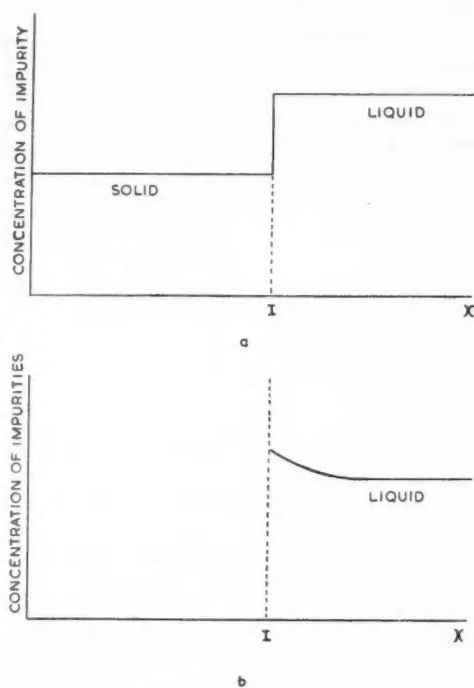
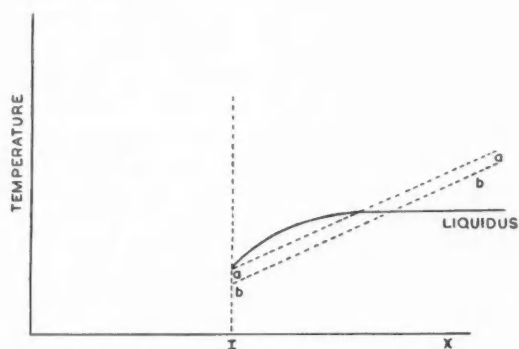FIG. 14.   Distribution of impurity: (a) interface stationary, (b) interface advancing.

FIG. 15.   Temperature distribution in the liquid.

cooled liquid, and so will reduce P. The advantage of a steep temperature gradient in the liquid is also explained. Consider the two temperature distribution lines bb and bb_1 in Fig. 16; it is evident that there is much less supercooled liquid when the temperature gradient is steep (bb_1) than when it is less steep (bb).
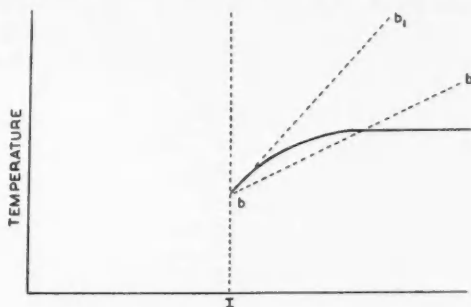

FIG. 16.   Effect of changing temperature gradient.

It follows from the foregoing, and it is amply established by experiment, that a low speed, a steep temperature gradient, and a pure metal are the desirable conditions. There are, however, a variety of reasons which may prevent these conditions from being sufficiently closely adhered to, and it is next necessary to consider how the material and design of the boat can influence the nucleation of strays.

(b) *Nucleation on the Boat*

The two types of supercooling that have been discussed above can occur quite remotely from the edge of the growing interface; they are a direct result of the fact that heat is conducted through the interface from the liquid into the solid. It is also possible, and perhaps much more common, that the loss of heat that is required to cause supercooling is at least contributed to by the lateral loss of heat that can occur through the boat or from the free (upper) surface of the metal. The former of these possibilities, namely the cooling of the surface of the liquid metal by contact with the boat, depends on the thermal conductivity of the material of the boat and on the temperature distribution across the cross section of the boat and the metal in it. Fig. 17 shows two possible shapes of interface and the corresponding isothermal surfaces in the boat. In Fig. 17a the boat is at a higher temperature than the adjacent liquid at all points near the interface; it is unlikely in such a case that there will be nucleation in the liquid near the edge of the boat; on the other hand, Fig. 17b shows the reverse case in which the boat is cooler than the adjacent liquid and it is much more probable that nucleation will be induced by the boat in such conditions. In the apparatus used for the production of single crystals by the method under discussion, heat is supplied locally at the hot end of the boat, and cooling is usually due to convection and radiation from the cooler end of the boat. It follows that the desirable condition, Fig. 17a, will be produced if the radial or outward flow of heat from

the metal to the outside is kept to a minimum compared to the longitudinal heat flow in the metal and the boat. In practice, this means that a boat of graphite, which has quite a high thermal conductivity, is satisfactory, from the thermal point of view, for metals which themselves have a high thermal conductivity, such as copper and silver. Difficulties arise with zinc, for example, unless the lateral heat loss is limited either by coating the cooler half of the boat with a refractory layer or by lining the inside of the boat with a separate thin graphite lining (3).
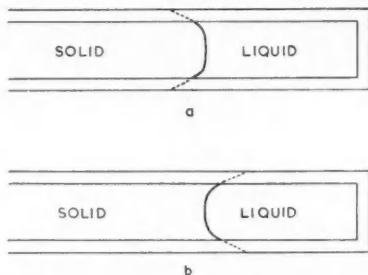
FIG. 17. Possible shapes of the interface.

(c) Nucleation at the Free Surface

When the surface of the metal is clean — i.e., free from oxide — its emissivity is low and little heat is lost from it; there is, therefore, little or no supercooling as a result of loss of heat from the surface, and stray crystals are not nucleated there; however, when there is a layer of oxide, the emissivity of the surface is increased and the loss of heat from the surface, and therefore the local supercooling, is increased. This increases the chance of nucleation of stray crystals. This is particularly noticeable when the oxide is present in small isolated particles, which have often been found to be associated with the initiation of stray crystals.

(d) Growth of Strays

The question of whether a stray that nucleates will grow or will be suppressed depends on two factors, namely the shape of the solid–liquid interface and the direction of the boundaries between the stray and the crystal in which it is growing.

Let us consider first the effect of the shape of the solid–liquid interface, and let us assume that the boundary between the stray and the crystal is always perpendicular to the interface. This assumption, which is not always true, will be reconsidered below.

Consider the three cases shown in Fig. 18, in which three different shapes of interface are shown. In each case, it is supposed that nucleation takes place at the point A. The direction of formation of the boundary, supposed to be perpendicular to the interface, is represented by the line AB in each case. It will be seen that the stray will increase in width as growth proceeds in Fig. 18a; in Fig. 18b it will remain of the same very small width which it has when it is

formed, while in Fig. 18c, it will immediately reach zero width. Thus, the concave interface of Fig. 18a is the only one in which the stray will grow. If it does not grow, it will disappear as a result of the movement of the boundary towards its center of curvature. It will be observed that the shape of interface shown in Fig. 18a is also the only one in which surface nucleation is likely to take place.
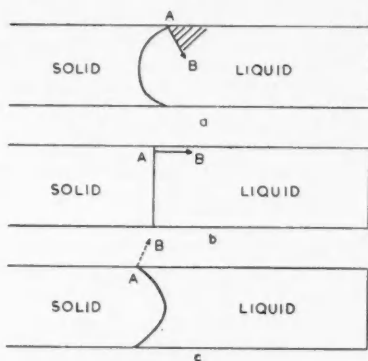

FIG. 18.   Effect of interface shape on the survival of strays.

It has already been shown that the boundary does not always grow in a direction perpendicular to the interface, although it always tends to do so at very low speeds of growth. At higher speeds, it tends to slope into the crystal whose orientation departs the most from the "orientation of easy growth", that is, the orientation in which the direction of easy growth is perpendicular to the interface. The result of this state of affairs is shown in Fig. 19, in which a crystal

FIG. 19.   Effect of relative orientation on survival of strays.

is supposed to be growing with a plane interface. Two nuclei N_1 and N_2 are considered to form with orientations such that N_1 is nearer to the direction of easy growth than the main crystal, while N_2 is further from it. The directions of formation of the boundaries between the strays and the crystal are shown by the arrows. The angle 2ϕ decreases as the speed is reduced. It follows that strays will only grow at a flat interface if they are more favorably oriented than the crystal. The probability of such nuclei forming is less as the crystal is nearer to the direction of easy growth. This explains why it becomes progressively more difficult to grow a single crystal as the required orientation departs more from the most favorable direction. It will also be apparent that the shape of the interface is much less critical when the crystal is at or near the most favorable orientation, and that it is much more important as the orientation departs further from it.

It should also be noted that the interface should be convex not only in the horizontal plane as illustrated in Fig. 18*a*, but it should also be convex in the vertical plane. This can only be verified by decanting the liquid so as to expose the whole of the interface.

Two common observations are explained on the basis of the principles discussed above; in the first place, it is found to be much easier to grow "thick" single crystals (of the order of 1 cm.² cross section) than thin ones (less than 1 mm.² cross section). This is because the convexity of the interface depends on the ratio of the heat lost radially from the specimen to the heat conducted longitudinally through the interface from the liquid into the solid. A thin cylinder has a higher surface to volume ratio than a thick one, and so is less likely to have a convex interface. Secondly, it has often been pointed out that single crystals grown without seeding have a strongly preferred orientation; this is accounted for by the fact that, if several nuclei are formed at the same time, at the region where freezing commences, and grow competitively, the one that most closely approaches the orientation of easiest growth is the one that will survive.

Finally, it is found that the preferred orientations that have been reported in connection with the columnar zone in castings can be accounted for in terms of the competitive growth of crystals of different orientations; in all the cases that have been examined so far, the observations have agreed with the deductions from the views expressed above.

ACKNOWLEDGMENTS

REFERENCES

1. AUST, K. T. and CHALMERS, B.   Proc. Roy. Soc. (London), A, 201: 210.   1950.
2. CHALMERS, B.   Proc. Roy. Soc. (London), A, 196: 64.   1949.
3. CRAIG, G. B. and CHALMERS, B.   To be published.
4. GOW, K. V. and CHALMERS, B.   Brit. J. Applied Phys. 2: 300.   1951.
5. GRENINGER, A. B.   Trans. Am. Inst. Mining Metal. Engrs. 117: 61.   1935.
6. RUTTER, J. and CHALMERS, B.   Can. J. Phys. 31: 15.   1953.
7. TEGHTSOONIAN, E. and CHALMERS, B.   Can. J. Phys. 29: 370.   1951.
8. WEINBERG, F. and CHALMERS, B.   Can. J. Phys. 29: 382.   1951.

ON θ VALUES IN METALS[1]

BY F. M. KELLY AND D. K. C. MACDONALD

ABSTRACT

Following a discussion of specific heat theories, it is suggested that, despite its limitations, the Debye theory is the most useful representation for general analysis. Four methods of calculating θ_D, the Debye characteristic temperature, are presented; specific heat data of lithium, sodium, and potassium are then analyzed and also compared with similar calculations of θ_R from resistance measurements made over a wide temperature range. It is shown that more realistic values of θ are obtained when θ is recognized as a temperature-dependent parameter in the mathematical derivation of the relevant equations. It appears that a considerable amount of useful information may be obtained from data analysis in this way.

I. INTRODUCTION

Many macroscopic properties of solid bodies are expressible within limits by a homogeneous function of θ/T where θ is a characteristic temperature and T the absolute temperature. The most commonly quoted characteristic temperature is the one introduced in the Debye theory of specific heats (10). A number of authors (e.g. Born and v. Kármán (6), Blackman (2, 3, 4), and Brillouin (8)) have pointed out that the Debye theory is an oversimplification. However, the extreme convenience and universality of Debye's treatment (the crystal structure and lattice parameters do not explicitly enter the theory) has led to its wide application for the presentation of experimental data. The purpose of this paper is to discuss the evaluation of the Debye characteristic temperature (θ_D), and the characteristic temperature (θ_R) which appears in the quantum theory of electrical resistance, and to compare critically the different methods of evaluating them. Data on the lighter alkali metals are presented and analyzed.

II. DISCUSSION OF LATTICE THEORIES

The first attempt to apply quantum rules to specific heats was made by Einstein (12) who assumed that each atom of the solid vibrated essentially independently with the same frequency. This very simple model leads to surprisingly good agreement with observation except at low temperatures where the theoretical values fall well below observations. Einstein himself realized (13) that the assumption of a monochromatic vibrational spectrum could only be a very rough approximation.

The Debye theory of specific heats is based on the assumption that a monatomic lattice may be treated as an isotropic elastic continuum with no dispersion of wave propagation. On this model is then imposed the condition that there is a unique maximum frequency ν_m for the modes of vibration determined by the condition that there must be in all $3N^*$ vibrational modes. This then yields a characteristic temperature θ_D, where $k\theta_D = h\nu_m$, for the metal which is the same for the longitudinal and two transverse modes of vibration.

---

*More strictly $3N - 6$.

This assumption of a single cutoff *frequency* has been criticized by Brillouin (8) who shows on general theoretical grounds that it is more realistic to use a single cutoff *wave length*. This may be appreciated qualitatively from the fact that the limiting feature for the transmission of elastic waves in the lattice is the inter-atomic distance rather than any particular frequency. Brillouin has shown that his assumption leads to equipartition in the modes, which is in agreement with a general theoretical result that in a gram molecule, the total number of vibrations for each particular type of elastic wave must be N, Avogadro's number. Debye's assumption does not provide equipartition in the modes but only the more general requirement that the over-all total number of vibrations must be equal to $3N$.

As a consequence of Brillouin's assumption of a common minimum wave length the over-all frequency distribution spectrum is changed rather radically from the simple ν^2 law of Debye to a distribution function with two or three maxima. Instead of a single Debye θ there are therefore three θ's, one for each of the two transverse modes and one for the longitudinal mode of vibration. At high temper-atures both Debye's and Brillouin's treatment naturally give the classical specific heat $C_v = 3R$. At low temperatures, also, on account of the cubic dependence of the specific heat on temperature $(C_v \propto T^3/\theta^3)$ and the general velocity relation $3/\bar{c}^3 = 1/c_l^3 + 1/c_{t_1}^3 + 1/c_{t_2}^3$, the two theories again give the same value of the specific heat. In an isotropic medium, $c_{t_1} = c_{t_2}$, and Brillouin's theory gives two maxima in the frequency distribution.

Thus far the specific lattice type has not been considered. If, however, we take into account the fact that all normal vibrations of the crystal lattice must be contained within a surface in reciprocal or momentum space characteristic of the lattice (the first Brillouin zone), then it follows (cf. Brillouin (8) and Slater (28)) that the simple ν^2 frequency density assumed obtains only so long as no wave vector has contacted the first zone boundary. Thereafter the frequency spectrum will decay progressively until the zone is finally filled with the $3N$ permitted vibrations. Only in the case of an "ideal" spherically symmetrical lattice, where the zone *itself* is then a sphere, would the cutoff be perfectly sharp.

If next the assumption of an isotropic medium is removed a clear distinction between transverse and longitudinal waves is no longer possible. Fuchs (15) has applied the Debye model to lithium but with the assumption that ν_m depends on the direction of propagation of the elastic waves, on account of the marked an-isotropy of the alkali metals (14). This assumption then also leads to an over-all frequency spectrum with a number of maxima agreeing with the simple Debye treatment only at low frequencies. In a recent paper by Post (23) the Debye method is extended to a more general anisotropic continuum. For a cubic crystal his analysis suggests that it is possible to define a *single* characteristic tempera-ture while for crystals of lower symmetry three at the most are required.

Finally, the influence of wave-velocity dispersion which is due fundamentally to the atomicity of the crystal lattice ought to be taken into account. Schrödinger (25) has suggested that the θ values determined from a continuum theory should be multiplied by a coefficient $2/\pi$ to account for the dispersion. This assumption

is based essentially on the behavior of a simple linear atomic chain (cf. Brillouin (8)). Cornish and MacDonald (9), when discussing the effect of dispersion on electrical resistance, have shown that dispersion can also produce maxima in the frequency spectrum.

The Debye theory, and the modifications mentioned above with one exception, are all based on the assumption that the crystal lattice can be replaced substantially by a continuous medium as far as the vibrations are concerned. Since they contain no reference to any particular lattice they can be applied generally. On the other hand they cannot be expected to take into account detailed lattice problems. An *exact* theory of the specific heat, etc., can only be based on a detailed dynamical treatment of the proper vibrations of the atoms in a lattice using atomic force constants. This calculation must be repeated for each type of crystal lattice and unless simplifying assumptions are made becomes extremely complicated. Almost at the same time as Debye's work, Born and v. Kármán (6) treated a cubic lattice by this method. In practice their calculations assume an isotropic medium, but the dispersion of the elastic waves is automatically taken into account by the lattice theory.

The lattice theory has been more recently extended by Blackman (2) and comparisons are made with the continuum theory. Blackman finds that "the main result has been the discovery of a number of maxima of the density of the vibrations" and suggests that some of the experimental agreement with Debye's theory is fortuitous. The conditions which a cubic crystal must fulfill in order to give a fair Debye curve are discussed. The fact that the frequency spectrum will exhibit two or more maxima has been confirmed by the work of Kellerman (18) on sodium chloride and Smith (29) on diamond.

The above outline indicates that in many ways the Debye model must be expected to be inadequate. This inadequacy is most pronounced in the frequency spectrum. However, while the serious limitations of the Debye model are fully recognized when applied to a real individual metal, it appears that it is the most suitable *general* representation for experimental data particularly appropriate for comparisons between similar metals. We wish now to present a systematic examination of the methods for *calculating* a Debye θ illustrated with experimental data obtained on the alkali metals.

III. DERIVATION OF CHARACTERISTIC TEMPERATURES

The Debye model specifies a frequency density distribution

$$[1] \qquad dn = \frac{4\pi V}{\bar{c}^3} \nu^2 \, d\nu$$

where $\bar{c}$ is the weighted mean velocity of the longitudinal and transverse waves. Using the Planck formula for the energy of a single oscillator the molar thermal energy of the Debye solid is then immediately given by:

$$U = 3RT \cdot 3(T/\theta_D)^3 \int_0^{\theta_D/T} \frac{x^3 \, dx}{e^x - 1} \text{ (omitting zero point energy)}$$

$$[2] \qquad = 3RT \cdot F(\theta_D/T)$$

where

$$F(\theta_D/T) \to 1 \text{ as } T \to \infty .$$

The zero point energy has been omitted since it does not contribute to calorimetric measurements. For the purpose of this paper the Debye characteristic temperature is defined by equation [2]. The molar specific heat is customarily obtained from this expression by (partial) differentiation with respect to temperature:

[3]
$$C_v = 3R \cdot 3(T/\theta_D)^3 \int_0^{\theta_D/T} \frac{e^x x^4 \, dx}{(e^x - 1)^2}$$
$$= 3R \cdot f(\theta_D/T)$$

where

$$f(\theta_D/T) \to 1 \text{ as } T \to \infty$$

and

$$\to (4\pi^4/5)(T/\theta_D)^3 \text{ as } T \to 0.$$

The Debye θ's in the literature are then usually derived from experimental data by comparison with equation [3].

In the foregoing differentiation of U, θ_D has been assumed constant, as would in fact be the case if a solid conformed precisely to the ideal Debye model. In practice, however, θ_D as deduced from [3] (or for that matter from [2]) varies with temperature to a greater or less degree. Moreover, the values deduced from [3] will not, in general, agree with those from [2]. Nor, indeed, would they in general agree with those derived from any other thermodynamic function, as for example the entropy (cf. Reference 17). Logically, then, equation [3] should be modified to include a term in $d\theta/dT$; or, we may integrate the observed C_v to determine U for comparison with [2].* The use of $\int C_v \, dT$ to give U at constant volume is justified in Appendix I.

A third method of determining θ_D is suggested by the ratio $C_v/(U/T)$ which is, of course, a thermodynamic function and which we shall denote by $\Sigma(T)$. This method is appropriate for comparison with an analogous method applied to the analysis of the electrical resistance of a metal. Moreover, the numerical constant, $3R$, then cancels out. The $3R$ arises from the fact that it has been assumed that the vibrations of the crystal lattice can be analyzed strictly into $3N$ normal modes. If for any reason, such as incipient vibrational anharmonicity, this assumption begins to break down, it appears then more appropriate to consider the use of this function—although strictly, of course, the basic validity of the model is now questionable.

The presence of C_v in $\Sigma(T)$ again calls for a "correction-term" in $d\theta/dT$. The

*In comparing fundamental theories (which will in general determine an energy function) with the results of experiment it is, of course, perfectly permissible to adopt any mutually consistent approach. I.e., if θ_D is taken constant in [3] for analysis of experimental data, then the same action must be taken in deriving a theoretical value.

function $\Sigma(T)$ in terms of θ_D/T has been computed from the data on the Debye function given in the Landölt-Bornstein tables and an extract is given in Table I.

TABLE I

$$\Sigma(T) = C_v/(U/T)$$

θ/T	0.0	0.1	0.2	0.3	0.4	0.5	0.6	0.7	0.8	0.9
0	1.0000	1.0381	1.0766	1.1161	1.1561	1.1972	1.2387	1.2809	1.3237	1.3671
1	1.4111	1.4555	1.5004	1.5457	1.5917	1.6376	1.6840	1.7306	1.7774	1.8243
2	1.8714	1.9186	1.9664	2.0125	2.0599	2.1065	2.1529	2.1969	2.2455	2.2914
3	2.3367	2.3827	2.4272	2.4719	2.5159	2.5592	2.6071	2.6446	2.6864	2.7276
4	2.7679	2.8082	2.8471	2.8853	2.9228	2.9602	2.9976	3.0321	3.0688	3.1024
5	3.1354	3.1680	3.1997	3.2301	3.2601	3.2893	3.3180	3.3455	3.3719	3.3978
6	3.4317	3.4505	3.4716	3.4943	3.5160	3.5383	3.5593	3.5786	3.5981	3.6165
7	3.6337	3.6508	3.6686	3.6848	3.7009	3.7155	3.7297	3.7431	3.7548	3.7672
8	3.7783	3.7895	3.7973	3.8095	3.8242	3.8313	3.8397	3.8483	3.8571	3.8654
9	3.8724	3.8811	3.8874	3.8922	3.9012	3.9049	3.9104	3.9149	3.9212	3.9248
10	3.9321									
11	3.9623									
12	3.9688									
∞	4.0000									

In this method the correction for the variation of θ_D with temperature can be made with suitable manipulation of equation [2] to obtain

[4]
$$\Sigma(T) \equiv C_v/(U/T) = 1 - \left(\frac{x}{F}\right)\frac{dF}{dx} + \frac{1}{F}\left(\frac{dF}{dx}\right)\frac{d\theta}{dT}$$

where $x = \theta/T$. A method of successive approximations must then be used to obtain a corrected θ_D from the results of method [3] where the effect of $d\theta/dT$ is now taken into account. To sum up, the four methods discussed for evaluating θ_D are tabulated below (Table II).

TABLE II

METHODS OF EVALUATING θ_D

No.	Method of obtaining θ_D	Mathematical assumption of behavior of θ_D
1	C_v: Equation [3]	Constant
2	U: Equation [2]	Variable parameter
3	$\Sigma(T) = C_v/(U/T)$: Table I	Constant
4	$\Sigma(T) = C_v/(U/T)$: Equation [4]	Variable parameter

It is then of considerable interest to compare the θ values obtained from specific heat data with those deducible from measurements of the electrical resistance. The variation of electrical resistance with temperature is given by the Bloch-Grüneisen (16) formula

[5]
$$R = \kappa \cdot \frac{T}{\theta_R^2} \cdot G\left(\frac{\theta_R}{T}\right)$$

where R is the electrical resistance, θ_R is the associated characteristic temperature, $G(\theta_R/T) \rightarrow 1$ as $T \rightarrow \infty$, and $\rightarrow 497.6(T^4/\theta^5)$ as $T \rightarrow 0$. The basic assumptions

about the character of the lattice vibrations underlying the development of this equation are similar to those in the Debye theory of specific heats.* In contrast, however, to the thermal energy where the numerical factor $(3R)$ is specified precisely, the electron-lattice interaction constant κ in equation [5] has not been determined with sufficient accuracy by theoretical means.** Thus, before θ_R can be calculated it is necessary to eliminate κ.

Four methods have been used by us to calculate the θ_R from the observed resistance: the assumptions made about the behavior of θ_R are similar to those made for θ_D and the last two methods will be found closely analogous to methods 3 and 4 for θ_D.

The first method assumes θ_R to be constant and κ is eliminated by taking the ratio of the resistance R at temperature T to the resistance R_0 at temperature T_0. In this case T_0 is usually taken as room temperature or the ice point. An initial estimate (θ_R') of θ_R is made and the process is then continued by successive approximation using the expression:

[6] $$G(\theta_R'/T) = (R/R_0) \cdot (T_0/T) \cdot G(\theta_R'/T_0).$$

Three or four approximations suffice to reach a final value of θ_R. (This method was used in earlier work by one of us (21, 19).) Alternatively, if a reference point (T_0, θ_0) can be chosen in a region *where θ is already known to be essentially constant*, then θ may be calculated immediately using:

[7] $$(T/\theta)^2 \cdot G(\theta/T) = (T/T_0) \cdot (R/R_0) \cdot \{(T_0/\theta_0)^2 \cdot G(\theta_0/T_0)\}$$

where the right-hand side can be evaluated immediately and the left-hand side can be tabulated in terms of (θ/T). This formula, in contrast to equation [6], recognizes θ intrinsically as a variable parameter. It should be noted that equations [6] and [7] assume that κ is essentially constant over a relatively wide temperature range.

The foregoing methods depend, as we have seen, somewhat critically on an appropriate choice of reference temperature. To avoid this difficulty two further methods based on the parameter $(dR/dT)/(R/T)$ at any temperature have also been used. This then corresponds directly to the use of $C_v/(U/T)$ for determining θ_D. On the other hand, it is then found that θ_R as derived in this manner can depend very critically on the slope (dR/dT); consequently the scatter may be rather great unless very accurate and closely-spaced experimental data are available.

On the assumption of a constant θ, θ_R may be deduced from the equation

[8] $$(dR/dT)/(R/T) = 1 + |(d \log G/d \log (\theta/T))|.$$

*Recent work of Rhodes (24) and Sondheimer (30) indicates that the Bloch formula is somewhat inaccurate in the region of intermediate temperatures $(T \lesssim \theta)$, but the error is not greater than $\sim 10\%$ and the over-all simplicity makes it most convenient to use. It is also assumed in all treatments to date that the conduction electrons are quasi-free. The possible deviations from equation [5]—particularly at very low temperatures—which might arise from this source have not yet been established with certainty (cf. (31) and (32)), although it seems very probable that an apparent fall in θ_R at low temperatures can arise in this manner.

**κ is a parameter which varies from metal to metal, involving specific assumptions about the degree of freedom of the conduction electrons, etc.

The function on the right-hand side of this equation has been calculated from the data given by Grüneisen (16) and in Figs. 1 and 2 is plotted against θ/T to facilitate the determination of θ_R.
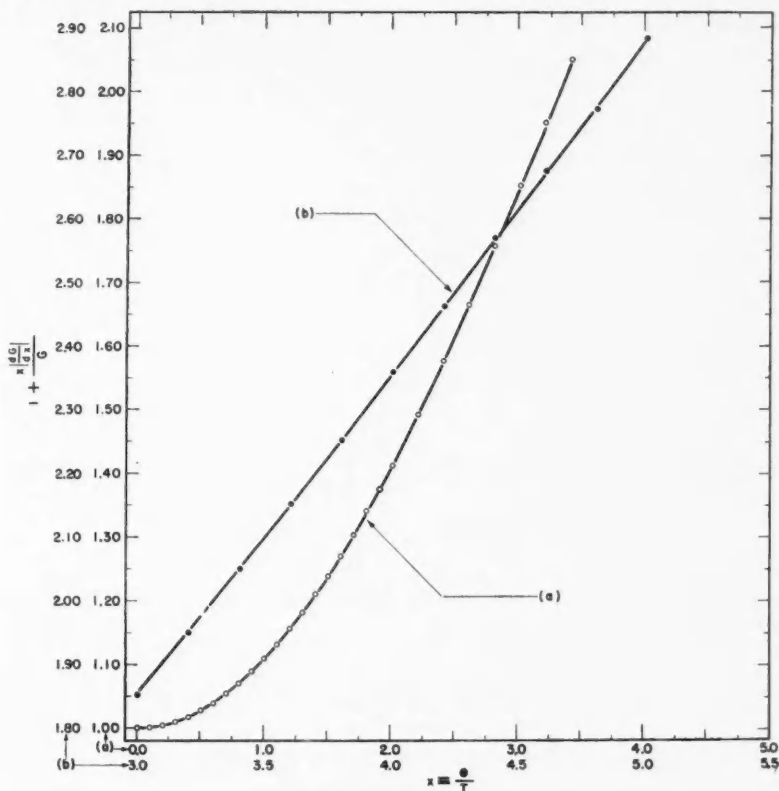

FIG. 1. $1 + \left|\dfrac{d \log G}{d \log x}\right|$ for $x = 0.0$ to 5.5 $(x = \theta/T)$.

If now θ_R is allowed to be a temperature-dependent parameter we have in place of [8]

$$\frac{d \log R}{d \log T} = 1 + \left|\frac{d \log G}{d \log x}\right| - \frac{1}{x}\frac{d\theta}{dT}\left\{ 2 + \left|\frac{d \log G}{d \log x}\right|\right\}$$

[9]
$$= 1 + \left|\frac{d \log G}{d \log x}\right| - \frac{d \log \theta}{d \log T}\left\{ 2 + \left|\frac{d \log G}{d \log x}\right|\right\}$$

where $x = \theta/T$. The final correction term in [9] is applied by successive approximation. When either equation [8] or [9] is used much of the previous dependence of θ_R on the assumed constancy of κ is eliminated.
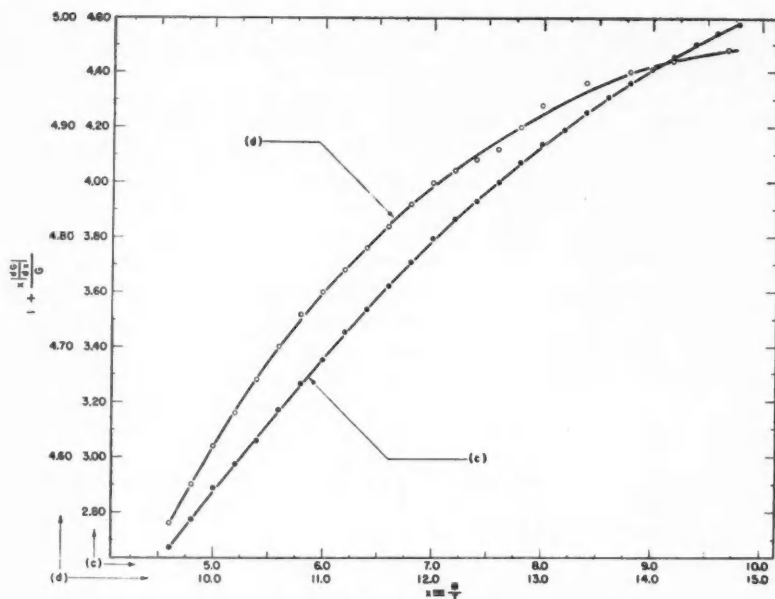
FIG. 2. $1 + \left| \dfrac{d \log G}{d \log x} \right|$ for $x = 4.0$ to 15.0 $(x = \theta/T)$.

To sum up again, the methods for determining θ_R are tabulated briefly in Table III.

TABLE III

METHODS OF EVALUATING θ_R

No.	Method of obtaining θ_R	Mathematical assumption of behavior of θ_R
1	From resistance ratio using reference temperature, Equation 6	Constant
2	From resistance ratio using reference temperature, Equation 7	Variable parameter
3	$(dR/dT) / (R/T)$, Equation 8	Constant
4	$(dR/dT) / (R/T)$, Equation 9	Variable parameter

It should be noted that the elastic waves which generally play the major part in electron scattering are the longitudinal ones. Thus, if the *Debye* model were an accurate description of the lattice, we would expect $\theta_D = \theta_R$ since in the Debye model the longitudinal and transverse modes have the same θ. In the *Brillouin* modification, however, $\theta_l > \theta_D > \theta_t$ where it has been assumed that the two transverse modes have the same θ, and we would expect $\theta_R = \theta_l > \theta_D$. (Since θ_D is determined mainly by the transverse modes, $\theta_D \doteq \theta_t$, remembering that $3/\theta_D{}^3 = 2/\theta_t{}^3 + 1/\theta_l{}^3$.) In practice, however, the Brillouin model does not appear

wholly adequate; Blackman (5) has shown that the quantitative agreement between θ_i as calculated from the elastic constants and θ_R is not good.

The electrical resistance, R, is proportional to the internal energy U since both are proportional to the mean square vibrational amplitude of the lattice (33) except at very low temperatures. Thus, as indicated above, there is a very close analogy between the functions $C_v/(U/T)$ and $(dR/dT)/(R/T)$, and consequently θ_R as derived from methods 3 and 4 (Table III) should be most suitable for comparison with θ_D from methods 3 and 4 (Table II).

IV. RESULTS

The variation of θ_D and θ_R with temperature has been determined for the monovalent alkali metals lithium, sodium, and potassium. The electrical resistance measurements were made in a Collins helium cryostat from room temperature to
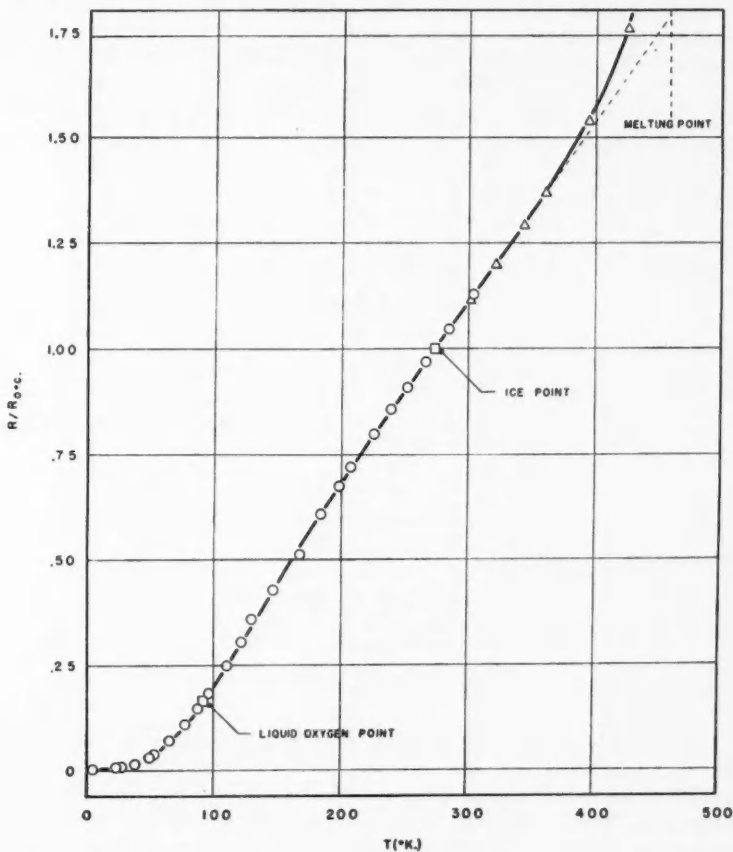
FIG. 3. Variation of electrical resistance of lithium with temperature. Two fixed temperature calibration points are shown.

helium temperature and in a paraffin bath up to the melting point of the metal (19, 20). The values of the specific heats of sodium and potassium were taken from the data of Simon and Zeidler (27) and lithium from Simon and Swain (26). While the electrical resistance of rubidium (19) and of cesium (c.f. also (21)) has also been measured in the cryostat no data on their specific heats are yet available.

(i) Lithium

The electrical resistance of lithium is given in Fig. 3 and shows no obvious anomalies in the region from helium temperatures to 300°K. The values of θ_R determined by the four methods are shown in Fig. 4.
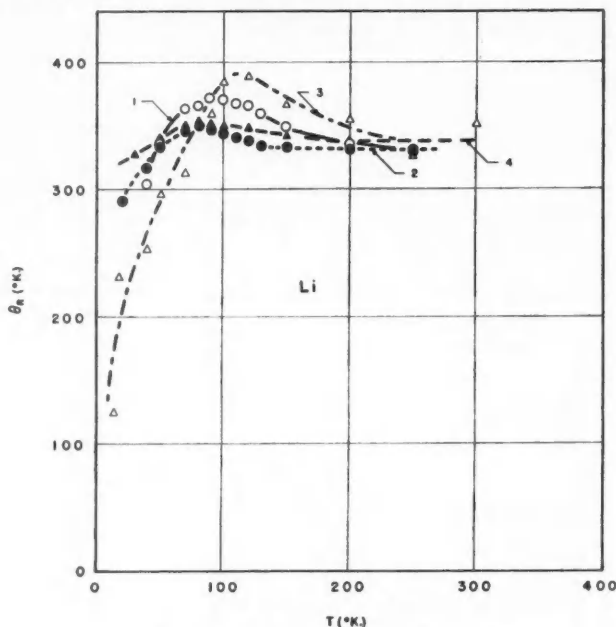
FIG. 4. θ_R for lithium. In this figure and Figs. 5-10,
Method 1: — O — O —
Method 2: - - ● - - ● - -
Method 3: - - △ - - △ - -
Method 4: - - ▲ - - ▲ - -

θ_R evaluated by means of method 1 becomes approximately constant at the highest temperatures but shows a pronounced maximum at 90°K. and falls sharply at low temperatures. The second method allows θ_R to be a temperature dependent parameter and the results show a much smaller net variation in θ_R. At the same time the position of the reduced maximum is shifted to 80°K. Method 3 results in a variation of θ_R even greater than method 1 with the maxi-

mum appearing at about 110°K. The fourth curve, which is derived using method 4, however, shows again that much of the apparent variation in θ_R arises from the assumption that θ is constant. The correction introduced by the term involving $d\theta/dT$ always tends to flatten the curve. Once more the maximum in θ_R is shifted to 80°K.

The curves obtained from methods 2 and 4 lie very close to one another. Since the results of method 2 would be affected by significant changes in κ while the results of method 4 are essentially independent of κ, it may reasonably be concluded that κ is independent of temperature in the range considered.

All four θ_R curves exhibit a maximum in the general region of 100°K. Since methods 2 and 4 allow for the temperature variation of θ_R they should give the more reliable determinations and both show the maximum of θ_R at 80°K. It appears probable that this maximum in θ_R is connected with the change in crystal structure of lithium which is believed to occur spontaneously at this temperature (1). It is particularly important to notice that no discontinuity or anomaly is apparent in the $R–T$ curve itself.

The results of the analysis of the *calorimetric* data of Simon and Swain (26) are given in Fig. 5. At the highest temperatures the values of θ_D become nearly
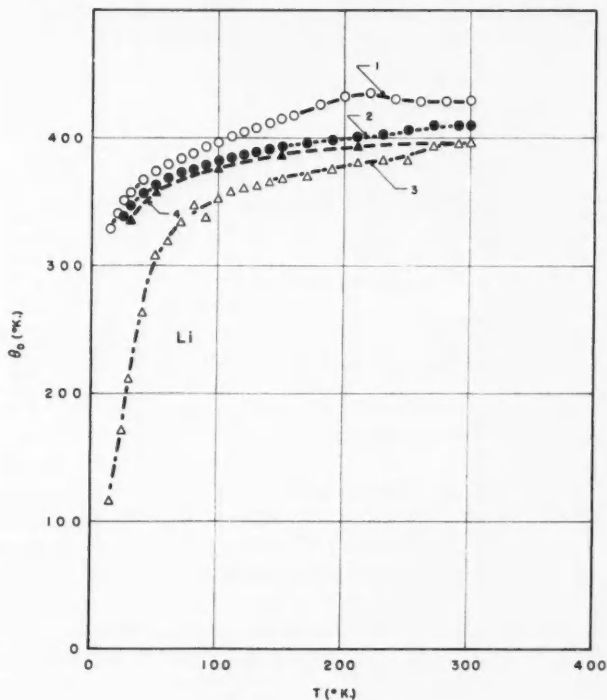
FIG. 5. θ_D for lithium.

constant while there is a rapid fall at low temperatures. However, as in the case of θ_R, much of the apparent variation of θ_D arises from the assumption of a constant θ in the equations used to derive the results.

The values of θ_D obtained from the energy U (method 2) and $C_v/(U/T)$ including the term in $d\theta/dT$ (method 4) agree within experimental error indicating that in the temperature range considered the numerical constant of equations 2 and 3 does in fact remain constant.

It should be noted that while there is a maximum in θ_R at 80°K., there is no such effect in the θ_D curve. This suggests perhaps that the cutoff wave length for the *longitudinal* vibrations on the Brillouin model goes through a minimum at this temperature during the structural change while the average cutoff wave length remains essentially unaltered.

A comparison of θ_R and θ_D from the analogous methods 3 and 4 is shown in Fig. 6. At the lowest temperature θ_R is approximately equal to θ_D while at higher
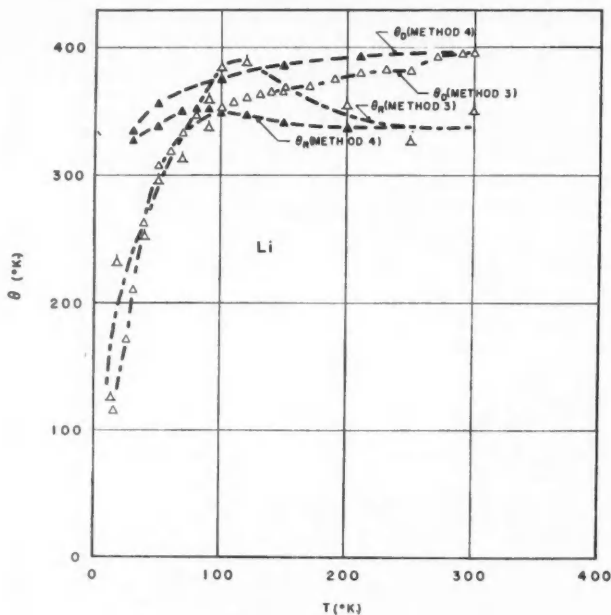
FIG. 6. Comparison of θ_R and θ_D for lithium.

temperatures $\theta_D > \theta_R$ where theory predicts $\theta_D < \theta_R$. No obvious explanation suggests itself for this very surprising behavior.

The maximum in the curve of θ_D arising from C_v at 220°K. is discussed in Appendix 2.

(ii) *Sodium*

The electrical resistance of sodium shows no anomalous behavior below 300°K. except that the straight portion of the curve does not project back through the origin (20) contrary to the prediction of the Bloch formula. This aspect of the problem may have important implications in a detailed theoretical explanation of the behavior of metals and is being examined elsewhere by Dugdale and MacDonald (11).
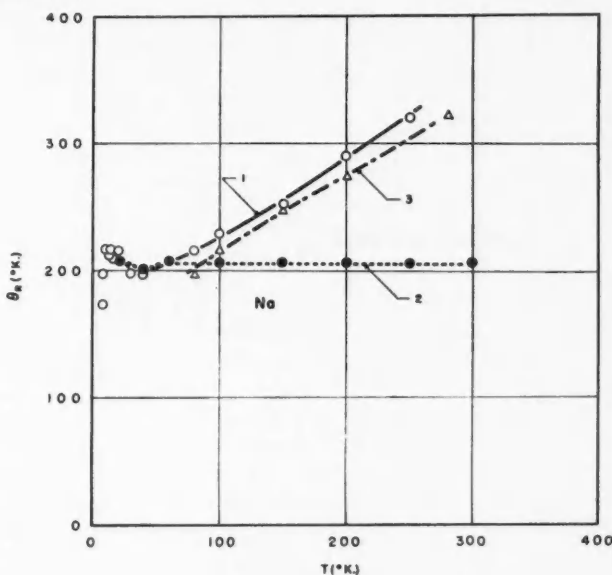
FIG. 7. θ_R for sodium.

Fig. 7 shows θ_R determined by means of the four methods. The points below 25°K. were determined from the data of MacDonald and Mendelssohn (21). Since θ_R as determined from the slope (method 3) becomes rather uncertain (see p. 152) at low temperatures, method 4 could not be applied. However, methods 1 and 2 using ratios show that much of the apparent variation of θ_R arises from the mathematical assumption of a constant θ.

The results of applying the four methods to determine θ_D for sodium are given in Fig. 8. In this case θ_D is constant at the lower temperatures.* The rapid fall in θ_D from method 1 is due to the fact that C_v becomes greater than $3R$ at approximately 200°K. It appears that more realistic values of θ_D are derived from methods 2 and 4 where θ is assumed to be a temperature dependent parameter.

Similarly to lithium, the values of θ_D derived from methods 2 and 4 lie close together suggesting that the constant of proportionality $(3R)$ in equations [2] and [3] does in fact remain constant.

*For data below 15°K. see Pickard and Simon (22).

Method 1 for obtaining θ_R indicates that θ_R is nearly constant below 60°. If we then assume that the slope (method 3) also gives a $\theta_R = 200°$ in this region the correction for $d\theta/dT$ will result in a curve of θ_R decreasing slightly with temperature and closely parallel to the curve obtained by method 2 (ratios with θ assumed to be a parameter). Thus, θ_D from method 4 would remain approximately 20% lower than θ_R in qualitative agreement with the predictions of the Brillouin model.
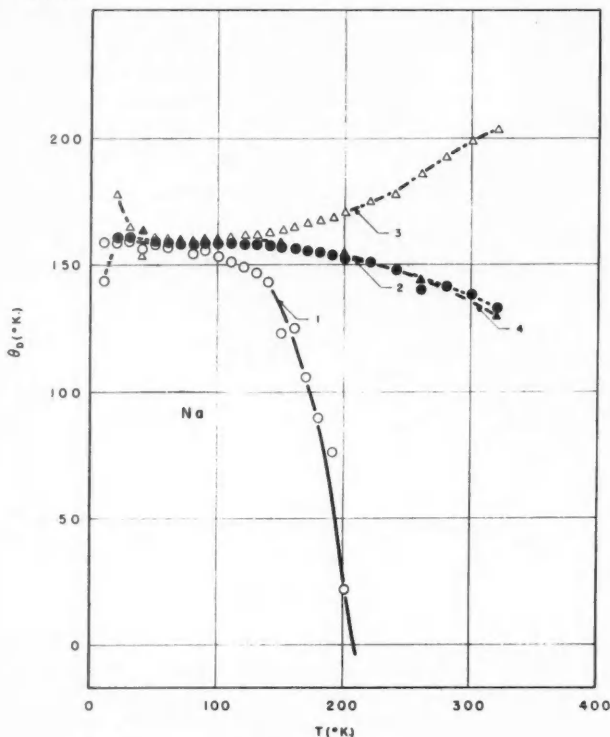
FIG. 8. θ_D for sodium.

(iii) Potassium

Above 150°K. the electrical resistance of potassium shows anomalies of the type observed in rubidium (19). This discussion of θ_R will, therefore, be confined to temperatures below 150°K.

In Fig. 9, θ_R for potassium shows a rapid drop at the lowest temperatures. Again much of this variation is due to neglecting $d\theta/dT$ in the calculation. Although the values of θ_R as obtained from methods 2 and 4 agree well at low temperatures, they diverge at higher temperatures. This suggests, in contrast to lithium and sodium, that the electron-lattice interaction constant κ does not remain constant but is now itself a significant function of temperature.
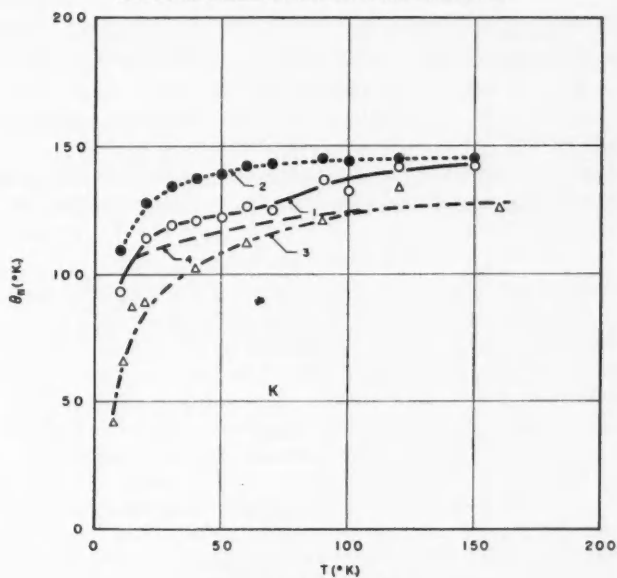
FIG. 9. θ_R for potassium.

The θ_D curves are displayed in Fig. 10. The specific heat of potassium goes above the classical value of $3R$ at 150°K. and this is reflected in the rapid fall of θ_D to zero at this temperature when θ_D is derived from C_v alone. As in the case of sodium, a much more reasonable value of θ_D can be obtained from the energy
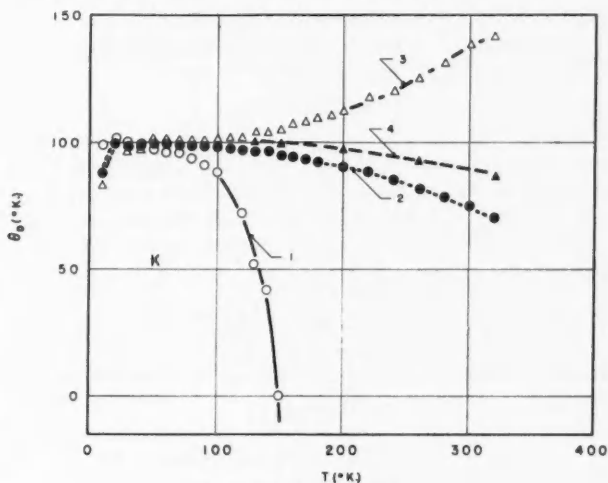
FIG. 10. θ_D for potassium.

(method 2). The results of all four methods are in agreement at low temperatures. Similarly to the behavior of θ_R, the values of θ_D calculated with methods 2 and 4 diverge at higher temperatures. This suggests that some effect takes place in potassium which causes the "constant" $3R$ to vary with temperature and which may well be related to the deviation from constancy of κ.

A comparison of θ_R and θ_D shows that except at the lowest temperatures θ_R is approximately 30% greater than θ_D again in qualitative agreement with the predictions of the Brillouin model.

V. CONCLUSIONS

The results of the calculations of θ_D and θ_R given in this paper show that the values obtained depend on the method used unless θ is strictly a constant in the temperature range under consideration. Much of the apparent variation of θ is due in fact to the use of formulae where θ has been assumed constant in the mathematical derivation. More realistic θ values over wide temperature ranges are obtained when θ is allowed to be a temperature dependent parameter. For example, above 200°K. θ_D for sodium actually becomes negative when derived conventionally from C_v, but when derived from U decreases by only some 13% up to 300°K. Before refined theories are proposed and developed to explain discrepancies in results—for example between θ_D and θ_R—care should be taken to ensure that appropriate θ values are being compared.

The systematic method of analyzing data presented here appears capable of yielding much information and suggests profitable lines of investigation. The Debye characteristic temperature appears the most suitable and convenient parameter for the general analysis of data. When applied consistently our results suggest that the simple Debye model of lattice vibrations is indeed a rather better over-all representation than might have been expected.

VI. ACKNOWLEDGMENTS

APPENDIX I

We wish to show that $U(T, V_0)$ (where V_0 is the volume at absolute zero under zero pressure) is very closely equal to $\int_0^T C_v \, dT$. Qualitatively this may be seen immediately since in the low temperature region there is negligible thermal expansion and therefore $V \doteq V_0$ while in the high temperature classical region ideally C_v is independent of V, having the classical value of $3R$.

A detailed calculation shows that

$$\Delta U = U(V) - U(V_0) = -p\left\{ T\left(\frac{\partial V}{\partial T}\right)_p + \frac{1}{2} p \left(\frac{\partial V}{\partial p}\right)_T \right\}.$$

Using data of Bridgman (7) for the compressibility of sodium, we find:

$$\Delta U = 61 \text{ cal.}$$

Now

$$U(V)(\doteq H(V)) = 1560 \text{ cal. (27)},$$

therefore

$$U(V_0) = 1499 \text{ cal.}$$

But

$$\int C_v \, dT = 1497 \text{ cal.}$$

by numerical integration, showing therefore excellent numerical agreement.

Similar calculations for potassium give equally satisfactory results.

APPENDIX II

When the values of θ_D for lithium are derived from equation 3 for C_v a definite maximum appears in the θ curve at 220°K. ((26), see also Fig. 5). There is no such maximum in the θ curve derived from equation 2 for U. It can be shown that spurious maxima in θ derived from C_v can indeed arise from neglecting terms in $d\theta/dT$.

The energy is given by equation 2:

$$U = 3RT \ F(\theta/T).$$

Differentiating with the assumption that θ is a temperature dependent parameter we obtain

[10] $$C_v = \frac{dU}{dT} = 3R \left\{ F(\theta/T) - F'(\theta/T) \cdot \left(\frac{\theta}{T} - \frac{d\theta}{dT} \right) \right\}.$$

Thus

[11] $$(C_v)_{\text{obs}} = C_v' + 3R \ F'(\theta/T) \frac{d\theta}{dT}$$

where $(C_v)_{\text{obs}}$ is the *experimentally* observed specific heat, C_v' the specific heat as conventionally computed without $d\theta/dT$, and the θ entering the equation is the "true" θ for the lattice. For reasons discussed in the text we shall take the "true" θ to be the one derived from the energy U for this discussion.
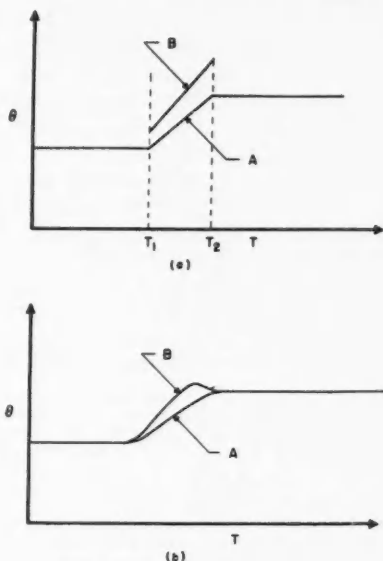
FIG. 11. Schematic curves illustrating the effect on θ of the term involving $d\theta/dT$.

In equation 11 $F'(\theta/T)$ is intrinsically negative. Hence when $d\theta/dT$ is positive the observed specific heat will be smaller than C'_v. Consequently, if we calculate θ from the observed specific heat using method 1 we will obtain a θ greater than would be obtained from method 2.

As a limiting case let us imagine that a body has a θ derived from U as shown in Fig. 11a, curve A. Then it follows that the θ derived from equation 3 for C_v' will appear as in curve B. First order discontinuities in B occur at temperatures where there is a second order discontinuity in A. When $d\theta/dT = 0$, curves A and B coincide.

In practice, smooth curves as in Fig. 11b might be expected, and these appear adequate to explain the experimental behavior of lithium.

REFERENCES

1. BARRETT, C. S. and TRAUTZ, O. R.   Trans. Am. Inst. Mining Met. Engrs. 175: 579. 1948.
2. BLACKMAN, M.   Proc. Roy. Soc. (London), A, 148: 365, 384. 1935.
3. BLACKMAN, M.   Repts. Progress Phys. 8: 11. 1941.
4. BLACKMAN, M.   Proc. Phys. Soc. (London), 54: 377. 1942.
5. BLACKMAN, M.   Proc. Phys. Soc. (London), A, 64: 681. 1951.
6. BORN, M. and v. KÁRMÁN, TH.   Physik. Z. 13: 297. 1912; 14: 15. 1913.
7. BRIDGMAN, P. W.   The physics of high pressure. George Bell & Sons Ltd., London. 1949.
8. BRILLOUIN, L.   Wave propagation in periodic structures. McGraw-Hill Book Company, Inc., New York and London. 1946.
9. CORNISH, F. H. J. and MacDONALD, D. K. C.   Phil. Mag. 42: 1406. 1951.
10. DEBYE, P.   Ann. Physik, 39: 789. 1912.
11. DUGDALE, J. S. and MacDONALD, D. K. C.   To be published.
12. EINSTEIN, A.   Ann. Physik, 22: 180 and 800. 1907.
13. EINSTEIN, A.   Ann. Physik, 35: 679. 1911.
14. FUCHS, K.   Proc. Roy. Soc. (London), A, 153: 622. 1936.
15. FUCHS, K.   Proc. Roy. Soc. (London), A, 157: 444. 1936.
16. GRÜNEISEN, E.   Ann. Physik, 16: 530. 1933.
17. GUGGENHEIM, E. A.   Thermodynamics. North Holland Publishing Co., Amsterdam. 1949. pp. 114 – 116.
18. KELLERMAN, E. W.   Trans. Roy. Soc. (London), A, 238: 513. 1940.
19. MacDONALD, D. K. C.   Phil. Mag. 43: 479. 1952.
20. MacDONALD, D. K. C. *et al.*   To be published.
21. MacDONALD, D. K. C. and MENDELSSOHN, K.   Proc. Roy. Soc. (London), A, 202: 103. 1950.
22. PICKARD, G. L. and SIMON, F. E.   Proc. Phys. Soc. (London), 61: 1. 1948.
23. POST, E. J.   Can. J. Phys. 31: 112. 1953.
24. RHODES, P.   Proc. Roy. Soc. (London), A, 202: 466. 1950.
25. SCHRÖDINGER, E.   Handbuch der Physik 10. Springer, Berlin. 1926. p. 311.
26. SIMON, F. E. and SWAIN, R. C.   Z. physik. Chem. B, 28: 189. 1935.
27. SIMON, F. E. and ZEIDLER, W.   Z. physik. Chem. B, 123: 383. 1926.
28. SLATER, J. C.   Introduction to chemical physics. McGraw-Hill Book Company, Inc., New York and London. 1939. pp. 231-233.
29. SMITH, H. M. J.   Trans. Roy. Soc. (London), A, 241: 105. 1948.
30. SONDHEIMER, E. H.   Proc. Roy. Soc. (London), A, 203: 75. 1950.
31. SUPEK, I.   Z. Physik, 117: 125. 1940.
32. VONSOVSKY, S. V. and SMIRNOV, A. A.   Physik. Z. Sowjetunion, 5: 115. 1934.
33. WILSON, A. H.   The theory of metals. Cambridge University Press, London. 1936.

NOTE

NOTE ON THE CONCEPT OF VACUUM IN QUANTUM ELECTRODYNAMICS

By F. A. Kaempffer

It is well known that certain difficulties arising from the existence of negative energy states in the relativistic theory of the electron can be avoided, according to Dirac (1), by assuming that in vacuum all states of negative energy are filled up with electrons. To make this assumption agree with experience it is further postulated that the electrons filling up the negative energy states do not produce an external field and do not give any contribution to the total energy and momentum of the system. Thus it seems, on first sight, that the introduction of Dirac's concept of vacuum means replacing a severe difficulty by an even more formidable one.

It is the purpose of this note to show that the situation in reality might not be quite as bad as that. Unfortunately there exists at present no mathematical formalism which allows one to calculate in a rigorous way the interaction energy of the completely degenerate Fermi gas representing the vacuum. The calculations presented here should therefore not be taken too seriously, as they can at best only illustrate the physical idea.

Assume, with Dirac, that in vacuum the states of negative energy are indeed filled up with electrons, say down to a lowest level of momentum P; assume further that these electrons behave in their ordinary way, i.e. that they possess mechanical energy and that they interact through the electromagnetic field. Then there exist two contributions to the total energy per unit volume of the system, calculated relativistically up to first order terms in e^2 and expressed as a function of the momentum of the lowest level $P = \sigma mc$:*

(1) The rest energy and kinetic zero-point energy of the electrons. This energy is negative and has the value

[1] $$ E_0 = - \frac{\pi c}{h^3}(mc)^4 \{\sigma(1 + \sigma^2)^{\frac{1}{2}}(1 + 2\sigma^2) - \text{arcsinh } \sigma\} $$

as is well known.

(2) The energy of the system due to the electromagnetic interaction of the electrons. This energy has the character of an exchange energy since (taking

---

* *If one believes that static interactions, i.e. interactions which do not involve emission and reabsorption of virtual photons, have a meaning in quantum electrodynamics, then there exists a third contribution of order e^2 to the total energy of the vacuum, namely the electrostatic interaction between the electrons of negative energy*

$$ E_2 = \frac{1}{2}e^2\rho^2 \iint \frac{dV\, dV'}{|\mathbf{r} - \mathbf{r}'|} $$

which cannot be evaluated or made finite without further assumptions regarding the geometrical structure of the electron. But whatever the numerical value of E_2, it will always be positive and thus support the argument put forward in this note.

into account only processes of first order in e^2) all that the electrons can do under the influence of their electromagnetic field is to make elastic collisions, in which an electron of momentum p_1 makes a transition to the state of momentum p_2, while the other electron which previously occupied this state p_2 jumps into the state p_1. Such a process amounts to an exchange of two electrons, a virtual photon of momentum $p_1 - p_2$ being emitted and reabsorbed during the transition. Using the complete Moeller interaction (2) one obtains after a somewhat lengthy though straightforward calculation for the exchange energy of the system the expression

$$[2] \qquad E_1 = \frac{\pi e^2}{h^4}(mc)^4\{6(\text{arcsinh } \sigma)^2 - 12\sigma(1 + \sigma^2)^{\frac{1}{2}} \text{ arcsinh } \sigma + 6\sigma^2 + 2\sigma^4\}.$$

Expansion yields for $\sigma \ll 1$ the well-known nonrelativistic exchange energy of the degenerate Fermi gas

$$[3] \qquad E_1^{\text{N.R.}} = -\frac{4\pi e^2}{h^4}(mc)^4\sigma^4$$

which is negative and entirely due to the Coulomb interaction of the electrons. For large σ, however, the magnetic interaction becomes dominant, E_1 turns positive, and only the last term of [2] is of importance. One sees that both E_0 and E_1 are proportional to σ^4 for large σ, but with opposite sign. It is clear, however, that one cannot expect here numerical compensation of E_0 by E_1, as even for small σ the perturbation formalism used for the calculation of E_1 does not converge (3). Furthermore problematic self-energy terms have been neglected here. Nevertheless one is tempted by the fact that E_1 turns positive for large σ to conceive of the vacuum as a state of total energy zero (or at least of minimum energy), the levels of negative energy being filled by electrons in such a way that the positive interaction energy compensates for the negative mechanical energy of the system. One should therefore expect that in a rigorous theory of the vacuum (which has not been found yet), there exists in fact a "bottom" of the Dirac sea, determined by the condition that the total energy of the vacuum be zero (or be at least a minimum), and depending on the numerical value of e^2/hc, as a comparison of the proportionality factors of E_0 and E_1 suggests. It is unlikely that the final clarification of this point can be found within the framework of contemporary quantum electrodynamics.

1. DIRAC, P. A. M.　Quantum theory, 3rd ed. Oxford University Press.　1947.
2. HEITLER, W.　Quantum theory of radiation, 2nd ed.　Oxford University Press.　1944.
　　　p. 101.
3. MACKE, W.　Z. Naturforsch. A, 5: 192.　1950.

DEPARTMENT OF PHYSICS,
UNIVERSITY OF BRITISH COLUMBIA,
VANCOUVER, B.C.

LETTERS TO THE EDITOR

Under this heading brief reports of important discoveries in physics may be published. These reports should not exceed 600 words and, for any issue, should be submitted not later than six weeks previous to the first day of the month of issue. No proof will be sent to the authors.

Some Reactions Produced in Ilford Emulsions

The beam from the 70 Mev. synchrotron at Queen's University has been used to irradiate a series of Ilford C_2 and E_1 emulsions 200 microns thick. A preliminary report on the reactions which have been identified is given below.

Using the method of momentum unbalance (1), 310 $C^{12}(\gamma,3He^4)$ stars have been identified. Corrections for surface loss have been determined experimentally and also theoretically on the basis of a simple model. Both methods give results that are in good agreement. Using the theoretical correction for surface loss and the flat spectrum between 10 and 30 Mev. found here experimentally (3), the cross-section curve shown in Fig. 1 has been calculated. It consists of two definite narrow resonances and several others whose existence is not certain on the basis of the present statistics. Agreement with the results of Goward and Wilkins (2) is as good as can be expected. Peak heights are probably low owing to a smearing-out effect caused by the width of the energy intervals used (1 Mev.). The cross-section curve for the $O^{16}(\gamma,4He^4)$ reaction shows a similar structure, but to date only 120 such stars have been measured with the corresponding photon energies varying from 21 to 54 Mev. The statistics are therefore not good enough to give the variation of the cross section with energy.

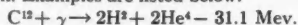CROSS SECTION FOR $C^{12} + \gamma \rightarrow 3\,He^4$ REACTION (310 STARS)
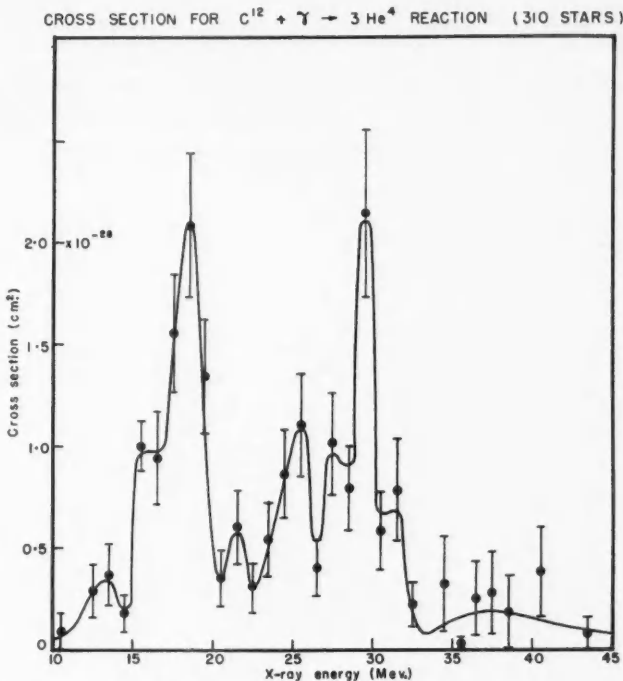
Fig. 1. Cross-section curve for the $C^{12}(\gamma, 3He^4)$ reaction. Energy intervals 1 Mev. wide have been used and probable errors indicated.

By taking suitable precautions it has been found that well over 50% of the stars observed have proton tracks. One group of such reactions is of the form proton plus alpha particle plus recoil. Several examples of each of the following reactions of this type have been identified.
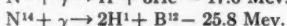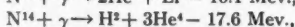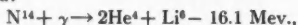
$$C^{12} + \gamma \rightarrow H^1 + He^4 + Li^7 - 24.6 \text{ Mev.}$$
$$N^{14} + \gamma \rightarrow H^1 + He^4 + Be^9 - 18.2 \text{ Mev.}$$
$$O^{16} + \gamma \rightarrow H^1 + He^4 + B^{11} - 23.2 \text{ Mev.}$$
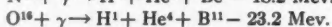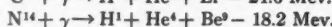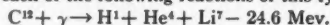
It is hoped that cross-section curves for these reactions will be obtained in course of time. These reactions, as well as the $N^{14}(\gamma, He^4)B^{10}$ and $O^{16}(\gamma, He^4)C^{12}$ reactions, can be of considerable use in determining the validity of theoretically determined range–energy relations for these recoils.

Reactions have also been identified in which, instead of an alpha particle, we get two deuterons or a proton and a triton. Examples are listed below.

$$C^{12} + \gamma \rightarrow 2H^2 + 2He^4 - 31.1 \text{ Mev.}$$
$$C^{12} + \gamma \rightarrow H^1 + H^3 + 2He^4 - 27.1 \text{ Mev.}$$
$$O^{16} + \gamma \rightarrow 2H^2 + 3He^4 - 38.4 \text{ Mev.}$$
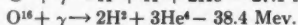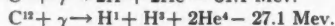
Frequently instead of a deuteron we apparently get a proton and a neutron. Reactions in which this occurs cannot be identified by the momentum unbalance method. However, one is fairly certain of their identity by a close visual examination of the star. In such cases grain counting methods will be used to discriminate between protons and deuterons.

In addition to the two reactions observed in nitrogen mentioned above, the following reactions have been identified:

$$N^{14} + \gamma \rightarrow 2He^4 + Li^6 - 16.1 \text{ Mev.,}$$
$$N^{14} + \gamma \rightarrow H^2 + 3He^4 - 17.6 \text{ Mev.,}$$
$$N^{14} + \gamma \rightarrow 2H^1 + B^{12} - 25.8 \text{ Mev.}$$

Only one example of the last-named reaction has been found. It was observed by I. B. McDiarmid. Mention of it is made because it was noticed in a G_5 emulsion, the decay electron from the B^{12} being visible. The energy of this electron was found to be 5 ± 1 Mev. from scattering measurements. This value happens to be very close to the most probable energy of the spectrum.

1. Goward, F. K. and Wilkins, J. J. Proc. Phys. Soc. (London), A, 63: 662. 1950.
2. Goward, F. K. and Wilkins, J. J. A.E.R.E. Memorandum G/M 127. 1952; Proc. Phys. Soc. (London), A, 65: 671. 1952.
3. McDiarmid, I. B. Phil. Mag. 43: 1003. 1952.

W. K. Dawson
C. B. Bigham

Synchrotron Laboratory,
Queen's University,
Kingston, Ontario.

The Half-life of Europium-152,154*

Europium-152,154 is being considered as a possible substitute for cobalt-60 in teletherapy of deep-seated cancer. The higher activation cross section and the possibly longer half-life make it very attractive. Wide deviations and uncertainties were noticed in the various values of the half-life quoted in the literature (1, 2, 3, 4, 5), and it was felt that a more definite knowledge of the decay rate of the mixed source would be worth while in view of its potential medical and industrial importance. A measurement of this decay rate is therefore being undertaken and a preliminary value has been obtained.

The source being used for the determination of the half-life is a normal europium sample irradiated in the Chalk River reactor. The gamma-ray intensity of this source is being compared with that of a 250 mgm. radium standard. The comparison is made with a high precision apparatus, the ionization chamber of which has been described by Laurence (7). This equipment is used for standardization of radium and cobalt-60 sources and the intensity ratios obtained in routine measurement have a probable error of less than 0.5%.

A careful comparison has been made at intervals of a few weeks for an observation period extending over more than 200 days. A least squares fitting of a decay curve to the data obtained indicates that the curve is reasonably linear over this period of time. The half-life of europium-152,154 corresponding to the slope is 15.6 years with a probable error of 1.5 years. This agrees with the new values of 13 ± 2 years for Eu^{152} and 16 ± 4 years for Eu^{154} obtained recently by Karraker, Hayden, and Inghram (6).

I wish to thank D. Green of the Commercial Products Division, Atomic Energy of Canada, Limited, for suggesting the need for a precise determination of the europium half-life. I also wish to thank H. Brown for his assistance in making the measurements.

1. FAJANS, K. and VOIGT, A. F.   Phys. Rev. 60: 533. 1941.
2. HAYDEN, R. J. and INGHRAM, M. G.   Phys. Rev. 71: 130. 1947.
3. HAYDEN, R. J., REYNOLDS, J. R., and INGHRAM, M. G.   Phys. Rev. 75: 1500. 1949.
4. HEIN, R. E.   I.S.C.-110, 7, *In* Nuclear Data, Natl. Bur. Standards, Circular 499, Suppl. 2, 1951.
5. KRISBERG, N. L., POOL, M. L., and HIBDON, C. T.   Phys. Rev. 74: 44. 1948.
6. KARRAKER, D. G., HAYDEN, R. J., and INGHRAM, M. G.   Phys. Rev. 87: 901. 1952.
7. LAURENCE, G. C.   Can. J. Research, 7: 103. 1932.

CANADIAN JOURNAL OF PHYSICS

Notice to Contributors

GENERAL: Manuscripts should be typewritten, double spaced, and the **original and one extra copy** submitted. Style, arrangement, spelling, and abbreviations should conform to the usage of this Journal. Names of all simple compounds, rather than their formulas, should be used in the text. Greek letters or unusual signs should be written plainly or explained by marginal notes. Superscripts and subscripts must be legible and carefully placed. Manuscripts should be carefully checked before being submitted, to reduce the need for changes after the type has been set. If authors require changes to be made after the type is set, they will be charged for changes that are considered to be excessive. **All pages, whether text, figures, or tables, should be numbered.**

ABSTRACT: **An abstract of not more than about 200 words, indicating the scope of the work and the principal findings, is required.**

ILLUSTRATIONS:

(i) *Line Drawings:* All lines should be of sufficient thickness to reproduce well. Drawings should be carefully made with India ink on white drawing paper, blue tracing linen, or co-ordinate paper **ruled in blue only**; any co-ordinate lines that are to appear in the reproduction should be ruled in black ink. Paper ruled in **green, yellow, or red should not be used** unless it is desired to have all the co-ordinate lines show. Lettering and numerals should be neatly done in India ink preferably with a stencil (**do not use typewriting**) and be of such size that they will be legible and not less than one millimeter in height when reproduced in a cut three inches wide. All experimental points should be carefully drawn with instruments. Illustrations need not be more than two or three times the size of the desired reproduction, but the ratio of height to width should conform with that of the type page. **The original drawings and one set of small but clear photographic copies are to be submitted.**

(ii) *Photographs:* Prints should be made on glossy paper, with strong contrasts; they should be trimmed to remove all extraneous material so that essential features only are shown. Photographs should be submitted **in duplicate**; if they are to be reproduced in groups, one set should be so arranged and mounted on cardboard with rubber cement; the duplicate set should be unmounted.

(iii) *General:* **The author's name, title of paper, and figure number should be written in the lower left hand corner (outside the illustration proper) of the sheets on which the illustrations appear.** Captions should not be written on the illustrations, but typed together at the end of the manuscript. All figures (including each figure of the plates) should be numbered consecutively from 1 up (arabic numerals). **Each figure should be referred to in the text.** If authors desire to alter a cut, they will be charged for the new cut.

TABLES: Each table should be typed on a separate sheet. Titles should be given for all tables, which should be numbered in Roman numerals. Column heads should be brief and textual matter in tables confined to a minimum. **Each table should be referred to in the text.**

REFERENCES: **These should be listed alphabetically by authors' names, numbered in that order, and placed at the end of the paper.** The form of literature citation should be that used in this Journal. **Titles of papers should not be given.** The first page only of the references cited should be given. **All citations should be checked with the original articles.** Each citation should be referred to in the text by means of the key number.

REPRINTS: A total of 50 reprints of each paper, without covers, are supplied free to the authors. Additional reprints will be supplied according to a prescribed schedule of charges. On request, covers can be supplied at cost.

Approximate charges for reprints may be calculated from the number of printed pages, obtained by multiplying by 0.6 the number of manuscript pages (double-spaced typewritten sheets, $8\frac{1}{2}$ in. by 11 in.) and making allowance for space occupied by line drawings and half-tones (not inserts). The cost per page is tabulated at the back of the reprint request form sent with the galley.

Contents